Development of Nitrogen Doped Resorcinol-Formaldehyde Gels for Carbon Capture

Ivan Alejandro Principe

Thesis submitted to the University of Strathclyde for the degree of Doctor of Philosophy

Department of Chemical and Process Engineering

University of Strathclyde

2017

Acknowledgments

I would like to thank a number of people for their support and help which was essential to complete this work and this stage of my education and life.

Firstly, I would like to thanks sincerely to my supervisor Dr. Ashleigh Fletcher. It would not have been possible to complete this work had it not been for her support, guidance and advices through all the process. My sincere gratitude.

I would also like to thanks Dr. Miguel Jorge for his help and contribution to my work. I want to extend my gratitude to the Chemical Engineering department and a special mention to the Chemical Engineering lab technicians, Jim Murphy, Ian Airdrie and Christopher Jones for their help and guidance in the usage of lab equipment.

I would also like to thank my colleagues and friends in the Chemical Engineering Department and my colleagues within my research group. A special mention to Francesco Pelizza, Vincenzo Infante, Maryam Derkani and Javier Cardona, this time would have not been the same without you.

Finally, I have to thank my family and particularly, the most important people in my life, my parents, my sister and my grandmothers, and my fiancée, for always believing in me and encouraging me for self-improvement, I would not have accomplished it had it not been for you. I also want to thank my fiancée for her support and help, and for being with me during the most stressful and difficult times as well, this would not have been possible without you.

‘This thesis is the result of the author’s original research. It has been composed by the author and has not been previously submitted for examination which has led to the award of a degree.’

Signed:

Date:

Abstract

Resorcinol-Formaldehyde (RF) xerogels are organic materials that have been widely studied due to their industrially relevant characteristics, such as high surface areas, suitable pore size and pore volume on which target species can be adsorbed; additionally, RF gels have significant potential to be tailored to specific applications, including catalysis, thermal insulation, filtration, energy storage, and gas treatment, especially CO_2 capture.

This research focuses on controlling the chemical and physical properties, on both the macroscopic and microscopic scale, with an investigation into the effect these changes have on the application of these xerogels as carbon capture materials. Xerogel properties have been tailored, within this study, by altering the synthesis procedure with focus on monomer concentrations and catalyst to monomer ratio.

Nitrogen has been incorporated into the gel structure in order to enhance the favourable Lewis acid-base interactions with CO_2. Melamine (M) is used in order to incorporate Nitrogen (N) into the gel structure; and partially replace the Resorcinol (R) traditionally used, resulting in a Melamine-Resorcinol-Formaldehyde (MRF) gel. Repeatability is crucial to method development and validation was achieved by the preparation of a number of gels using a variety of synthetic conditions and process routes.

There are a number of parameters that can be altered when synthesising a gel, namely, R/C (catalyst) and R/F molar ratios, concentration of M, solids content, solution pH, catalyst, solvent, temperature, time, and agitation. This research aims to tailor the gel structure (pore size and volume, surface area, etc.) to enhance the CO_2 adsorption capacity and kinetic performance. It will also be important to obtain a better understanding of the N-CO_2 interaction. Amongst all the parameters mentioned above, there are two main aspects influencing the sol-gel chemistry of xerogels synthesised by base catalysed routes, which are the concentration of monomers and catalyst, and the initial pH of the sol. Hence, R/C and R/F molar ratios, and M concentration, were chosen for in depth analysis. These factors were varied and their effect on gel properties characterised, allowing a better understanding of how gel characteristics can be tailored and their impact on gel performance. The remaining parameters were held constant throughout the experiments. RF gels produced were subsequently characterised using volumetric and gravimetric analysis to determine porous structure and quantify CO_2 capture capacities and kinetics.

The results obtained indicate that the family of materials synthesised in this study offer potential routes for carbon capture materials, through a combination of micropore structure development and incorporation of favourable Lewis acid-base interactions between MRF sorbents surface and CO_2 molecules.

This work has demonstrated that CO_2 adsorption capacities of MRF xerogels have been enhanced as a consequence of incorporating nitrogen functionalities into their structure. This is important because the amount of sorbent required for a given uptake is reduced, which is a key factor for industrial applications given that volumes of equipment and vessels needed for MRF xerogels reduce in comparison to RF materials.

The incorporation of melamine have been found to impact the structure of MRF xerogels similarly as R/C. Increasing the melamine content tend to reduce surface area while pore size and pore volume increase. However, the nitrogen functionalities on the surface of MRF xerogels promote successful interactions with CO_2 molecules, resulting in higher capacities. Additionally, it was observed that higher R/F (0.75 and 1.0) results in weaker crosslinking and, consequently, the probabilities of gelation failing are high and, also, pore size becomes a random parameter. On the contrary, low R/F (0.25 and 0.5) offers a better control for pore size.

Additionally, a fast kinetics of adsorption and desorption have been observed for MRF materials. Cycling studies have been performed using MRF xerogels, which have demonstrated high stability to cycling and an enhanced working capacity compared to RF sorbents. On another matter, flue gases are a complex mixture of different species, therefore, CO_2 selectivity have been tested for MRF sorbents using different binary systems, and results show a significant increase, compared to RF xerogels.

Table of Contents

List of Figures

List of Tables

List of Schemes

List of Reactions

Chapter 1

Introduction

1 Introduction

The greenhouse gas (GHG) effect results from the accumulation of gases in the atmosphere, which increases the global temperature by trapping heat. GHGs emit and absorb radiation in the range of the thermal infrared. This mechanism works in the way that these gases let through most of the incoming solar radiation, which heats the Earth's surface. These gases also impede part of the outgoing energy to be emitted to space; therefore part of this heat gets trapped in the Earth's atmosphere. Consequently, GHG makes the Earth habitable given that, because of their presence in the atmosphere, the global temperature is on average 15 °C, which would drop to about -18 °C without the GHG effect [1].

However, since the industrial revolution and the associated increase in the use of fossil fuels, the GHG concentration in the atmosphere has increased considerably, up to the point that if this upward trend continues then the global temperature would also inevitably continue to increase, and the consequences for Earth's habitability would be devastating, with major impacts on ecosystems, biodiversity and the livelihoods of humans [2].

The main GHG present in the Earth's atmosphere are water vapour, carbon dioxide (CO_2), methane (CH_4), nitrous oxide, ozone and chlorofluorocarbons. Water vapour is one of the main GHG; due to its volatility, it evaporates and condenses with thermal fluctuations. However, increasing the concentration of water vapour, within a scenario of global warming, would reinforce heat absorption by the other gases [1].

The concentration of GHG has varied naturally according to different geological stages, nevertheless, through increase of human activities, this effect has been accentuated, particularly, the concentration of anthropogenic GHGs, including CO_2, CH_4 and nitrous oxides. As a result, CO_2 concentration has increased from 270 - 280 ppm in the pre-industrial years to 340 - 520 ppm at present [3]. Moreover, the increase in CO_2 concentration can drive global climate change and, for this reason, it is of vital importance that appropriate action be taken.

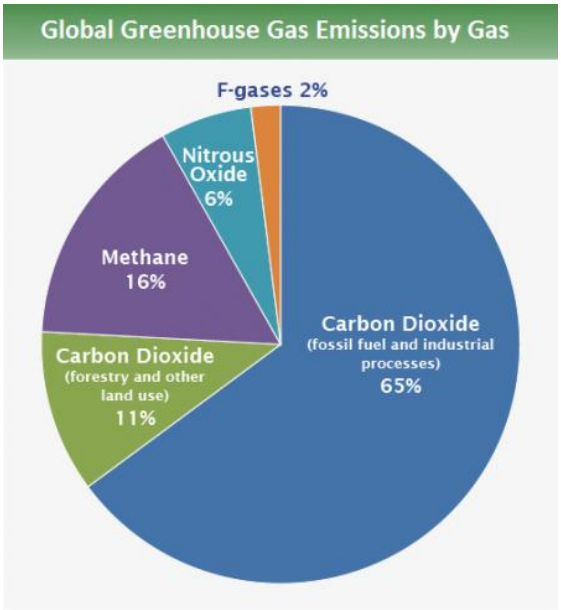

Figure 1: **Global GHG emission of carbon dioxide, methane, nitrous oxide and fluorinated gases based on 2010 data. Source: IPCC [3].**

As a measurement to assess the overall impact of a fuel, in terms of the GHGs emitted and the energy produced, life cycle GHG assessment refers to the total cycle of the production of a fuel and the electrical energy generated by that source. The parameter is expressed in units of global warming potential (CO_2-equivalent) per unit of energy generated (kilowatt hour; kWh). The objective is to include and assess the complete life of a given source, starting at material and fuel mining, and including construction, operation and waste management.

It is important to emphasise that the main reason for implementing carbon capture and storage (CCS) technologies is to reduce the concentration of CO_2 in the atmosphere, by controlling and decreasing anthropogenic emissions of CO_2. However, executing a CCS project requires the construction of infrastructures and installation of facilities (such as scrubbers, heat transfer units, pipelines, compressors, etc.), use of additional chemicals, solid waste and water disposal, etc. Additionally, energy is needed to run the aforementioned facilities, transporting materials, construction, and chemical production, among other things. All these activities would generate emissions. Therefore, it is of vital importance to carry out a life cycle analysis on GHG emissions to determine whether a given CCS technology would effectively result in a net reduction of anthropogenic gas emissions.

There are many studies on life cycle analysis in the literature. For instance, for a coal fired power plant using amine based absorbents the emission of GHGs was found to be considerably reduced [4]. That important decrease was observed for different technologies such as pre-combustion, post-combustion and oxyfuel systems. Other studies show that emissions from power plants fed with three different types of fuels and different configurations, such as supercritical pulverized coal (super-PC), natural gas combined cycle (NGCC) and integrated gasification combined cycle (IGCC), are significantly different with and without carbon capture systems [5]. Results from that study showed a reduction of 75 - 84% of GHG emissions and a CO_2 capture of 90%.

A life cycle study usually involves four steps, namely, goal and scope definition, inventory analysis, impact assessment and improvement assessment [6]. The first two steps of the process include the definition of the system boundaries and calculation of impacts of all processes involved. The last two points study the impact on human health and environment by energy and materials used, and, from this, conclude with recommendations for reducing emissions and negative effects. Hence, the assessment of GHG emissions includes not only net reduction due to the capture strategies for combustion technologies, but, also, emissions resulting from all activities, such as fuel and material procurement, waste disposal, and transport associated to a given capture technology. These emissions become a main parameter when they are included in CCS assessment.

1.1 Carbon Capture System

The increasing demand for energy and the consequently abundant use of fossil fuels has become a cause of concern, particularly due to CO_2 emissions, which is a major anthropogenic GHG. Therefore, a lot of effort has been put in developing new technologies to reduce the emissions of CO_2 to the atmosphere.

CO_2 is considered an important pollutant due to its major impact in global warming and climate change [3]. According to the Emission database for global atmospheric research [7], the world total global emission in 2014 was 35.6 billion tonnes, which is 49% more than the total emission in 1990. Notably, the 2014 level is only 5.9% greater than 2010; however, the general trend is still an increase in total emission. The CO_2-equivalent concentration in 2011 was estimated to be 430 ppm (with an uncertainty range of 340 to 520 ppm) [3], in contrast to the 280 ppm during pre-industrial times, which would lead to an increase of the global temperature causing climate change. Therefore, in December 2015, at the Paris climate

conference (COP21), 195 countries signed an agreement on setting policies to limit global warming to below 2 °C [8] in comparison to pre-industrial temperature levels. The agreement is set to be introduced in 2020. Estimation of CO_2 level for year 2030, if this trends continues, is that it will increase by 25 – 90 % over the year 2000 level, with CO_2 concentration growing to as much as 600 – 1550 ppm [9].

Carbon capture and sequestration (CCS) is considered a key part of the strategy to meet CO_2 emission reduction targets [10, 11]. Therefore, a good understanding in all areas involving CCS is required, namely:

- Technologies for CO_2 capture
- CO_2 separation
- CO_2 transport
- CO_2 storage
- CO_2 leakage
- CO_2 monitoring
- CO_2 life cycle analysis

CCS is considered to be technically feasible at commercial scale [12], and CCS technologies would be in addition to existing gas injection for enhanced oil recovery in the oil and gas sector.

1.1.1 CO_2 Capture Technologies

The selection of a specific CO_2 capture technology depends on the type of plant generating CO_2 and the fuel used.

CO_2 is generated from many sources, such as power plants and industry sectors, which currently account for about 60% of CO_2 emissions, including natural gas processing, and biomass processes, among others sources [13]. One of the major causes of CO_2 is as a product of combustion reactions; a suitable CO_2 removal process will depend on the type of combustion. Although there are a variety of capture technologies on the market, their elevated cost (70 – 80 % of the total cost of a full CCS – including capture, transport and storage) is a major drawback for implementation.

There are three main CO_2 capture systems:

1. Pre-Combustion

2. Oxyfuel combustion
3. Post-Combustion

1.1.1.1 *Pre – Combustion*

Pre-combustion systems are based on treating the fuel (coal or natural gas) prior to combustion. To do so, it is necessary to take the fuel to a gasification (partial oxidation) stage. This technology is already developed to a reasonable level, which makes it suitable to be retrospectively installed in existing plants. The process consists of forming syngas (CO and H_2) [14, 15], which subsequently undergoes a water-gas shift reaction with steam, producing more H_2, while CO gas is converted to CO_2. Then, CO_2 is separated from H_2, which used in conjunction with air, generates power and heat.

If coal is used as the feedstock, pre-combustion treatment involves gasification, in a gasifier under low oxygen levels, to form syngas. Alternatively, natural gas can be used to produce CO and H_2 by a reforming reaction with steam; where after the amount of H_2 produced can be increased by the water shift reaction.

Gasification: $Coal \rightarrow CO + H_2$

Steam reforming: $CH_4 + H_2O \rightarrow CO + H_2$

Water – Gas shift: $CO + H_2O \rightarrow H_2 + CO_2$

The high concentration of CO_2 (>20%) in the H_2/CO_2 fuel as mixture facilitates its separation [12, 16]. This technology could be applied to integrated gasification combined cycle (IGCC) [16, 17] power plant using coal as fuel with the corresponding loss in energy efficiency of 7-8%. On the other hand, for advanced combined cycle gas turbine plants using natural gas as fuel and applying this pre-treatment results in a CO_2 capture efficiency of 80% [14].

Pre-combustion systems have issues in some areas where there is opportunity to enhance the technology [14]. One aspect is the high energy requirements for regeneration of sorbents. Additionally, there is a lack of experience about pre-combustion systems because there are only a few plants working with such systems. There have also been reports of problems associated with heat transfer related to the temperature and a decline in efficiency when using hydrogen rich gas as turbine fuel, while there is a high capital cost associated with the installation and operation of this technology.

1.1.1.2 *Oxyfuel Combustion*

In oxyfuel combustion, oxygen is used instead of air for combustion reactions, reducing the amount of N_2 in the exhaust gas, which affects the subsequent separation processes (besides NO_X content reduction) [18]. Some of the advantages of oxyfuel systems are that the CO_2 concentration is very high, which facilitates and enhances the efficiency of separation. Additionally, the technologies to concentrate O_2 from air are matured and, because pure oxygen is used in combustion, it leads to a smaller volume of gas for processing, which reduces the size of boilers and other equipment.

Flue gas is mainly composed of water, solid particles, CO_2, and SO_2 [19]. Most particles can be removed by conventional electrostatic precipitators, and SO_2 can be separated by flue gas desulphurization methods. On the other hand, the effluent gas, which has a high concentration of CO_2 (80-98% depending on fuel used), can be compressed, transported and stored.

Oxyfuel combustion is a feasible process [18], but the main drawback would be the higher cost to produce oxygen from an air separation unit [20]. In addition, high SO_2 concentrations carry corrosion problems in desulphurization units.

Chemical looping combustion would be an option to overcome the cost of air separation unit. This technology uses metal oxide (for instance: Fe_2O_3, NiO, CuO, and Mn_2O_3) as an oxygen carrier instead of using pure oxygen directly for the combustion (oxyfuel) [21]. Thus, the metal oxide is reduced to metal while the fuel is being oxidized to CO_2 and water; therefore CO_2 is the main product of combustion. After that, the metal is oxidized in another stage and recycled in the process. Water can be removed by condensation (process by-product), while pure CO_2 can be obtained without consumption of energy separation. This technology prevents the CO_2 dilution with the flue gases. Additionally, NO_X formation is reduced because combustion occurs in a free Nitrogen mixture. It can be said that, chemical looping combustion is a promising technology for CO_2 capture. However, there is an important lack of experience in this technology, given that it has not been tested in large scale operations [22]. Therefore, this process is still under development stage. The availability of oxygen carriers will determine the commercial scale up of this process [21].

1.1.1.3 *Post – Combustion*

As the name suggests, in post-combustion processes, CO_2 is removed from the flue gas after combustion occurs. Such technologies are the preferable option for existing power plants. For instance, post-combustion CO_2 capture has already been proven at a rate of 800 t/day [17]. This technology has already been demonstrated as easily retrofitted into existing plants, both for coal-fired and gas fired sites. A major drawback of these technologies is the low CO_2 concentration in flue gases; 7 - 14 % for coal fired, and 4% for gas fired [23], resulting in a large parasitic load. Given that for transportation and storage, CO_2 concentration is required to be above 95.5%, there is an important energy penalty; as an example the U.S. National Energy Technology Laboratory estimated that by using this technology the cost of electricity production would increase by 70% [24]. Therefore, it is essential that a significant effort is made aiming to reduce this energy penalty by increasing the efficiency and reducing cost of new technologies.

1.1.2 CO_2 Separation Technologies - Post Combustion

There are a number of technologies already developed and more under development for post-combustion processes. Given that this thesis focuses on CO_2 capture from flue gases by adsorption processes; this section will briefly outline the different options for post-combustion CO_2 separation:

1.1.2.1 *Membrane Separation*

Membranes are made of a composite polymer; a thin selective layer is bonded to a thicker non-selective and low cost layer that provides mechanical support. Membranes are used to allow only CO_2 to pass through, while excluding other components of flue gas. In this way, membranes are already used to separate CO_2 from raw natural gas components [25]. This technology can reach CO_2 separation efficiency from 82 - 88 %. However, membrane performance is affected by the flue gas conditions (such as low CO_2 content), and pressure; these are the main hurdles to apply this technology. Generally, membrane technologies have low capital cost and no regeneration is required; this reduces the complexity in the equipment design. Additionally, no solvent is used, which is environmentally friendly. However, the main challenges includes physical aging, conditioning, poor balance between permeability and selectivity, and penetrant induced plasticization [25]. A membrane has to have a number of characteristics to be economically and technically feasible; such as high selectivity, high permeability, high surface area, and stability at the operating temperature,

pressure and chemical environment. The main challenge is that is it very difficult for a single membrane to satisfy all the requirements [26].

1.1.2.2 *Hydrate-based Separation*

The exhaust gas containing CO_2 is exposed to water under high pressure forming hydrates; water molecules connect to each other by hydrogen bonding forming cavities. Then, the CO_2 is selectively engaged in the cages of hydrate (clathrates) and is separated from other gases. The gas molecules get stabilized in the cavities predominantly by van der Waals interaction forces [27]. This mechanism is based on the equilibrium of CO_2 with other gases, where CO_2 can form hydrates easier than other gases such as N_2. Besides, the stability of the cages is affected by the composition and the pressure, particularly in the presence of multiple particles or gases. Improving the hydrate formation rate and reducing hydrate pressure can improve the CO_2 capture efficiency [28] for a technology which has small energy penalty. However, hydrate based separation is still in the research stage; therefore, hydrate technology is not ready to be used in industry, not even in small scale applications. One of the main drawbacks to solve is that as the CO_2 decreases, the equilibrium conditions come to be extreme; as it occurs for the mixture CO_2-H_2 or CO_2-N_2. Therefore, the separation of CO_2 from flue gas by the hydrate method is not favoured [27]. For this reason, combined methods to separate CO_2 are necessary, such as hydrate/membrane or hydrate/absorption [29].

1.1.2.3 *Cryogenic Distillation*

This process is used to treat gases to separate their components. Cryogenic distillation consists in a distillation at cryogenic conditions, ergo low temperatures and high pressures. Cryogenic distillation is analogous to conventional distillation process; but, it is used to separate gaseous components, instead of liquids, based on their different boiling points [16, 20, 30]. Flue gases have to be cooled to desublimation temperatures (-100 to -135 °C); in this way the solid CO_2 is separated from the other gases. Finally the solid/liquid CO_2 is compressed to high pressures (100 -200 bar) [14, 30]. The CO_2 recovery can reach 90 – 95 % of the flue gas. On the other hand, this is a very energy intensive process given that it is conducted at very low temperature and high pressure [20]. Besides, it is only technically viable for high CO_2 concentrations (>90%) [14, 16].

1.1.2.4 *Absorption*

Absorption consists in the use of liquid or aqueous sorbent to absorb the CO_2; typically monoethanolamine (MEA), dietanolamine (DEA), diglycol amine (DGA), N-methyldiethanolamine (MDEA), 2-amino-2methyl-1-propanol (AMP) and potassium carbonate) [16, 31-34]. After absorption, once the CO_2 has been recovered from the sorbent, the sorbent has to undertake a regeneration stage, which is done by stripping or regenerative process by heating and/or depressurization [14]. MEA is one of the most efficient liquid sorbent for CO_2 absorption with efficiency over 90% [35]. Absorption has been applied to capture CO_2 from gas streams in natural gas, refinery off-gases and synthesis gas processing [34]. The main problems of absorption processes arise because of the regeneration of solvent, which is high energy intensive and technically complicated due to the large volume of sorbent and water to handle. Additionally, amines undergo degradation, which results in solvent loss and it requires large volume of solvent make up. It also produces problems to the equipments such as corrosion and the generation of volatile compounds [36], which can be nocuous for the environment. Emissions from amines can give rise to the formation of harmful products to the human health and the environment, such as nitrosamines and nitramines. For instance, when these liquid sorbents are applied to fossil-fuel based thermal power plants, one of the major challenges is the large volumetric flow rate of flue gases that has to be handled. The CO_2 partial pressure is quite low (7-14% for coal-fired and 4% for gas-fired), the flue gas is usually at atmospheric pressure and its temperature varies in the range of 50 – 150 °C [34, 37]. The CO_2 absorption efficiency would depend on the CO_2 concentration. Another important issue comes from the presence of NO_X and SO_X, and the relatively high O_2 partial pressure in the flue gas [34].

1.1.2.5 *Adsorption*

Adsorption consists in using solid sorbents to attract the CO_2 onto its surface by chemisorption or, mostly, physisorption. The sorbent has to satisfy a specific criterion; such as large surface area (large capacity), high selectivity to the adsorbate, easy regeneration abilities, chemical stability and low cost. The most typical solid sorbents used are activated carbon (ACs), zeolites, molecular sieves (MSc), calcium oxides and metal organic frameworks (MOFs), among others. Adsorption requires, usually, high pressure, but in order to release the adsorbate (CO_2) the pressure is lowered, typically, to atmospheric pressure for desorption. During desorption the adsorbed CO_2 is removed for further uses.

Pressure swing adsorption (PSA) or temperature swing adsorption (TSA) can be applied to regenerate the sorbent [38]. PSA is commercially available with an efficiency of 85%. Likewise, when applying TSA, the adsorbed CO_2 can be released by increasing the system temperature by hot air or steam injection. TSA requires longer regeneration time than PSA, but purity higher than 95% and recovery higher than 80% can be achieved.

Generally, solid sorbents offer greater capacity than liquid sorbents (amines) and require less energy to regenerate overall because of the absence of large quantities of water [34]. The main challenges of adsorption technologies are focused on enhancing adsorbent CO_2 selectivity, achieve high porous structure integrity, separation of CO_2 from CH_4 applied to production of natural gas from low grade reservoirs, and when applied to other processes such as separation of light olefins from the corresponding paraffins and adsorptive storage of fuel gases (H_2 and CH_4) [26]. As it was stated in the previous section, CO_2 concentration in flue gases is very low; therefore selectivity becomes a very important parameter to enhance CO_2 capture from the treated gas. One of the main aims in the improvements of solid sorbents is to enhance the adsorption capacity at flue gases conditions; which would be at atmospheric pressure and temperatures in the range of 50 to 150 °C. This contrast with the fact the usually solid adsorbents exhibit high CO_2 capacity at low temperature and high pressures, despite of the low kinetics conditions at low temperature. Another, common issue for solid sorbents is that Impurities such as NO_X and SO_X reduce the sorbent performance.

There are a number of solid sorbents available for adsorption processes, which are further discussed in Section 1.6.

1.2 CO_2 Transport.

This is a key stage of the carbon capture and storage strategy, regardless of the final destiny of the CO_2. After CO_2 is separated from the flue gas, it has to be transported to the storage sites or used as part of industrial processes. The transport method used will depend on the volume of CO_2 produced; the options would be road tankers, ships or pipelines

Aspelund *et al*. have studied the transport by ship tanker in the North Sea which uses a similar technology to liquefied petroleum gas (LPG) [39]. That study showed that shipping the CO_2 could be competitive and feasible with a cost of 20 - 30 USD/ton if more than 2 Mton of CO_2 is transported per year within the North Sea. However, in the scenario of a

fully developed carbon capture system, the CO_2 would need to be transported through long distances. Therefore, pipelines are believed to be the most suitable option for that situation [40].

Another important aspect to evaluate is the phase in which the CO_2 is transported in the pipe. The best way to optimize the mass and volume ratio is transporting the CO_2 as a dense phase. The preferred state for pipelines is supercritical, but liquid state would also be an option. For a supercritical phase the physical conditions are temperature above 32.1 °C and pressure 73.8 bar. Even so, the range most commonly used is pressure between 85 and 150 bar and temperature between 13 and 44 °C, in order to guarantee that a single phase (liquid or supercritical) flow is obtained in the pipeline [41].

Impurities in the CO_2 streams represent a serious problem for a number of reasons [11]:

- The presence of impurities may vary the ranges of pressure and temperature in which a single phase is stable.
- Water above 50 ppm may lead to the formation of carbonic acid which can be corrosive.
- Similarly, hydrates could form inside the pipe affecting the functioning of valves, compressors and equipment.

According to the International Energy Agency Report of 2014, exist approximately 6500 km of CO_2 pipeline worldwide. However, most of those pipelines are used for Enhance Oil Recovery projects, but also some of those pipelines are already used or are under development for CO_2 storage projects [42]. The development of an extensive network of pipelines would be totally necessary to commercialize CCS projects. However, given that all the sources of CO_2 would merge together, it will be required that the CO_2 produced in the different sources have the same quality (P, T and water content) before being discharged to the pipeline network [42]. From an economical point of view, as the flow of CO_2 is increased through the network, the cost of transporting would decrease exponentially.

Because of lack of experience in transporting CO_2 through pipelines for a long period of time, there is lack of data regarding the pipeline integrity and the effect of the flow conditions required for CO_2 transport. Therefore, this is an aspect for further development particularly regarding to corrosion, potential fractures and supercritical CO_2 leaking.

Moreover, the pipelines should be monitored and the fluxes metered. Another issue could be the legal aspect for trans-national transporting of CO_2 that would need to be evaluated.

1.3 CO_2 Utilization

A lot of effort has been put in the separation and capture of CO_2. However, it is likewise important to design strategies for using the captured CO_2. Given the high cost of transportation (explained in Section 1.2), the use of CO_2 in situ must be the first option to be considered.

Current CO_2 utilization accounts only for 2% of total emissions, but further applications such as Enhanced Oil Recovery (EOR - this is explained in Section 1.4) or conversion of CO_2 into CH_4 and/or methanol (CH_3OH) represent future challenges [43, 44].

Therefore, the first option to evaluate is the reuse of CO_2 in the industry; agriculture and energy production, food and beverages, refrigerants, and fire extinguishing gases. For instance, there are reports stating the use of captured CO_2 from ammonia processes to produce urea at a rate of 160 ton/day [45]. Additionally, Aresta *et al*. studied the use of CO_2 as a building block in different applications such as synthesis of carboxylates, carbonates, carbamates, as well as to produce fuels or C_n molecules like formic acid or methanol [43]. Regarding methanol, the world's largest CO_2-methanol plant (Carbon Recycling International) located in Svartsengi – Iceland began production at the end of 2011 and was fully operating by 2012 [46]. This plant increased its production from 1.3 million litres per year to more than 5 million litres per year. The use of recycled CO_2 for the production of methanol accounts for approximately 5.5 thousand tonnes per year. The CO_2 is captured from the flue gases released by the geothermal steam emissions that feed the geothermal power plant, which provides energy to the plant. Basically, the plant uses electricity to produce hydrogen which reacts with CO_2 (in a catalytic reaction) producing methanol.

Another industrial application of CO_2 has been demonstrated by Novomer, which has put in the market a family of polypropylene carbonate (PPC). This is a family of materials based on the transformation of CO_2 into polyols and polymers. The content of CO_2 in these materials can be up to 50% and can be applied to a variety of uses such as flexible foams, polyurethanes in automotive applications, rigid foams and plastics [47]. Similarly, Bayer has developed a technology to make polyurethanes from CO_2, which can be used to produce soft foam. This process has been used by Covestro which is the material science section of

Bayer. The discovery of this application has been a research breakthrough in the sector. This process uses CO_2 as a raw material, and the reaction became achievable when the right catalysts that triggers the reaction reducing the energy requirements and making the process viable economically and ecologically was found [48].

1.4 Geological Storage

To store CO_2 in geological formations is considered the most practicable and suitable option to accumulate large quantities of CO_2 [49-51]. Carbon dioxide can be stored in geological formations such as: deep saline aquifers, unmineable coal beds (to recover CH_4), depleted (or nearly depleted) oil & gas reservoirs (EOR), and deep ocean storage (environmental concern: acidification and eutrophication).

The geological storage of CO_2 basically depends on its injection at depths of more than 1 km. At that depth, the temperature and pressure would be above the critical value for CO_2 (31 °C and 73.8 bar). The geological sites for CO_2 storage have to be selected based on a number of criteria: porosity, thickness, and permeability of the reservoir rock, a cap rock with good sealing capability, and a stable geological environment [50]. However, there are other parameters that could became important when selecting a geological storage site, such as distance to the source of CO_2, storage capacity, potential for leaking and economic pressures.

In the UK exist a wide range of geological sites that account for a total capacity of 78 Gt [52]. This represents about 187 years of emissions at current rate for the UK (approx. 415 million ton/year) [7]; however a big portion of that is in saline aquifers.

1.4.1 Enhanced Oil Recovery

Oil & gas companies have been researching and using this system for the last decades to extract more fossil fuels from nearly depleted oil & gas reservoirs. The CO_2 can be injected and used to increase the pressure to extract more fuels while the CO_2 remains stored. There is an obvious economic reason to use CO_2 for EOR, therefore this technology is already mature and there are a number of studies on different areas of it such as injection technologies, modelling migration, geochemical, and leakage and monitoring.

1.4.2 Unmineable Coal Beds

Similarly to EOR, CO_2 can be injected into coal beds to enhance the recovery of CH_4 by allowing it to escape from the pore structure of coal beds. This technology is mature and

has been used in the past, mostly in USA. In addition, there is an economic incentive for this technology considering the large coal beds that can be used as CH_4 source worldwide [53].

1.4.3 Saline Aquifers

These formations are usually found at about 700 to 100 metres below ground level both onshore and offshore. The saline aquifers are believed to have a huge potential for CO_2 storage [13]. However, regardless of the big potential of saline aquifer to store CO_2 there is less knowledge about it when comparing to the EOR and coal beds.

When the CO_2 is injected there are different trapping mechanisms that occur: hydrodynamic, residual, solubility and mineral. The CO_2 gets trapped in different phases: supercritical fluid, gas phase, dissolved liquid phase and reacted solid phase respectively. There are a number of studies in the literature about the storage in saline aquifers and the mechanisms driving it. Additionally, during the past two decades a number of projects for storing CO_2 in saline aquifers were put in place. Therefore, there is already enough experience on this technology, and it can be said that it is technically feasible and with a low or null impact on the environment [54].

1.4.4 Deep Ocean Storage

This is the most controversial option among the geological formations proposed for CO_2 storage. Oceans represent more than the 70% of the earth surface and are the natural CO_2 sink. Oceans naturally absorb CO_2 from air, at an annual rate of 1.7 Gt; it is expected that the oceans accumulate approximately 38,000 Gt of carbon. At the same time the ocean produces annually about 50 – 100 Gt carbon in form of phytoplankton; it is worth to mention that this represents more than the vegetation intake in the world [55]. Therefore, oceans play a key role not only in the ecosystem on earth but also on the CO_2 levels in the atmosphere.

Different studies suggest that at depth greater than 3 Km, the CO_2 would liquefy and sink to the bottom due to its higher density than the sea water at that depth [56]. There are studies and mathematical models that suggest that CO_2 could be stored in this way for long periods of time. However, this option is quite controversial due to the impact that large amounts of CO_2 could have on the sea water and its ecosystem; particularly to the chemistry of the sea water. Increasing the CO_2 concentration may acidify the sea water; therefore, its pH would be reduced. Moreover, there are already studies about the impact

of water acidification near volcanic areas, causing a reduction of biodiversity and serious consequences to the marine ecosystem [57]. Likewise, the increase of global temperature would deplete the ocean resistance to the acidification.

Perhaps, to store CO_2 in the ocean is not the most promising and viable option given the high risk associated comparatively to the other geological formations such as depleted oil & gas fields or coal beds. Therefore, deep ocean storage needs further research and field studies to assess properly its consequences before any implementation.

1.4.5 In Situ Carbonation

This technology is based on the chemical reaction between the injected CO_2 with the surrounding host rock and in this way forming different carbonates in the presence of specific minerals [58]. Some of the most promising host rocks for this technology would be basalts and ophiolite. Basalts are the most common rock on the planet; this is the main reason which makes this technology a promising option. However, this is in the beginning stage of development and little knowledge has been accumulated on this topic, consequently further studies are needed to identify the suitable injection areas, the reactivity of the rock with CO_2 and to solve the technical issues associated to it.

1.5 Leakage and Monitoring

In order to prevent the stored CO_2 to return to the atmosphere it is necessary to monitor the store sites and prevent any leakage back to the atmosphere or to underground water streams. Therefore, the leakage of CO_2 would not only have a negative impact on the effectiveness of the CO_2 storage but also on the surroundings of the geological site.

1.5.1 CO_2 Leakages

Considering the starting point of the process after the point when CO_2 is captured, the leakage could occur in two places: during CO_2 transportation or from the geological store site. Many studies can be found in the literature about the dispersion of CO_2 to the atmosphere from the pipelines used for its transportation. However, the leakage of CO_2 from geological formations is more complex. There are mainly two main mechanism for this: leakage through cap rock and leakage through permeable pathways; generally the former would be slow taking thousands of years [59], while the later can be faster provoking more concern. A number of studies on the gas leakage through the cap rock have been conducted; it was found that the sealing pressure of the cap rock has to be

determined before starting the CO_2 injection in the geological formation; additionally during the injection the pressure should not overtake that pressure [60]. This is important to prevent the migration of the CO_2 to higher rock formations which could lead to permeable pathways and back to the atmosphere.

1.5.2 CO_2 Monitoring

The key of CCS projects is to capture and store the CO_2 for a long period of time. Some studies state that a leakage of 0.1% of CO_2 back to the atmosphere per year would be enough to nullify any control of CCS on the global warming [61]. The monitoring would not only cover the leakage of CO_2 back to the atmosphere but also the interaction of it with the immediate environment, particularly the water.

The monitoring comprises three stages: pre, during and post injection. The techniques used to monitor are in place to ensure the integrity of the reservoir, prevent leakages and measure the volume of CO_2 injected. Therefore, the monitoring is useful to gather data and test the aims of the project, measure the performance and long term stability.

There are a number of techniques developed to monitor the store sites, the application of each one would depend on the type of information required and the characteristics of the geological formation being monitored. The different methods used to monitor the reservoir are: seismic monitoring, geoelectrical methods, temperature logs, gravimetry methods, remote sensing, geochemical sampling, atmospheric monitoring, tracers, soil gas and microbiology.

- ***Seismic monitoring***: this technique is not only about recording with geophones tremors and micro earthquakes produced underground (passive method), but it can also be applied actively, which consists in generating acoustic waves that would be detected and interpreted to gain information about the geology of the reservoir, structural integrity, tracking the evolution of the CO_2 plume and generating 3D images or 4D data (evolution of plume over time) [62].
- ***Geoelectrical methods***: When CO_2 is injected into a reservoir other fluids would be displaced. This technique measures the resistivity variation as the CO_2 displaces other fluids, therefore it can be used to measure the grade of saturation of the store site and CO_2 distribution [63]. Obviously, the greater the conductivity difference between the fluids in the reservoir and the CO_2, the stronger would be

the signal. When CO_2 gets dissolved in water the signal is no longer measurable so this method can be used only before dissolution of CO_2.

- ***Temperature logs***: this is based on the temperature changes during injection (for instance Joule-Thompson cooling); it would allow to detect the flow paths for the CO_2 in the reservoir [64].
- ***Gravimetry methods***: similarly to the geoelectrical methods, when CO_2 is injected it would displace other fluids and changes in the density can be monitored due to that [64].
- ***Remote sensing***: the surface of the reservoir or store site can be monitored to detect any change due to high internal pressure that may cause deformations [65].
- ***Atmospheric monitoring***: leakages can be detected by measuring the CO_2 concentration on the surrounding of the reservoir [66].
- ***Tracers***: Some chemical compounds can be injected together with the CO_2 and used as a fingerprint in order to detect any escape from the store site [67].
- ***Soil gas***: this method is based on monitoring the composition of the soil gas. It can be measured previously and during the injection. Similarly to the tracer, any variation would lead to detect leakages from the site [68].
- ***Microbiology***: this method consists of biological analysis of fluids and sediments prior to and during injection to understand if there are possible biogeochemical processes that could obstruct the CO_2 diffusion into the reservoir [68].

1.6 Solid Sorbents

Post-combustion technologies have been demonstrated as a key factor to control the emissions of GHG [11, 12, 14, 16, 17]. Consequently, there are a number of potential technologies being developed for post-combustion CO_2 capture. Currently, absorption systems are the technology mostly applied in CCS commercial projects [16, 31-33, 35, 36, 69]. However, as it was introduced in Section 1.1.2.5, adsorption processes are a promising option for the near future. For this reason, there are a range of solid sorbents available for post combustion CCS systems, involving adsorption processes. These sorbents have to satisfy given criteria in order to be economically and operationally feasible for CO_2 capture from flue gases:

- ***Adsorption Capacity***: The quantity of adsorbate that an adsorbent can adsorb, which determines the amount of sorbent required, defines the volume of equipment and vessels. This parameter is determined from the adsorbent equilibrium isotherm. Therefore, if the sorbent has a high adsorption capacity, the total amount of sorbent required would be reduced and, in consequence, the size of the equipment would be reduced as well. In order to compete with liquid sorbents (MEA scrubbing systems), solid sorbents should exhibit a CO_2 adsorption capacity of 3 - 4 mmol/g [34].
- ***Selectivity for CO_2***: Selectivity is defined as the ratio of CO_2 adsorbed in comparison to the quantity adsorbed of any other gas present in the flue stream, for instance N_2. This is a very important parameter not only from a technical point of view, but also for the economics of a CO_2 capture process. The selectivity of the adsorbent has a major influence on the concentration or purity of the CO_2 adsorbed. Therefore, it will affect the stages of transportation and storage of CO_2. The flue gases from a power plant normally contain large volumes of N_2, O_2 and water vapour; consequently, it is very important that the sorbent exhibits high selectivity for CO_2 in the presence of these other gases.
- ***Adsorption/desorption Kinetics***: It is necessary that sorbents have fast adsorption/desorption kinetics for CO_2 at given operational conditions. This has an impact on the total volume of sorbent required, and it controls the cycle time of a fixed-bed adsorption system. Thus, for a particular sorbent, the faster its kinetics the smaller amount of material that would be required to adsorb a specific CO_2 volume. The kinetics of adsorption would be influenced, not only by the reaction (chemisorption) or physical interaction (physisorption) of the sorbate to the surface of the sorbent or functionalized surface groups, but also by the diffusion of gas through the porous material. The type of functional groups or the porosity of the material can be tailored to enhance the kinetics of adsorption/desorption.
- ***Mechanical strength of sorbent***: The sorbent experiences cycles of adsorption and desorption, exposed to high flow rate of flue gases, vibrations and operating conditions (pressure and temperature). Consequently, the sorbent can suffer disintegration of particles, a considerable reduction of its kinetics performance or a considerable drop in capacity. To avoid such issues, the sorbent must exhibit microstructural and morphological stability. The mechanical strength of the

material becomes critical to process cost effectiveness given that degradation or partial loss of material would determine the sorbent make up.

- ***Chemical stability***: Solid sorbents have to be able to tolerate impurities and contaminants, such as NO_X, SO_X, and heavy metals, and be stable in the oxidizing environment of flue gas. These contaminants should be removed from the flue gas as they affect the CO_2 adsorption capacity of the sorbent.
- ***Regeneration of sorbent***: This is of vital importance for an industrial process to be economically viable. The energy required for desorption (regeneration), which is defined as the heat of adsorption, should be low. Obviously, the heat of adsorption for physical adsorption (25 - 50 KJ/mol) is lower than that for chemical adsorption (60 - 90 KJ/mol). Besides, the regeneration should be technically and economically feasible, considering that the CO_2 adsorption capacity should remain at high efficiency through the cycles of adsorption/desorption.
- ***Sorbent cost***: The cost of the sorbent represents one of the most delicate characteristics for CCS implementation. If the cost of the sorbent reaches $15/kg, it is no longer economically feasible, on the other hand, a cost of $5/kg is a very competitive scenario [70]. Therefore, a cost around $10/kg or lower, would be competitive [34].

The criteria mentioned above are the characteristics desired for an ideal adsorbent. However, it is unlikely that a single adsorbent can satisfy all the criteria stated. Therefore, those sorbents that offer effective and economically feasible capture of CO_2 from a gas stream would be considered suitable adsorbents.

1.6.1 Physical Sorbents

There are a number of solid materials that can be used as sorbents for CO_2 capture from flue gas. These sorbents can be classified in different ways; some authors do so according to their operational temperature: low-temperature (<200 °C), intermediate temperature (200-400 °C) and high temperature (>400 °C) [71]. Likewise, solid sorbents can be differentiated by composition, for instance porous carbonaceous, zeolites, alumina, silica gel, and metal-organic frameworks (MOFs), among others. These solid materials can be used to physically adsorb CO_2 from flue gas, wherein physisorption occurs for CO_2 on a solid sorbent by the mechanism described in Reaction 1:

$$CO_2 + Surface \leftrightarrow (CO_2) \cdot (Surface)$$

Reaction 1: Physical adsorption mechanism.

Here, CO_2 adsorption results from van der Waals forces between CO_2 molecules and the sorbent surface, or electrostatic interactions among the CO_2 and the ionic and polar sites of the solid surface.

Inorganic carbon materials are frequently used by industry due to their wide availability and the low cost of raw resources. These materials, which include activated carbons (ACs), graphenes, carbon molecular sieves (CMSs), and carbon nanotubes (CNTs), are used in a number of industrial applications such as gas purification, water treatment, PSA among others [72].

1.6.1.1 *Activated Carbon*

Carbon based sorbents show some interesting characteristics, such as low cost, high surface area, tuneable pore size, optional functionalization, fast kinetics and low energy regeneration. All that makes carbon based materials suitable and promising for CO_2 capture. Adsorption on carbon materials is mostly physical, which translates into weak interactions between the adsorbate and the surface, implying poor selectivity and sensitivity to temperature. The adsorption capacity decreases as the temperature increases, which is one of the main drawbacks given the relatively high temperature of flue gas, 50 - 150 °C [37]. Additionally, the pore size and shape can impact the CO_2 adsorption capacity. Particularly, the CO_2 adsorption capacity is linked to the proportion of narrow nano- and micro-porous volume in the material [73]. As a consequence, the design of this type of material should be such to include a high proportion of small micropores in order to obtain high CO_2 adsorption capacity. Most carbon materials are mesoporous, therefore selectivity is affected; likewise, the presence of water vapour and contaminants such as NO_X and SO_X will affect selectivity to CO_2, given their competition to adsorb on the surface.

In comparison to zeolites, ACs show lower adsorption capacity and selectivity at low partial pressures [74], given their non-favourable adsorption isotherms under those conditions.

1.6.1.2 *Carbon Molecular Sieves*

CMS are a particular case type of carbon material, and these types of sorbent are used for gas separation as well as CO_2 capture. One of the main requirements for a CMS to be useful for gas separation is that it must exhibit a narrow pore size distribution (PSD); therefore,

high micropore volume and pores of molecular sizes. These characteristics have a direct impact on selectivity and capacity [75]. An uptake of 2.27 mmol/g has been reported at 30 °C and atmospheric pressure, for a CMS developed by Burchell *et al.* [76]. This uptake is reduced as temperature increases due to the physical nature of the adsorption interaction.

1.6.1.3 *Carbon Nanotube*

The new generation materials of CNTs have become of interest for gas separation and CO_2 capture based on selecting a suitable pore size and shape, as well as the optimal operation conditions [77]. Razavi *et al*. [77] argued that CNTs selectivity for CO_2 over N_2 is higher in comparison to other carbon materials. For purified single-walled carbon nanotubes (SWCNTs) a high surface area (1587 m^2/g Brunauer-Emmett-Teller method) and large pore volume (1.55 cm^3/g), of which 0.28 cm^3/g were micropores, have been observed. The adsorption capacity of SWCNTs with such characteristics is twice of that of activated carbons [78].

1.6.1.4 *Zeolite Sorbents*

Zeolites, both synthetic and natural, have been applied to gas purification and separation. Zeolites are microporous materials based on a silicon dioxide framework. Zeolite frameworks are tuneable, that is to say that the Si in the structure can be partially substituted by Al, which leads to a negative charge in the framework. Hence the charge compensation is obtained with cations added in the structure such as Na or other alkaline or alkaline-earth metals. Subsequently, those cations can be exchanged in order to tune not only the pore size but also the adsorption characteristics, on which there are a lot of studies on the different ions that can be incorporated into the framework. Given the defined framework of these materials, the pore size distribution is uniform, normally within the range of 0.5 - 1.2 nm [79], allowing zeolites to treat gas or separate components based on a molecular sieving effect. Some gases, such as CO_2, can be favoured to be selectively adsorbed on the surface of zeolites given the relatively high energetic dipole and its quadrupole moment [34]. The kinetics of adsorption of these materials is usually fast. In contrast, zeolites are highly influenced by temperature and pressure. The adsorption capacity for CO_2 decreases as the temperature increases, as for most of the materials discussed here, but, by contrast, capacity increases as the partial pressure of CO_2 increases in the gas stream. It is also important to take into account the effect of the presence of water on the capacity, given that water competitively adsorbs onto the zeolite surface.

Silica based sorbents are mainly used as a support on which amines are impregnated or added to adsorb CO_2. One of the main reason for which silica based sorbent have attracted a lot of research is its structural characteristic such as large surface area and pore volume, narrow pore size distribution and relatively stable regeneration abilities [71]. Therefore, the research on this topic is focused on choosing the appropriate type of silica (nanoparticles, nanotubes, aerogel, hollow spheres, etc.) and the amine groups [80, 81].

1.6.1.5 *Metal-Organic Frameworks*

Metal organic frameworks (MOFs) consist of crystalline units composed by metal ions or clusters linked by organic spacers. One of the main interests for this type of material lies in the possibility of exchanging the organic species, and this leads to a large number of synthetic options. Thus, there is a huge opportunity to tune or control the pore size, pore shape and the chemical potential of the adsorbing surface, which translates into control of selectivity, kinetics and capacity of adsorption [34].

The bonding in MOFs, usually covalent coordination, is weaker than for metal oxides, resulting in the fact that the crystal structures observed may not necessarily be maintained after solvent removal. This allows MOFs to be classified, according to their ability to maintain their structure, as first, second and third generation [82]. The former refers to those structures that collapse and are no longer porous on desolvation. Second generation are those frameworks that exhibit a consistent structure and reversible gas sorption isotherms. Lastly, the latter denotes those materials with a flexible and reversible structure depending on the guest, analogous to a sponge.

Generally, MOFs present high capacities at high pressures but at low or atmospheric pressure the capacity drops significantly and is, in fact, lower than other sorbents. Also, MOFs, usually, exhibit important heat sensitivity, for which they might degrade at high temperatures, which complicates the regeneration of this materials and could result in collapse of their structure. Another problem associated with MOFs is their sensitivity to moisture, which make more difficult to handle them and the processes in which they are used.

1.6.1.6 *Polymeric Sorbents*

This type of materials have drawn attention of researchers given a combination of features such as high surface area and synthetic diversity, light weight, flexibility to structural

modification and thermal stability [71]. Many polymers present good CO_2 selectivity and high capacity in ambient conditions. For instance, melamine formaldehyde (MF) resin is a well-known example that has been considered as a cheap and available material suitable for CO_2 capture [83].

1.6.2 Chemisorbents

Chemisorbents are taken into account given the fact that the majority of physisorbents exhibit low performance when exposed to flue gas with low CO_2 partial pressure. Therefore, by incorporating modifications to the sorbent surface it is sought to create a stronger interaction between the acidic CO_2 molecule and the basic sites on the surface. In this way, both the capacity and selectivity for CO_2 can be increased. One of the major drawbacks of this technique is the added difficulty of regeneration of these materials, increasing considerably the energy consumption.

A large variety of porous materials exist that are capable of supporting amine function to enhance CO_2 adsorption and selectivity. The supports used are based on silica, polymers or zeolites. Aminated sorbents can be classified in three types. Firstly, those sorbents where the amine groups have been impregnated onto its surface. Secondly, when the amine is covalently attached to a support. Thirdly, there are those sorbents where the amine polymers polymerize together with the polymer support, which can be considered as a hybrid of the other two cases.

Within this category there are a number of materials which can be functionalized; such as carbonaceous materials (activated carbons), solid resin sorbents, polymeric sorbents, silica based and zeolite based. The adsorption mechanism is based on a chemical reaction between the CO_2 adsorbed and the amine groups in the surface. The mechanism accepted for this reaction is based on the model proposed by Caplow [84] and later reinforced by Danckwerts [85], where the overall reaction is:

$$CO_2 + 2R_2NH \rightarrow R_2NCOO^- + RNH_2^+$$

Reaction 2: Reaction mechanism of CO_2 with primary or secondary amines.

The adsorption capacity for primary and secondary amines, taking into account only the amine acting as a base, would be dictated by the stoichiometry of the acid-base reaction, which is 0.5 mol of CO_2 to 1 mol of amine. However, if sterically hindered primary and secondary amines are taken into account, there is only one important reaction with CO_2. This reaction is the formation of bicarbonate as shown in Reaction 3 [86], which

corresponds to the base catalysed hydration of CO_2. Thus, the stoichiometric of this reaction permits the adsorption of 1 mol of CO_2 per 1 mol of amine.

$$CO_2 + H_2O + R_2NH \rightarrow HCO_3^- + R_2NH_2^+$$

Reaction 3: Formation of bicarbonate.

The tertiary amines do not react directly with the CO_2 to form carbamates. In contrast, the primary and secondary amines do react with CO_2 forming the carbamates. However, the tertiary amines do produce protonated amine and bicarbonate in the presence of water (moisture) as shown in Reaction 3. This increases the capacity in 1 mol of CO_2 per mol of amine (stoichiometrically); however the kinetics is considerably slow.

The CO_2 adsorption capacity for different amine functionalized materials has been tested by a number of researchers [87, 88]. Carbon nanotubes have shown a considerable increase in CO_2 adsorption followed by zeolites and granulated activated carbon [87, 89, 90].

In summary there have been a lot of studies on amine enrichment of carbonaceous materials, and it has been shown to be effective. However, the impregnation resulted in a loss of surface area, pore blockage and loss of mesoporous and microporous volume. Obviously, this mechanism will be affected by the size and shape of the molecules of the amines used to fill the pores [34].

Zeolites present a large surface area and porosity which makes them a potential material for CO_2 adsorption. However, because zeolites have shown a considerable decrease in adsorption with increasing the temperature there are just a few studies on amine incorporation on zeolites.

It has been observed an increase of adsorption on aminated zeolites both at room temperature and high temperature (120 °C). It was suggested that while at low or room temperature physisorption played a dominant role on the adsorption, at high temperature the chemical interactions between CO_2 and the amine functionalized sites are favoured [91, 92].

Functionalized polymers has already been used to capture CO_2 (in low concentrations <1%) in some applications such as submarines, aircrafts and space shuttles [93, 94]. The manufacturing procedures of these materials are divided into two pathways [95]: firstly, by impregnation method or covalent chemical reaction of polymer or oligomers which have a

high content of amines on a given support. Another option is the synthesis of polymers which contain amine monomers or monomers that can be functionalized through a reaction of the functional groups.

The main impediment to introduce these sorbents in industrial applications is their elevated cost, which makes them not suitable for large scale applications such as carbon capture and storage (CCS). Despite the fact that some researchers have reported a considerable high CO_2 capacity for this type of materials such as 10 mmol/g for a variation of solid polymethyl methacrylate (PMMA) supported tetraethylenepentamine (TEPA) [96].

Functionalized silica supported sorbents, for instance PEI- impregnated MCM-41 (3.02 mmol/g at pure CO_2 atmosphere and 75 °C) [97], exhibits an increase in CO_2 adsorption capacity compared to other sorbents such as activated carbons and zeolites. However, low capacity was reported at low temperatures, which is assumed to be because of the slow kinetics of the adsorption process given to diffusion limitations. Additionally, a series of studies of performance and stability for MCM-41-PEI were reported [98-100]. Those studies tested the separation of CO_2 from a simulated flue gas stream, flue gas from a natural gas-fired boiler, and simulated humid flue gas. The adsorbent was placed in a packed bed column. The sorbent exhibited good selectivity for CO_2 over N_2 and O_2, and stability after 10 cycles of adsorption/desorption at 75 °C. However, the system was not stable at operational temperatures above 100 °C, and NO_X were adsorbed together with CO_2, which indicates that a previous separation of NO_X is required. Summarizing, amine impregnated silica support sorbents have been demonstrated to be capable of adsorbing CO_2 effectively. Nevertheless, the major drawback of these materials is the durability and regeneration kinetics, as well as the adsorption kinetics which has been shown to be slow. Additionally, the leaching of amines represents a considerable environmental hazard.

Alkali metal carbonate materials are based on the formula M_2CO_3, where the cation can be K, Na or Li. For supporting the carbonates different materials can be used, such as activated carbon, silica, ceramics and zeolites. Given that these materials operate at temperatures below 200 °C they are being considered for CO_2 capture from flue gas. The reaction of CO_2 with the material forms the corresponding bicarbonate. Then, by decarbonation reaction the material can be regenerated and the CO_2 liberated from the sorbent.

Chemisorbents have great potential as sorbents for CO_2 capture given the high CO_2 capacity reported and good CO_2 selectivity. However, the regeneration of these materials requires high energies and long time. Additionally, it was observed that SO_2 has a negative impact on CO_2 removal from the sorbent, therefore a prior separation of SO_2 before the adsorption would be required [101].

1.7 Gels

Organic material can be formed from gels, and particularly, Formaldehyde-Resorcinol (RF) resins, which are a type of carbon materials that have attracted attention due to their potential application in many processes, such as, catalysis, thermal insulation, carbon capture, filtration, energy storage and as precursor of electrically conducting carbon material.

RF gels, generally, exhibit a high pore volume, low density, large surface area and an amorphous structure. These parameters can be controlled and tailored as a function of the synthesis procedure [102], this characteristic make RF gels very attractive for a number of applications.

Gels exhibits solid-like behaviour which is a consequence of a continuous network which extends throughout the volume of a liquid (solvent). The network is formed by cluster or group of molecules which are linked and interconnected. There are different contributions to this links such as methylene bridges, ether bridges, hydrogen bonding or chain entanglements.

Organic aerogels, xerogels and carbon based materials have received a significant attention due to their potential applicability to gas treatment (adsorption) processes. Therefore, a lot of effort have been put to understand and control the synthesis parameters to tailor the structural properties to match specific requirements on given applications. The tune-ability of gels is attributed to the sol-gel process by which this materials are produced. The current state of the art on this matter is described in the following sections.

1.7.1 The Sol-Gel Process

The Sol-Gel process is a synthesis method used to produce gels. It lies on solid particles or nanoparticles being dispersed and agglomerated in a solution forming a net (gel) through the liquid, which can be defined as a colloid. The term colloid is used to refer to a continuous phase (gas, liquid or solid) where a substance is dispersed.

For instance for a sol, the liquid is the continuous phase and the solid is the dispersed phase. When comparing a non-colloidal liquid to a sol the difference is that if the latter is put to a centrifuge the particles would precipitate, whereas for a non-colloidal solution this would not occur.

On the contrary, for gels the dispersed phase is liquid and the continuous phase is a solid. The gel is a solid network which occupies the total volume of the liquid. Generally, gels have a density similar to the liquid and cohesion similar to a solid.

1.7.1.1 *Sol Production*

Mainly any solid phase dispersed in a liquid o solution so that the solid does not precipitate would form a sol. The sol production can be classified in two main ways:

- Nanoparticles are formed in the liquid and then these particles would net together forming a gel, which is the case for Silica aerogels and Resorcinol-Formaldehyde (RF) gels [103-107].
- Nanoparticles are synthesized and later dispersed through the liquid. This is the case for newer generation of gels such as metal chalcogenide aerogels or carbon nanotube aerogels [108, 109].

1.7.2 Resorcinol – Formaldehyde Gels

The RF gel formation can be summarized in the following steps [104, 105]:

- Hydroxymethylated resorcinol is formed by the reaction of resorcinol with formaldehyde.
- The formation of nanometer-sized clusters is allowed by the condensation of the hydroxymethyl groups; in this way the gel is formed by the crosslink of those clusters.
- In any sol-gel process, the formation and growth of those clusters are influenced by typical sol-gel parameters such as pH of solution, temperature and concentration of monomers.

Initially, the RF gels were produced by the polymerization of resorcinol and formaldehyde, using as a catalyst sodium carbonate [110-112]. However, a number of researchers studied the production of aerogels from phenol and formaldehyde [113, 114].

Typically, methylene ether (-CH_2OCH_2-) or methylenes (-CH_2-) are the two main groups bonding the aromatic moieties in the synthesis of phenolic resins. Similarly, for RF gels, the linkages of the different aromatic groups are facilitated by the presence of the same mentioned groups. The concentration of those groups depends on a number of parameters such as pH, catalyst and monomer concentration. RF gels can be synthetized by either basic or acid conditions and resorcinol reacts with formaldehyde similarly as phenol does. However, the ability of resorcinol to crosslink forming clusters is higher than for phenol because resorcinol can bond up to three formaldehyde groups; with these additions producing mainly ether bridges.

The resorcinol – formaldehyde reaction generally occurs in aqueous system. At room temperature, the reaction of R and F is favoured; however, it is very slow. For this reason, a catalyst is typically added to accelerate the rate of reaction, which, it is worth noting, is consumed and not recoverable after the reaction. The catalyst most commonly used for basic catalysis is sodium carbonate, in which sodium is representative of Group I in the periodic table (Li, Na, K and Cs) [103]. For gels synthesised in basic conditions, gelation requires long time and high temperature. Instead, for gels originating in acidic conditions, gelation occurs at room temperature and faster, even in the range of few hours. The catalysts used in acidic synthesis are usually acetic acid, perchloric acid or hydrochloric acid.

1.7.2.1 *Acid-Catalysed Gelation*

The main difference between acid and basic catalysis lies on the activation of the reaction. In the acid catalysis the activation is due to the increase of electrophilicity of formaldehyde (Reaction 4); instead, in the basic case the activation lies on the electron donating ability of resorcinol from -OH to O^- to activate the aromatic ring (Reaction 5).

Formaldehyde undergoes a protonation reaction (1), which allows the hydroxymethylation of resorcinol (2) to occur. Because of the acid environment, the hydroxymethyl protonates (-OH_2) (3) and permits the formation of o-quinone methide (4). This intermediate specie can react in two ways, condensation (10 - Reaction 5) or to produce a methylene bridge (5) with another resorcinol (R). These reactions give rise to the RF gel formation, by enhancing the crosslinking in the structure.

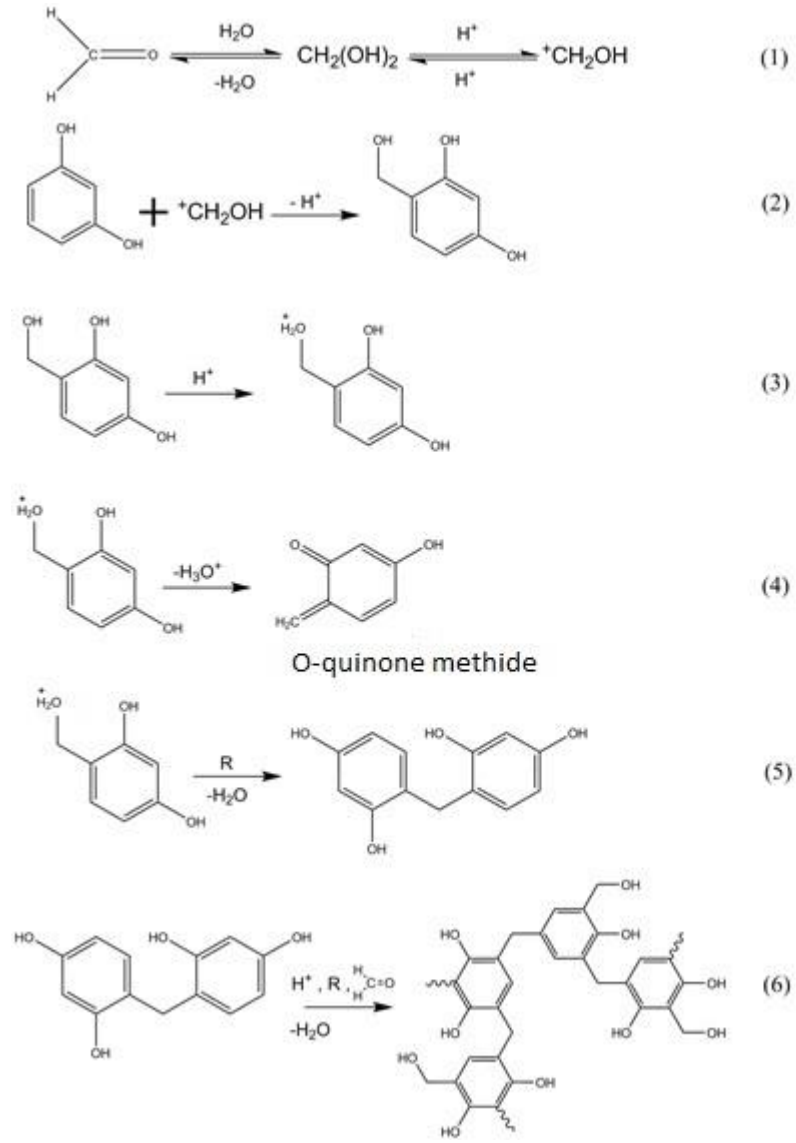

Reaction 4: Mechanism of the acid-catalysed RF aerogel synthesis, reactions adapted from Aerogels handbook [115].

1.7.2.2 *Base-Catalysed Gelation*

In this study, base-catalysed gelation is used for the RF gel synthesis. The base-catalysed gelation can be more attractive than acid gelation for different reasons. In spite of that the acid rout (hydrochloric acid) required, generally, shorter gelation times than gels promoted by a base [116]. Gels promoted by an acid-catalysed gelation (e.g. nitric acid) might lead to gels with reduced porosity (higher density), which is an important parameter for a material meant to be applied to gas treatment, such as CO_2 adsorption [117]. The increase of density was explained as, for acid promoted gels, the aggregation levels of clusters increases, and, consequently, the space between them is reduced [117]. Additionally, another important reason, from an industrial perspective, is to avoid the use of acids, which is always an

advantage, because it facilitates the process, reduces risks, and, therefore, becomes cheaper.

As was mentioned above, the resorcinol, in basic environment, gets deprotonated into its anion form. The $–CH_2OH$ group can bond to the resorcinol due to the increased electron density at the position 4 or 6 as shown in the schematic 7a in Reaction 5. The addition of one molecule of formaldehyde produces the hydroxymethylation and it activates a second position to add another $–CH_2OH$ group, giving rise to the dihydroxymethylation (8). After this, the basic catalyst allows the formation of the intermediate o-quinone due to the deprotonation of hydroxymethylated resorcinol. Similarly to the acid catalyst, the o-quinone intermediate is able to react and form a methylene bridge (10) with another resorcinol molecule. Basically, the formation of that intermediate and the ability to increase the electron density (position 2, 4 and 6 or resorcinol ring) explains the higher reactivity of resorcinol compared to phenol.

The polymerization or condensation reaction of RF clusters can be attributed to the active sites on the resorcinol, and it can be said that the crosslinking of these clusters can mainly occur due to the methylene bridges [118].

Summarizing, the formation of hydroxymethyl of resorcinol and its condensation by methylene bridges ($-CH_2-$) are the two main reactions in the base catalysed formation of RF gels.

Most of the physical features of these gels, such as surface area, density, particle size and pore size distribution, can be potentially tailored by controlling process parameters, for instance concentration of monomers, catalyst and solution pH.

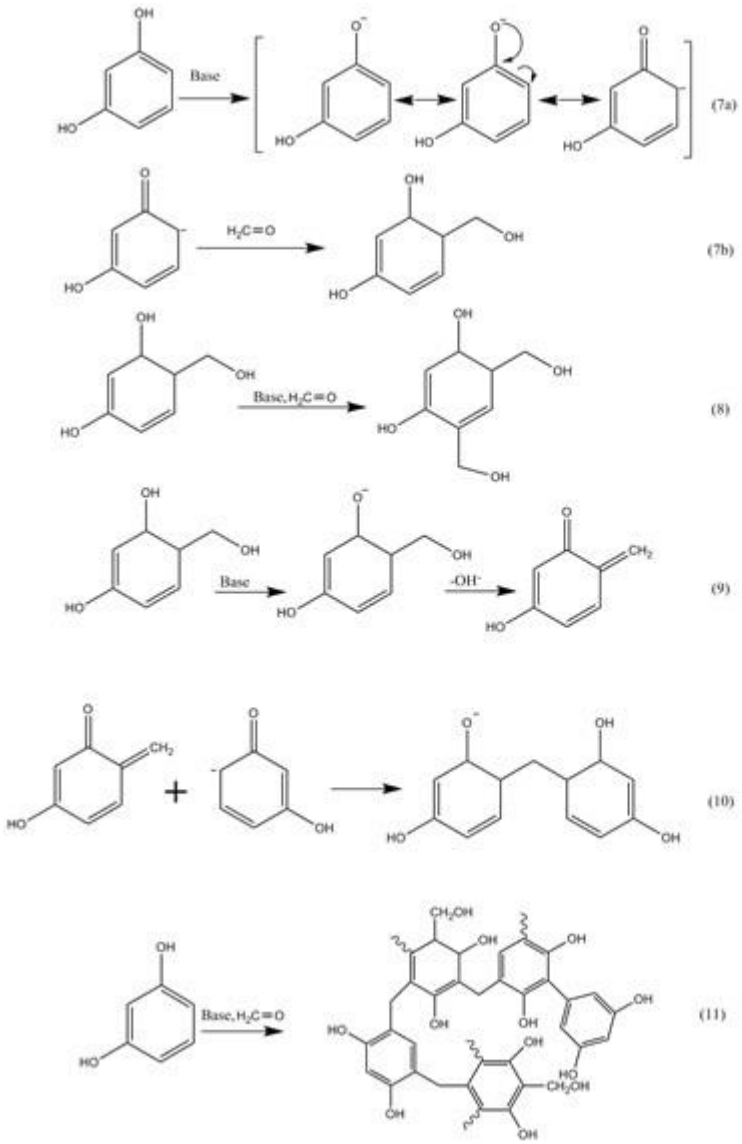

Reaction 5: Mechanism of the base-catalysed RF aerogel synthesis, reactions adapted from Aerogels handbook [115].

1.7.3 Melamine - Formaldehyde

Melamine and formaldehyde (MF) undergo a similar type of reaction as resorcinol – formaldehyde. MF reaction produces stable polymeric resins, which indeed have a very similar synthesis procedure and chemistry compared to phenolic resins [119].

The reaction of MF produces six possible products, of which the most stable is the hexamethylolmelamine [120]. Hoodgind *et al.* stated that this compound can be produced in two ways, either by heating melamine with an excess of neutral formaldehyde at 90 °C or by allowing the melamine to react with formaldehyde at room temperature for a prolonged

period of time (15 to 18 h) [120]. The first of those options is similar to the conditions used in this research.

The reaction of MF is controlled by similar parameters as the RF reaction such as ratio of monomers, catalyst, time of reaction and temperature [120, 121]. The properties of the final product of the MF reaction can be controlled and tailored by those parameters.

The reaction can be divided into two stages: formation of methylolmelamines (Reaction 6) and condensation (Reaction 7). The formaldehyde in the solution reacts with the dissolved melamine, but melamine has a low solubility at room temperature in water, 0.5 g/100 ml at 25 °C and 5 g/100 ml at 100 °C. Methylolmelamine is formed as a result of that reaction; this compound exhibits a higher solubility than the melamine and as a result of this the solution changes from a suspension to a clear solution.

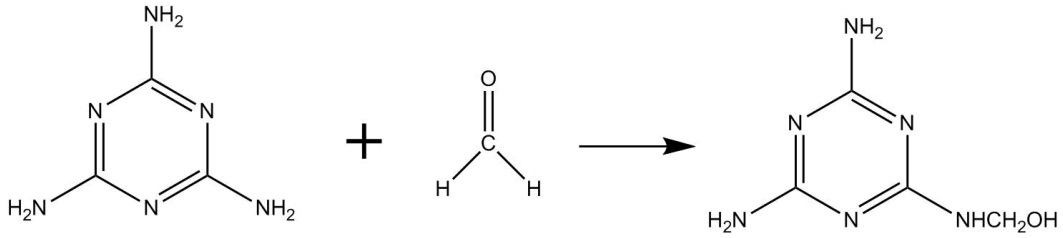

Reaction 6: Formation of methylolmelamines

The crosslinking of clusters of methylolmelamines happens by two types of linkages or bridges, the ether bridge or the methylene bridge [121]. Jahromi explained that those two types of linker depend on the pH of the solution; at low pH, values of 7 – 8, the methylene bridges are favoured while at pH higher than 9 ether bridges are predominant [83]; see Reaction 7.

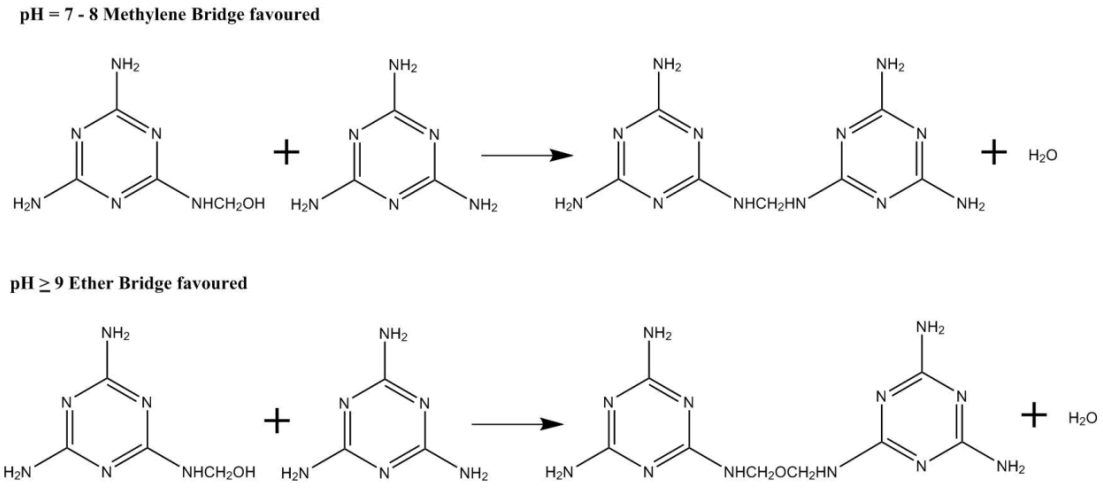

Reaction 7: Methylene and ether bridge formation depending on the solution pH.

1.7.3.1 *Resorcinol – Melamine – Formaldehyde Reaction*

Zhou *et al.* showed that both systems RF and MF can produce large microspheres of polymer at hydrothermal conditions and even without catalyst [119]. They have also shown that the condensation of MF into the RF system can produce a homogeneous MRF microspheres network.

The crosslinking reaction among the MF and RF microspheres would be facilitated by the methylene and ether bridge of the hydroxymethyl groups, in this way forming small clusters. Those small clusters would act as the nucleation sites, which trap inside enough unreacted particles that would continue to react and consequently produce the cluster growth. This process could be compared to the Stöber process where the nucleation is fast and then the clusters grow, without the need of new nucleation sites [122, 123].

1.7.4 Sol-Gel Transition

A sol becomes a gel simply when the solid nanoparticles agglomerate forming a solid network throughout the liquid. In the particular case of RF gels in a basic medium, the unstable intermediate o-quinone methide is formed and reacts with a resorcinol molecule forming a more stable methylene bridge, which leads to the formation of clusters that crosslink through the volume of the solution [105].

When the gel is formed, its viscosity tends to infinity meaning it is no longer able to flow. This stage in the process is called gelation. When this occurs throughout the total volume of the solution is defined as gelation point.

1.7.5 Process of Making RF Aerogel via Base-Catalysed Route

Depending on the desirable final physical properties of the RF gels, there are two main parameters to be controlled: the resorcinol to catalyst ratio (R/C) and the resorcinol to water ratio (R/W).

Step 1: Preparation of solution.

The calculated amount of resorcinol is dissolved in water, then the catalyst is added (typically sodium carbonate or a similar base catalyst). Once this is mixed, the formaldehyde is added and stirred to enhance the mixture of solutes.

Step 2: Gelation and Aging.

Once the solution is stirred, it is placed in an oven at a temperature in the range of 85 ± 5 °C. Particularly, that temperature is what was used by Pekala in his work [111]. The temperature affects particularly the gelation time, always decreasing it as the temperature is increased.

After the gel reaches the gelation point, the samples are usually cured for a period of time. The curing time can vary from hours to days according to the gel composition. This stage enhances the crosslinking within the structure improving its mechanical properties.

Step 3: Solvent Exchange.

It is important to remove the solvent (generally water) from the pores and cavities and replace it with a less polar solvent (commonly acetone). In this way the capillary forces acting on the wall of the pores are reduced and this helps to prevent the collapse or shrinkage of the structure of the gel.

Step 4: Drying.

The drying could be done in different ways: supercritical drying, freeze drying or ambient temperature drying. Pekala used supercritical CO_2 drying in his original thesis [111] and it became a very popular method since then. But, from an industrial point of view this is expensive, dangerous and difficult at that scale. In contrast, subcritical drying and under vacuum techniques have been developed. In this case, the wet gel, after solvent exchange, is placed in a vacuum oven at a temperature of 90 °C in order to remove all the remaining solvent from the gel pores.

1.7.6 Type of Gels

The type of gel will be defined according to the drying method used. The gel can be classified as aerogel, xerogel or cryogel. The drying method is a very important stage in the gel formation because it has to be able to empty the pores of the gels without collapsing its structure.

In order to understand the importance of the drying method, it is necessary to describe first some parameters such as contact angle, surface tension and capillary forces.

When two immiscible fluids, or a fluid and a solid surface are in contact, there exist forces that act across the interface. These forces are called the capillary pressure or capillary forces. Therefore, the capillary forces, P_C, depend proportionally on the surface (interfacial) tension (ϒ) and the contact angle (θ) of the two phases, and are inversely proportional to the radius (r) of the interface or the capillary. The capillary pressure is defined by the Young-Laplace equation (Equation 1):

$$P_C = \frac{2\,\gamma\,Cos\,\theta}{r} \qquad \text{Equation 1}$$

The surface tension is a property of fluids which describes its capacity to reduce the interfacial area as much as possible. The surface tension defines the result of two forces acting on the surface of a fluid, which are the attraction of the molecules to each other (cohesion) and the attraction to the other phase in contact (adhesion). The contact angle describes the interaction of a fluid and a surface, expressing the wettability of the surface of the solid phase.

As it can be deduced, for a smaller capillary radius, the capillary pressure is higher. Therefore, when this is applied to a porous material, with pores in the range of nanometres, the capillary pressure inside the material is strong enough to collapse the structure. This occurs when the gel is allowed to dry in ambient temperature giving rise to what is called a xerogel. In this case, the structure collapses and shrinks forming a very dense material with small pore sizes, but because of the shrinkage, the porosity of the material is lost and its pore volume (capacity) decreases considerably.

When the gel is dried at ambient temperature, the pressure in the pores increases, but the system (wet gel and surrounding air) will tend to equilibrium. Therefore, the pressure will tend to atmospheric (see diagram in Figure 2) while evaporating the solvent and causing the pore collapse.

The most common process of drying used is supercritical drying (SCD). This method consists in the transformation of the liquid (solvent) in the pores into gas. In this way the surface tension is reduced considerably and so does the capillary forces inside the pores. The following pressure/temperature diagram represents the path followed by the different types of drying method. The diagram represents the phase change of the solvent in the pores. In the SCD the pressure and temperature are increased above the critical point of the solvent, in this way, the liquid – gas transformation occurs via the supercritical fluid

area but there is no evaporation which leads to the pore collapse, and the surface tension is eliminated therefore there is no capillary pressure. This produces the so called aerogel.

Another option is freeze drying which consists of sublimating the solvent in the pores. The freeze drying has some drawbacks, such as that it is more expensive than SCD which is of a big concern particularly for industry. Additionally, if the sublimation is not done properly, the solvent could do the transition to gas through the liquid state, which would increase the capillary forces and produce the collapse of the structure. Also, the process of crystallization of the solvent might increase cluster growth and this could damage or break the structure, therefore the resulting cryogel is weaker.

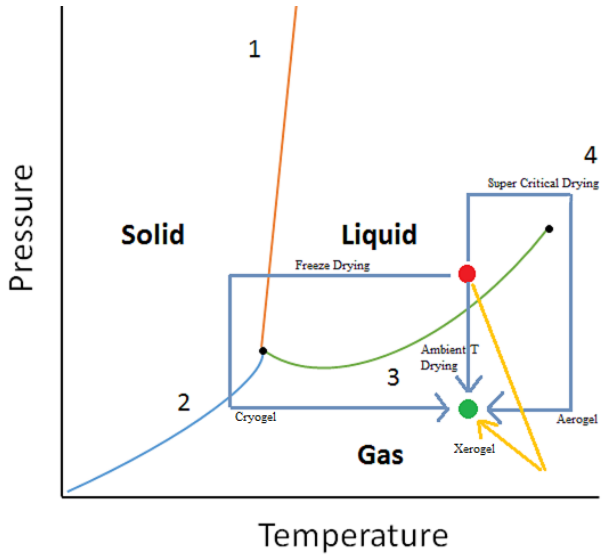

Figure 2: Phase diagram for solvent inside a porous solid material.

However, as it was explained before in Section 1.7.5, the solvent plays a crucial role in the drying stage. Therefore, the surface tension of the solvent is a very important parameter affecting the drying stage. The process of making the RF gel proposed in this thesis includes the solvent exchange step. The solvent, water, is replaced with acetone which possesses a considerably lower surface tension. At 20 °C the surface tension of water is 0.073 N/m while that of acetone is 0.0252 N/m [124]. Therefore, this would reduce the impact of the drying stage, avoiding the collapse of the structure in the material. The drying stage in this research would follow the definition of xerogel by subcritical drying. The material would be placed under vacuum and heated; this reduces the time of drying drastically and as a consequence the time the material undergoes the drying. The subcritical drying could result in the collapse and destruction of the structure due to the high capillary forces promoted

by the evaporation of the solvent. Therefore, by introducing the solvent exchange step replacing the water by a solvent with lower surface tension (acetone) the drying of the wet gel is simplified. This is important from an industrial point of view because cost as well as the technical complexity would be reduced compared to the freeze drying or the supercritical drying.

1.7.7 Factors affecting the structure and properties of RF gels

There are a number of important factors such as solvent, temperature, chemical reaction, time, catalyst, agitation, but among them there are two main aspects influencing the sol-gel chemistry of aerogels synthesised by base catalysed route, which are the concentration of monomers and catalyst and the initial pH of the Sol.

Solvent plays an important role in the gel formation. Also, temperature plays an important role in terms of chemical kinetics in the same way as for any chemical reaction. Therefore, the temperature may accelerate the formation of clusters or nanoparticles which would affect the gelation time [103]. Depending on the reaction it could produce a heat release, which might lead to an even faster reaction. The gelation time is an important aspect of gel formation, being generally the slower the better.

The agitation of the sol would have an impact on the uniformity of the gel formed. It is important that the solid dispersed phase in the sol is uniformly dissolved.

1.7.7.1 *The Initial pH of the Sol*

The initial pH of the Sol has an impact on the size of the pores in the gel as it is generally understood that increasing pH the surface area increases [110, 125-127]. For higher values of pH, the formation of hydroxymethyl derivatives of resorcinol is favoured producing highly branched clusters. This leads to more unstable structures which produce a larger number of particles and smaller interconnections between them [105]. In contrast, when the pH is lower the effect is the opposite. Thus, the formation of anions of resorcinol is less favoured which, as a consequence, leads to less branched structures, therefore the polymerization would take longer and the particles formed would be larger. Obviously, the nucleation regime would control the size of the pores and voids in between the particles of the polymer, thus controlling the mesoporosity of the gel. Therefore, lower pH tends to produce larger pore sizes. In contrast, higher pH favours the crosslinking in the gel reducing the pore size [126].

1.7.7.2 *Resorcinol – Formaldehyde Molar Ratio*

The stoichiometric ratio for resorcinol to formaldehyde (R/F) is typically set at 1:2. However, the relative quantities can be varied to affect, the degree of crosslinking, hence, the density and structure of the final gel. This study will investigate how the R/F parameter affects an unmodified gel, and in a related investigation how the increase of nitrogen containing additives affects the gel properties, i.e. the ratio of R to additive (e.g. melamine or ammeline) is also varied and the effect on final gel structure is studied. This means that both R/F and the role of substituting R and varying the associated F in the reaction are studied.

1.7.7.3 *Resorcinol – Catalyst Molar Ratio*

Regarding the concentration of monomers, the ratio resorcinol to catalyst (R/C) is one of the most important factors dominating the gel physics properties. The R/C ratio has a direct impact on density, surface area and mechanical strength of Resorcinol-Formaldehyde gels. In general, as this ratio decreases so does the pore diameter, while density is increased [112, 128]. Different authors indicate that using lower R/C values, which means higher content of catalyst, the resulting gels have smaller particles with a diameter in the range of 3 – 5 nm and large neck size (fibrous appearance). On the other hand, higher R/C ratio, lower catalyst content, would lead to larger particle sizes (11 – 14 nm) and the shape as a 'string of pearls' [104, 112]. This structural difference is related to the shrinkage of the gel during drying stage. For instance, colloidal gels incur in a little shrinkage during supercritical drying, which affords them with lower surface area and weaker structures than polymeric gels [105]. Simultaneously, low R/C values (high catalyst content) lead to the formation of small particles, which means microporosity. In contrary, high R/C values (low catalyst content) results in mesoporosity.

The different shrinkage rate has an impact on the density of RF gel as well. For instance, for a constant R/F ratio the lower the R/C ratio used, the higher the density [129]. Nevertheless, comparing gels with similar density, polymeric gels (R/C = 50) were three times stiffer than colloidal (R/C = 200), which demonstrates the impact of neck particles on the mechanical properties.

During the polycondensation reaction between resorcinol and formaldehyde, highly crosslinked particles are formed. The R/C ratio is the main parameter that controls the size of interconnected particles and consequently the final pore size [104]. Additionally, other

authors have shown that R/C ratio is also the most influencing parameter controlling the surface area, pore volume and mechanical properties [102]. Mirzaeian *et al*. showed, that for the same RF gel, increasing the R/C ratio leads to an increase in the volume of N_2 adsorbed [102]. Additionally, Yamamoto *et al*. showed that the pore size distribution increases with increasing R/C ratio for a constant ratio of resorcinol to water [128].

1.7.7.4 *Catalyst*

The catalyst plays a key role in the gel formation, gelation time and the physical characteristics of the gel. For example, comparing catalysts of group I it was demonstrated that Li, Na, K have similar ability to stabilize the RF colloidal suspension. This occurs by destabilizing the oligomers, in this way increasing their solubility and leading to small clusters [103]. Instead, Cs is less able to stabilize the colloidal suspension, the oligomers becomes less soluble, which leads to larger clusters [103]. Therefore, gels produced with Li, Na or K as a catalyst are generally applied to gas phase separations while gels of Cs catalyst are better suitable for aqueous phase processes.

1.7.7.5 *Total Solid Content*

For a constant R/C ratio, increasing the ratio of resorcinol to water (which increases the solid content) leads to a decrease in the value of the peak of the pore size distribution; while surface area does not depend on the resorcinol to water ratio [128]. Increasing the solid content in the solution means less solvent in the mix. Therefore, the density of the final RF gel would be increased, as observed by Fairen-Jimenez *et al.* [130]. As a consequence, increasing the density would lead to a smaller pore size due to the increase of reactant quantity for a given volume, as shown by Bock *et al.* [131]. This would also influence the pore size distribution as observed by Tamon *et al.* They observed that high solid content results in monodisperse pores while low solid content exhibits a heterogeneous polydisperse porosity [104].

1.7.7.6 *Melamine Content*

There is not much research into this parameter; Zhou *et al*. defined this as the ratio of M/R and have stated that increasing the melamine content in the solution decreases the particle size significantly from 15 µm to 1 µm [119]. Given the basic character of M, increasing the M content should accelerate the reaction of polymerization between R and F; therefore, it would increase the crosslinking density and the molecular weight of polymers. However, the steric hindrance observed for larger chain structures increases their incompatibility

with water, which, in turn, increases nucleation rates but decreases the time of cluster growth. Overall, increasing the melamine content would result in smaller microspheres.

1.7.8 Application of RF Gels

Most applications of RF gels are linked to their porous characteristics and the ability to tune their structural properties, such as pore size, pore volume and surface area, depending on the particular application. These properties can be tuned by altering the RF synthesis procedure; moreover, the physical shape (monolith, powder and/or film) of the organic RF gel is tuneable according to the requirements of a given process [132].

Due to their high surface area, an important application is the use of RF gels as catalyst supports, and they have found recent application for energy storage, gas separation and as adsorbents, as a result of their tuneable micropore and total pore volumes. The latter is the primary focus of the work presented here. RF gels have also been combined with membranes, in order to increase their selectivity towards specific gases, such as CO_2 [133].

In addition to exploiting the porous structure for storage, RF gels have also been found to be good insulators, with very low thermal conductivity ($\sim$0.012 W m^{-1} K^{-1}) at room conditions, while other materials such as silica have slightly higher value ($\sim$0.016 W m^{-1} K^{-1}) [134]. Again, it is the porous structure that effects these excellent characteristics, this time acting to reduce the diffusion of air and reduce thermal transport. Additionally, aerogels are very good acoustic insulators; the propagation of acoustic waves depends on the gas trapped in its pores and the pressure, aerogel density and its structure [106]. Aerogels also have applicability to electrical uses such as batteries and as capacitor electrodes, due to their super-low dielectric constant [106].

Chapter 2
Aims and Objectives

2 Aims and Objectives

RF xerogels have many potential applications, as detailed in Section 1.7.8, for which, many of them, depend on the structural properties of the material. Therefore, understanding the effects of controlling the synthesis parameters and their impact on the final xerogel properties is vital to achieve materials with the required specifications. There are a variety of additives that can potentially be used in order to alter the properties of the synthesised gels, with some offering the opportunity to enhance the CO_2 adsorption capacity of these materials; such an additive could be melamine. There still a general lack of understanding as to how the incorporation of certain additives would modify gel formation and the impact on final xerogel properties.

2.1 Overall Aim

Hence, the main aim of this project is to study the modification of the synthetic procedure used to manufacture Resorcinol-Formaldehyde (RF) xerogels, in order to incorporate an additive, in this study melamine, into the structure, forming MRF xerogels (Chapter 5). Characterization of the materials obtained is undertaken to determine the chemical and textural properties with the objective of determining their effect on CO_2 adsorption capacity compared to RF xerogels (Chapter 6, 7 and 8).

2.1.1 Objective 1: Synthesis of a Suite of Modified Xerogels

In order to determine the effect of selected synthetic variables on the final gels, several parameters will be kept constant, thereby allowing each of the following factors to be probed:

- Molar ratio of resorcinol to catalyst (R/C).
- Molar ratio of resorcinol to formaldehyde (R/F).
- Percentage of resorcinol mass substituted by additive, in this study melamine ([M]).

Ranges of values for the three factors will be selected by considering the previous literature but also to push the bounds of the synthesis procedure to fully evaluate each parameter, which is explored in Chapter 6.

2.1.2 Objective 2: Textural and Chemical Characterisation of Modified Xerogels

Various characterisation techniques, detailed in Chapter 6 and 7, that will be used to probe the materials include:

- Nitrogen adsorption measurements at low temperature to obtain textural properties of the MRF xerogels, allowing the variations observed to be linked to the variables studied.
- Thermal stability of MRF xerogel will be analysed using TGA, providing insight into the potential of these materials in regenerative processing, and proximate analysis will provide information on the bulk composition of the materials.
- Surface analysis techniques (FTIR, XPS and Boehm titration) will be used to analyse the MRF xerogels to gain an understanding of the impact of incorporating melamine into the MRF xerogels on their final chemistry.

2.1.3 Objective 3: Evaluation of Selective CO_2 Adsorption on Modified Xerogels

Gravimetric adsorption measurements will be carried out on selected MRF xerogels to obtain:

- Pure component adsorption isotherms and kinetics for CO_2, CH_4, H_2 and N_2.
- Cycling adsorption studies on selected modified xerogels; samples will be selected on the basis of thermal stability.
- Selectivity challenges of selected modified xerogels using gas mixtures of CO_2-N_2, CO_2-CH_4 and CO_2-H_2.

The data obtained in these experiments will allow determination of (results shown in Chapter 7 and 8):

- Adsorption capacities of modified xerogels for CO_2.
- Heats of adsorption from thermodynamic equilibrium isotherm measurements for CO_2 adsorption.
- Kinetics of adsorption for CO_2 adsorption on modified xerogels.
- Activation energies for CO_2 adsorption, from kinetic profiles for CO_2 adsorption.
- Determine of cycling working capacities for CO_2.
- Selectivity of modified xerogels for CO_2 over competing species of CH_4, H_2 and N_2, determined using IAST theory.

The results from Objective 2 will provide detailed understanding of the trends obtained for Objective 3, thereby allowing insight into the interactions controlling adsorption onto modified xerogel materials. This study, therefore, aims to provide sufficient information to

understand the role of [M] as a synthesis parameter and assess the CO_2 adsorption enhancement as a consequence of the increased surface basicity of modified xerogels due to the incorporation of melamine.

Chapter 3
Characterization Techniques

3 Characterization Techniques

The previous chapter briefly introduced carbon capture systems as a way of controlling the increasing atmospheric CO_2 concentration. It was mentioned that CO_2 separation from flue gas can occur at different stages (pre-combustion, post-combustion or oxyfuel), and a number of technologies, available for CO_2 capture in post combustion processes, were introduced. Among them, absorption has been widely studied and applied industrially, but this study will focus on adsorption systems, particularly xerogels based on resorcinol-formaldehyde resins, which can be categorized as potentially suitable materials for post-combustion separation. Therefore, this chapter focuses on the adsorption theory applied to gas-solid interactions as a main characterization technique; as well as other methods such as Fourier transform infrared spectroscopy, scanning electron microscopy, elemental analysis, thermogravimetric analysis and titration.

3.1 Adsorption Theory

The fact that solid particles can uptake large volumes of gases had already been noticed at least in 1777 by Fontana [135]. Some years later, by 1814, it was noticed that the volume of uptake varies from gas to gas and from material to material (in this case charcoal); therefore, it was suggested that the uptake depends on the available surface of solid material [136]. Additionally, in 1843, Mitscherlich suggested the importance of pores in the solid material and estimated the approximate diameter based on the adsorption of carbon dioxide forming a condensed layer [137]. In 1881, the term adsorption was introduced by Kayser [138] stating the difference between adsorption and absorption.

Those discoveries set the precedent for two of the most important factors in adsorption, namely surface area and porosity (pore size and pore volume). These concepts, nowadays, are extended not only for charcoal but for all types of solids.

Firstly, it is necessary to define the components in an adsorption system; such as adsorbent and adsorbate. The former defines the substance on which adsorption occurs; while, the latter is the substance itself that is adsorbed on the adsorbent. Additionally, adsorptive is the substance that is potentially capable of being adsorbed by the adsorbent. In summary, the adsorptive is capable of being adsorbed on the adsorbent, forming what is defined as adsorbate.

Adsorption occur when molecules, atoms or ions from a gas or liquid, adhere to the surface of a solid or liquid, forming a layer, or atomic film, on the surface of the adsorbent. This phenomenon is different from absorption, where a given substance diffuses into a solid or liquid forming a solution. Therefore, the main difference between these two mechanisms is that in absorption there is a uniform distribution of the absorbed substance in the entire bulk. On the contrary, adsorption phenomenon occurs exclusively on the surface of the adsorbent [139]. However, the term sorption involves both processes. Adsorption can occur at an interface between any two phases, such as, liquid-liquid, gas-liquid, gas-solid or liquid-solid interfaces.

3.1.1 Adsorption Mechanism

Considering a gas-liquid or gas-solid interface, *Langmuir* stated that when a gas molecule impinges onto the surface of a solid or a liquid, the molecule does not rebound elastically; instead the gas molecule condenses on the surface for a period of time [139]. The condensation of the gas molecule on the surface is a result of the field of force that occurs on the surface of the atoms. Hence, the length of time that the gas molecule remains condensed on the surface of the adsorbent, before its evaporation, would depend directly on the intensity of those surface forces. As a result, it can be said that adsorption is the consequence of that period of time where the gas molecule remains condensed on the surface of the adsorbent. The nature of the surface forces will define the adsorption, if those forces are intense the rate of evaporation would become negligible; thus the surface of the solid would be completely covered. On the other hand, if those forces are weak it will result in partial coverage of the solid surface; given that the evaporation rate would become high.

The adsorption mechanism would also depend on the size of the adsorptive molecule, the width of the pore and the energetic interaction between them. If diffusional effects are not taken into account, the adsorptive would be adsorbed first on those pores of higher energy, followed by filling of larger pores (decreasing energy). It is also worth noting that adsorption is a dynamic process, ergo an equilibrium exists of molecules being adsorbed and desorbed.

3.1.2 Adsorption on Solids and Liquids

Adsorption on liquids can be understood by considering that the molecules present at the surface of liquids are exposed to unbalanced forces, and therefore, they are attracted

inwards. This results from the fact that molecules in the bulk of the liquid are equally attracted from all directions by the surrounding molecules. Instead, molecules at the interphase are in contact with other liquid molecules only on one side; thus differences in forces for these layers of unbalanced molecules give rise to surface tension.

In the case of solids, these unbalanced forces, or residual forces, are generated on the surface. The occupancy of these available sites results in adsorption. In the particular case of gas adsorption on solids, the gas molecule approaches the surface of the solid and stays condensed for a period of time before returning to the gas phase. The duration of that time will depend on many variables such as nature of the adsorptive, type of adsorbent, temperature, pressure, capillary forces and surface heterogeneities, among others.

3.1.3 Types of Adsorption

Adsorption can be distinguished by two different mechanisms: chemical adsorption (chemisorption) and physical adsorption (physisorption). The main difference between these mechanisms is in the nature of the attractive forces existing between the adsorbate and adsorbent.

In *chemisorption,* the forces of attraction between adsorbate and adsorbent are very strong, due to the chemical bonds formed between them on the surface.

In *physisorption*, the forces of attraction between adsorbate and adsorbent (usually gas and solid molecule, respectively) are a consequence of the formation of intermolecular electrostatic interactions, either London dispersion forces or relatively weak van der Waals' type.

Thermodynamically, the process of physical adsorption is always exothermic due to the decrease in entropy of the system as a result of ordering of the adsorbate on the surface.

$$\Delta G = \Delta H - T\Delta S \qquad \text{Equation 2}$$

Therefore, the amount physically adsorbed is affected by the temperature of the adsorption system. The amount adsorbed would increase as temperature is decreased, according to Le Chatelier's principle [140].

However, in chemisorption, due to the fact that a chemical reaction is involved, the overall process may be exothermic or endothermic according to the type of reaction occurring between the adsorbate and adsorbent.

3.1.3.1 *Chemisorption*

Chemisorption implies that the adsorbate bonds chemically to the surface of the adsorbent. Thus, there is an exchange of electrons between them, which causes the formation of different compounds on the surface due to the valence bonds. The bonds formed are considerably stronger that physical interactions, given that the heats of adsorption for chemisorption are in the range of 600 kJ/mol (C-N bonds) to 800 kJ/mol [141]. Consequently, chemisorption requires large amounts of energy to break the formed bonds (desorption).

Chemisorption does not cover all the surface of the adsorbent. On the contrary, it only occurs between specific adsorptives and sites on the surface; and only if the sites are unoccupied by another species. Therefore, chemisorption forms just a single layer of adsorbate on the surface of the adsorbent. However, it is possible that a sorbent chemisorbs an adsorptive forming a single layer and physisorption occurs forming subsequent multilayers. Therefore, hybrid cases of physisorption and chemisorption exist [141].

One of the most characteristic features of chemisorption is that the nature of the adsorptive, after desorption, may be different to the one previous to adsorption; hence, the species adsorbed may not be recoverable. Therefore, chemisorption could be a non-reversible process, as it is based on a chemical reaction, which is not always reversible [142]. As it is the case for any chemical reaction, chemisorption involves energy, which would be of the magnitude of a chemical reaction, and, as it was mentioned before, the energy involved in chemisorption could be exothermic or endothermic as for any chemical reaction. Likewise, the first step of chemisorption requires an activation energy.

Another important aspect is that the isotherm obtained for chemisorption (in the case of chemisorption only) allows evaluation of solely the surface corresponding to the active sites that are able to form a covalent bond with the adsorptive. Generally, most chemisorption processes are described by a Langmuir isotherm (Section 3.2.6.1).

3.1.3.2 *Physisorption*

Physical adsorption processes are controlled by dynamic equilibria between the adsorbent and adsorbate; this equilibrium is the result of the ratio of molecules being adsorbed and desorbed from the sorbent surface. In this process there are no chemical reactions; therefore, no chemical bonds are formed. Physically adsorbed molecules may diffuse along the surface or to the bulk of the adsorbent and are typically not bonded to a specific location on the solid. As previously stated, physical adsorption is driven by weak van der Waals forces attracting the adsorbate onto the adsorbent, or by London dispersion forces. The electronic density of the adsorbent molecules fluctuates rapidly, producing the dispersion forces which induce electrical moments in other atoms [143]. Physisorption may also depend on the physical features of adsorbent, such as surface area, pore size and pore distribution.

Physisorption occurs with the formation of multilayers of adsorbate on the adsorbent. Physical adsorption occurs on all surfaces when temperature and pressure conditions are favourable, which, for adsorption, is when pressure increases or temperature decreases. Adsorption energy usually does not exceed 80 kJ/mol, with typical energies being considerably less (20 – 40 kJ/mol). Physical adsorption is a relatively easy to reverse process, in comparison to chemical adsorption; desorption is favoured by decreasing pressure (Pressure Swing Adsorption - PSA) or increasing temperature (Temperature Swing Adsorption - TSA) [38].

3.2 Physical Adsorption

The aim of this work is to study the adsorption capacity of melamine-resorcinol-formaldehyde solid resin, particularly for CO_2 capture. The mechanism of adsorption in such processes is mainly physical; therefore, physisorption is described in more depth. As stated previously, the interaction between adsorbent and adsorbate is driven by van der Waals forces, which is explained in the following section.

3.2.1.1 *Dispersion Forces: van der Waals Forces.*

Dispersion forces were first detected by London [144], who noticed that the variation of electron density in one atom induces an electrical variation in nearby atoms, which would lead to attraction forces between the atoms involved.

These types of forces can act, not only between atoms, but also between molecules, which basically follows the same patterns. The redistribution of the electron density in one molecule produces an instantaneous dipole in that molecule, which itself produces and induced dipole in another molecule.

London showed, by quantum-mechanical perturbation theory, that the potential energy $U_A(r)$ of two isolated atoms, separated by a distance *(r)*, is expressed as [143]:

$$U_A = \frac{-C}{r^6} \qquad \text{Equation 3}$$

The constant *C* derives from the polarizabilities of the two atoms and the negative sign indicates attraction. It can be observed that potential energy becomes more important as the distance between the atoms decreases. However, dispersion forces also become stronger as the atoms involved become larger and a similar trend is observed for molecules. This is because, as the electron cloud becomes larger, the polarizability of the molecule increases.

However, a repulsion force also exists between two atoms; this can be expressed as:

$$U_R(r) = \frac{b}{r^m} \qquad \text{Equation 4}$$

where *b* is an empirical constant, usually taken as 40% of U_A, given the difficulty to calculate it, and the index *m* is usually considered as 12, because repulsion would become significant only at a short distance [143]. Thus, the total potential energy *U(r)* for two isolated atoms would be the sum of attraction and repulsion forces as:

$$U_r = \frac{b}{r^{12}} + \frac{-C}{r^6} \qquad \text{Equation 5}$$

where the r^{-12} term describes the repulsion at short ranges produced by the overlapping electron orbitals, and the term r-6 describes the attractive interaction at long-range such as van der Waals forces or dispersion forces.

The total potential energy, *U(r)*, curve against *r* would generally have the form:

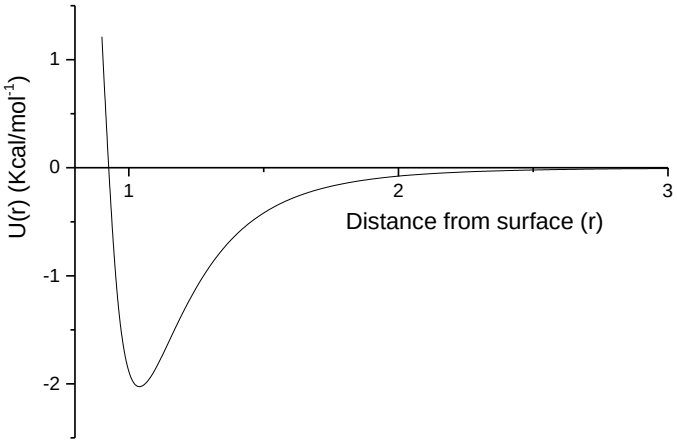

Figure 3: **The Lennard-Jones potential energy U(r) represented as a function of the distance r between a pair of isolated atoms.**

The energy of adsorption can be derived from a graph of total potential energy *U(r)* versus *r*. Thus, the force of attraction *F* can be calculated from the total potential energy by taking its first derivative, this represents the force normal to the plane of the surface to the centre of the atom or molecule:

$$F = -\frac{dU(r)}{dr} \qquad \text{Equation 6}$$

That force is zero at the minimum value of *U* on the *Y* axis [143], which means that the corresponding distance *r* is the equilibrium distance for the adsorbate with respect to the adsorbent. Then, the value of potential energy *(U)* at that minimum y-value represents the energy of adsorption; which is negative when denoting adsorption or positive if referring to desorption. This represents the energy that needs to be provided to the adsorbate to make it return to the gas phase; calculated energies of desorption have been found to be close to those determined experimentally [145].

3.2.2 Porosity

As previously mentioned, two of the most important parameters in pure physisorption are surface area and porosity. Adsorption is a phenomenon that occurs on the surface of an adsorbent. Therefore, increasing the available surface area may enhance adsorption. Obviously, if a given solid is presented in the form of a fine powder the surface area would

be increased. Thus there is an inverse relationship between surface area, *SA*, and particle size, *l*, and density, *ρ*, as expressed by [143]:

$$SA = \frac{6}{\rho l} \qquad \text{Equation 7}$$

This equation is able to predict the surface area, at least the order of magnitude, for those more complicated systems where particles exist at different sizes. As an example, there are systems where the particles tend to stick together forming aggregates or secondary particles, as occurs for xerogels. In such systems, the grain or primary particles formed would crosslink together while their dispersion in the sol (solution + disperse solid face) is driven by Brownian motion, which is defined as random motion of particles that are suspended in a fluid medium.

The particles of aggregate formed may vary in shape and size, and as they condense together, to form a network of particles as the structure of the material, it creates pores in the spaces between them. The pores are pathways that allow matter, such as gases and vapours, to flow between the external and internal surface of the sorbent. In this context, external surface area refers to all that surface area which is non-microporous, therefore external surface area includes meso- and macro-pores. A high degree of porosity is desirable for most of the applications that require an adsorbent, such as catalysis or purification and separation processes. Within a porous solid, the pores can be classified depending on their configuration as (Figure 4):

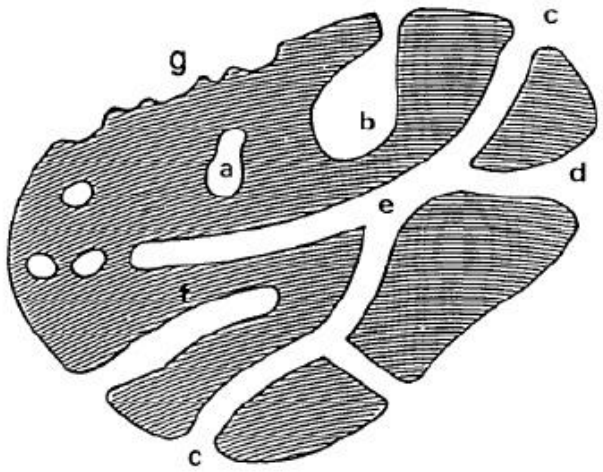

Figure 4. Different pores types in porous solids

Different regions can be identified; pore (a) is defined as closed pore, given that it has no interaction with the external fluid and can be considered as isolated. In any case, such pores play an important role in the material's bulk density, mechanical strength and thermal conductivity. Pores (b), (c), (d), (e) and (f) are classified as open pores due to their connection to the external surface. These pores can be further defined as blind pores, (b) and (f), which are only connected to the outside by one end of the pore. Pores (c), (d) and (e) are considered through pores or transport pores, because they connect to the external surface at both ends and to the inner microporosity. The region (g), which is a surface roughness, is not classified as porosity, given that these areas are wider than they are deep; they are also defined as external surface. The total surface of the solid is the sum of external surface and, predominantly, the internal surface.

When describing solids of high surface area, it is important to distinguish between external and internal surface area. Solid materials exhibit defects or cracks that may penetrate quite significantly through the structure of the material. These fissures or cracks would contribute to the total surface area available for the material. Those prominences can appear due to many reasons, such as imperfections in the crystal (dislocations), from the presence of impurities or fluctuations during cluster growth. However, to differentiate between the contributions of these fissures or cracks to the external or internal surface is totally arbitrary. Nevertheless, is has widely been accepted that these prominences, which are wider than deeper, are quantified as external surface area. Therefore, those fissures or cracks that are deeper than they are wide would contribute to the internal surface. In conclusion, this classification groups materials where the internal area is larger by many orders of magnitude than the external surface, such as gels and zeolites, among others. On the other hand, materials such as fine powders would exhibit negligible or null internal surface area, however, when those particles aggregate some of that external area would be converted to internal surface.

Adsorption occurs mainly in the pores of porous materials, therefore, the pores are classified according to their sizes [146]. However, it is worth mentioning that physisorption can also occur on the surface of non-porous structures:

(i) Pore width > 50 nm → Macropores

(ii) 2 < Pore width < 50 nm → Mesopores

(iii) Pore width < 2 nm → Micropores

One of the main reasons for this classification is the pore filling mechanism. Obviously, those limits have been set arbitrarily, to some extent, because the mechanism will also depend on the shape of the pore, the nature of the adsorptive and the adsorbent-adsorbate interactions[146]. Nevertheless, to define the mechanism of pore filling might be very complicated; however, it can, generally, distinguish micropore filling from surface coverage, which occurs on the walls of the meso- and macro-pores. In mesopores, physisorption can usually be divided into two stages, which are monolayer/multilayer coverage, and capillary condensation, these mechanisms will be described in more detail later.

3.2.3 Adsorption Isotherms

If a solid is exposed to a gas in a closed environment, after some time, the solid will start adsorbing part of that gas. It can be noticed, if the partial pressure of the gas is being monitored, that the partial pressure will decrease after the same period of time, or if the solid is placed on a sensitive scale, then its change in weight can be recorded. Thus, this gives two ways of calculating the amount of gas adsorbed; by application of the ideal gas law, if the volumes of the vessel and solids are known, then the decrease in pressure of the gas gives a measure of the gas adsorbed or, if a scale is used, the mass of gas adsorbed can be recorded directly. Additionally, the amount of gas adsorbed will reach a plateau, at equilibrium, for the pressure of exposure. Therefore, to increase the amount of gas adsorbed, it would be necessary to increase the partial pressure of the adsorptive gas. In conclusion, the representation of the quantity of molecules absorbed and the pressure, at constant temperature, is called an adsorption isotherm.

The measurement of the amount of gas adsorbed can be represented in many units, such as moles, millimoles, grams, milligrams or volumetric units such as cm^3, usually, represented at normal temperature and pressure (NTP) which is the volume that the gas would occupy at those conditions.

3.2.3.1 *Classification of Adsorption Isotherms*

The representation of the quantity adsorbed as a function of pressure at constant temperature forms an isotherm. The international union of pure and applied chemistry (IUPAC) grouped, in its recommendations of 1984, the isotherms into six types [146]. However, during the last decades, a number of characteristic and new subtypes of isotherm

were reported showing to be related to the pore structure of sorbents. Therefore, in the last IUPAC report of 2015, the classification of isotherms was updated as follows (Figure 5):

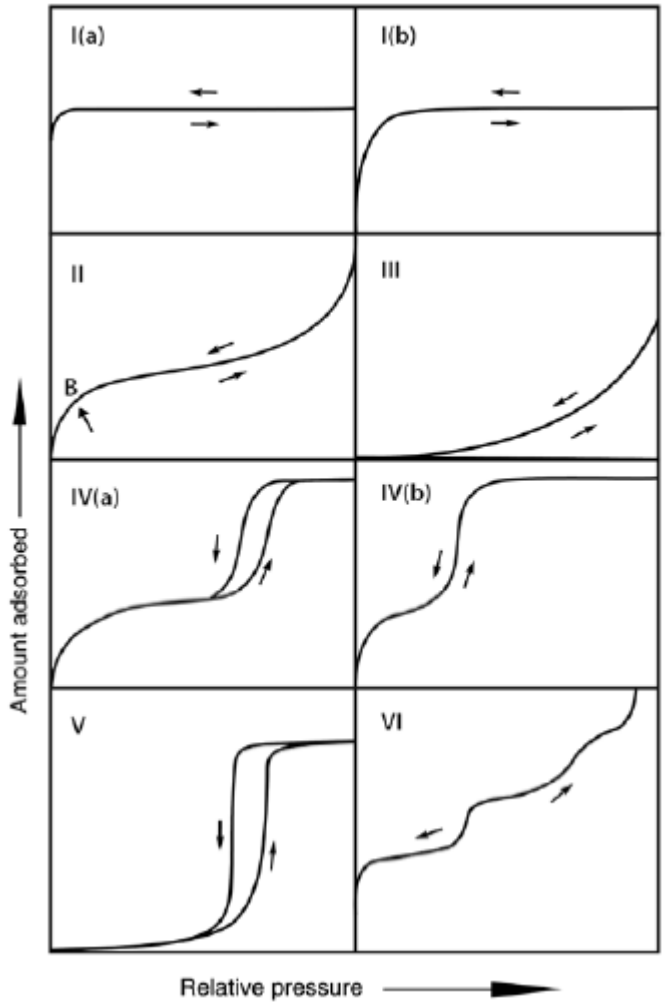

Figure 5: Physisorption isotherms according to IUPAC [147].

Most physisorption isotherms can be grouped into the types shown in Figure 5 or as a combination of two or more. At low pressure, the isotherms reduce to a linear form ($n^a \alpha P$), usually referred to as Henry's Law [148].

Reversible Type I: this type of isotherms is observed for microporous materials, with small external surfaces, which have narrow pore (~1 nm) size distribution (Type Ia) or a wider (<~2.5 nm) distribution including wider micropores (Type Ib). The Type I isotherm is a concave curve to the partial pressure (P/P_O) axis, the quantity adsorbed tends to a limiting value as the partial pressure of the gas tends to unity. This means that the maximum uptake is controlled by accessible microporosity rather than internal surface area. Examples

of materials that show this behaviour are activated carbons, molecular sieve zeolites and some porous oxides.

Reversible type II: nonporous or macroporous materials exhibit this type of isotherm for physisorption of gases. The point B indicates, if the knee is sharp, the completion of monolayer uptake and beginning of multilayer adsorption. Instead, when B is less distinctive, the transition from monolayer to multilayer adsorption is more gradual. Additionally, the uptake seems to increase continuously when P/P_O tends to unity.

Reversible type III: it can be note that there is no point B and consequently monolayer formation cannot be detected. This is an evidence of weak adsorbent-adsorbate interactions. Instead, the adsorption occurs due to molecules clustering on the most favourable sites of a nonporous or macroporous adsorbent. When P/P_O tends to 1, in contrast to Type II, the uptake remains finite.

Type IV: It can be seen that the curve follows a similar path as the isotherm type II; this is associated to the monolayer-multilayer adsorption occurring. Mesoporous materials follow this Type of isotherm. In mesoporous solids, the adsorption is driven by the adsorbent-adsorptive interactions and also by the capillary condensation effects that occurs in the mesopores. The capillary effect consists in the phenomenon by which the gas molecules condense to a liquid-like state inside pores at a pressure *p* less than the saturation vapour pressure of the liquid. Another important characteristic of Type IV isotherm is that a final plateau or saturation of variable length is observed; sometimes this plateau appears as a simple inflexion point. Type IVa isotherm presents an hysteresis loop. This occurs when the pores are wider than a certain width, which depends on the adsorption system and temperature (e.g. hysteresis loops have been reported in adsorbents with cylindrical pores wider than 4nm for nitrogen and argon adsorption at -196 °C and -186 °C respectively) [149]. Instead, completely reversible isotherms (Type IVb) have been identified for materials with smaller mesopores, and also with conical and cylindrical pores which are closed at the conical end.

Type V: this isotherm behaves similarly to Type III at low P/P_O, which is related to weak adsorbent-adsorbate interactions. At high P/P_O, pore filling occurs after molecular clustering.

Type VI: As it can be deduced, this type of isotherm represents stepwise multilayer adsorption which usually is characteristic of a uniform non-porous surface. The sharpness of the step depends on the system tested and its temperature. The capacity of each layer is represented by the step-height, which generally is constant for the first two or three layers of adsorption.

3.2.3.2 *Adsorption Hysteresis*

Hysteresis is usually related to capillary condensation when appearing in the multilayer physisorption. Hysteresis loops are usually attributed to adsorption metastability and/or network effects [147]. According to IUPAC recommendations, for open ended pores, metastability of the adsorbed multilayer is a result of the delayed condensation of adsorbate in the pores. Therefore, it can be deduced that the adsorption branch of the hysteresis is not in thermodynamic equilibrium and the behaviour of adsorbate is comparable to reversible liquid-vapour transition. On the contrary, the thermodynamic equilibration is reached in the desorption branch of the hysteresis loop. However, the hysteresis can also be related, in the desorption step, to network effects in complex pore structures, as occurs for wide pores connected to the external surface through narrow paths or necks. When necks are too small, the mechanisms of desorption can implicate cavitation. Hysteresis loops may show a wide variety of shapes, as shown in Figure 6:

From Figure 6 we can appreciate two extreme cases, H1 and H4/H5. Both remain parallel over a wide range of P/P_O but the former has vertical branches and the latter nearly horizontal (Type H4). The H2 and H3 types may be considered as intermediates between these two extremes. A feature common to many hysteresis loops is that the steep region of the desorption branch, leading to the lower closure point, occurs at a relative pressure which is nearly independent of the nature of the porous adsorbent but depends mainly on the nature of the adsorptive. Additionally, the shapes of hysteresis loops have often been associated with specific pore structures [147]

The Type H1 is, generally, attributed to porous materials, agglomerates or compacts with uniform spheres in regular array, hence, narrow distributions of uniform mesopores. The steep and narrow loop is mostly associated to delayed condensation effects, and it follows that the network effects are minimal

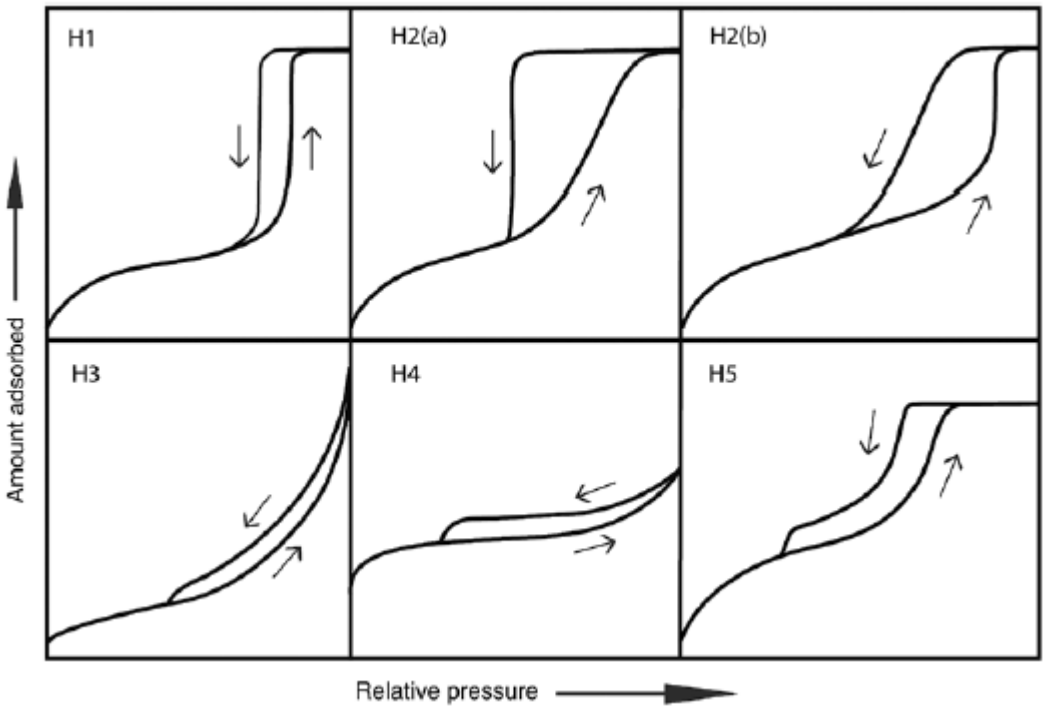

Figure 6: Classification of hysteresis loops according to IUPAC [147].

The Type H2 is a result of more complex pore structures, such as inorganic oxide gels and porous glasses. For these systems the pore distribution and shapes are not well defined, usually it is related to 'ink bottle' shape (narrow neck and wide body). The Type H2a exhibits a steep desorption in the hysteresis, which is usually attributed to pore blocking/percolation or cavitation. H2b is associated as well to pore blocking, with the difference that the pore neck sizes have a wider distribution.

The two main characteristics of Type H3 hysteresis loop is that, firstly, the adsorption branch is similar to the isotherm Type II. The second feature is that the closure of desorption branch is found at the cavitation-induced P/P_O.

The Type H4 hysteresis loop is associated to narrow slit-like pores; but in this case the Type I and II isotherm character is indicative of microporosity.

The Type H5 is unusual; it is associated to certain open and partially blocked mesopore structures.

As mentioned above, the sharp closure of the hysteresis loop at a specific P/P_O, as observed in H3, H4, and H5, is a characteristic of a given adsorptive and temperature, e.g. at P/P_O ~0.4 – 0.5 for nitrogen at -196 °C.

3.2.3.3 *Nitrogen Adsorption/Desorption*

One of the techniques most used to characterise porous materials is by obtaining information of nitrogen adsorption by varying the gas pressure at -196 °C. This allows the surface area, pore size, pore distribution and volumes of pores, among other parameters to be determined. This procedure has been accepted by the International Union of Pure and Applied Chemist (IUPAC) [147].

3.2.3.4 *Polanyi Theory*

Michael Polanyi published his first paper related to adsorption in 1914, in which he proposed a model for adsorption of gases on solids [150]. In it, he made two main assumptions; first, that a gas molecule near the surface of an adsorbent behaves according to a potential similar to gravity of electric fields [151]. Therefore, adsorption is the result of attraction forces due to that potential, which implies that the potential depends on the spatial position of the adsorbate and is independent of any other molecule in that field. The second assumption was that when the adsorbate is subject to the aforementioned potential, it behaves according to the equation of state [150].

Polanyi adsorption model is applicable to gases on the surface of an adsorbate at constant temperature; under this condition gas molecules approach the surface of the adsorbent when the partial pressure is higher than the equilibrium vapour pressure. Polanyi published a second paper in 1916, where a number of experimental verifications of his model were shown. Additionally, Herbert Freundlich published in his *Kapillarchemie* book, in 1922, about Polanyi's theory and expressed that he was completely committed to this theory [150].

The Polanyi adsorption model is based on a change in potential, which depends on the distance between the gas molecule and the surface; this can be calculated using the equation for the variation of chemical potential:

$$d\mu = -S_m dT + V_m dP + dU_m \qquad \text{Equation 8}$$

where μ is chemical potential, S_m is molar entropy, V_m is molar volume and U_m is molar internal energy. When a molecule of a gas is in equilibrium, this means that its chemical potential μ, at a distance x, is equal to that at an infinite distance from the surface. Therefore, at equilibrium the integration of the chemical potential is zero. Remembering

that the temperature is constant, Equation 8 can be integrated for the partial pressure P_x at a distance x and the partial pressure P at an infinite distance.

$$\int_{P}^{P_x} V_m dP + U_m(x) - U_m(\infty) = 0 \qquad \text{Equation 9}$$

This equation can be simplified by setting the molar internal energy at infinite distance equal to zero; using the ideal gas law, and knowing that the gas condenses into a liquid on the surface when the pressure is higher that the equilibrium vapour pressure, P_O, it can be assumed that the liquid forms a film on the adsorbent of thickness x_{film}. Therefore, the energy at P_O is:

$$U_m(x_{film}) = -RT \cdot Ln\frac{P_O}{P} \qquad \text{Equation 10}$$

Then, knowing that the partial pressure is proportional to the concentration, the adsorption potential ε_s can be written as follows:

$$\epsilon_s = -RT \cdot Ln\frac{C_s}{C} \qquad \text{Equation 11}$$

Where C_S is the saturated concentration of adsorbate and C is the equilibrium concentration of adsorbate.

A few years later, a number of discoveries about the electrical interactions or electrical forces, which could explain cohesive forces, were published, such as Bohr's atomic model, ionic structure of chloride (Bragg) and Debye's dipoles. Therefore, a number of theories arose seeking to explain the interactions described above by electrostatic interaction of fixed quadrupoles (Keesom), induced dipoles (Debye) and chemical bond interactions due to positive and negative ion interactions (Kossel). This new insight into atomic forces and the fact that electrical forces could not be derived from Polanyi spatial potential theory caused Polanyi's model to be rejected. This was reinforced by Langmuir who published three papers during 1916 to 1918, demonstrating the formation of an adsorbate film on an adsorbent and presenting a model to account for adsorption proving the existence of electrostatic interactions, for which work he was later awarded with the Nobel Prize, in 1932. All this evidence seemed to ignore the short range electrical forces (valences) which

originate at given points of the atomic lattice of adsorbent [150]. A few years later, in 1930 F. London published his theory of cohesive forces, which is based on quantum mechanical resonances between the polarization of electronic systems [144]; this lead Polanyi to relate these forces to the spatially fixed adsorption potential [150].

3.2.4 Dubinin-Radushkevich Equation

The Dubinin-Radushkevich model (DR) is based on the Polanyi's potential theory of adsorption, and is able to explain the adsorption of vapours on porous adsorbents for a wide range of pressures until saturation [152].

It is known that adsorption tends to fill the micropores with adsorbate at low relative pressures, typically $P_O/P > 0.3$ [143]. This effect is often correlated with the existence of enhanced dispersion forces, which are a consequence of the proximity of the micropore walls. Dubinin *et al*. have paid attention to that low pressure region of the isotherm and extended the Polanyi potential theory to later develop the theory of volume filling of micropores [153, 154].

The theory of volume filling of micropores for vapour adsorption has two main assumptions:

1. Using an affinity coefficient β, characteristic curves for different adsorbates on the same adsorbent can be superimposed; for instance:

$$E = RT\ ln\left(\frac{P_O}{P}\right) = \beta f(V) \qquad \text{Equation 12}$$

   where E is the free energy of adsorption and V represents the volume filled with adsorbate.

2. The DR characteristic equation for adsorption of vapour on microporous sorbents has the form:

$$\frac{V}{V_O} = \left(exp\frac{-KE^2}{\beta^2}\right) \qquad \text{Equation 13}$$

   where K is a constant, V_O is total available adsorption micropore volume which defines the adsorption at a given value of E.

Combining equation 12 and 13 the DR equation takes the form:

$$V = V_O \, exp\left[-\left(\frac{RT}{\beta E}\ln\frac{P_O}{P}\right)^2\right] \qquad \text{Equation 14}$$

which represents the volume of adsorbate adsorbed at a given relative pressure and temperature *T*.

Another form of the DR equation is the Dubinin-Ashtakhov (DA) equation, which is in the form:

$$V = V_O \, exp\left[-\left(\frac{RT}{\beta E}\ln\frac{P_O}{P}\right)^m\right] \qquad \text{Equation 15}$$

The equation 15 is a more flexible form of the DR equation, given it that contains a new parameter *m* which is related to the pore size distribution. The DA equation holds three parameters to fit (β, V_O and *m*) while the DR equation only has two (β and V_O). However, both equations, DR and DA, are based on the potential theory of adsorption of Polanyi [152].

It has been found that the DR equation deviates from linearity in the Henry's law region (low values of P_O/P); which means that it is not thermodynamically consistent in that region [155, 156]. This deviation has been attributed to capillary condensation effects in transitional pores or due to multilayer formation on the walls of the macropores [157].

3.2.5 Gas- Solid Adsorption Models

A variety of surface features of solid materials can be determined by observation of adsorption processes on them, given that uptake of a surface depends on several variables, including surface energy distribution, surface area and porosity of solids as well as adsorptive properties, temperature and pressure of the system.

Gas-solid adsorption models represent several methods to explain and obtain information regarding the adsorbent-adsorptive interactions. These methods are based on given assumptions, where it is clearly classified as monolayer and multilayer systems.

3.2.6 Monolayer Adsorption

A gas-solid model can be thermodynamically described using a simple system at constant temperature and pressure. The species in the system can be defined as adsorptive, present

in the gas phase, near the surface of a solid, which is capable of forming a film of adsorbed gas. In this scenario, it can be stated that the density of the gas adsorbed is a function of the distance from the surface, and at a given distance its density would be equal to that of the bulk gas density. Therefore, the adsorbed gas would form a layer of thickness *x* on the adsorbent. Under these conditions, it can be assumed that the pressure of the adsorbed gas is the same as the hydrostatic pressure of the system.

The simplest representation of the adsorbed film on the adsorbent can be made using the Henry's law [148], which relates the concentration of a given species, a constant, and the pressure of the system:

$$n_A = \frac{P_A A_A}{RT} = K_H P \qquad \text{Equation 16}$$

where P_A is the pressure of the adsorbed film, A_A is the area occupied by the adsorbed film, R is the gas constant, and T the temperature of the system. K_H is the Henry's constant and P the pressure of the system. Henry's law is the simplest description of adsorption at low relative pressure, where the relationship between the concentration of the adsorbed film and the pressure is linear. At higher relative pressures, this relation is no longer linear, therefore, further explanation is required.

3.2.6.1 *Langmuir Adsorption Isotherm Model*

In 1916, Irving Langmuir presented his model for the adsorption of gases on surfaces of glass, mica and platinum [158]. A year later, in 1917, he also published a paper about surface chemistry of oil films [159]; for these works later, in 1932, he was awarded with the Nobel Prize in Chemistry.

The Langmuir adsorption model is based on a number of assumptions, which are only valid for a simple case of a single adsorbate on the surface of a solid with energetically equivalent sites:

1. The surface of the adsorbent is completely homogeneous; it means that the sites available are of equal size and shape, and energetically homogeneous. Therefore, the probabilities of a given species being adsorbed onto any available space are the same.
2. There are a fixed number of available sites on the surface of the adsorbent.

3. The adsorbate reaches a dynamic equilibrium between molecules being adsorbed onto and desorbed from the surface.

$$A(g) + B(s) \leftrightarrow AB$$

Reaction 8: Adsorption-desorption of a gas molecule *A* on a solid *B*.

where *A* represents a gas molecule and *B* is the available solid site; *AB* denotes the adsorbed gas on the solid site.

4. Adsorption is only monolayer, meaning that, there is only one molecule per site on the surface; multilayer adsorption is not considered.
5. There are no interactions between adsorbate molecules.

3.2.6.2 *Kinetic Derivation of Langmuir Adsorption Isotherm Model*

As stated before, it is assumed that the adsorption system is in a dynamic equilibrium between molecules of gas being adsorbed and desorbed [160]. The rates of adsorption *(r_{ads})* and desorption *(r_{des})* are defined as:

$$r_{ads} = k_{ads} P_A [S_{active}] \quad \text{Equation 17}$$

$$r_{des} = k_{des} [S_{Occup}] \quad \text{Equation 18}$$

where k_{ads} and k_{des} are the kinetic constants of the adsorption-desorption reaction shown in Reaction 8. P_A is the partial pressure of gas *A* on the surface of the solid; $[S_{active}]$ is the number of available sites on the surface of the adsorbent expressed in number per metre square; and $[S_{occup}]$ represents the concentration of gas adsorbed in molecules per metre square.

At equilibrium, the rates of adsorption and desorption are equal; therefore, equation 17 and 18 would define an equilibrium constant *(K_{eq})*:

$$K_{eq} = \frac{k_{ads}}{k_{des}} = \frac{[S_{occup}]}{P_A [S_{active}]} \quad \text{Equation 19}$$

The number of all sites $[S_{Total}]$ on the surface of the solid is assumed to be fixed and is defined as:

$$[S_{Total}] = [S_{active}] + [S_{Occup}] \quad \text{Equation 20}$$

Combining equation 19 and 20 gives:

$$[S_{Total}] = \frac{[S_{Occup}]}{K_{eq}P_A} + [S_{Occup}] = \frac{1 + K_{eq}P_A}{K_{eq}P_A}[S_{Occup}] \quad \text{Equation 21}$$

If the fraction of sites covered with adsorbed molecules (θ_A) is defined as:

$$\theta_A = \frac{[S_{Occup}]}{[S_{Total}]} \quad \text{Equation 22}$$

Finally, expressing Equation 21 in terms of surface coverage gives the Langmuir adsorption isotherm:

$$\theta_A = \frac{K_{eq}P_A}{1 + K_{eq}P_A} \quad \text{Equation 23}$$

Note that coverage can also be expressed in terms of volume of adsorbed gas with respect to the monolayer volume, or in mass units, as mass of gas adsorbed per mass of monolayer.

The concentration *(C)* of molecules of a gas *A* competing for a site can be obtained using the ideal gas law:

$$C = \frac{n}{V} = \frac{P}{RT} \quad \text{Equation 24}$$

where *n* is moles of gas, *V* is container volume, *P* is pressure, *R* is gas constant and *T* is system temperature.

For a system at equilibrium, and knowing that volume and temperature are constant, the concentration of gas *A* being adsorbed *(C)* can only be varied with pressure. Therefore, *C* depends only on the pressure for a system under those conditions. Combining *C* with the equilibrium constant K_{eq} to give a constant value *(b)* gives the Langmuir isotherm expressed as:

$$\theta_A = \frac{bP_A}{1 + bP_A} \quad \text{Equation 25}$$

The Langmuir adsorption isotherm describes only monolayer coverage for adsorption, and thus is able to describe most chemisorption systems. This isotherm model forms a curve which is asymptotic for a coverage that tends to a value of 1.

The parameter *b* is directly proportional to the surface energy [141], which means that an increased value of *b* results from an increase in surface energy; therefore, the probability of adsorption occurring at a given pressure is increased. Consequently, higher values of *b* would increase the coverage at a given pressure. However, *b* is also related to the temperature of the system; and it is known that molecular energy increases with increasing temperature thus the probability of adsorption at a given pressure is decreased.

3.2.6.3 *Limitations of Langmuir Adsorption Isotherm Model*

The Langmuir adsorption isotherm model is applicable to chemisorption, in the case of the reaction being reversible [150], but its application to physisorption systems shows some limitations given that experimental fits deviate considerably, at higher pressures, from Langmuir's model. Langmuir theory assumes that the adsorbed gas behaves ideally in the vapour phase; however, this is only valid at low pressure. Hence, The Langmuir adsorption model is only applicable to a system under low pressure conditions, as the gas molecules would exhibit high thermal energy and escape velocity; consequently, the number of molecules near the surface of the solid would be decreased.

Another important assumption made by Langmuir is that adsorption occurs only in the monolayer, which is only valid at low pressure. For a system at high pressure, multilayer adsorption occurs, as the gas molecules are strongly attracted to each other. Brunauer, Emmett and Teller proposed the so called BET theory (Section 3.2.6.8) which accounts for the multilayer adsorption process.

Langmuir theory also assumes that the surface of the adsorbent is homogeneous with sites of equal size and shape, and similar affinity (e.g. adsorption energy) for the adsorbate. However, homogeneous surfaces are difficult to achieve; in most cases, solid sorbents present heterogeneous surfaces. Additionally, Langmuir assumed that molecules do not interact with each other during adsorption, which is impossible given that weak forces of attraction/repulsion exist between all molecules. Langmuir theory also states that the adsorbed molecule has to be localized, which means that entropy is zero. This condition is

not possible despite the liquefaction of adsorbed gases, whereby randomness (entropy) is decreased but not to zero.

3.2.6.4 *Freundlich Adsorption Isotherm Model*

In 1909, Freundlich published an empirical equation that relates the isothermal adsorption of a gas by unit mass of adsorbent (solid) to the variation in pressure [161]. The resulting equation is known as the Freundlich adsorption isotherm model. The main difference between this model and Langmuir's proposal is that the former contemplates the rough surfaces of adsorbents.

At low pressure, the increase in adsorption is linear with respect to increasing pressure, which means that *x* would be proportional to the pressure *(P)* raised to the power of 1. By contrast, at high pressure adsorption becomes independent of pressure, i.e. adsorption is proportional to pressure *(P)* raised to power of zero. Therefore, for intermediate values of pressure, adsorption is proportional to the pressure raised to the power of 1/n (where n > 1). Thus, the Freundlich isotherm equation is:

$$\theta = \frac{x}{m} = KP^{\frac{1}{n}} \qquad \text{Equation 26}$$

where ϑ is surface coverage, *x* represents mass of gas adsorbed, *m* is mass of adsorbent, *P* is pressure and *k (adsorption constant)* and *n* are constants, the value of which depends on the adsorbate, temperature and adsorbent. The Freundlich isotherm accurately represents adsorption at low pressure, but it deviates significantly at higher pressures. If a log-plot is made it will fit a straight line.

3.2.6.5 *Freundlich Adsorption Isotherm Model - A Special Case of the Langmuir Equation*

Considering the Langmuir adsorption isotherm shown in Equation 23, for low pressure conditions the denominator can be approximated to 1, given that KP<<1. Therefore, the Langmuir equation would take the form:

$$\theta = KP \qquad \text{Equation 27}$$

Equation 27 shows a linear relationship between surface coverage, or adsorption, with pressure. Conversely, for high values of pressure, the denominator of the Langmuir

equation (Equation 23), can be approximated to KP given that KP>>1. Therefore, the Langmuir equation would take the form:

$$\theta = \frac{KP}{KP} = 1 \qquad \text{Equation 28}$$

This suggests that adsorption becomes independent of pressure under high pressure conditions, equivalent to adsorption becoming proportional to pressure raised to the power of zero. Therefore, intermediate values of pressure would take the form:

$$\theta = KP^{\frac{1}{n}} \qquad \text{Equation 29}$$

This is in agreement with the Freundlich isotherm stated in Equation 26. In conclusion, it can be said that Freundlich adsorption isotherm is a singular case of the Langmuir model.

3.2.6.6 *Limitation of Freundlich Adsorption Isotherm Model*

The Freundlich model demonstrates similar limitations to the Langmuir model, however, the Freundlich isotherm also fails to accurately represent adsorption at high pressures.

3.2.6.7 *Multilayer Adsorption*

When the Langmuir adsorption isotherm model, or any of the other monolayer models, is applied to higher ranges of partial pressure, deviations are observed, resulting in overestimation of the surface area. Langmuir theory successfully represented adsorption behaviour at low pressure, but failed at high pressure because it did not account for multilayer formation. At high pressure, the thermal energy of the molecules of a gas would be decreased; therefore, the number of molecules competing for the site of a unit area would be increased. Consequently, multilayer formation occurs. The shape of the isotherms, particularly Types II and IV, suggest that adsorption occurs in two different stages. Firstly, adsorption occurs on the homogeneous sites on the surface of the sorbent and, secondly, adsorption occurs onto the first layer of adsorbate. In this way, an adsorbed molecule becomes an adsorption site for subsequent molecules to be adsorbed. Multilayer adsorption can occur on any adsorbent, when it is exposed to an adsorptive, under suitable temperature and pressure conditions, as required for adsorption.

Another important characteristic is that when multilayer formation is considered, each layer exhibits different energy of adsorption. However, the energy for those layers where a

gas adsorbs onto itself would be similar to bulk liquid condensation; therefore, the heat would approach the heat of liquefaction.

3.2.6.8 *Brunauer-Emmett-Teller Adsorption Isotherm Model*

Brunauer, Emmet and Teller (BET) were the first to derive a model for multilayer adsorption, which was published in 1938 [162]. This model is an extension of Langmuir theory, and introduces multilayer formation; hence, BET theory is used to explain the physical adsorption of gases by solid sorbents, and the determination of surface area is based on this model.

BET theory is based on the following assumptions:

1. At the saturation pressure, an infinite number of layers of adsorbed molecules on the surface of the solid can be formed, this is equivalent to the sample being in contact with a liquid phase.
2. Each adsorbed molecule becomes an adsorption site for another molecule.
3. The molecule in the upper layer is in equilibrium with the gas, which means that the rates of adsorption and desorption are equal (dynamic equilibrium).
4. Molecules of different layers do not interact with each other.
5. The desorption mechanism is dominated by kinetics. All molecules adsorbed in a given layer have the same heat of adsorption. The first layer exhibits the heat of adsorption between the gas and solid material, and for the following layers the heat of adsorption is equal to the heat of liquefaction.

As a result, the BET equation takes the form [162]:

$$\frac{P}{V(P_o - P)} = \frac{1}{V_m C} + \frac{C-1}{V_m C}\left(\frac{P}{P_0}\right) \qquad \text{Equation 30}$$

where V is volume of adsorbed gas, V_m is volume of gas in the monolayer, P is pressure, P_O is saturation pressure and C is the BET constant.

A BET plot allows the C constant and monolayer capacity to be determined, whereafter then the total surface area can be obtained from:

$$S = \frac{V_m A_m L}{M} = N_m A_m L \qquad \text{Equation 31}$$

where A_m is the cross-sectional area (m^2) of an adsorbate molecule, which for nitrogen is 16.2 A^2 (1.62 $.10^{-19}$ m^2), *L* is Avogadro's number, *M* is mass of adsorbent (g), V_m and N_m are monolayer volume adsorbed (cm^3/g) and monolayer quantity adsorbed (mmol/g) respectively, and surface area *(S)* has units of $m^2\ g^{-1}$.

The BET *C* constant is related to the heat of adsorption H_{Ads} and heat of liquefaction H_{Liq} by the following expression:

$$C = exp\left(\frac{H_{Ads} - H_{Liq}}{RT}\right) \qquad \text{Equation 32}$$

The *C* constant is related to the affinity of a given adsorbent towards the molecules of an adsorptive; a higher value of *C* means stronger solid-gas interactions. Therefore, the constant will always be a positive value, which varies with the strength of the intermolecular forces involved in the gas-solid interaction.

However, limitations have been observed for BET model when it is applied in given systems, such as microporous materials. This is explained in more detail in Section 3.2.7.4.

3.2.7 Characterization Tools

The models explained above are used to obtain adsorption equilibrium data for characterising solid sorbents and obtain structural information such as pore size, pore volume, surface area, microporosity, adsorption capacity and adsorption kinetics for a given adsorbate. This section will describe how those models are applied as well as their limitations.

3.2.7.1 *Determination of Pore Volume and Pore Size Distribution in Porous Substances*

The determination of pore volume and pore size is based on the theory established by Elliot P. Barret, Leslie G. Joyner and Paul P. Halenda which is usually refer to as BJH theory and was published in 1951 [163]. Their theory is based on the desorption branch of nitrogen adsorption for mesopore materials. Therefore, it is consistent for pores in the mesoporous range, which means that the micropore volume cannot be derived from it.

The BJH theory is based on two main assumptions: 'firstly, that the pores are cylindrical and that the pore volume and capillary volume are related to each other. Secondly, the quantity of an adsorbate in equilibrium with the gas phase remains adsorbed mainly due to two mechanisms (a) physisorption on the pore walls and (b) capillary condensation in the inner capillary volume' [163].

Both the adsorption and desorption isotherm can be used, but generally desorption branch is used in order to obtain meaningful data for estimating the pore size. This works in a way that the relative pressure $(P/P_O)_1$ is decreased to a lower value $(P/P_O)_2$. Therefore, this allows the measure of a differential volume ΔV_n of adsorbate desorbed, which is later related to the area of each pore A_P. The reduction of relative pressure will not only produce the emptying of the largest pore from its capillary condensate, but also a reduction in the thickness Δt_1 of the physically adsorbed layer. The BJH equation for the computation of pore volume distributions with respect to the pore radii is:

$$V_{pn} = R_n \Delta V_n - R_n \Delta t_n \sum_{j=1}^{n-1} C_j A_P \qquad \text{Equation 33}$$

where Rn is capillary radii after desorption; and C_J is a parameter that relates the average pore radii before and after desorption together with the radius r_P of the physically adsorbed

layer previously emptying the pore and thickness of the physically adsorbed layer. The summation term represents the accumulation measured for the consecutively desorption steps, and it is simply the summation of the average area in unfilled pores including all but the n_{th} step.

One of the main characteristics of mesoporous solids is the hysteresis loop observed in their isotherms; this phenomenon is governed by the capillary condensation and the pressure at which it occurs can be determined by the Kelvin equation, which implies that the vapour pressure of a gas in equilibrium with a material with planar surface differs from the vapour pressure of the same gas over a curved surface [164]:

$$Ln\frac{P}{P_o} = -\frac{2\gamma V_L}{rRT} \qquad \text{Equation 34}$$

where γ is the surface tension (N/m)

V_L is the volume of adsorbate adsorbed (m^2)

r is the pore radio (m)

R is the gas constant (J/mol K)

T Temperature (K)

Finally, a relationship between the pore volume and pore diameter is obtained; which normally is a Gaussian distribution curve.

3.2.7.2 *Micropore Analysis: the t- Method*

When a gas is adsorbed on an adsorbent, it forms a layer on its surface; a layer with a characteristic density profile (which depends on the temperature). This concept is underpinned by the main conjecture when analysing adsorption data to quantify the surface area, which is that it is assumed that the adsorbed layer exhibits a uniform thickness. This assumption allows the calculation of a statistical thickness for the adsorbed film.

The statistical thickness can be calculated for a given adsorbate knowing the diameter of the molecule adsorbed. For nitrogen, assuming that the molecules are packed in a hexagonal shape, the monolayer depth can be taken as 3.54 Å [165]. Therefore, the thickness can be calculated as [165]:

$$t = 3.54\frac{W_a}{W_m} = \frac{V_{liq}}{S} \cdot 10^4$$ Equation 35

where t is thickness of adsorbed film in Å, W_a is weight of adsorbed film and W_m is monolayer weight, or if the adsorbed film is expressed in units of volume, V_{liq} is adsorbed volume ($V_{liq} = V_{ads}$ (STP) x 15.47 for nitrogen) and S is total surface area.

The t-method is based on plotting the volume of liquid adsorbed (V_{liq}) against the thickness, t, of the film; these are known as *V-t* curves [166]. This method is applied to isotherms exhibiting Type II or Type IV behaviour. This technique allows the calculation of micropore volume, micropore surface area, and non-micropore surface area. Non-micropore surface area defines any area which is non-micropore, including meso- and macro-pores.

There are a number of equations proposed to calculate the thickness depending on the type of adsorbent tested. Most of the equations are obtained for nitrogen adsorption at -196 °C. For instance, de Boer [166] proposed an equation for non-porous adsorbents with oxidic surfaces, like siliceous materials. Another popular equation was proposed by Harkins-Jura [167], which is based on data gathered for non-porous aluminium oxide materials.

As RF gels are carbon-based materials, the equation used to calculate the thickness in this work is the ASTM standard D-6556-01 [168], which was derived for carbon-like materials.

$$t = 0.88\left(\frac{P}{P_O}\right)^2 + 6.45\left(\frac{P}{P_O}\right) + 2.98$$ Equation 36

The application of the t-method and the information that can be obtained depends on the type of material assessed and its isotherm type. It is important to note that if the linear section of the V-t curve is extrapolated to the origin, it would mean that there is no microporosity in the material. In this case, the surface area calculated from Equation 37 would be the total surface area which should agree with the total surface area calculated using the BET model [165].

$$S(m^2/g) = s \cdot 15.47$$ Equation 37

If the material tested contains micropores, on the other hand, the linear section of the V-t curve will have a positive intercept I, which is related to the micropore volume, V_{mp} [165].

$$V_{mp}(cm^3) = i \cdot 0.001547$$ Equation 38

In the case of a microporous material, the slope of the linear section of the V-t curve will be related to the non-micropore surface area S_{NmSA} calculated using Equation 37. Therefore, the micropore area can be estimated by:

$$S_{micro} = S_{BET} - S_{NmSA}$$ Equation 39

However, it is then critical to select the appropriate linear section of the V-t curve, and this needs to be in agreement with filling of the micropore region, which can be observed from the isotherm.

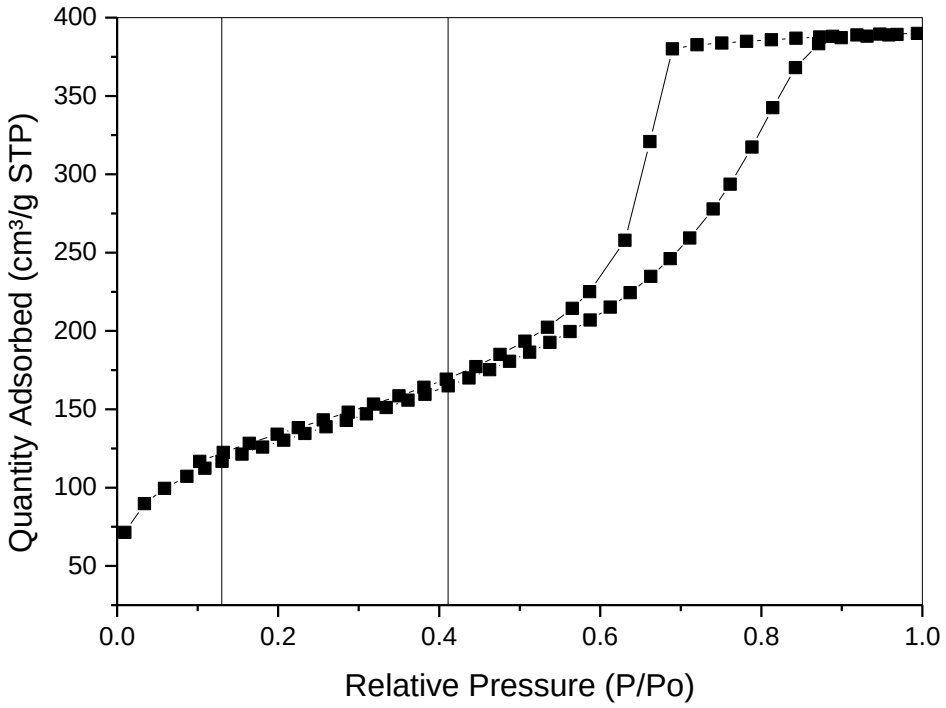

Figure 7: Nitrogen adsorption isotherm for a resorcinol-formaldehyde gel of R/C 200 and R/F 0.25.

The linear section of the isotherm shown in Figure 7 corresponds to the region after the micropores have been filled, for the partial pressure range from 0.13 – 0.41. Hence, the corresponding statistical thickness can be calculated using Equation 36. The linear section of the V-t curve will be proportional to that corresponding to the same partial pressure range shown in Figure 7, as can be seen in the Figure 8:

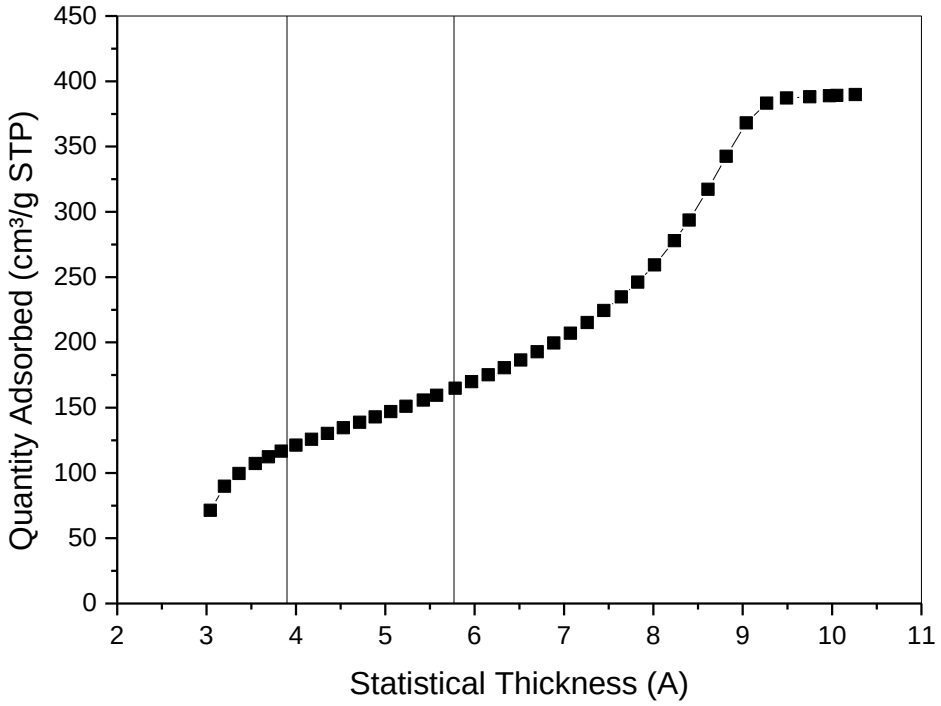

Figure 8: **V-t curve for the isotherm data shown in Figure 7.**

Consequently, the linear section selected on the V-t curve can be fitted, and the micropore volume and micropore surface area can be calculated from its intercept and slope, respectively.

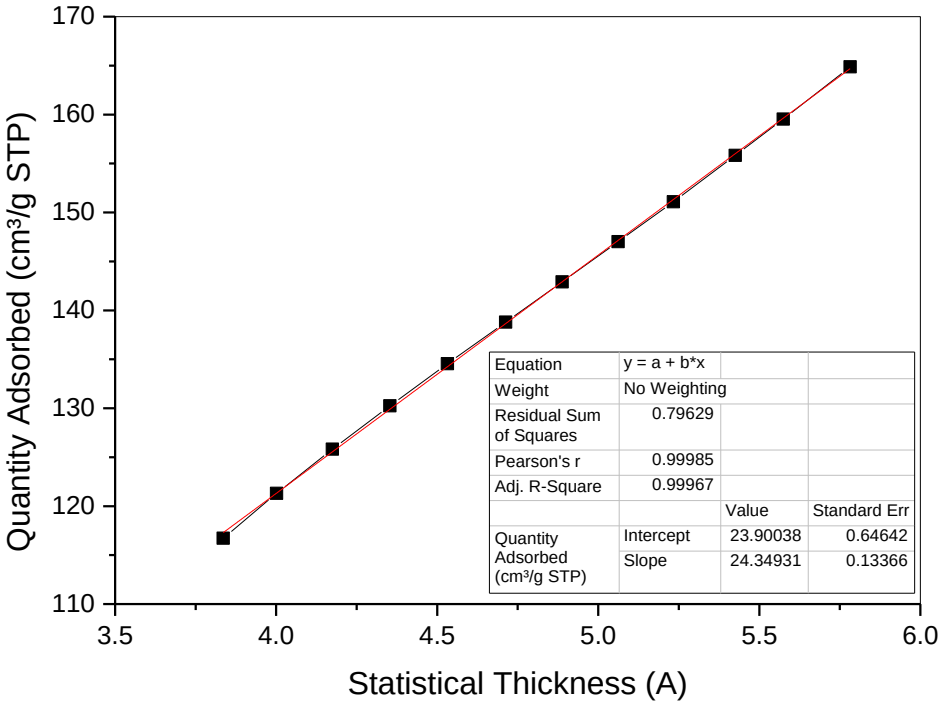

Figure 9: **Linear fitting of the linear section of V-t curve selected in Figure 8.**

The fitting shown in Figure 9 gives a micropore volume of 0.0369 cm^3/g and a micropore surface area of 87.70 m^2/g; where the total surface area is 464.38 m^2/g, a non-micropore surface area of 376.68 m^2/g, and a total pore volume of 0.6034 cm^3/g.

The micropore surface area shown previously was calculated using Equation 39. However, in the case where enough data has been gathered at low partial pressure, the micropore surface area, S_{micro}, can be calculated using the following equation as well:

$$S_{micro} = \left[\left(\frac{V_{liq}}{t}\right)_{low(\frac{P}{Po})} - \left(\frac{V_{liq}}{t}\right)_{upper(\frac{P}{Po})}\right] \cdot 10^4 \qquad \text{Equation 40}$$

where the first term, at low (P/Po), means the slope of the line that goes through the origin for adsorption at low partial pressure. The slope of this line (see Figure 10) would give a comparative total surface area to the one calculated using the BET model. The second term, at higher partial pressure, corresponds to the line shown in Figure 8 and Figure 9, the slope of which corresponds to the non-micropore surface area. Therefore, the difference between these two terms is the micropore surface area.

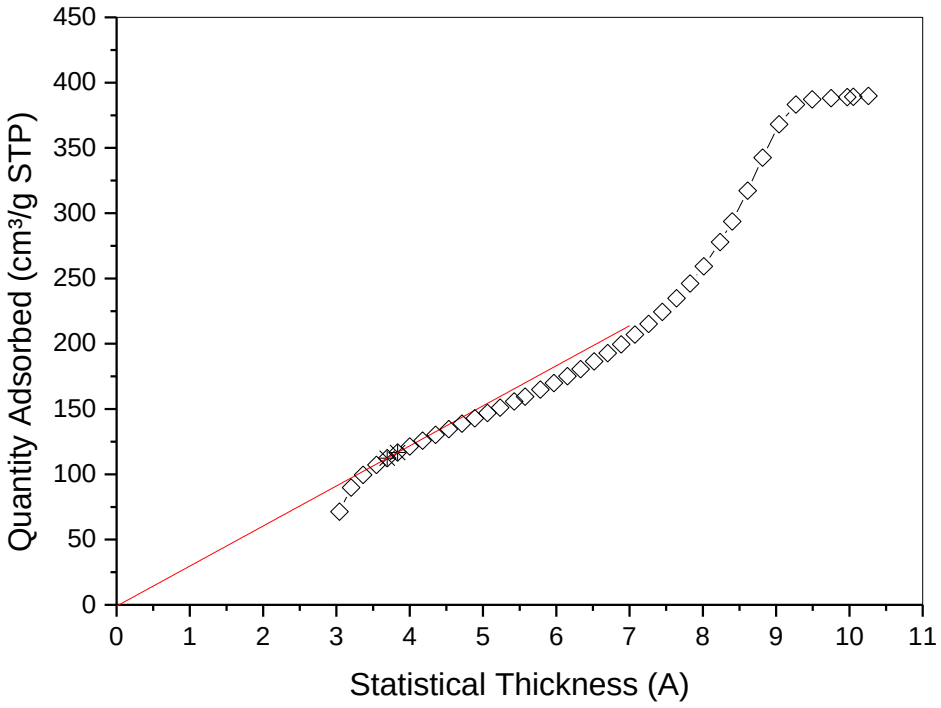

Figure 10: **Line through the origin for calculating a total surface area using t-method.**

As mentioned before, in order to use Equation 40, is important to have enough data at low partial pressure, which is not the case for the example shown here. However, the micropore surface area calculated using this equation gives a value of 97.96 m^2/g and a total surface area of 474.64 m^2/g. Comparing these values to the ones obtained using Equation 39, discrepancies can be seen for the total surface area, given that the best line through the origin, shown in Figure 10, could only be fitted using two data points. Despite of that uncertainty, it can be seen that when there is sufficient data, at low partial pressure, Equation 40 will give an accurate value, comparable to that obtained using Equation 39.

3.2.7.3 *Application of Adsorption Models to Microporous Adsorbents*

It is important to understand the limitations in applying the different adsorption models to each particular case. The previous section explored the limitations of adsorption isotherms models (Langmuir, Freundlich and BET). However, even knowing that the BET model is not suitable for microporous materials, it is still being applied to calculate surface area, even for materials where the presence of micropores is probable. Having said that, the materials studied in this thesis are based on resorcinol-formaldehyde resins doped with melamine (MRF gels); depending on the concentration of the reactants, these materials exhibit significant microporosity. Thus, it is important to understand the applicability of these adsorption models in greater depth to assess microporous materials.

3.2.7.4 *Applicability of BET Model*

According to the IUPAC isotherm classification system, microporous materials tend to exhibit Type I isotherms [146]. One might, therefore, tend to think that the Langmuir adsorption isotherm model would be applicable to microporous materials. In contrast, most microporous materials exhibit a combination of Type I and II character (microporous and non-micropore surface), or Type I and IV behaviour if mesopores are present. Additionally, taking into account the assumptions on which the Langmuir model is based, it is evident that the Langmuir model was derived for the particular case of chemisorption of a gas in contact with a solid phase. This is different from adsorption in micropores, in which adsorption is not limited to specific sites; instead, pore filling can occur and the adsorbate might not necessarily be in contact with the gas phase [158].

BET theory has been widely applied to estimate monolayer capacities, thus surface areas. However, the applicability of this model to microporous materials is still questionable [169]. It is known that to calculate monolayer capacity, BET theory has to be applied to the

straight line section of the isotherm. However, a question arises when deciding which points to include in that linear section. Generally, the BET equation is applied to those points of adsorption lying in the relative pressure range 0.05 - 0.3 [146]. However, when one applies the BET model there is scope for a subjective choice of points to fit within that range. Therefore, a method is required to avoid this subjective choice, and thus, reduce error. The problems arise from the fact that microporous materials do not necessarily exhibit a linear behaviour within the aforementioned range, instead, it is noted that various linear sections occur within that range. Therefore, selection of the appropriate range becomes crucial to accurately determine the surface area.

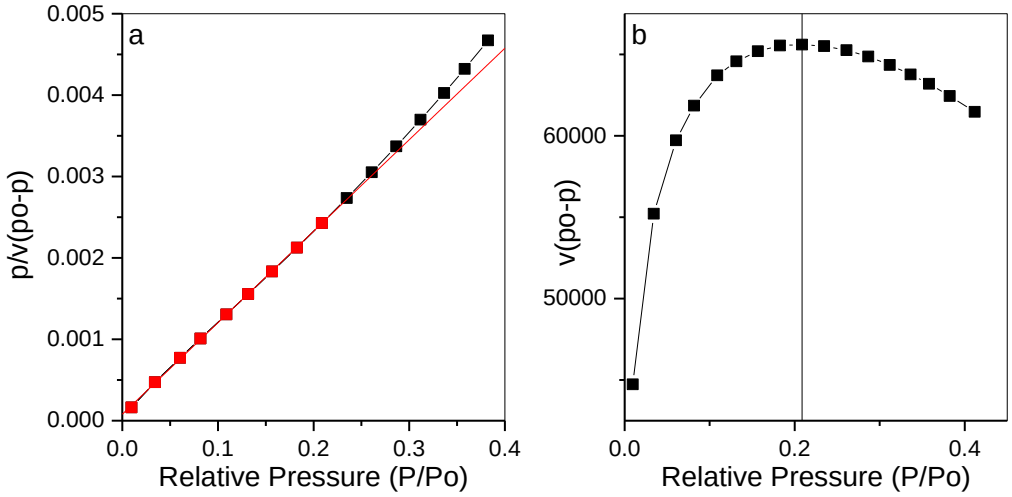

Figure 11: **(a) BET plot for a Melamine-Resorcinol-Formaldehyde 10% for Nitrogen adsorption. (b) Plot of the term v(Po - P) vs P/Po.**

Figure 11a shows the fitting of adsorption data to the BET model. It can be observed that the data tend to deviate from linearity. Therefore, it is important to decide, objectively, on the range of data that is meaningful for accurate determination of the monolayer capacity. Rouquerol *et al*. proposed a method for the selection of the range of partial pressure when applying the BET model to microporous materials [169]. However, there are two critera that have to be met to correctly apply the method. Firstly, the range of partial pressures chosen determines a line, and its intercept on the ordinate axis defines the constant *C* of adsorption, therefore, it is important that the intercept is positive, because a negative intercept would lead to a negative *C* value, which is meaningless. The second criterion, which is the tool to select the range, is shown in Figure 11b. The term $v(P_O-P)$ should continuously increase and the range of selected partial pressure should be up to the last positive increase of $v(P_O-P)$ [169].

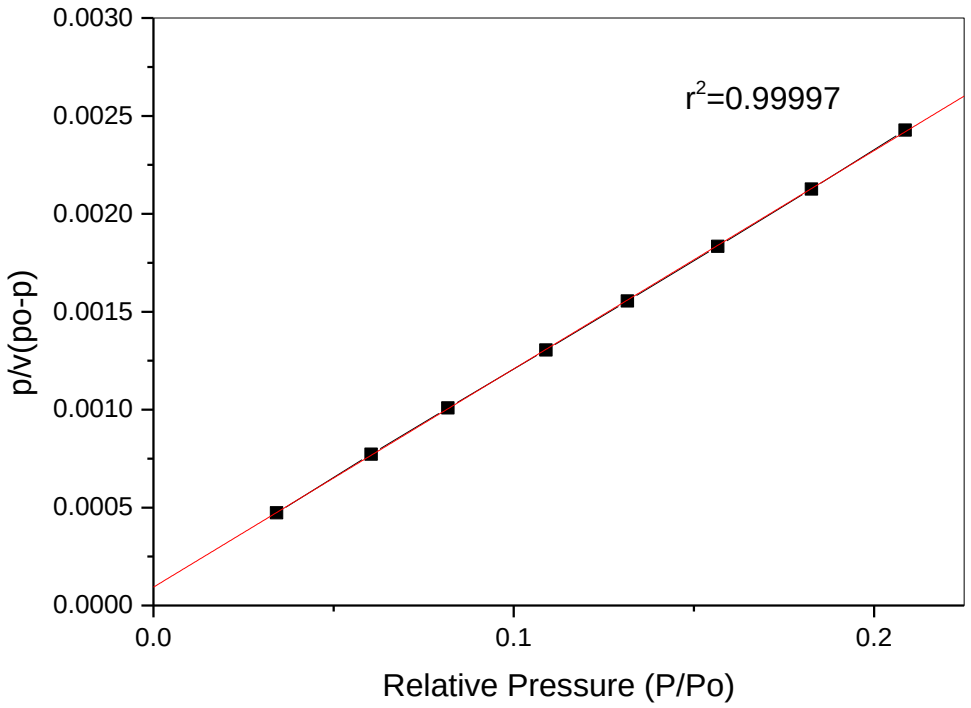

Figure 12: **BET plot with the selected range obtained using *Rouquerol* correction for sample shown in Figure 11.**

There are two consistency checks, which should be performed, to validate the application of this correction. Firstly, the calculated monolayer capacity has to correspond to a partial pressure included in the selected range. Secondly, the term (P_O/P) can be calculated from the C value obtained (Equation 41), making V = V_{mono} (see Equation 30); this value can be compared to the partial pressure read from the experimental data which corresponds to the calculated monolayer capacity. These two values should not differ by more than 10% [169]. The values for the materials used as an example in Figure 11 and 12 are a partial pressure of 0.082 (calculated from the value of C=124.333) and the partial pressure read from the experimental data has a value of 0.087.

$$\frac{P}{P_O} = \frac{1}{\sqrt{C}+1} \qquad \text{Equation 41}$$

To conclude, it is known that the concept of 'BET monolayer capacity' has no clear meaning for microporous materials; therefore, Rouquerol *et. al*. suggested that this should be called the 'BET strong retention capacity', which includes the 'monolayer content' (for the non-micropore surface) and the 'micropore capacity' [169]. The monolayer content is easily determined using the α_s-method or the t-plot method [165].

As a result, the BET method, using the correction explained above, will be used in this work to assess the 'BET strong retention capacity'; when it applies, the t-plot method will be used to determine the non-micropore surface area, and by subtracting this value from the 'BET strong retention capacity', the microporous capacity will be determined.

3.2.7.5 *Estimation of Micropore Area Using t-Model*

One of the most sensitive steps, when applying the t-model to assess the microporosity, is the selection of the range of the linear section of the V-t curve (see Figure 7 and Figure 10), an error here could lead to misleading calculations. Therefore, it is very important to select these ranges carefully.

After the application of the Rouquerol correction explained in the previous section, it is recommended to use Equation 39 to estimate the micropore surface area rather than Equation 40. Both equations would lead to the same value, theoretically; however, the latter requires sufficient data, at low partial pressure; and, besides, individual subjectivity in selecting the data range used can occur. Instead, when using Equation 39, the total surface area is calculated using the BET model and the Rouquerol correction; therefore, it is a value where subjectivity in data selection is eliminated or at least significantly reduced.

3.2.7.6 *Determination of CO_2 Adsorption Capacity and Adsorption Kinetics by Intelligent Gravimetric Analysis*

The Intelligent Gravimetric analyser (IGA) is a gravimetric adsorption system that measures the mass of gas adsorbed as a function of the applied pressure, in real time. Pressure is increased step-by-step, and the system is allowed to equilibrate fully, i.e. reach mass relaxation, at each pressure point. The main difference between gravimetric and the alternative of volumetric measurements is that in the latter, pressure is allowed to equilibrate, while in gravimetric measurements, the pressure is held constant during weight equilibration (at each step). Holding the pressure constant (at constant temperature) until equilibrium is achieved guarantees that boundary conditions are held constant. This allows data collection for pressure and weight of gas adsorbed, at a constant temperature, which produces an adsorption isotherm, such as:

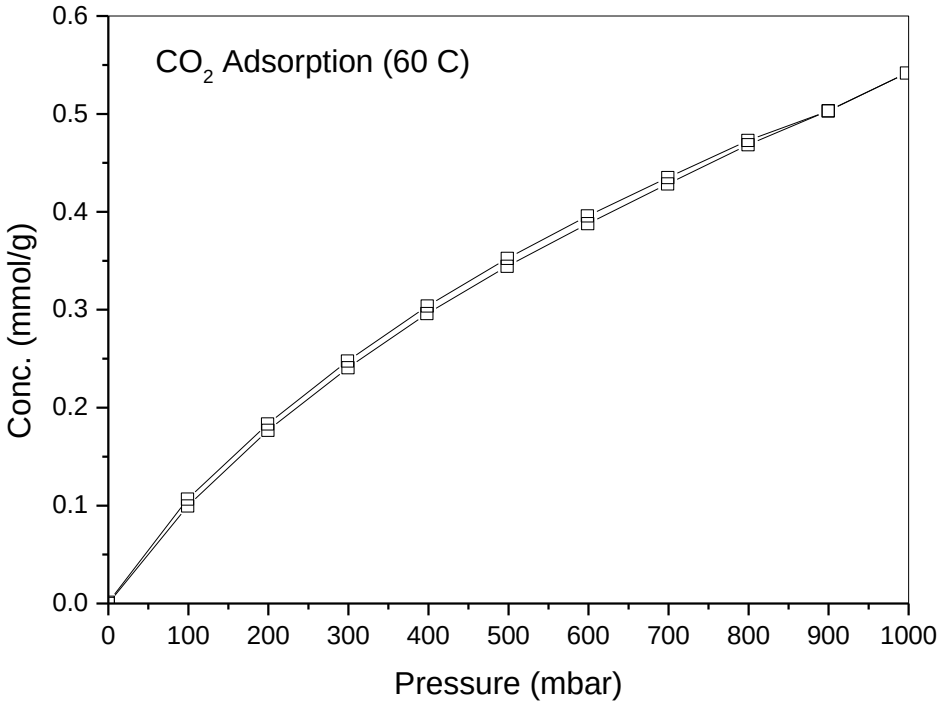

Figure 13: CO_2 adsorption and desorption at 60 °C on a Resorcinol-Formaldehyde resin with Sodium carbonate catalyst and a ratio of R/C 200 and R/F 0.25.

The use of adsorption isotherm allows direct comparison of adsorption capacity for a given gas on different materials and under different conditions of temperature and pressure. Additionally, the selectivity of the material, for a given adsorptive, is potentially tested given that mixtures of gases can be used as well, however, this needs a specialized setup.

The mass adsorbed is monitored in real-time, relating the variation in mass adsorbed to time until the relaxation time is reached for each step. Then, as pressure is increased by steps, brings the opportunity to study the kinetics of the process, both for adsorption and desorption. A representative plot of data collected for the equilibration of a typical adsorption step of the isotherm is shown in Figure 14.

Figure 14 shows an equilibration profile for a step with increasing pressure. Such data is collected for each point in an isotherm, and can be used to determine the kinetics of adsorption.

Additionally, gravimetric measurements can be used to study the cycling capacity of a material, and in this way, determine the lifetime of a given material.

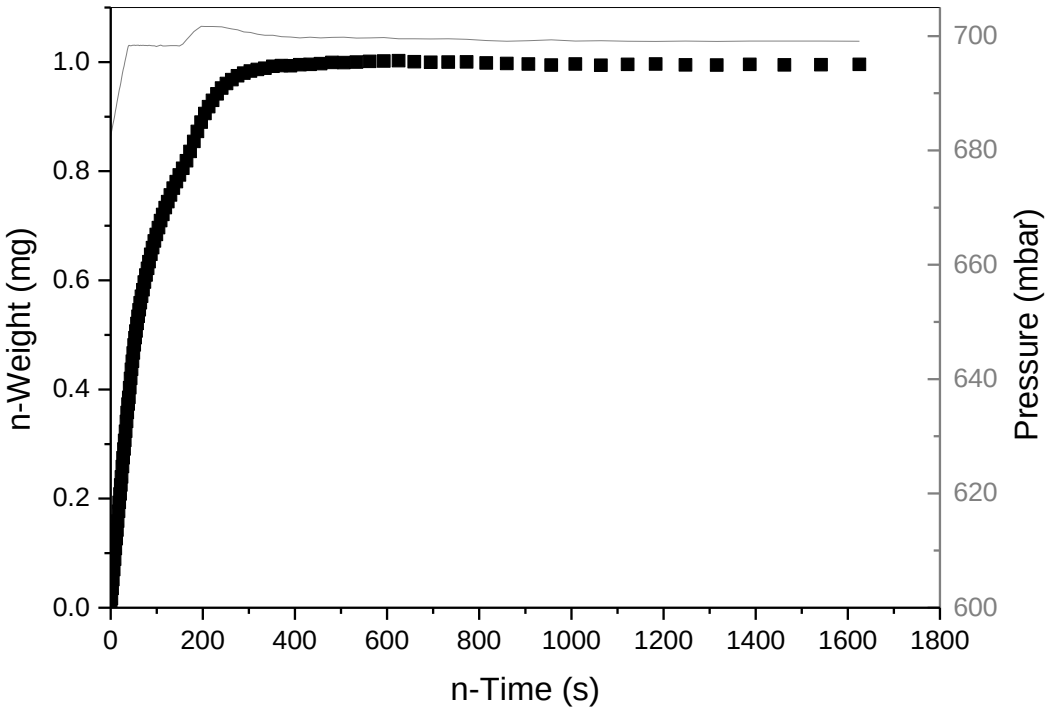

Figure 14: **Equilibration of the mass adsorbed over time for a given step increasing pressure for the same material shown in Figure 13. The dotted line corresponds to the weight increase and the solid line to the pressure step.**

3.2.7.7 *Kinetic Models*

The kinetic profiles obtained for small pressure increments for adsorption on porous materials, such as resorcinol-formaldehyde resins, can be fitted using a series of nested models based on the double-stretched exponential model (DSE), which is defined as:

$$\frac{M_t}{M_e} = A_1\left(1 - e^{-[k_1 t]^{\beta 1}}\right) + (1 - A_1)\cdot\left(1 - e^{-[k_1 t]^{\beta 2}}\right) \qquad \text{Equation 42}$$

where M_t is the mass uptake at time t, M_e is the uptake at equilibrium, k_1 and k_2 are the rate constants for two concurrent adsorption processes, for which β_1 and β_2 are the exponents and A_1 and $(1\text{-}A_1)$ are their fractional contributions to the overall mechanism driving the adsorption process. As a consequence, this equation includes two different contributions to the kinetics.

Other simpler models can be derived from the DSE, such as the double exponential (DE), the stretched exponential (SE) and the linear driving force (LDF) models, as shown below:

$$\frac{M_t}{M_e} = A_1\left(1 - e^{-k_1 t}\right) + (1 - A_1)\cdot\left(1 - e^{k_2 t}\right) \qquad \text{Equation 43}$$

From Equation 43, it can be seen that $\beta_1 = \beta_2$ and that it is a nested model of DSE. Similarly, the SE model is a reduced form of the DSE model, where $\beta_1 = \beta_2$ and $k_1 = k_2$; this model is described by:

$$\frac{M_t}{M_e} = 1 - e^{-kt^{\beta_1}} \qquad \text{Equation 44}$$

Finally, the LDF model is the simplest form, where β=1, and is defined as:

$$\frac{M_t}{M_e} = 1 - e^{-kt} \qquad \text{Equation 45}$$

The criteria to accept the fitting of a selected kinetic model to a set of experimental data is that 99% of the residual should be within ±0.02 of the profile of the data fitted. Authors suggest that when different models meet the requirements, the one with the least number of variables should be considered [170].

3.3 Fourier Transform Infrared Spectroscopy: the Infrared Spectrum

Fourier transform infrared (FTIR) spectroscopy is a method used to detect the molecular vibrations of complex molecules by applying infrared light to matter. FTIR is a technique used to obtain an absorption infrared spectrum which is directly related to the molecular vibrations' interaction of light with matter [171]. In organic chemistry, most vibrations occur within the range of 2.5 – 16 µm, which corresponds to frequencies of 4000 cm^{-1} (high frequency) to 625 cm^{-1} (low frequency).

Each functional group exhibits characteristic vibrations in a set range of frequencies, which helps with allocation of observed peaks. In this way, functional groups can be identified using the absorption spectrum, where the infrared spectra show a characteristic profile of the sample, which is considered as a molecular fingerprint for its components.

Additionally, by analysing the infrared spectra produced by FTIR, qualitative information about the molecules present in the sample can be obtained and, by the proportion of the areas below the peaks, the relative concentrations can be quantitatively assessed [171].

The absorbance spectrum of light is the result of the interaction between the electric vector, which composes the light (electric and magnetic waves), with matter [171]. The electric vector's amplitude changes over time and oscillates, alternating the polarity of the vector (see Figure 15). As the wave travels, it moves a distance λ for each cycle, the units of wavelength are distance per cycle, however, typically only the distance units are distinguished.

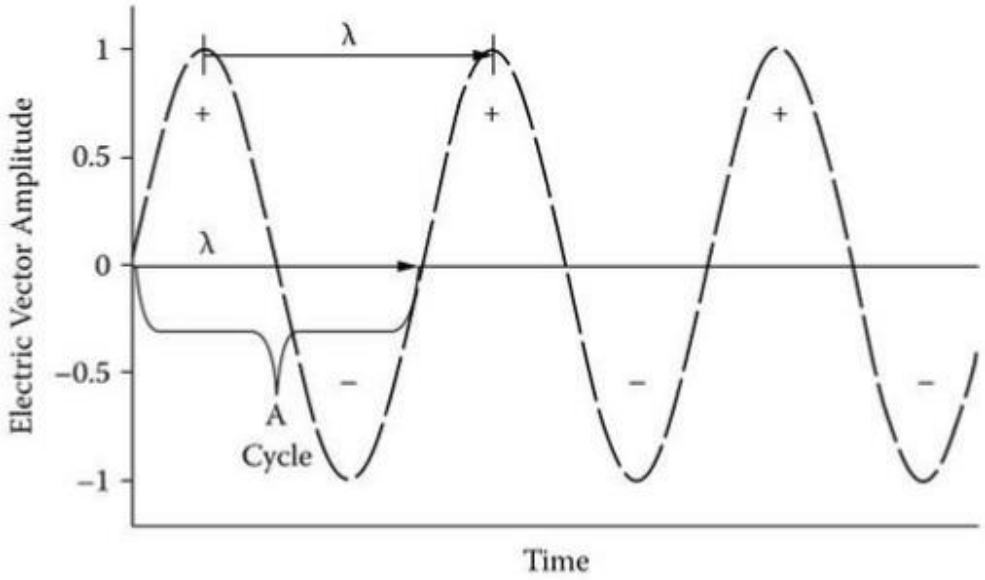

Figure 15: Electric vector of light wave. The signs + and - describes the change in polarity as it oscillates. The symbol λ denotes the wavelength.

Another important parameter is the wavenumber, $\tilde{\nu}$, which means the number of cycles that a wave undergoes per unit of length. Typically, $\tilde{\nu}$ is measured in units of number of cycles per centimetre, and is usually denoted as cm^{-1}. Therefore, when a peak is observed in a FTIR spectrum at a wavenumber of 2500 cm^{-1}, it means that the sample has absorbed infrared light cycling at 2500 times per centimetre.

Infrared spectra are mainly used from ~4000 to 500 cm^{-1}, for instance, the following figure shows a typical absorption spectrum for a resorcinol-formaldehyde gel of R/C 50, R/F 0.75 and using sodium carbonate as catalyst, in the stated range.

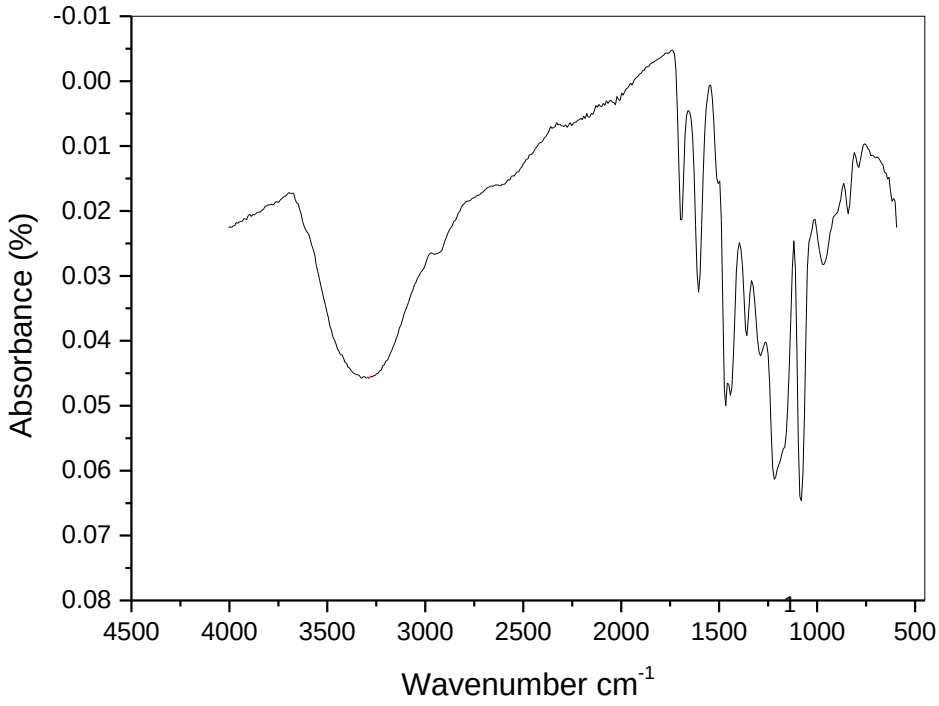

Figure 16: Infrared absorption spectrum for a Resorcinol-Formaldehyde gel.

As wavenumber is proportional to energy (see Equation 46), then high wavenumber light has more energy than low wavenumber light [171]. Therefore, the x-axis of Figure 16 also indicates energy, where energy decreases toward the right.

$$E = hcW \qquad \text{Equation 46}$$

where *E* is energy of a light as a function of the velocity of light *c*, the plank constant *h* and wavenumber *W*.

Experimentally, infrared light is emitted, covering the whole frequency range of the infrared spectrometer, typically 5000 to 400 cm^{-1}. This light is split into two beams; depending on the type of spectrometer, either one beam passes through the sample, or both are passed, however one of the beams travels a longer path. From the combination of the two beams, an interferogram is obtained, which is an interference pattern that results from the sum of all the interferences observed by each wavelength in the beam. An interferogram is not an absorption spectrum but it is converted by applying Fourier transformation into an absorbance - wavelength relationship.

A plot of energy absorbed by the sample with respect to some property of light, such as wavenumber, is called infrared spectrum, an example has been shown in Figure 16. There

are a large number of vibrational modes associated with a complex molecule. As a good approximation, some of those modes correspond to vibrations of specific bonds, which are called localized vibrations. The types of localized vibrations are: stretching, bending, rocking, twisting, or wagging.

When reading the peaks in an absorption spectrum, the range at high wavenumber (typically higher than 1450 cm^{-1}) is called the functional group region, and low energy (wavenumber lower than 1450 cm^{-1}) is called the fingerprint region, and it is used to identify the sample under analysis, as different samples will produce different patterns in that region. However, due to the complexity of the fingerprint region, it can be significantly difficult to identify individual bonds, but the functional group region can be used to detect specific functional groups present. As a summary, when a spectrum is analysed, the region above 1500 cm^{-1} shows absorption bands that can be assigned to specific groups while the fingerprint region (below 1500 cm^{-1}) shows a spectra characteristic of the compound in question [172]. It is worth noting that a particular bond may shift its position in the spectra according to the exact substitution pattern, for this reason, in most tables, a range of wavenumbers is given for each type of bond.

The use of FTIR can provide information regarding which molecules are present in a sample or allow comparison of the spectra for two different samples to determine whether they are the same compound. Additionally, using Beer's law , Equation 47, absorbance (height of a peak or its area below the curve) can be related to concentration by a calibration curve [171].

$$A = \varepsilon l c \qquad \text{Equation 47}$$

where A is absorbance, ε is absorptivity, l is path-length and c is concentration.

The main advantages of FTIR are that it is a universally applied method, the spectra are rich in information, it is relatively quick and easy to perform, inexpensive (despite the cost of the equipment), and offers high sensitivity. The main disadvantage is that some molecules cannot be detected, because they do not produce vibrations with the infrared spectrum. Furthermore, complex samples (mixtures) produce complicated spectra that can become difficult to interpret, while the presence of water in the sample can mask other peaks in the same region of the spectra.

3.4 Scanning Electron Microscopy

This technique uses a type of microscope, which involves scanning the surface of the sample with a focused beam of electrons to produce images. The images produced are the result of interactions between the beam of electrons and the atoms at various depths producing information about topography and composition of the sample [173]. Consequently, Scanning Electron Microscopy (SEM) can produce significant, high resolution images of the sample's surface for features smaller than 1 – 10 nm in size.

SEM produces various types of signals, such as secondary electrons, back-scattered electrons, photons, light, absorbed current and transmitted electrons, and secondary electron detectors are standard in all SEM equipment.

Samples used for SEM analysis need to be electrically conductive, at least at the surface, and, additionally, they need to be electrically grounded in order to prevent the accumulation of electrostatic charge at the surface. Therefore, metal samples do not require significant preparation except for cleaning and mounting on the specimen stub. On the other hand, nonconductive samples are usually coated with an ultra-thin (10-20 nm) coating of an electrically conductive material [173], applied via low-vacuum sputter coating or high vacuum evaporation. The most common materials used for such coatings include gold, palladium, platinum, osmium, tungsten and graphite.

The magnification of SEM images range over six orders of magnitude, from ~10 to 500,000 times. This magnification is not controlled by objective lens power, whose function is to focus the beam to a given area; rather, magnification is a result of the ratio of the dimensions of the raster on the sample and the raster on the display device.

3.5 Elemental Analysis: Combustion Analysis.

Elemental analysis is one of a group of techniques used to determine qualitative and quantitative information of the composition of a sample. In organic chemistry, this technique almost always refers to CHNX analysis, i.e. the determination of carbon, hydrogen, nitrogen and heteroatoms (usually halogens or sulphur) of a sample [174].

When performing combustion analyses, in the presence of excess oxygen, the collection of any combustion products, generally carbon dioxide, water and nitric oxide, can lead to the determination of the masses of these products and, therefore, the composition of the

sample. The results are presented as percentages of carbon, hydrogen and nitrogen in the burned sample. This can be later related to the chemical formula of the sample if it is known.

3.6 Proximate Analysis by Thermogravimetric Investigation

Thermogravimetric analysis (TGA) is an analytical technique based on measuring the mass of a sample while the temperature is varied under a given atmosphere. Therefore, the mass is monitored against time and/or temperature [175]. This method can provide different types of information about a given sample, such as purity, water content, carbonate and organic content and, of course, it allows the study of decomposition reactions with respect to temperature [175]. Further important information that can be obtained with this technique is the rate at which a given property changes with temperature, i. e. kinetics. This is called derivative thermogravimetry (DTG), the curve offers insight into determining and interpreting the reactions occurring as the temperature is increased.

A typical TGA instrument relies on at thermo-balance and a furnace, which controls the heating or cooling of the sample (temperature program). The sample is placed on the sensitive microbalance, which monitors any change in mass with respect to temperature and time. The sensitivities of the mass changes are of the order of 0.1 µg. The ranges of temperature conditions for the furnace are in the range of ambient temperature to 1500 or 1700 °C. The crucibles used are often made of alumina or mullite.

The TGA measurements are usually affected by the sample size, heating rate, buoyancy, electrostatic effects, gas flow, and sample holder. These aspects should be controlled and taken into account when deciding upon the test conditions, in order to minimize any error.

The output of this technique includes a TG graph (mass loss) and a DTG curve. This allows determination of mass loss with temperature and information about the decomposition of the sample as it is heated or cooled, and any structural changes that this may produce. Therefore, the applications of TGA include thermal stability and decomposition mechanisms, material identification and purity tests as the TG and DTG curves could be used as fingerprints of given compounds, corrosion studies, and composition analysis [175].

3.7 Titration of Amines

It is known that the adsorption behaviour of an adsorbent material, such as carbon, will be affected by the chemical state and composition of its surface [176, 177]. Boehm titration can be used to identify surface functional groups, such as amine groups on the surface of the melamine-resorcinol-formaldehyde gels used in this study. The so called Boehm titration method has previously been applied to identify oxygen surface groups on carbon materials [176-178].

In this work, the surface chemistry of the materials may be influenced by the amine groups introduced via melamine incorporation into the gel structure. Therefore, the surface chemistry will be tested by titration with strong acid (hydrochloric acid) and strong base (sodium hydroxide).

Aspects that need to be considered, in order to ensure the accuracy of results, include the ratio of carbon to reaction base, the period of time for which samples are stirred or shaken, whether expulsion of CO_2 has been performed on the test solution, and precise determination of the titration endpoint [179, 180].

CO_2 expulsion becomes an important factor for such titrations as any additional acidity from CO_2 dissolved in the solution could result in an excess of base being used during the titration therefore producing a misleading result. Many suggestions have been made as to how best to achieve CO_2 removal, such as boiling the solution, degassing with a flow of N_2, conducting the titration in a N_2 atmosphere, or subtracting the value of a blank titration (with no solid test material) from the final result [179]. Degassing the sample with N_2, or boiling, could result in an additional error within the volume of titrant used, as a consequence of possible evaporation of solution, therefore, a change in concentration; hence, it is important to standardize the time for which the sample is exposed to the gas stream. Authors suggest a total time of 2 hours of degassing prior to titration [179].

To determine titration endpoint, colour indicators are commonly used; there are many options, such as phenolphthalein, methyl red, and methylene blue. In this work, methyl red will be used, and the colour change appears at pH 6.2, and noting that for strong acid-base interaction the equivalence point should be close to pH of 7.0. Therefore, the equivalence point cannot be seen with the indicator, and it could result in the excess of base or acid added during titration. However, the titration curve for strong acid-base interactions is

almost vertical at the equivalence point, therefore, any difference when using the indicators should not be significant [179].

3.8 X-ray Photoelectron Spectroscopy

X-ray photoelectron spectroscopy (XPS) is a sensitive technique used to the analyse surfaces of solids materials, allowing measurements of elemental composition, empirical formula, chemical state and the electronic state of the elements at the surface. It is one of the most used surface analysis techniques, due to its applicability to a broad range of materials. The average depth of analysis by XPS is ~5 nm [181].

XPS instruments, analogously to SEM (scanning electron microscopy), irradiate the material with a beam of X-rays to obtain the resulting spectra, comprising binding energies. Simultaneously, it measures the kinetic energy and quantifies the number of electrons that are emitted from the surface of the material. In this way, binding energies are quantified from the difference between the energy of the X-ray photons being used (which is known) and the kinetic energy measured, as well as a work function, φ, which depends on both the material and spectrometer [181].

$$E_{binding} = E_{photon} - (E_{kinetic}) + \phi \qquad \text{Equation 48}$$

XPS requires high levels of vacuum, in the range of $\sim 10^{-8}$ mbar, or ultra-high vacuum which reaches pressures below $\sim 10^{-9}$ mbar. In principle, XPS detects all elements, however, in practice, it detects all elements with an atomic number (Z) of 3 or above, because hydrogen and helium are difficult to detect. In most instruments, the detection limit is in the range of parts per thousand (ppt), while levels of parts per million (ppm) can be reached, it requires special conditions and long analysis times.

XPS is generally used to analyse a large number of materials, such as polymers, glasses, ceramics, paints, papers, woods, bones, oils, glues and many others, hence, it is appropriate to be used for surface analysis of xerogel materials.

3.9 Thermodynamic Analysis by Ideal Adsorbed Solution Theory

Ideal Adsorbed Solution Theory (IAST) is used to determine the equilibrium composition of the adsorbed phase and bulk gas, for binary systems [182]. It is important to note that IAST is based on the thermodynamic equilibrium properties of the pure components of the

system studied. IAST gives useful information for the prediction of the selectivity of an adsorbent for the separation of a particular mixture.

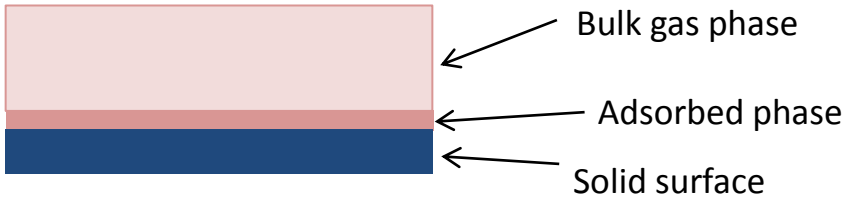

Figure 17: Representation of a gas in contact with the surface of a solid.

IAST can also be applied to porous solid adsorbent materials to predict their ability to separate a gas mixture. IAST is analogous to Raoult's Law (Equation 49) for vapour-liquid equilibrium of ideal solutions (negligible interactions between molecules), which states that, for each component of an ideal mixture of liquids, the partial vapour pressure, P_i, is equal to the product of the vapour pressure of the pure component, P_i^o, and its mole fraction, X_i, in the mixture.

$$P_i = P_i^o \cdot X_i \qquad \text{Equation 49}$$

This equation is derived by equating the chemical potentials, μ, of the liquid and vapour phases.

The adsorbed phase is assumed to behave as an ideal mixture, which is accurate enough to describe the mixture of simple gases adsorbed in microporous materials [183]. Spreading pressure, ω, is a thermodynamic property of the adsorbed phase (J/m^2), used to define the vapour pressure, P_i^o:

$$\omega(P_i^o) = \frac{RT}{A_S}\int_0^{P_i^o} \frac{N_i^o(P)}{P}\,dP \qquad \text{Equation 50}$$

where R is the universal gas constant, T is temperature, A_S is surface area of the material, N_i^o is molar adsorbed amount (obtained from the adsorption isotherm) at pressure P. This equation is based on the Gibbs-Duhem equation.

Therefore, applying this to the two components within a binary system, and combining with Raoult's Law, it gives two equations, one for each component. It is important to note that the mole fractions in each base (bulk gas and adsorbed phase) must add up to 1.

Adsorption data is processed by applying the Langmuir isotherm model for each pure component to obtain the individual molar uptake; two parameters are obtained for each pure component from the isotherm, K (bar^{-1}) and C_m (mol/g), the constant of the Langmuir isotherm and the monolayer uptake, respectively. Combining this with the spreading pressure equation, and including the relationship mentioned above for mole fractions and Equation 50, a system of 6 equation with 6 unknown parameters are obtained:

(1) $$Py_1 = P_1^o(T, \omega) \cdot X_1$$ Equation 51

(2) $$Py_2 = P_2^o(T, \omega) \cdot X_2$$ Equation 52

(3) $$y_2 = 1 - y_1$$ Equation 53

(4) $$X_2 = 1 - X_1$$ Equation 54

(5) $$\omega(P_1^o) = \frac{RTC_{m1}}{A_S} ln(1 + K_1 P_1^o)$$ Equation 55

(6) $$\omega(P_2^o) = \frac{RTC_{m2}}{A_S} ln(1 + K_2 P_2^o)$$ Equation 56

Once this system is solved, the adsorbed quantity for each component in the adsorbed phase is obtained from the mole fractions calculated, X_i:

$$\frac{1}{N_t} = \frac{X_1}{N_1^o} + \frac{X_2}{N_2^o}$$ Equation 57

where N_i^o is the amount adsorbed for each pure component in the adsorbed phase, and N_t is the total amount adsorbed.

The selectivity, S, of the adsorption process is subsequently defined as:

$$S_{12} = \frac{X_1 y_2}{X_2 y_1} = \frac{P_2^o}{P_1^o}$$ Equation 58

Chapter 4
Experimental Procedures

4 Experimental Procedures

This chapter describes the methods used to synthesise and characterise MRF xerogels. These xerogels are produced following a sol-gel process, which starts by the preparation of the sol, through gelation, curing, solvent exchange and the drying of the final material obtained. This section also explains how the characterisation techniques used were carried out.

4.1 Hydrogel Synthesis

Selected synthesis variables were altered producing several different compositions of hydrogel to investigate its effect on the final properties of the material. All samples were prepared following the same procedure allowing comparisons to be made. The incorporation of melamine as a reactant required adaptation of the standard RF gel synthesis method [184]. The observation of the effect of varying the selected variables allows various comparisons to be made.

4.1.1 Standard Synthesis at Room Temperature

The synthesis procedure follows the previous established method [184] within the Fletcher research group, which allows comparison among xerogels produced by different members within the team. The standard hydrogel procedure uses a single metal (Group I or II) carbonate as catalyst, a given stoichiometric ratio and room temperature/pressure.

4.1.2 Synthesis Preheating the Solution – Melamine Solubility

The low solubility of melamine in water at room temperature (~0.324 g of melamine in 100 g of water at 19.9 °C) requires the usual synthetic temperature to be increased up to ~50 °C (~1.04 g of melamine in 100 g of water at 49.8 °C) [185]. Previous observation determined that cluster growth begins when the solution reaches 55 °C [103], which limited the preheating temperature.

4.2 Preheated hydrogel Synthesis

In the preparation of Melamine-Resorcinol-Formaldehyde (MRF) gels all variables were kept constant, with the exception of R/C ratio, R/F ratio and melamine concentration. Sodium carbonate was used as the catalyst (C) for all gels produced, the volume of the solution was set as 30 mL and the solids content (M+R+F+C) was kept as 20 % wt/vol. The variables selected for investigation in this work were set as shown in Table 1. The

combination of the chosen levels for M, R and F produced 100 different recipes for MRF gels.

Table 1: MRF synthesis variables studied in this work, R/C ratio, R/F ratio and [M], and levels selected for each.

R/C	50	100	200	400		
R/F	0.25	0.5	0.75	1.0		
[M] %	0	1	10	20	30	40

Note that [M] refers to the percentage of resorcinol substituted by melamine, therefore R/F denotes (R+M)/F, but for simplification it will be named as R/F from now on. The number of gels produced sum up to 100 because four gels also need to be added corresponding to R/F = 1, with [M] = 100 (R=0), for the four R/C levels stated, which results in a MF gel. This is incorporated to include also MF gels as the opposite to MRF0 gels (RF); See Tables 126 and 127 in Appendix K.

4.2.1 Naming of Samples

It is necessary to ensure easy identification of samples to guarantee consistency, therefore a sample naming system was defined. All samples were synthesised using sodium carbonate as a catalyst; consequently it is not necessary to indicate the catalyst as a part of the sample name. However, it is worth mentioning the variables that change through the study, which are the R/C and R/F molar rations and melamine concentration. The sample name takes the form of MRFX_Y_Z where X is the percentage of melamine in the sample, Y is the R/C molar ratio and Z is the R/F molar ratio. For example, a sample produced with 10% of melamine, R/C of 100 and R/F of 0.5 would be labelled as MRF10_100_0.5.

4.2.2 Reactant Quantities for Hydrogel Synthesis

Given that the solids content is fixed to 20 % wt/vol and the solution volume is kept as 30 mL, therefore the solids content must be equal to 6 g, which corresponds to addition of the weights of M+R+F+C.

The individual masses of M, R, F and C were calculated for each combination shown in Table 1 first on molar basis and then converted to a weight basis as a percentage of the total 6 g of solids. Hence, according to the R/C, R/F molar ratios chosen and the melamine weight concentration the masses of M, R, F and C were varied as required. As an example, Table 2 shows the calculations and results for MRF0_50_0.25.

Table 2: hydrogel reactant composition for MRF0_50_0.25.

	Equivalent Moles	Moles	Mass (g)	Percentage Mass (%)	Percentage Moles (%)
Resorcinol	1	0.0258	2.8432	47.3867	19.9203
Formaldehyde	4	0.1033	3.1021	51.7010	79.6813
Sodium carbonate	0.02	0.0005	0.0547	0.9123	0.3984
Melamine		0	0	0	0
Total		0.1296	6	100	100

Formaldehyde is provided as a solution, known as formalin, which contains 37 wt % formaldehyde and 10-15% methanol as a stabiliser, and has an overall density 1.09 g/ml. Consequently, it was necessary to calculate the volume of formalin that contains the calculated mass of formaldehyde for each case, as follows:

$$Volume\ of\ formalin\ (ml) = \frac{mass_{formaldehyde}}{\rho_{formalin} * Wt\%} = \frac{mass_{formaldehyde}}{1.09\ \left(\frac{g}{ml}\right) * 0.37}$$

$$= \frac{mass_{formaldehyde}}{0.4033}$$

Formaldehyde has a density of 0.815 g/mL, therefore the volume of formaldehyde in formalin is:

$$Volume\ of\ F\ in\ formalin\ (ml) = \frac{mass_{formaldehyde}}{0.815}$$

The remaining volume is water and methanol, and this volume is calculated as follows:

$$Volume\ of\ H_2O\ /\ MeOH(mL)$$
$$= Volume\ of\ formalin\ (mL) - Volume\ of\ F\ in\ formalin\ (mL)$$

This volume will also contribute to the total volume of the sol (30 mL), consequently, the volume of deionised water used in the solution is given by:

$$Volume\ of\ deionised\ H_2O = 30 - Volume\ of\ H_2O\ /\ MeOH(mL)$$

The following table shows the calculated values for MRF0_50_0.25 corresponding to the reactant composition shown in Table 2.

Table 3: Calculated volume of reactants required for MRF0_50_0.25 hydrogel synthesis.

Vol. Formalin (mL)	Vol. due to Formaldehyde (mL)	Vol. H_2O/MEOH (mL)	Vol. H_2O added (mL)
7.69169	3.806207	3.885483	26.114517

The corresponding volumes calculated for all samples synthesised are shown in Appendix A to D.

4.3 Hydrogel Preparation

For each chosen R/C ratio, Resorcinol/Formaldehyde ratio and melamine concentration, the required melamine (99% - SigmaAldrich) was weighed out and placed in a sealable 500 mL jar with 25 mL of deionized water, produced in house (Millipore Elix 5 system). The melamine solution was heated up to 50 °C and stirred magnetically until completely dissolved. Then, the required resorcinol (ReagentPlus, 99% - SigmaAldrich) and sodium carbonate (catalyst - anhydrous, ≥ 99.5%) were weighed out and added to the solution while it was continuously stirred, until completely dissolved. The required volume of formalin (37 wt % formaldehyde, stabilized with 10 – 15 % methanol) was added to the jar, together with the additional water to make the volume up to 30 mL, the jar was subsequently sealed and stirred for 30 min.

4.4 pH Measurement

Once the stirring period was finished, the ph of the initial solution was recorded using a Hanna Instruments ph20 pH meter fitted with an HI 1110-B pH probe (Figure 18). This probe was calibrated during the solution stirring interval using basic and acidic solutions buffer of pH 10.01 and 4.01 (Fluka Analytical), respectively.

Figure 18: Hanna Instruments pH 20 pH meter.

4.5 Gelation Method

Once pH was recorded, the jar was re-sealed tightly and placed in a preheated oven (Memmert ULE-500) at 85 ± 5 °C. The jar was left for 3 d to allow gelation and curing of the hydrogel. The RF and MF reaction occurs also at room temperature, however the time scale is reduced significantly at elevated temperatures.

4.6 Solvent Exchange in the Synthesised Hydrogels

As previously detailed in Section 1.7.5, it is necessary to remove the water entrained within the cured gel network with the aim of reducing the shrinkage during the drying stage. The solvent used was acetone (ACS reagent, ≥99.5%, SigmaAldrich), which is frequently used in the literature, is a relative cheap solvent, and most importantly with a considerable lower surface tension (compared to water) which reduces the capillary pressures inside the pores preventing shrinkage.

Once the 3 days' period for gelation was completed the jar containing the cured hydrogel were removed from the oven and allowed to cool down to room temperature. Once the gel is cooled, it was cut down to small pieces to increase the contact between acetone and the gel and therefore making the solvent exchange process more effective. Then, 30 mL of acetone was added and the jar was firmly shaken for 5 min, before draining it. This step is performed to increase the effectiveness of the solvent exchange because this first wash will remove most of the water and any unreacted. Then, 90 mL of acetone is again added to the

jar and this is placed in a shaker unit (VWR 3500 Analog Orbital Shaker) for 3 d to ensure full solvent exchange within the pores of the gel.

4.7 Drying of Solvent Exchanged Gels

Drying can be undertaken in different ways: supercritical drying, freeze drying or ambient temperature drying. Supercritical CO_2 drying is very popular in the literature [111, 186, 187], but, from an industrial point of view this is expensive, dangerous and difficult at that scale. In contrast, subcritical drying and under vacuum techniques have been developed, such dried gels are defined as xerogels and this is the technique employed in this study.

Once the solvent exchanged phase was complete, the jar containing the wet gel was placed in a vacuum oven, for subcritical drying at 90 °C allowing the removal of all remaining solvent from the gel network. The oven used was a Townson and Mercer 1425 Digital Vacuum oven equipped with a Vacuubrand MZ 2C NT vacuum pump. The jar was covered with a piece of aluminium foil, into which several holes were made to allow the gassed solvent passed through. The acetone recovered was condensed in solvent traps fitted with ice water. For safety lab policy the vacuum pump and oven were switched off during night, however, the chamber was isolated at vacuum for that period. The drying process was repeated for a second day, where no more acetone was collected in the traps ensuring a dry gel.

4.8 Sample Storage

Once the drying phase was finished, the xerogel was collected and stored in 50 mL containers which were labelled and kept in the laboratory at room temperature until further analysis.

The same hydrogel preparation, gelation, solvent exchange and drying processes as described above were used for all hydrogels produced allowing the elimination of these steps as factors influencing the xerogel structure formation.

4.9 Scanning Electron Microscopy

Scanning electron microscopy tests were carried out in Advanced Materials Research Laboratories (AMRL) in the University of Strathclyde. A Hitachi SU-6600 Field Emission Scanning Electron Microscope (FE-SEM) was used to obtain the images. MRF xerogel

sample preparation for this test involved a degassed to remove any moisture or contaminants from the sample followed by 1 min gold coating of the surface.

4.10 Surface Area and Porosity Measurements by Nitrogen Adsorption

A Micromeretics ASAP 2420 system (Figure 19) was used to obtain surface area and porosity by N_2 adsorption/desorption equilibrium measurements at -196 °C, using ~0.5 g sample. This test was carried out for all samples produced allowing comparison between these properties by varying the synthesis conditions. The analysis method previously detailed in chapter 3 was used to determine surface areas and pore size distributions of the xerogels.

Figure 19: Micromeritics ASAP 2420 surface area and porosity analyser.

Surface areas were calculated by applying the Brunauer-Emmett-Teller (BET) theory [162] combined with Rouquerol correction for BET application to microporous materials [169]. Pore volume was calculated from the equilibrium measurement of nitrogen adsorbed at ~0.98 bar (i.e. the saturation vaporous pressure of N_2 at -196 °C). The pore size distribution and average pore size were obtained by application of the Barrett-Joyner-Halenda (BJH) method [163].

4.10.1 Sample Degassing Prior to Surface Area and Porosity Analysis

All samples were degassed before the surface area and porosity test in order to remove any remaining solvent or moisture from the material surface, because it would affect the

measurements. The effectiveness of this test would be compromised by the effectiveness of degassing, given that incomplete degassing would lead to adsorption sites and/or pores to be blocked, which would result in underestimation of surface area and porosity.

∼0.5 g sample of MRF gel was accurately weighed out and placed into a sample tube. This tube was attached to a degas port of the equipment, the sample was evacuated by a vacuum pump first to 5 mmHg, and then to 10 µmHg, while the sample was heated up to 50 °C for 30 min using a heating mantle surrounding the sample tube (Figure 20). Then, the temperature was ramped to 120 °C and these conditions were held for 120 min. Next, the sample was allowed to cool down to room temperature and the tube was backfilled with pure nitrogen. Once degas was completed the sample was reweighed to quantify the mass loss during degas and to update the actual dry mass of the sample before the adsorption/desorption measurements.

Figure 20: Micromeritics ASAP 2420 sample tube.

4.10.2 Analysis of Xerogels by Nitrogen Sorption

Once degas was completed and the sample tube backfilled with nitrogen, the sample (and tube) was removed and reweighed accurately, which allows calculation of the real dry mass of sample, which is updated in the sample file. This new mass was used to calculate the surface area and porosity measurements. Once the sample was reweighed a clean glass rod was introduced in the sample tube for volume displacement, in order to reduce the empty volume inside the tube sample. Additionally, an isothermal jacket was applied to the outside of the neck of the tube, which allows maintaining a constant temperature at the

tube surface. Then, the tube is attached to an analysis port on the instrument (Figure 19). Analysis was performed at -196 °C, obtained by a dewar filled with liquid nitrogen surrounding the sample tube. The analysis was performed between the nitrogen relative pressure range of 0.01–1 with 40 adsorption points and 30 desorption steps from 1 to 0.01 relative pressure.

4.11 Elemental Analysis

Carbon, Hydrogen and Nitrogen analysis test were carried out on a Perkin Elmer 2400 Series II CHNS Analyser. Results were obtained as a percentage by weight, and were measured as a function of thermal conductivity. Sample sizes were ~1-2mg of MRF xerogels. These tests were carried out by Alexander Clunie in the Department of Pure and Applied Chemistry –Microanalysis Services of the University of Strathclyde.

X-ray photoelectron spectroscopy (XPS Thermo Scientific Theta Probe) was performed using a monochromated Al K-a source to quantify the carbon, nitrogen and oxygen content of the MRF xerogels. MRF xerogels samples were degassed prior analysis to pressures of ~$1.33x10^{-11}$ bar. These tests were carried out by Dr Billy Murdoch of NEXUS Team in the Stephenson Building of Newcastle University.

4.12 FTIR Analysis of Xerogels

Fourier transform infrared (FTIR) spectroscopy is employed to detect the molecular vibrations of complex molecules by applying infrared light to matter, producing absorption infrared spectra, which are directly related to the interaction of light with individual molecular vibrations [171]. Each functional group exhibits characteristic vibrations within a set range of frequencies, which allows assignment of observed peaks. In this way, functional groups can be identified using an absorption spectrum, which shows a characteristic profile of the sample, considered as a molecular fingerprint for its components.

4.12.1 Sample Preparation

Xerogel samples were fully ground prior to FTIR analysis. The solid sample was placed into a mortar which was carefully ground using a pestle (Figure 21), to a homogeneous particle size.

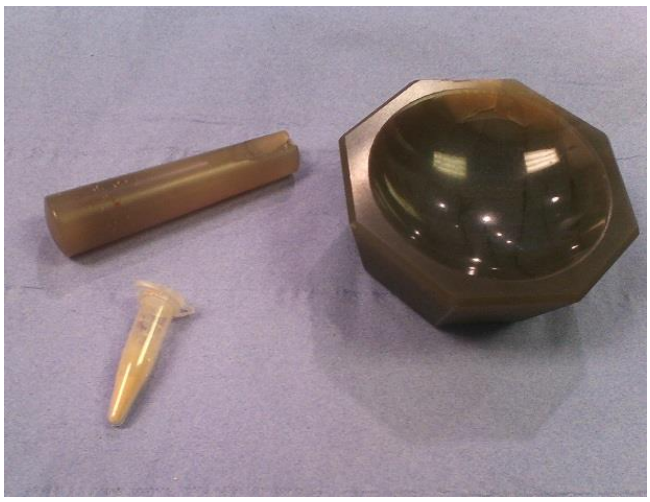

Figure 21: Mortar and pestle for grinding MRF xerogel to powder for FTIR analysis.

4.12.2 FTIR Xerogel Analysis

All samples were analysed by Fourier transform infrared spectroscopy (FTIR) for surface characterization (ABB Instrument MB3000 series S FTIR spectrometer with internal reflection elemental of diamond, each spectrum was the average of 86% scans with spectra resolution 4 cm^{-1}, Figure 22). Analysis was performed for a range of frequencies from 4000 cm^{-1} (high frequency) to 625 cm^{-1} (low frequency), which is the common range used for most organic systems. The sample is irradiated and the emitted light is split into two beams which follow different paths. When the beams are recombined an interference pattern is created as an effect of the different paths covered by the beams, this is transformed into an absorbance or transmittance curve as a function of the wavelength by the equipment software utilising a Fourier transform.

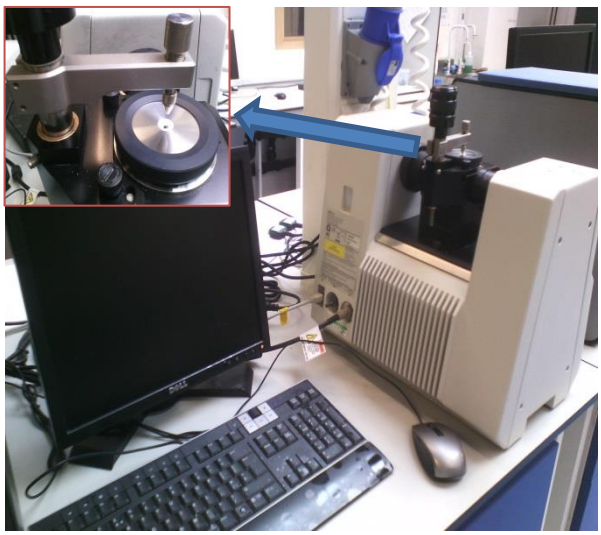

Figure 22: FTIR equipment (ABB Instrument MB3000 series S FTIR spectrometer)

4.13 Proximate Analysis by Thermal Gravimetric Examination

Thermal stability and proximate analysis of samples were performed on xerogel samples to understand the proportion of moisture, volatile matter, fixed carbon and ash in the material. This analysis was performed using a Netzsch STA 449 F3 Jupiter model. Thermal gravimetric analysis (TGA) was used to monitor the mass loss in xerogel samples as a function of temperature. Additionally, Differential Scanning Calorimetry (DSC) was used to determine the energy transitions (exothermic or endothermic) occurring as a function of temperature. The equipment is fitted with a highly sensitive balance and a silicon-carbide furnace, which controls the temperature ranging from room temperature up to ~1500 °C.

4.13.1 Sample Preparation

Samples did not require special preparation for this test. The mass of xerogel used ranged from 23 to 35 mg. Small pieces of xerogel were accurately weighed and placed inside an alumina (Al_2O_3) crucible which was positioned on the top head balance together with a reference crucible of the same material. The sample was placed on the balance and furnace is lowered over it (Figure 23).

Figure 23: Thermal gravimetric analyser Netzsch STA 449 F3 Jupiter model.

4.13.2 Sample Analysis

Once the sample was weighed and placed on the balance, the furnace was lowered over the balance. A constant flow of nitrogen (20 mL min^{-1}) was set to protect the balance and a flow of 50 mL min^{-1} was set over the sample. Once the mass was stable, the temperature was raised from ambient to 30 °C at a rate of 1 °C min^{-1}, before holding at this temperature for 30 min. This was followed by an increase in temperature to 120 °C at a rate of 20 °C min^{-1}, held for 75 min. Next, temperature was increased to 920 °C, at the same temperature rate, and this temperature was maintained for 30 min, followed by a decrease of temperature to 820 °C at the same rate. The gas flow was changed when 820 C° was reached (from nitrogen to air at a flow of 50 mL min^{-1}), allowing oxygen to contact with the sample for a period of 60 min. The mass change was recorded continuously using Proteus software, which provided the mass loss over time as a function of temperature allowing the calculation of mass loss in percentage and the derivate with respect to time, together with DSC.

4.14 Density Measurements

Density is defined as the ratio of mass over volume for a given material:

$$\rho = \frac{mass}{volume} \qquad \text{Equation 59}$$

A known mass of sample, weighed on an analytical balance, was placed in a 5 mL volumetric flask. Successively, the flask was filled up to the reference point with a known volume of deionized water, produced in house (Millipore Elix 5 system). The flask was then sealed and left on a shaker for a period of ~5-10 min to allow the water to fill the pores of the MRF xerogel. Then, a known volume of deionized water was used to fill the flask back up to the reference point, if needed. Finally, the density was calculated by the ratio of the known mass and volume.

4.15 Titration

Boehm titration is a method developed to identify oxygen groups on the surface of carbonaceous materials [179, 180], and is based on the principle that oxygen groups have different acidities and, therefore, can be neutralised by bases of different strengths. In this way, the strongest base normally used is sodium hydroxide (NaOH) and it is assumed that all acid groups (phenols, lactonic and carboxylic acids) are so neutralised. Sodium carbonate (Na_2CO_3), neutralises carboxylic and lactonic groups (lactone and lactol) and finally, sodium

bicarbonate ($NaHCO_3$) neutralises carboxylic acids. Therefore, these bases can be used to assess and quantify the different acidic contributions from each group. Analogously, hydrochloric acid (HCl) is used to evaluate the total basic surface groups. In all measurements, there are important parameters to ensure that titration results are comparable and standardised, such as the length of time for which samples are shaken, the CO_2 removal method used, and titration endpoint determination [179, 180]. Surface functionalities were studied using a titration procedure based on Boehm's method, allowing evaluation of basic and acidic functionalities.

4.15.1 Sample Preparation

A known mass of MRF sample (~0.5 g) was added to 25 mL of 0.1 M HCl (when evaluating basic functionalities), as shown in Figure 24:

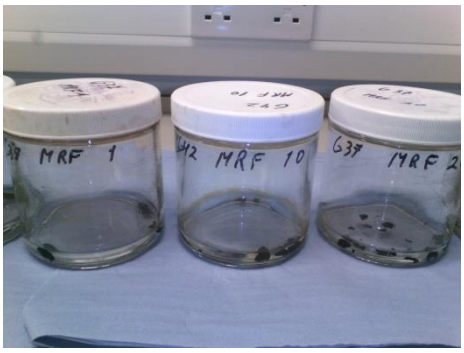

Figure 24: MRF xerogel samples in HCL solution 0.1 M

The samples were shaken for 3 d, followed by ~45-60 min of N_2 bubbling to remove CO_2 from the solution (Figure 25)

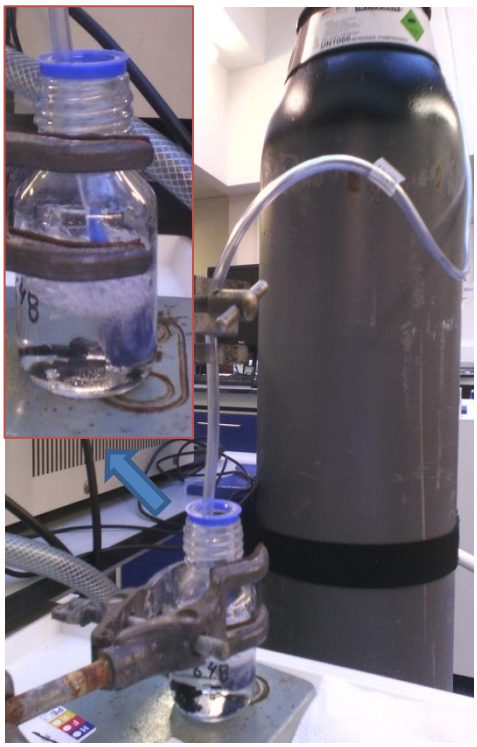

Figure 25: Nitrogen bubbling through HCl solution to remove CO_2 dissolved.

4.15.2 Sample Analysis

Two 10 mL aliquots were produced from each sample and they were direct titrated by 0.1 M NaOH (when evaluating basic functionalities). All titrations were performed at room temperature, and in two ways. Firstly, a graduated glass burette was used to measure the volume of NaOH used for titration by endpoint determination using methyl red, which changes colour at pH 6.2. For strong acid-base titrations, the titration curve is close to vertical around the equivalence point, therefore differences or excess of titrant should not be significant [179]. Secondly, a series of titration tests were performed using a syringe pump (Figure 26) set at a flow rate of 2 mL min^{-1} and the endpoint was determined by recording pH using a data logging programme.

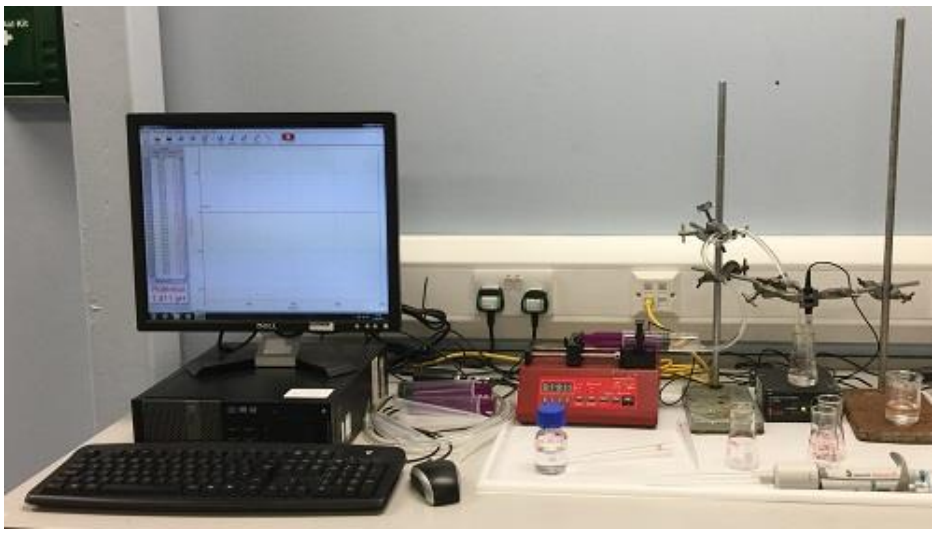

Figure 26: Syringe pump, flow controller and dedicated computer unit.

Moles of carbon surface functionalities were determined in all cases using the following equation:

$$n_{CSF} = [Sol] \cdot V_{Sol} - [Titrant] \cdot V_{Titrant} \cdot \frac{V_{Sol}}{V_{aliquot}} \qquad \text{Equation 60}$$

Where n_{CSF} represents the moles of basic/acidic functionalities on the surface of each MRF material reacted with the base (or acid) used in the solution; *[Sol]* and V_{Sol} are the concentration and volume of the solution, which represent the moles of base (or acid) available in the solution to react with the surface groups of the MRF; *[Titrant] and* $V_{Titratnt}$ are the concentration and volume of titrant used, which represent the moles of titrant that react with the remaining moles of base (or acid) from the solution after reaction with the sample, and $V_{aliquot}$ is the volume of the aliquot taken from the solution for titration.

4.16 Adsorption Capacity and Kinetics of CO_2 Adsorption (IGA)

An Intelligent Gravimetric Analyser (IGA) was used to perform adsorption capacity tests and to determine kinetics of adsorption. Both IGA models 001 and 003 supplied by Hiden Isochema Ltd (Figure 27) were used in this study. Gas adsorption tests were performed on selected MRF samples using N_2, CH_4, H_2 and CO_2, the latter gas being that of major interest in this work. Adsorption tests were conducted at two chosen temperatures (0 °C and 60 °C), with either static or dynamic flowing set ups.

The IGA equipment is formed of various components, including a highly sensitive microbalance, a controlled gas handling supply system which is fed from gas cylinders for static measurements or from a mass flow controller (MFC) for dynamic measurements, a computer unit which controls set ups and outputs from various control components, and a PC, which runs the bespoke software package (IGASwin) for interfacing with the IGA computer unit. Temperature is controlled either by furnaces or an external bath unit (thermo-stirrers), which can control temperature in a wide range according to the liquid used, i.e. water bath for temperatures ranging from 15 to ~75-85 °C or a mix of ethylene glycol –water for temperatures below ~10 to ~−30 °C. The temperature inside the reactor chamber was monitored using a Type K thermocouple (resolution of ± 1 °C). The thermo-stirrer unit controls the temperature at the set point by recirculating either heating or cooling fluids through a jacket surrounding the chamber. This system is automated control by a PC allowing a control of ±0.1 °C.

IGA internal components require a constant temperature of 55 °C to ensure both pressure and weight measurements are accurate. Internal temperature is measured by a platinum resistance thermometer (accuracy of 0.01 °C), and the temperature is controlled at the set point by an internal fan heater.

This equipment allows for precise measurement of adsorption uptake and kinetics as a result of the various gauges and controllers that comprise the IGA, permitting accurate control of processes parameters such as temperature, pressure and buoyancy corrections for mass measurements, thereby minimising errors.

Figure 27: **IGA models 003 supplied by Hiden Isochema Ltd, flow controller, bath for temperature control and dedicated computer unit.**

4.16.1 Sample Degassing and Analysis Procedure

Prior to introducing the MRF sample into the reactor chamber, it is important to ensure that both temperature and pressure inside the chamber are at atmospheric conditions, inert gas (such as N_2) or air (introduced through the air admit valve) can be used to filled the reactor chamber to atmospheric pressure. At this point, the chamber was unsealed and lowered to reach the hanging sample container. The sample bulb hangs from a tungsten wire attached at the top to the microbalance. Once the bulb was removed, it was cleaned and hung back from the wire and the chamber was replaced to prevent air currents from destabilising the balance. Once bulb weight was stabilised and sway reduced to minimum the empty pan reading was recording, effectively zeroing the mass reading. Then, the bulb was removed again from the wire to add approximately 55-60 mg of MRF sample, and the bulb is hung from the wire one last time to allow the weight to stabilise and any sway to reduce to ~zero. The reactor chamber was then sealed tight using a new copper gasket on the chamber flange.

All samples were degassed prior to analysis, aiming to remove moisture or any sample guest species from the surface of the samples. To do so, it was required to heat the samples to intermediate temperatures, typically 110-120 °C. A standard furnace, supplied by Hiden Isochema Ltd, was used at this stage, which was capable of maintaining temperatures between 100-500 °C (at a max ramp rate of 3 °C min^{-1}). Simultaneously, a rotary vacuum pump was started to lower the pressure below 20 mbar, whereafter a turbomolecular pump started to bring the vacuum to levels of 10^{-6}-10^{-7} mbar. Once this vacuum pressure was reached, a pressure isolation valve (PIV1) was opened, allowing the chamber to be exposed to the full vacuum force, valve PIV1 can only be opened at this low pressure otherwise equipment damage may occur. Outgassing, combined with heating conditions, was typically held for ~12-14 h, normally completed overnight. The mass profile was monitored continuously to observe when the mass loss level stabilised at a value lower than the initial weight of sample, typically this mass loss represented ~10% of the initial mass.

Once degassing was complete, the sample temperature was stabilised at the desired temperature for analysis by using a thermo-stirrer. Once the analysis temperature was achieved, the dry mass and zero pressure were recorded into the IGASwin software, and

PIV1 was closed. The pressure steps were subsequently entered into the software for isothermal adsorption and analysis started.

4.16.2 Analysis of Adsorption Capacity and Cycling

Performing single gas adsorption capacity tests is the simplest configuration possible. Pressure steps and temperature are selected for a cycle of adsorption-desorption. The IGASwin software allows the control parameter for the pressure to be set, which are directly fed from gas cylinders. It is also, required to set a minimum and maximum time for equilibration between pressure steps. MRF xerogels exhibited 'fast' kinetics of adsorption in most cases; therefore equilibration times were set to 30 min as a minimum and 180 min as a maximum. When performing a single isotherm analysis is set to 2 scans, while for cycling measurements, IGASwin allows a maximum number of adsorption-desorption scans of 1000 (500 cycles).

The software allows the continuous collection of both isothermal and kinetic data. Isothermal data includes time, weight, pressure, temperature and concentration for each pressure step of the isotherm. Similarly, kinetic data allows the collection of time, weight, pressure and temperature, recorded during the equilibration of each pressure step on the adsorption isotherm.

This data can be used to obtain the adsorption isotherm and the kinetics of adsorption by manually fitting the mass profile to different mass transfer models and therefore obtaining the corrected value of equilibrated mass for each step. Additionally, the software performs a correction of the measured weight for effect of the gas, a buoyancy correction, which is explained in detail in the Hiden IGA manual.

4.16.3 Adsorption Capacity set up Conditions

Single adsorption capacity tests were carried out for CO_2, N_2, H_2 and CH_4. CO_2 adsorption tests were carried out at both 0 °C and at 60 °C, controlled using an ethylene-glycol and a water bath, respectively. Pressure was increased from ~0-1000 mbar using steps of ~100 mbar, desorption was carried out using the same pressure steps in reverse. Similarly, N_2, H_2 and CH_4 adsorption tests were only carried out at 60 °C, with pressure steps, within ~0-1000 mbar, of ~100 mbar both for adsorption and desorption.

4.16.4 Cycling Adsorption set up Conditions

All cycling tests were performed in static mode at a temperature of 60 °C controlled with a water bath. In all cases, a 'wet' (before degassing) sample mass of ~55 mg was used. Pressure was increased to 1000 mbar at a ramp rate of 150 mbar, allowing the mass to equilibrate for 15 min. Subsequently, pressure was decreased to 50 mbar at the same ramp rate and equilibration was allowed for 15 min again.

4.16.5 Competitive Adsorption Analysis: Selectivity

A mixture of gases can be used by feeding the mass flow controller (MFC) from different cylinders. The MFC can be set at different flow rates and different compositions of gases. In the selectivity tests performed in this study, binary mixtures have been used, including CO_2+N_2, CO_2+CH_4 and CO_2+H_2.

Mass flow measurements usually require a mass spectrometer analyser connected to the outlet gas in order to measure the gas composition. Knowing the outlet composition of the gas stream and given that the inlet composition is known, the calculation of the gas adsorbed becomes straight forward. However, this equipment was not available in laboratory; therefore alternatives had to be considered.

It is important to notice that when performing flow measurements the recorded weight is affected by the flow of gas through the reaction chamber. The stress forces mentioned are defined for an object of any shape as:

$$F_D = C_D \frac{1}{2} \rho V^2 A_P \qquad \text{Equation 61}$$

Where F_D is drag force, ρ the density of the flow, V the velocity of the flow, and A_P is the projection of the solid object on a plane normal to the direction of the flow [188]. The drag forces around the sample bulb will be defined by its specific drag coefficient (C_D) as a function of the velocity of the flow and ultimately as a Reynolds number.

$$C_D = f(Re) \qquad \text{Equation 62}$$

This flow of gas will create stress forces onto the surface of the bulb, which will sway it away from the centre stable position. These forces onto the walls of the bulb depend on the velocity or regime of the flow: laminar or turbulent, being stronger as the flow

approaches a turbulent regime. The pressure inside the chamber is controlled by both inlet and outlet valves (Scheme 1). The adsorption isotherms were generally set to start from vacuum to 1 bar. Therefore, at lower pressure, the valves will be positioned in a more open state than at higher pressure, because in order to increase the pressure in the chamber valves will gradually close. Therefore, the effect of the stress forces onto the bulb will be larger at lower pressure, because the valves will be in a 'more' open position, which favours a 'more' turbulent regime (higher velocity) of the gas flowing through the chamber. On the contrary, as the pressure in the chamber is increased, the valves, particularly the outlet valve, will turn to a 'more' closed position, therefore, the velocity of the flow in the chamber will be reduced, tending to a 'more' laminar flow regime inside the chamber (Figure 28).

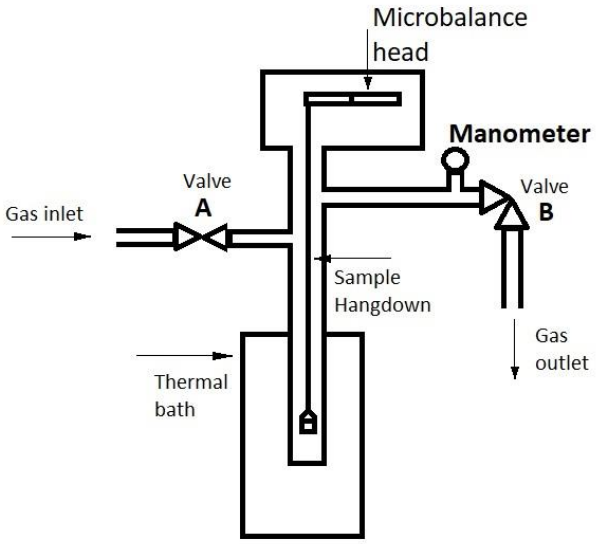

Scheme 1: IGA configuration scheme.

As a consequence, the stress forces will be weaker and therefore the weight measurements less affected. Measures of the flow conditions (laminar or turbulent) and stress forces onto the sample bulb surface were not practically possible for a number of reasons. The valves in the equipment were not fitted with connections for a manometer to read drop pressure along the reactor chamber, and, similarly, a lack of anemometer available in the laboratory to read the flow velocity inside the chamber, or the gas density for different mixtures of gases. Additionally, further experiments would have been required to define and measure the C_D coefficient for the sample bulb used. Moreover, this work exceeded the scope of the project.

A calibration method was developed to overcome this problem, in order to allow a correct measurement of the mass adsorbed when flow measurements were performed. This calibration requires a test that is, arbitrary, called a 'blanK'. This consists of using pieces of stainless steel (no adsorbent material) that weighs a similar mass as the typical mass of MRF sample used (~55-60 mg). The 'blank' tests were carried out at the same conditions used for the MRF sample, i.e. temperature, pressure steps and flow rate of gas.

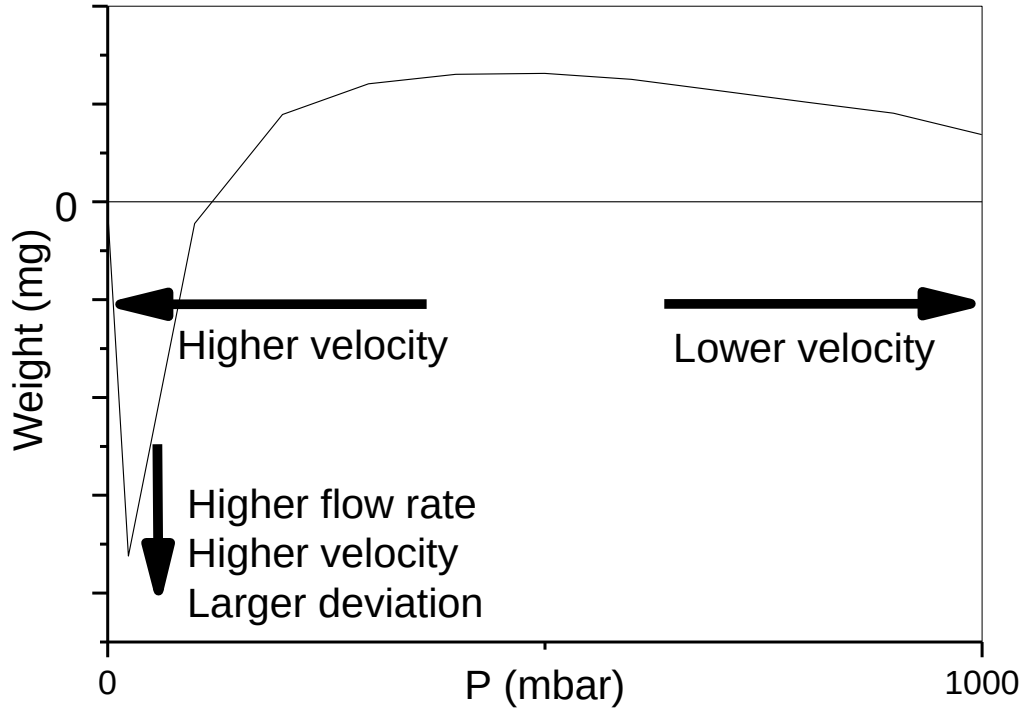

Figure 28: Flow regime inside the reactor chamber.

The calibration curve obtained looks like the example shown in Figure 28. At a given flow rate, the lower the pressure that is desired in the reactor chamber is, the larger will be the velocity of the gas stream through the chamber because the outlet valve is in a 'more' open position, while at higher pressure the opposite occurs. Additionally, as the flow rate is increased, so is the deviation from zero weight. Therefore, in this way a factor of deviation in weight is obtained for each pressure step used in this mode. This factor can be subtracted from the mass readings to obtain a corrected value of mass adsorbed, from which concentration can be derived. Different gases, with different molecular weights will result in different disruption of the mass readings. Therefore, a calibration 'blank' is required for each gas (or mixture of gases) used.

4.16.6 Calibration for a Mixture of CO_2-N_2

A calibration was obtained for a specific CO_2-N_2 mixture of 15 and 85 %, respectively. A 'blank' test was carried out at different flow rates to show the aforementioned influence of the flow rate on the mass readings. This calibration was carried out using a known mass of stainless steel, the weight is zeroed at the start of the test and considering this is a non-adsorbent material this mass should stay at zero. The 'blank' was performed under the same conditions used for the adsorption tests, i.e. 60 °C, pressure conditions of ~0-1000 mbar with ~100 mbar steps and a gas flow rate of 200 mL min^{-1}. The calibration curves obtained for this particular mixture are shown in Figure 29:

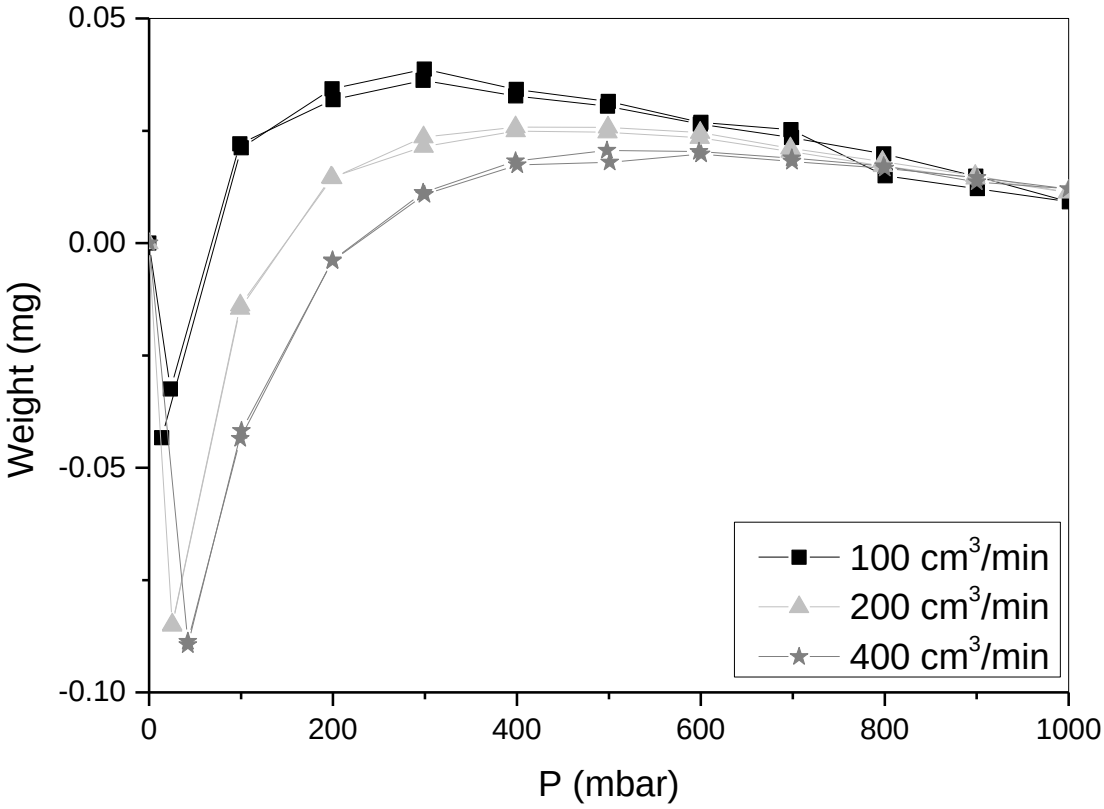

Figure 29: Calibration curve for a mixture of CO_2-N_2, 15 and 85 % respectively, at 60 °C.

4.16.7 Calibration for a Mixture of CO_2-CH_4

A calibration was obtained for a specific CO_2-CH_4 mixture of 15 and 85 %, respectively. As detailed above, the conditions used were the same as for the adsorption test, i.e. 60 °C, pressure conditions of ~0-1000 mbar with ~100 mbar steps and a gas flow rate of gas of 200 mL min^{-1}. The calibration curves obtained for this particular mixture are shown in Figure 30:

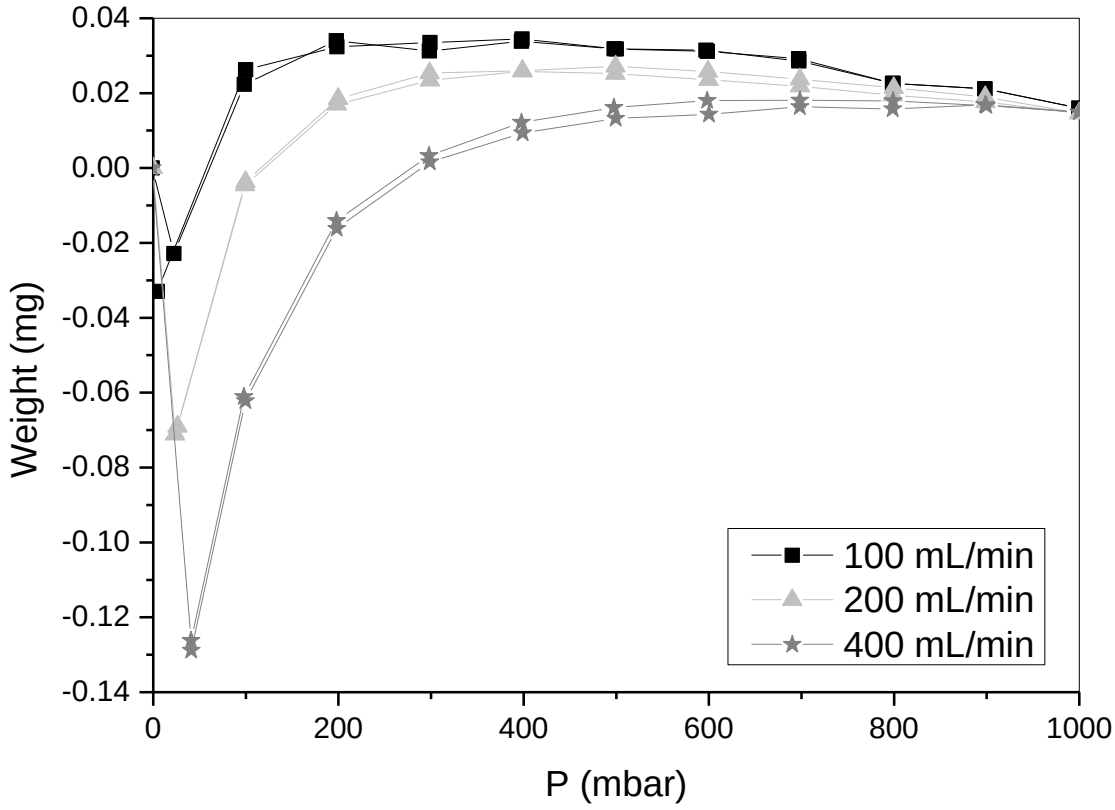

Figure 30: Calibration curve for a mixture of CO_2-CH_4, 15 and 85 % respectively, at 60 °C.

4.16.8 Calibration for a Mixture of CO_2-H_2

A calibration was obtained for a specific CO_2-CH_4 mixture of 15 and 85 %, respectively. As detailed above, the conditions used were the same as for the adsorption test, i.e. 60 °C, pressure conditions of ~0-1000 mbar with ~100 mbar steps and a gas flow rate of gas of 200 mL min^{-1}. The calibration curves obtained for this particular mixture are shown in

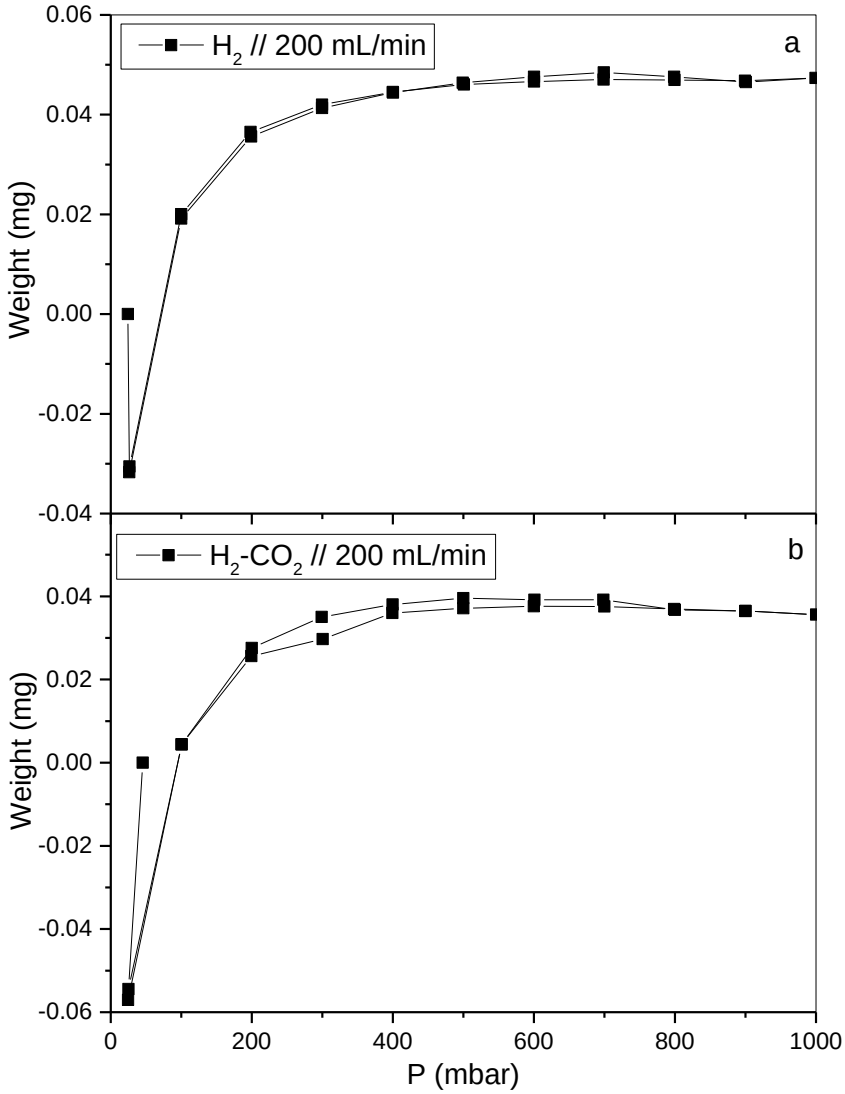

Figure 31: Calibration curve for (a) pure H2 and (b) mixture of CO_2-H_2, 15 and 85 % respectively, at 60 °C.

Chapter 5

Results Part I

5 Results Part I - Gel Synthesis

Melamine-Resorcinol-Formaldehyde (MRF) xerogels were synthesised following the procedure detailed in Chapter 4; synthesis parameters were varied within this method to determine their relative effects on xerogel production. Repeatability of synthesised gels was studied by comparing surface area and porosity measurements obtained by nitrogen adsorption analysis of a number of samples. All samples were analysed using elemental (CHN) analysis to assess the relative composition of the final xerogels. A number of samples were prepared by the standard synthesis method for resorcinol-formaldehyde gels. A total of 27 gels were produced, of which 20 samples were synthesised using the standard procedure, 3 samples were synthesised with a variation in the size of the container, and a further 4 samples were synthesised using a process that included stirring during the gelation step. Additionally, a total of 28 samples were synthesised using a modified procedure that involved preheating the solution; 24 samples were synthesised by preheating alone, while another 4 samples were produced with both preheating and a variation in container size. All 55 gels were prepared with an R/C ratio of 100, an R/F ratio of 0.5, using Na_2CO_3 as the catalyst and included variation of the percentage of melamine (1, 7, 10, 20, 30 or 40 %). The main aim of this section is to demonstrate that melamine is incorporated into the xerogels structure and that the synthesis procedure is repeatable. All the samples mentioned were characterized, however only results of selected MRF xerogels synthesised by the preheating method are shown in this chapter.

5.1 Gels Prepared by Standard Synthesis Method

All samples synthesised exhibited two layers of different colour for gels synthesised with [M] > 20%; therefore, changes in the synthesis procedure were studied in order to minimize this effect of phase separation-like behaviour. Firstly, for samples comprising the two layers of gel, the separate sections were examined by elemental (CHN) analysis in order to quantify whether there was a significant difference in the concentrations of the component species, which would be an indication of different chemical structures within the gel fractions. This analysis was primarily focussed on those samples where the colour difference between the layers was more evident. An unmodified RF gel, synthesised to act as a reference, was analysed along with samples from both layers of MRF 20, MRF 30 and MRF 40, designated top and bottom in the results presented in Table 4.

Table 4: Carbon, Hydrogen and Nitrogen (CHN) contents for MRF xerogels produced in this study.

MRF layer	C (% Found)	H (% Found)	N (% Found)	N (% Expected)
RF	57.32	4.56	Nil/Trace	-
	57.49	4.69	Nil/Trace	
MRF 20%	56.83	4.68	14.27	13.3
	56.86	4.78	14.10	
MRF 20% Top	56.82	4.65	14.22	13.3
	56.62	4.79	14.07	
MRF 20% Bottom	56.00	4.76	16.54	13.3
	56.14	4.60	16.93	
MRF 30% Top	52.56	4.47	19.40	19.1
	52.70	4.70	19.10	
MRF 30% Bottom	52.18	4.53	20.12	19.1
	52.37	4.75	20.31	
MRF 40% Top	50.10	4.49	24.87	26.6
	46.87	4.57	31.39	
MRF 40% Bottom	46.30	4.63	32.26	26.6
	47.45	4.37	29.89	

Based on the data shown in Table 4, it can be seen that nitrogen is successfully introduced into the gel structure, which confirms that the additive (melamine) is reacting to form the final gel. Consequently, nitrogen content in the gel increases as more additive is added to the solution. This is important because it demonstrates that the additive is still being incorporated into the structure for concentrations up to and including 40%. For [M] up to 30%, it is evident that the phase separation-like behaviour has little effect on the final composition of the final gel by fraction; however, 40% does suggest an experimental limit for solubilising the melamine adequately and this is manifest in the CHN results obtained (Table 4), where some differences between layers can be appreciated. There are a number of potential explanations for the colour difference between the two layers, such as i) a possible temperature gradient during gelation, which may imply a gradient of gelation velocities, ii) different particle sizes formed during aggregation, which could interact differently with incident light producing different colours, iii) a difference in the drying process given that the gel might still be partially wet, or iv) the additive may not dissolve homogeneously when the solution is prepared, however, this is less likely as the final compositions are similar for both fractions. It is important noting that as melamine content increases (particularly 40%) more it deviates from the nitrogen content expected. However, it must be noted that CHN analysis was performed on specific section taken from the samples. MRF xerogels can be expected to have some degree of heterogeneity. During

cluster aggregation those cluster containing more resorcinol would tend to stay on the upper layers given its lighter molecular weight compared to melamine.

The main aim of this section was to develop a method to produce homogeneous gels, that said, it is worth mentioning that difficulties in dissolving melamine in water at room temperature were observed. Chapman *et al.* reported mean solubilities for melamine in 100 g of H_2O of 0.324 g at 19.9 °C and 1.045 g at 49.8 °C [189]. Additionally, for an R/C ratio of 100, it was reported that cluster growth begins when the samples reached approximately 55 °C [103]; therefore, a pre-heating step, increasing the solution temperature to ~50 °C, was introduced to the synthetic procedure outlined previously. In this way, melamine solubility is increased, and cluster growth is not initiated until the sample is placed in the oven for gelation.

5.2 MRF Xerogel Synthesis Repeatability

Once the final synthetic procedure was established (Section 4.1.2), a number of MRF samples were prepared, using melamine concentrations of 1%, 7%, 10% and 20 % to allow direct comparison between the final xerogels on the basis of [M]. The synthetic procedure is required to produce consistent results between different batches of material in order to be validated, therefore, repeatability from one batch to another of the same type of gel. Figure 32 shows the relationship between nitrogen included in the synthetic procedure and adsorption behaviour, which should change with [M] but also remain consistent across batches.

The isotherms shown in Figure 32*a*, *b*, *c*, *d* and *f* can be classified as Type IV according to the IUPAC classification system [147] (Section 3.2.3); these isotherms exhibit a characteristic hysteresis loop, which is associated with capillary condensation within mesopores. At low relative pressure, these isotherms follow the same path as a Type II, which is due to the transition from monolayer to multilayer adsorption. There is a clear trend in the shape of the hysteresis loop between the isotherms shown in Figure 32a to f; Figure 32a for the unmodified RF material shows a Type H2 hysteresis loop (Section 3.2.3.2), and the same observation can be made for the isotherms obtained for MRF 1%, MRF 7% and MRF 10% (Figure 32b-d); while isotherms obtained for MRF 20% exhibit Type H1 hysteresis loop. The trend observed for these samples suggests that, as melamine content increases the closure point of the hysteresis loop occurs at higher relative pressures, while, at the same time, the hysteresis loop gradually narrows toward Type H1, as observed for MRF 20%.

Hysteresis loops provide information on the pore size and distribution of the material; however, there are anomalies that can occur within these profiles. For example, the closure point of the loop occurs at a given relative pressure (and temperature) for a known adsorptive, and represents a characteristic feature of the adsorptive, which is generally independent of the nature of the porous adsorbent e.g. for N_2 adsorption at -196 °C this point occurs at P/P_O ~0.42 [146]. This is evident for the RF and MRF 1% samples shown in Figure 32a and b; it is less clear for MRF 7% and is potentially slightly increased from this value. It can be seen that the closure point of the hysteresis loop then occurs at higher relative pressures for both MRF 10% and MRF 20%, indicating that the observed behaviour is more characteristic of the material than the adsorptive.

Type H1 hysteresis loops are usually related to compact and uniform spheres distributed in a regular array, therefore, materials exhibiting such behaviour should tend to have narrow pore size distributions; while Type H2 hysteresis loops are indicative of more complicated systems, they can be associated with a number of factors:

- Difference of mechanism for condensation and evaporation process.
- The pore shape is usually referred to as 'ink bottle' (narrow neck and wide body).
- The network distribution may also affect the shape of the hysteresis loop, which can occurs when wide pores are connected to the surface by narrow necks. During desorption, the neck of these wide pores will fully desorb before the adsorbate from wide pores can desorb (percolation). For this reason, the desorption branch of isotherms exhibit information about the size of the pores neck.

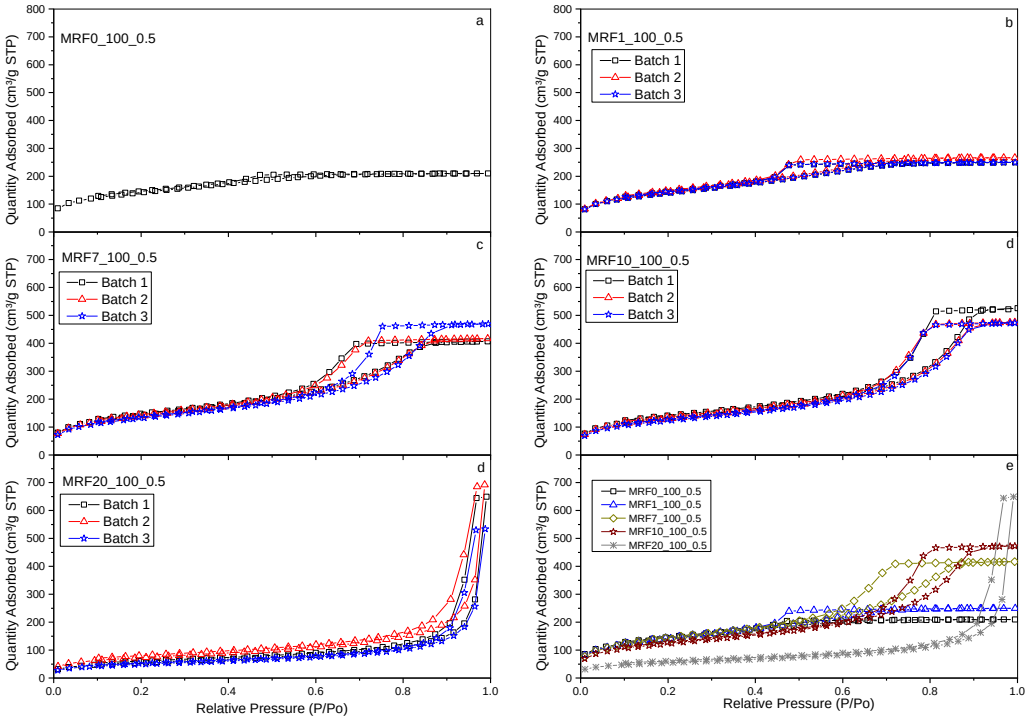

Figure 32: Nitrogen adsorption isotherms for (a) RF xerogel, (b) 1% MRF xerogel, (c) 7% MRF xerogel, (d) 10% MRF xerogel, (e) 20% MRF xerogel and (f) comparison of representative isotherms for each concentration.

The data plotted in Figure 33 shows the pore size distributions for all materials analysed and suggests that average pore size increases as [M] is increased, a similar trend is also observed for pore volume. It can be seen that the Gaussian distribution widens as [M] increases, which can be attributed to differences in pore sizes within the network leading to a less uniform gel in terms of pore distribution. This, at the same time, is in agreement with experimental observations where an increase in additive content produces less uniform gels [190].

There are other important parameters that can be quantified from nitrogen adsorption, such as surface area, micropore area, pore size, pore volume and micropore volume. The isotherm data obtained for the samples studied was analysed using BET theory to determine surface area and pore volume Equation 30 and 31 were used in these calculations, and the cross sectional area of nitrogen was taken as 1.62×10^{-19} m^2/molecule. The general trends observed are shown in Figure 34 and are summarised as:

- Increasing N_2 content suggest a decrease in surface area; therefore, as expected, pore size and pore volume increase.
- All gels produced in this study show average pore sizes in mesoporous range.

Table 5: Surface area and pore volume data obtained from BET analysis and recalculated values.

Gel	MRF 1%		MRF 7%	
	SA (m^2/g)	pV (cm^3/g)	SA (m^2/g)	pV (cm^3/g)
Batch 1	502.9	0.386	508.9	0.629
Batch 2	521.0	0.412	496.7	0.645
Batch 3	460.0	0.340	474.5	0.726
Gel	**MRF 10%**		**MRF 20%**	
	SA (m^2/g)	pV (cm^3/g)	SA (m^2/g)	pV(cm^3/g)
Batch 1	485.6	0.813	196.2	1.004
Batch 2	469.9	0.735	264.0	1.071
Batch 3	445.4	0.732	177.1	0.826

The data presented in Figure 34 suggest a relationship between different textural properties, i.e. surface area, average pore diameter or pore volume (Figure 34a, b and e), and gel composition. The formation of the gel structure and, hence, the final material has been shown to be highly affected by R/C and R/F, as discussed above, while, in this study, resorcinol is also substituted by melamine in the synthetic matrix. Therefore, the decision was taken to study the three main synthesis variables, namely R/C, R/F and [M], in greater depth, with an overall aim to correlate the effect of compositional changes on xerogel textural properties.

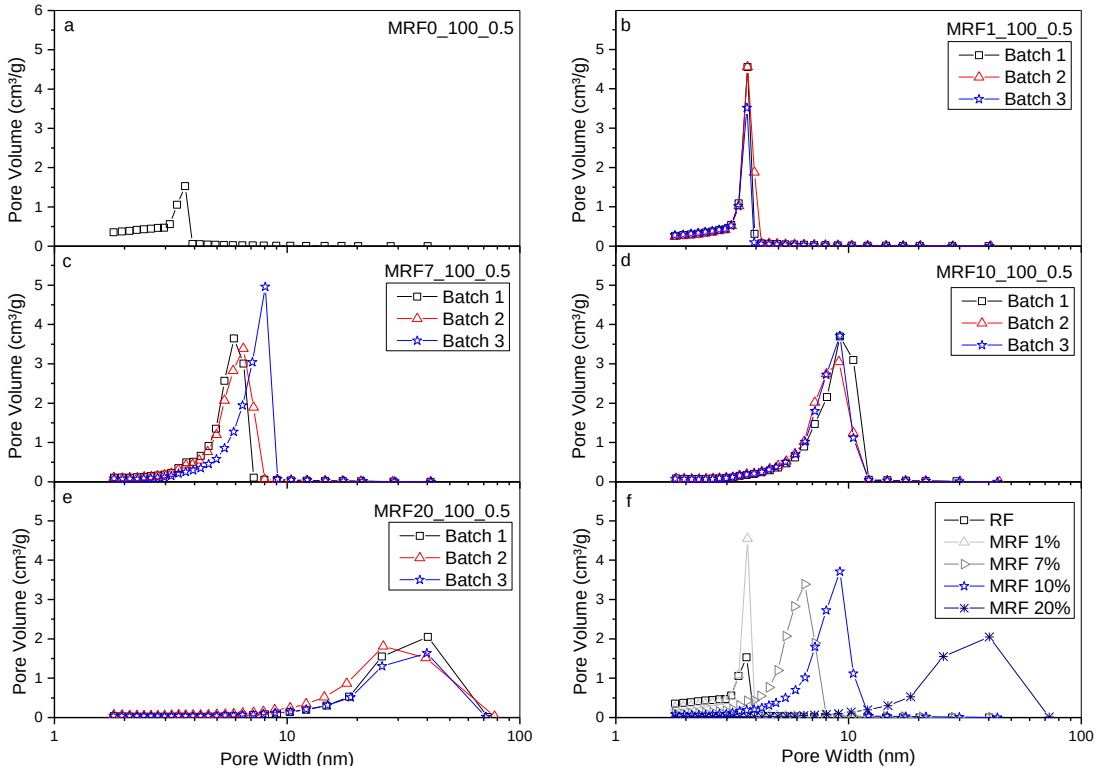

Figure 33: **Pore Size distribution for (a) RF xerogel, (b) 1% MRF xerogel, (c) 7% MRF xerogel, (d) 10% MRF xerogel, (e) 20% MRF xerogel and (f) comparison of representative pore size distributions for each concentration.**

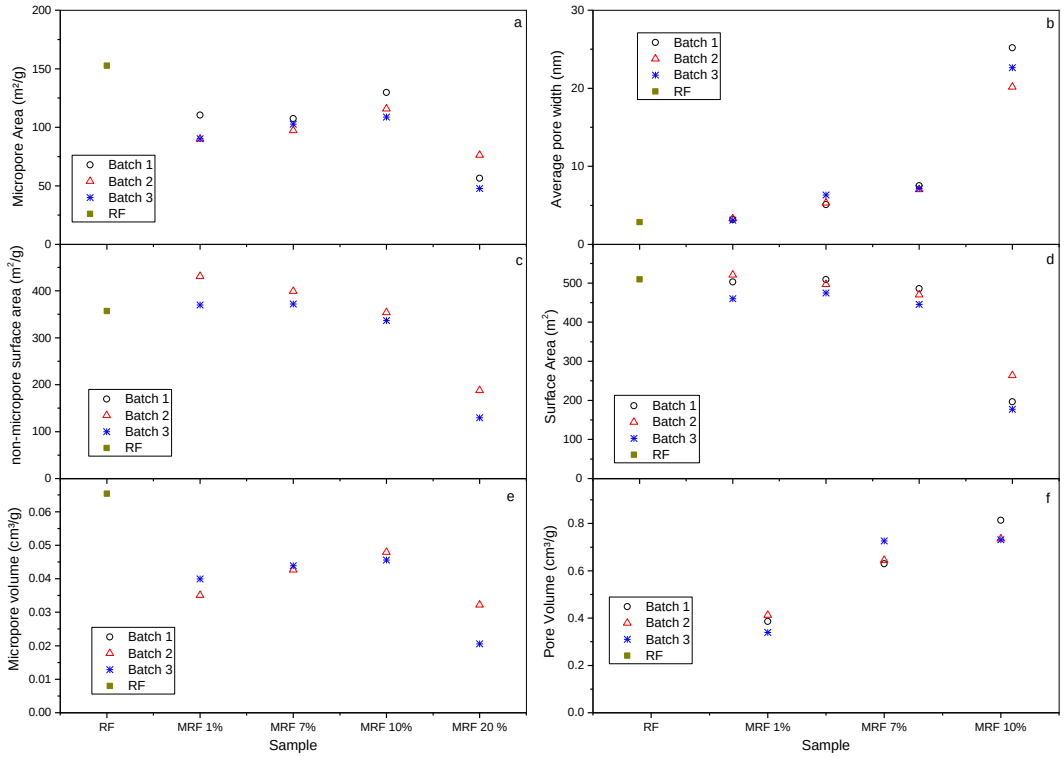

Figure 34: **(a) Surface area, (b) pore Volume, (c) micropore area, (d) micropore volume, (e) average pore width and (f) non-micropore surface area. Parameters obtained by BET analysis for MRF 1%, MRF 7%, MRF 10% and MRF 20%.**

5.3 Key Findings

It was found that the pre-heating synthesis method is more suitable for production of MRF xerogels. Additionally, it was demonstrated that melamine is successfully incorporated into the structure of MRF xerogels, however, as this content increases heterogeneities within the structure are more probable. Nevertheless, it must be noted that repeatability, up to a high degree, is achievable, as observed in Figure 32 and 33. In a related topic, it would be important to quantify the statistical variation within batches of MRF xerogels, this is a key parameter for industrial production of MRF xerogels, however, this exceeds the scope the project.

Chapter 6
Results Part II

6 Results Part II – Study of Synthesis Variables

This chapter focuses on the impact of varying selected synthesis variables (as outlined in Section 1.8.7) on final xerogel structural properties; the main emphasis here is on three variables, namely resorcinol/catalyst molar ratio (R/C), resorcinol/ formaldehyde molar ratio (R/F), and melamine content [M].

6.1 Effect of R/C, R/F and M

The effect of varying R/F in unmodified gels was studied, and in a related investigation the impact of incorporating nitrogen containing additives was also probed. To achieve this, the ratio of resorcinol to additive (e.g. melamine) was varied and the effect on final gel structure was studied. This means that both variation in R/F, and the role of substituting resorcinol again with a change in formaldehyde are investigated. Thus, the interplay between these three variables was investigated and the following table shows the levels chosen for each variable:

Table 6: MRF synthesis variables studied in this work, R/C ratio, R/F ratio and [M], and levels selected for each.

R/C	50	100	200	400		
R/F	0.25	0.5	0.75	1.0		
[M] %	0	1	10	20	30	40

There are a resulting 100 possible recipes (see Section 4.2 and Appendix K) for the levels chosen for these three variables, hence, all other synthesis variables, i.e. solids content, catalyst, ageing time, solvent exchange and drying method, were kept constant throughout the analysis. The gels produced by these recipes were analysed using several characterization techniques, with the aim of understanding the impact of these variables on final xerogel properties, such as micropore volume and surface area.

A Micromeretics ASAP 2420 system was used to obtain surface areas and porosities by N_2 adsorption/desorption equilibrium measurements at ~-196 °C using ~0.5 g of sample. Each sample was degassed, at ~120 °C for 120 min, prior to analysis by N_2 adsorption. Surface areas were calculated by applying Brunauer-Emmett-Teller (BET) theory [162] combined with the Rouquerol correction for application of BET theory to microporous materials [169]. Pore volumes were calculated from the equilibrium quantities of N_2 adsorbed at ~0.98 bar (i.e. the saturation vapour pressure of N_2 at -196 °C). Pore size distributions and average pore sizes were obtained by application of the Barret-Joyner-

Halenda (BJH) method [163], while the t-plot method [166] was used to calculate micropore volumes and micropore surface areas of all samples. Elemental analysis was used to quantify the concentration of carbon, nitrogen and hydrogen; and all samples were analysed by Fourier transform infrared spectroscopy (FTIR) for surface moiety characterization.

It is important noting that 38 gels failed during gelation due to reasons that can be attributed to the concentration of monomers, these gels are summarised in Tables 126 and 127 in Appendix K. The failing during gelation can be attributed to two main reasons, firstly MF fails at the conditions used here and, secondly, gels with higher R/F (0.75 and 1.0) fail more often during gelation due to a lack of formaldehyde available, this is explained in more detailed during this chapter.

6.2 Surface Characterization by Scanning Electron Microscopy

A selected set of material were tested by SEM, result are shown in Figure 35 and 36.

The pictures of MRF0_50_0.75, MRF10_50_0.75 and MRF20_50_0.75 (Figure 35) show that as melamine concentration increases the particles size is larger, suggesting an increase in the size of voids between them, which consequently increases pore size. Similar results were observed for MRF0_50_0.5, MRF1_50_0.5, MRF10_50_0.5 and MRF20_50_0.5 (Figure 36). Pores and channels seem to be “better connected” as melamine is incorporated, which may help the gas diffusion through the material and enhance the adsorption capacity. However, in order to fully characterise the textural properties at the microscopic level further analysis are required, as detailed in the following sections.

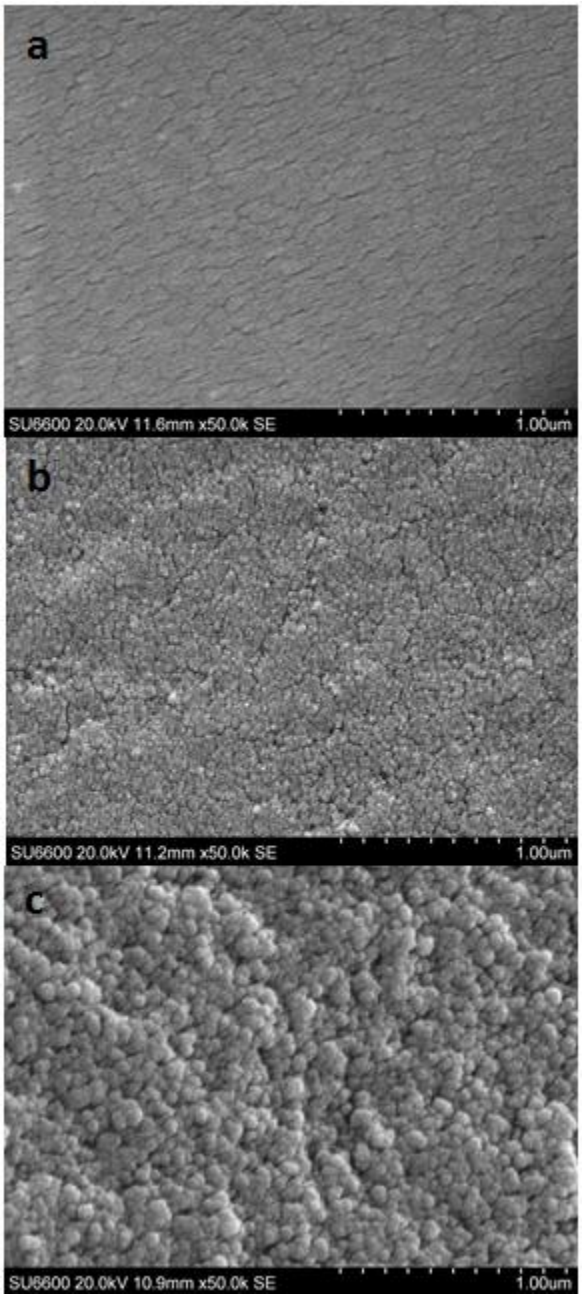

Figure 35: Scanning electron microscopy results at 50.0K SE for a) MRF0_50_0.75, b) MRF10_50_0.75 and c) MRF20_50_0.75.

Pictures at higher magnifications had poor resolution probably because of the interactions of the electron beam with the surface charges. However, it is important to note the limitations of this technique due to the localization of the analysis. Pictures at similar magnifications of different point of a surface may differ as a consequence of the heterogeneity of the surface, position of the surface with respect to the electron beam and coating.

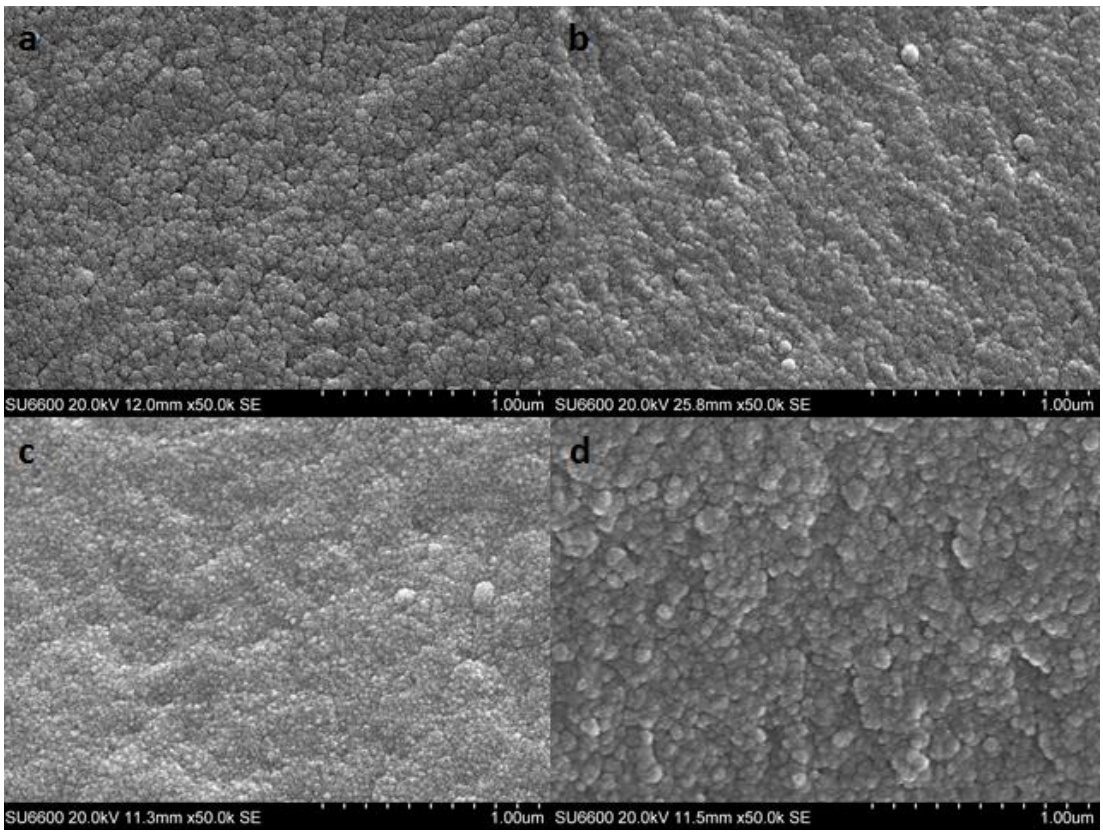

Figure 36: Scanning electron microscopy results at 50.0K SE for a) MRF0_50_0.5, b) MRF1_50_0.5, c) MRF10_50_0.5 and d) MRF20_50_0.5.

6.3 N_2 Adsorption Isotherms and Pore Size Distributions

All samples were studied by N_2 adsorption using the BET model, as explained in chapter 3 providing surface areas and porosities; sorption isotherms and pore size distributions obtained are shown in Figure 37 to 42. In general, increasing R/C reduces gel adsorption capacity significantly. Increasing [M] also decreases adsorption capacity; however, as R/C is increased the onset of this reduction occurs at lower [M], suggesting that, for given R/C (and R/F), there is a maximum level of [M] that can be successfully incorporated into the gel matrix before the pore size becomes so large that surface area decreases drastically and, therefore, adsorption capacity is reduced significantly.

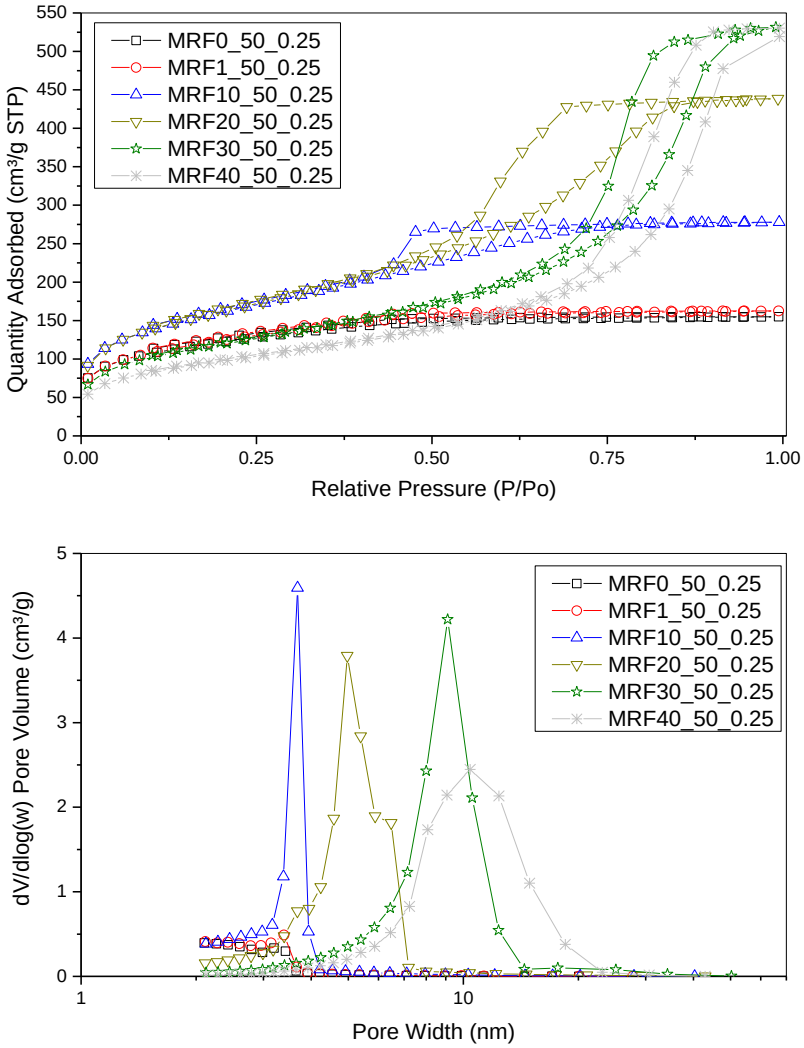

Figure 37: (a) N_2 adsorption isotherms and (b) pore size distributions for MRF xerogels synthesised in this study using R/C 50, R/F 0.25, and [M] 0-40 w/w%.

N_2 adsorption capacities for xerogels produced with R/F 0.25 and R/C 50 increases continuously with increasing [M] until 30 w/w% of melamine, and MRF40_50_0.25 shows an uptake similar to that of MRF30_50_0.25 (Figure 37) where a plateau is reached. By contrast, the N_2 adsorption capacity for MRF40_50_0.5 shows a significant reduction with the increase of [M] from 30 to 40 w/w% (Figure 38).

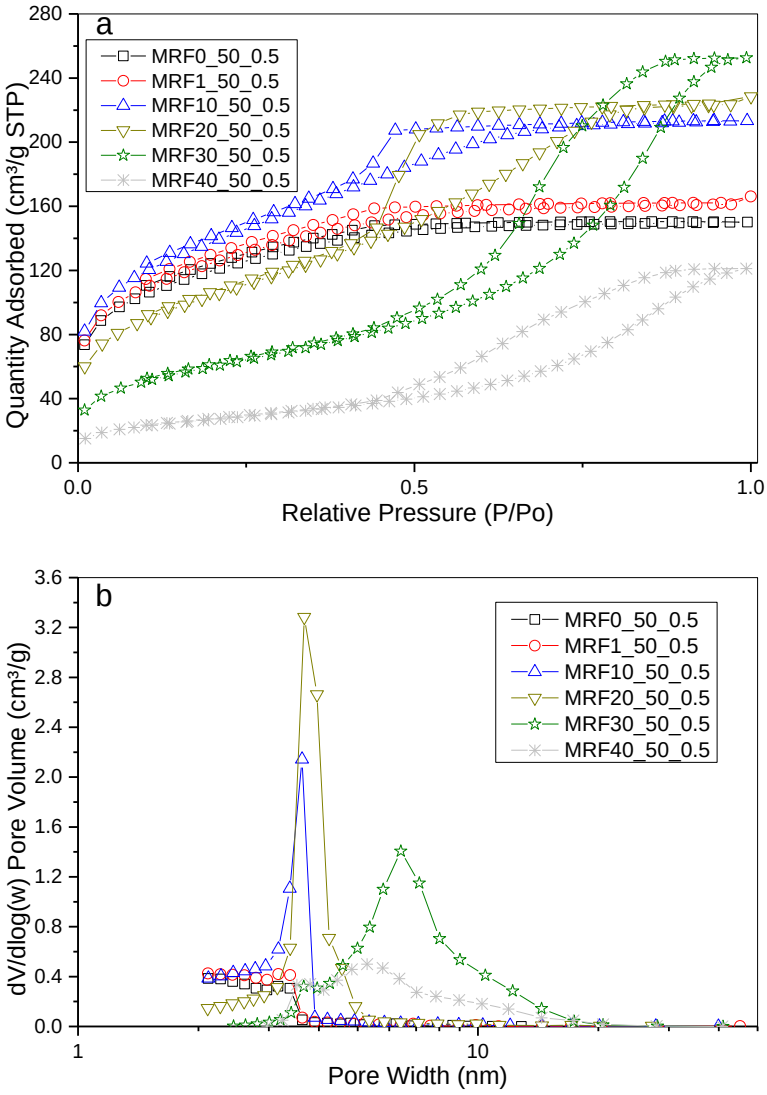

Figure 38: **(a) N_2 adsorption isotherms and (b) pore size distributions for MRF xerogels synthesised in this study using R/C 50, R/F 0.5, and [M] 0-40 w/w%.**

The isotherms obtained can be classified as Type IV, indicative of mesoporous adsorbents; initial monolayer coverage and micropore filling are followed by multilayer adsorption and capillary condensation in pores. At higher pressures, final saturation is characterized by a plateau of variable length, or sometimes seen only as a point of inflexion. The phenomenon of capillary condensation is often accompanied by a hysteresis loop, here observed in most cases, which occurs when the pores are wider than a critical width; however, it is also dependent on the adsorption system and temperature at which the test is carried out. The closure point of the hysteresis loop, in the case of N_2 adsorption at -196 °C occurs for those pores wider than 4 nm [147]. This is confirmed here for MRF0_50_0.25 and MRF1_50_0.25, with average pore sizes of 2.4 and 2.5 nm, respectively (Figure 37);

isotherms for these gels exhibit very small deviation between the adsorption and desorption branches, and it can be said that their hysteresis loops are not significantly open. A similar observation can be made for MRF0_50_0.5 (pore size of 2.4 nm) and MRF1_50_0.5 (pore size of 2.6 nm), where only the latter shows a hysteresis loop (Figure 38).

The hysteresis loops observed can be classified as Type H1 and H2 depending on the synthetic parameters used; at low [M], the hysteresis loops tend to be Type H2(a), which is generally the case for MRF0 and MRF1, before shifting to Type H2(b) for MRF10 and, finally, to Type H1 for MRF20, MRF30 and MRF40. According to the recent IUPAC technical report [147], hysteresis loops of Type H2 indicate complex structures, in which network effects become important, the steep desorption branch is associated with pore-blocking or percolation in narrow pore necks, or even to cavitation due to the effect of lowering the pressure; this, therefore, suggests ink bottle like pores (narrow neck and wide body). Type H1 loops, on the other hand, are often observed for ordered mesoporous carbons [147], and this suggests a transition from pores with restricted access to open mesopores as [M] increases, potentially the result of a decrease in crosslinking as resorcinol is substituted by melamine.

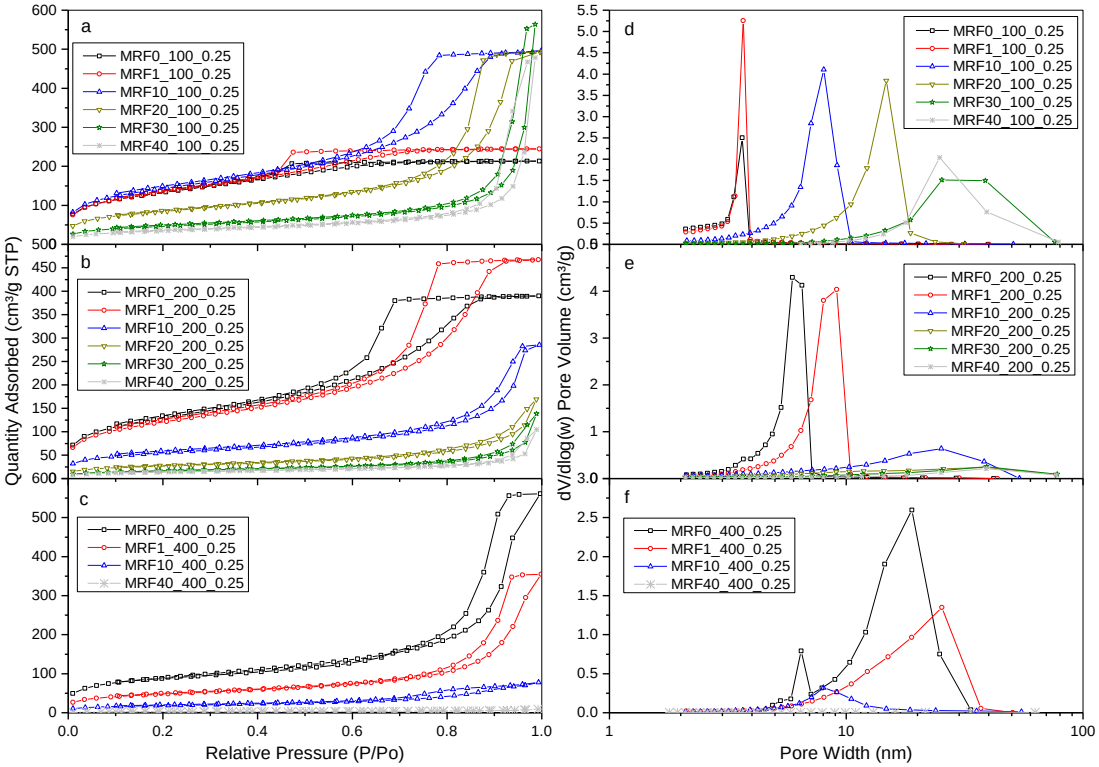

Figure 39: **(a) N_2 adsorption isotherms and (d) pore size distributions for MRF xerogels synthesised in this study using R/C 100, R/F 0.25, and [M] 0-40 w/w%; (b) N_2 adsorption isotherms and (e) pore size distributions for MRF xerogels synthesised in this study using R/C 200, R/F 0.25, and [M] 0-40 w/w%; (c) N_2 adsorption isotherms and (f) pore size distributions for MRF xerogels synthesised in this study using R/C 400, R/F 0.25, and [M] 0-40 w/w%.**

There is a caveat in this sequence of transition between hysteresis loops, as it is not seen for all sample suites; the reason being that, as R/F is increased, this change is delayed, therefore, for higher R/F, only the change from H2(a) to H2(b) is observed, likely due to the lack of F and, again, the associated impact this has on crosslinking of the materials. Pore widening is evident across all R/C values as [M] increases; however, as R/C increases, the shift from H2(a) to H2(b) loop occurs at lower [M], which indicates that the influence of [M] is greater when less catalyst is present in the system (Figure 39 to 40).

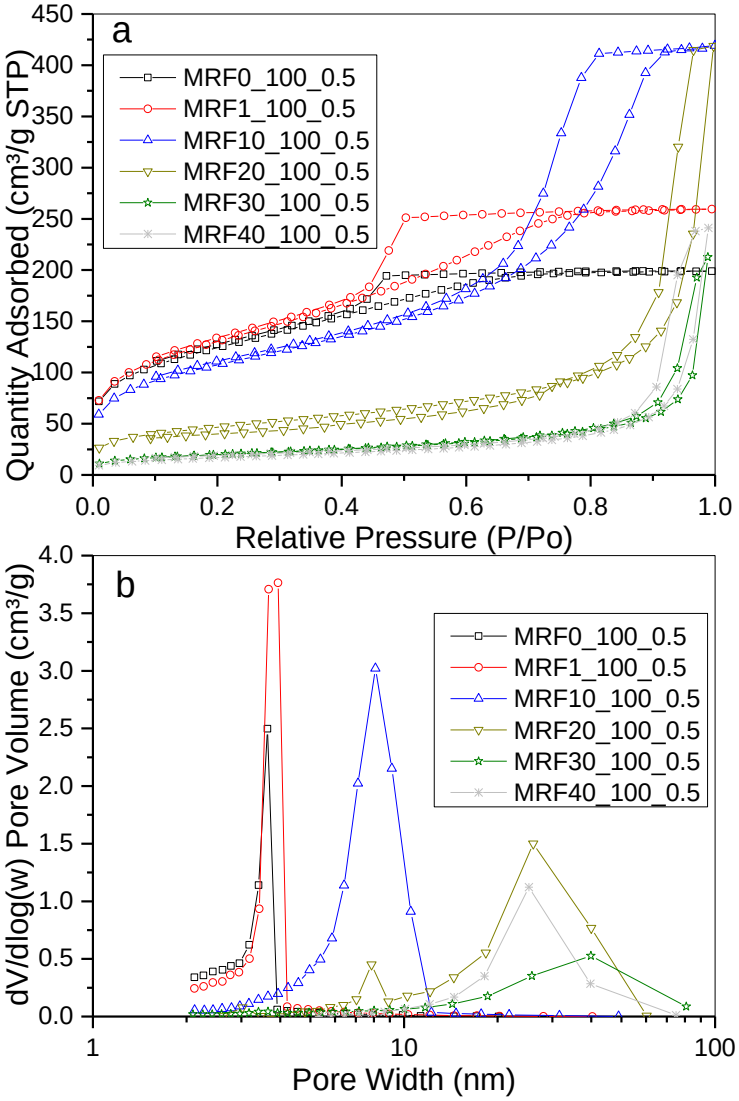

Figure 40: **(a) N_2 adsorption isotherms and (b) pore size distributions for MRF xerogels synthesised in this study using R/C 100, R/F 0.5, and [M] 0-40 w/w%.**

As [M] increases, the cured gel obtained (after gelation) becomes softer, similarly, synthesis with higher R/C results in softer xerogels. The increase of R/C results in wider pores, which is in agreement with previous observations [104, 111], similarly, as [M] is increased, for given R/F, the pore size becomes larger, reducing the surface area while simultaneously increasing the pore volume, which results in higher N_2 uptake. However, while the trend described is a general one, it is also observed that surface area and N_2 uptake increase with [M] up to a maximum, usually for MRF10 and MRF20 or MRF30 for specific low R/C and R/F, and a reduction of these parameters for higher [M]. Instead, the pore size tends to become

larger as [M] increases and, therefore, pore volume is observed to increase for most of the series.

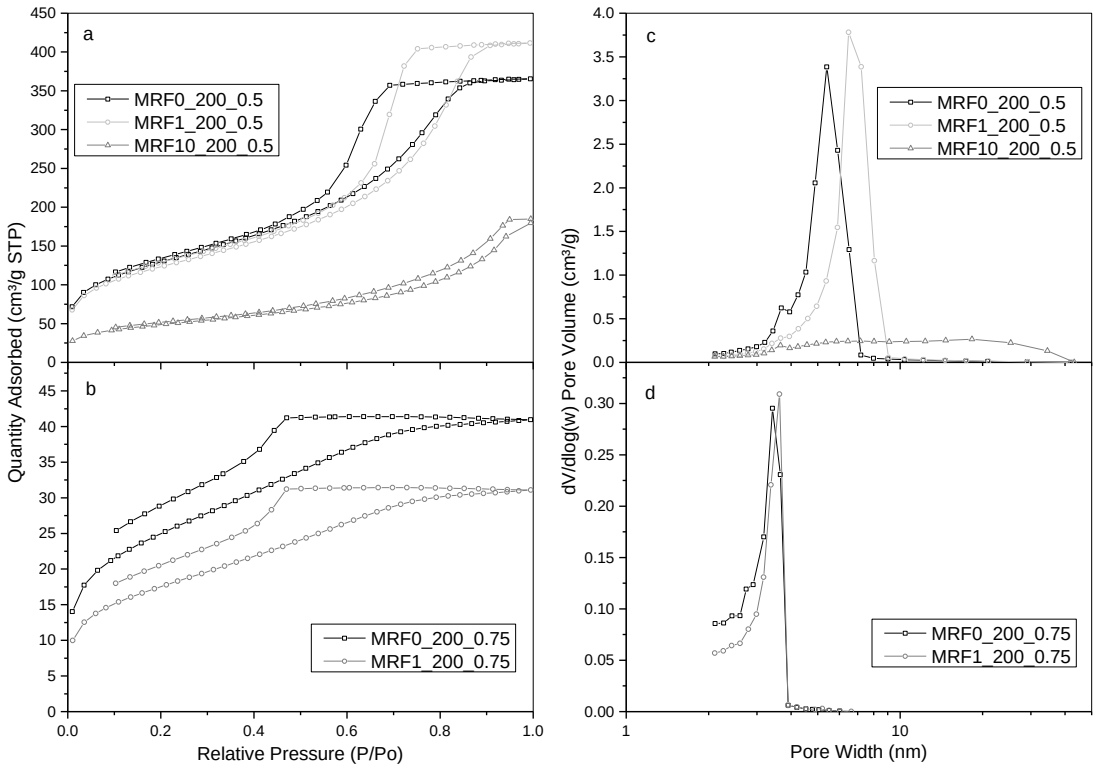

Figure 41: (a) N_2 adsorption isotherms and (c) pore size distributions for MRF xerogels synthesised in this study using R/C 200, R/F 0.5 and [M] 0-10 w/w%; (b) N_2 adsorption isotherms and (d) pore size distributions for MRF xerogels synthesised using R/C 200, R/F 0.75, and [M] 0-1 w/w%.

It is important to differentiate the trends previously stated for low and high R/C and R/F. For low R/C (50), maximum surface area and N_2 uptake are observed for MRF20 and MRF30, respectively (Figure 37); while MRF40 shows a similar N_2 uptake as MRF30, despite the lower surface area (Section 6.7). Comparing N_2 adsorption isotherms obtained for R/C 50 and 100, with constant R/F (0.25) (Figure 37 and 39), it is observed that the maximum surface area is now obtained for MRF10 (for R/C 100) and the larger N_2 uptake is obtained with MRF30, with a bigger fall between this and MRF40, suggesting a drop in capacity as [M] is further increased. A significant increase in pore size is also observed, suggesting both an effect of increasing R/C on this parameter but also stronger effect of increasing [M] given that, for MRF20 (R/C=50 and R/F=0.25), the average pore size obtained is 4.6 nm (Figure 37) and for MRF20 (R/C=100 and R/F=0.25) it is 11.2 nm (Figure 39) while, for the isolated effect of R/C, pore size of MRF0 increases only slightly from 2.4 nm to 2.9 nm.

In contrast, increasing R/F does not result in a significant change in pore size, while a decrease in N_2 adsorption capacity is observed, which is more of an impact at higher [M], as seen Figure 39 and 40.

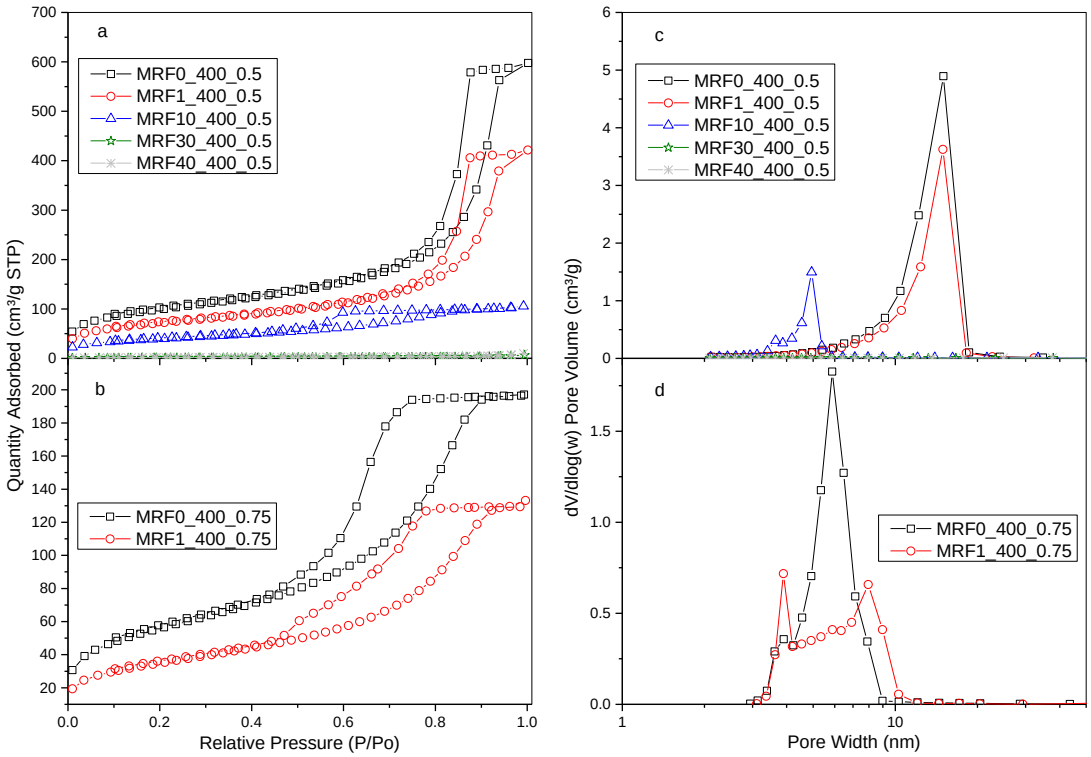

Figure 42: (a) N_2 adsorption isotherms and (c) pore size distributions for MRF xerogels synthesised in this study using R/C 400, R/F 0.5 and [M] 0-40 w/w%; (b) N_2 adsorption isotherms and (d) pore size distributions for MRF xerogels synthesised using R/C 400, R/F 0.75, and [M] 0-1 w/w%.

As R/C is increased (200 and 400) gelation fails more often at higher [M], this is attributed to the effect of less catalyst in solution, which results in a fewer activated resorcinol anions, combined with weaker crosslinking as [M] increases. This effect is reinforced as R/F is increased as a consequence of fewer F molecules being available in solution for reaction.

6.4 Elemental Analysis: Carbon, Hydrogen and Nitrogen Contents.

Results obtained for CHN analysis were as expected. Due to their chemical compositions (Table 7), both resorcinol and melamine contribute significantly to the total carbon content of each sample but the overall relative contributions vary due to their individual carbon proportions (carbon contents of 65.5% and 28.6%, respectively).

Table 7: **Carbon, hydrogen, nitrogen and oxygen contents of resorcinol, melamine and formaldehyde.**

	Resorcinol ($C_6H_6O_2$)	Melamine ($C_3H_6N_6$)	Formaldehyde (CH_2O)
C (w/w %)	65.45	28.57	40
H (w/w %)	5.49	4.79	6.71
N (w/w %)	-	66.64	-
O (w/w %)	29.06	-	53.29

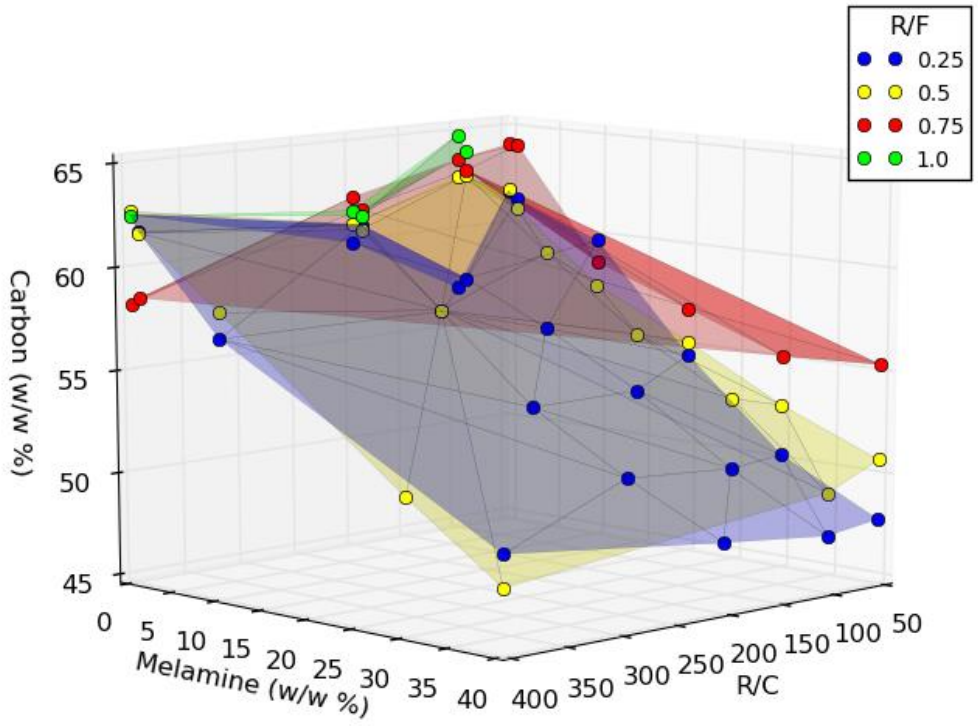

Figure 43: **Elemental composition (w/w %) of carbon for MRF xerogels synthesised in this study using R/C 50-400, R/F 0.25-1.0, and [M] 0- 40 w/w%.**

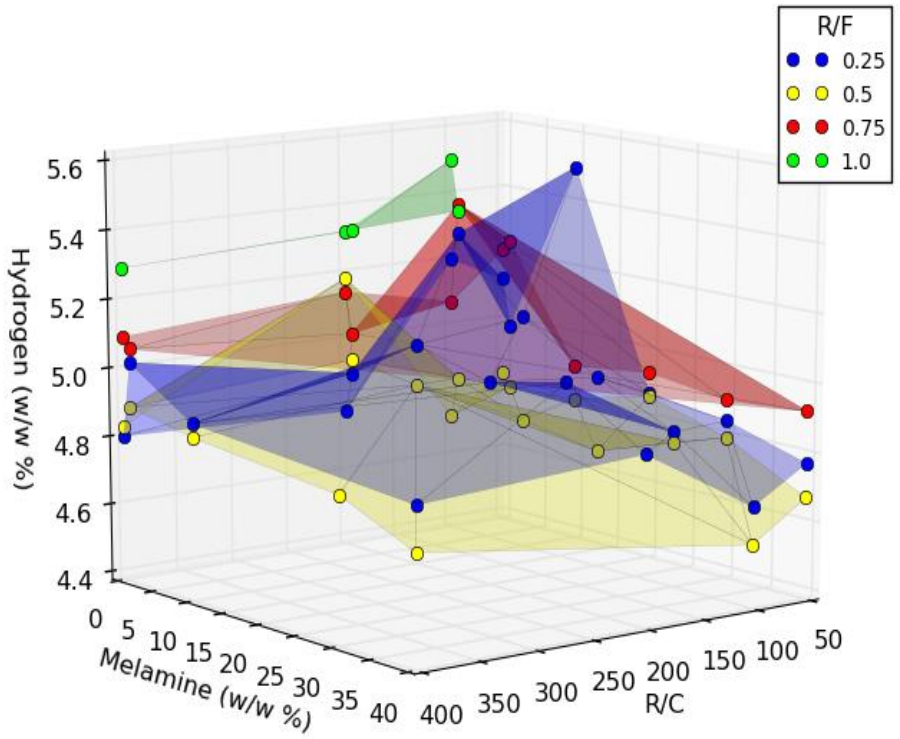

Figure 44: **Elemental composition (w/w %) of hydrogen for MRF xerogels synthesised in this study using R/C 50-400, R/F 0.25-1.0, and [M] 0- 40 w/w%.**

Therefore, as resorcinol is substituted by melamine, the carbon content decreases (Figure 43), while hydrogen content is not significantly different for resorcinol and melamine, only a small decrease is observed as melamine substitutes resorcinol (Figure 44).

Melamine is composed of 66.64% nitrogen, therefore, the nitrogen content of the synthesised gels increases linearly with [M] (Figure 45); these results are confirmed by CHN analysis for all samples produced in this study.

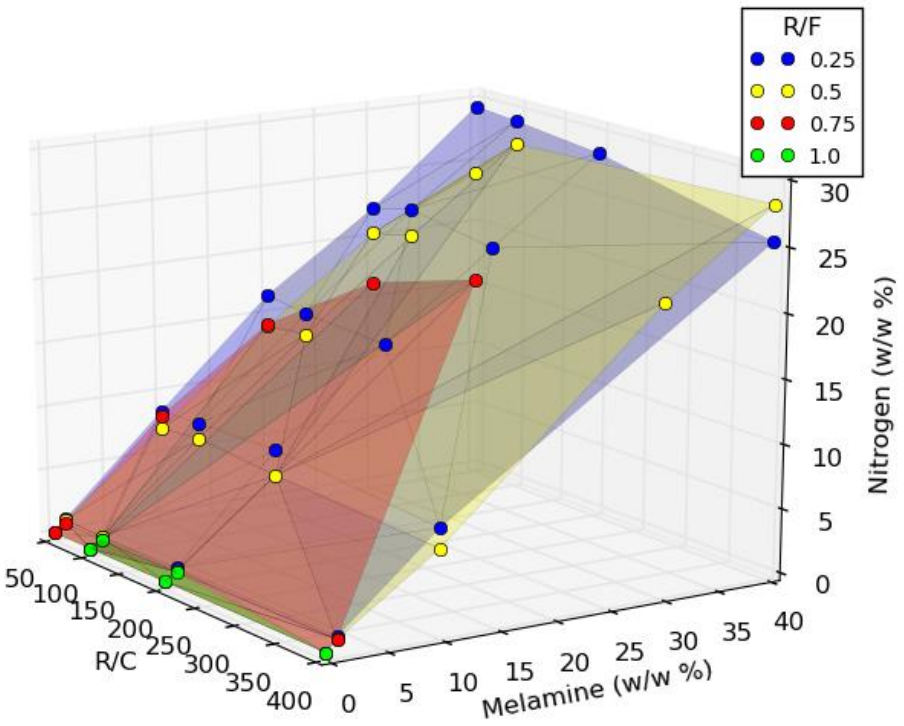

Figure 45: **Elemental composition (w/w %) of nitrogen for MRF xerogels synthesised in this study using R/C 50-400; R/F 0.25-1, and [M] 0-40 w/w%.**

6.5 Initial pH of Solution

As outlined in Chapter 1, initial solution pH can markedly affect gel formation; in this study the pH tends to decrease as R/C is increased, as a result of decreased basic catalyst concentration, and also tends to decrease slightly as R/F decreases. In support of the first observation, the lower pK_b for sodium carbonate (3.67, Table 8) means it will have the greatest impact on pH but it is imperative to remember that the concentration of catalyst is small in comparison to those of resorcinol, melamine or formaldehyde.

Table 8: **pK_a and pK_b values of reactants for Melamine-Resorcinol-Formaldehyde xerogels.**

Reactant	pK_a	pK_b
Resorcinol	9.15	-
Formaldehyde	13.27	-
Melamine	-	9.0
Sodium Carbonate	-	3.67

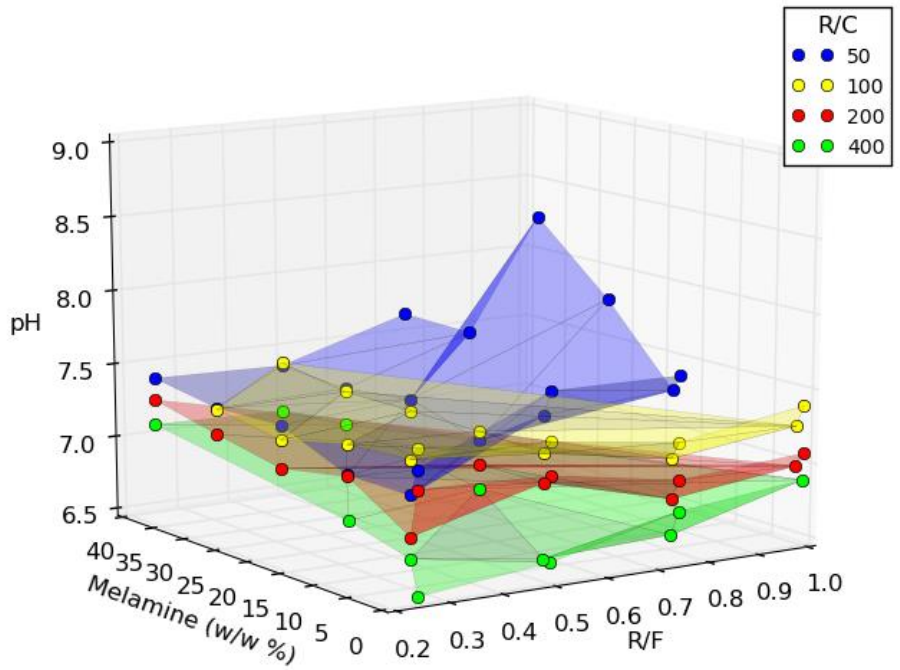

Figure 46: **Initial pH of solution for MRF xerogels synthesised in this study as a result of R/F and [M] for different R/C.**

In the second case, formalin (formaldehyde solution) has a pH of 2.8-4.0 (as mentioned in chapter 4), therefore, as R/F increases, less formalin is used, and pH is affected accordingly, with less acidic component influences on the final value.

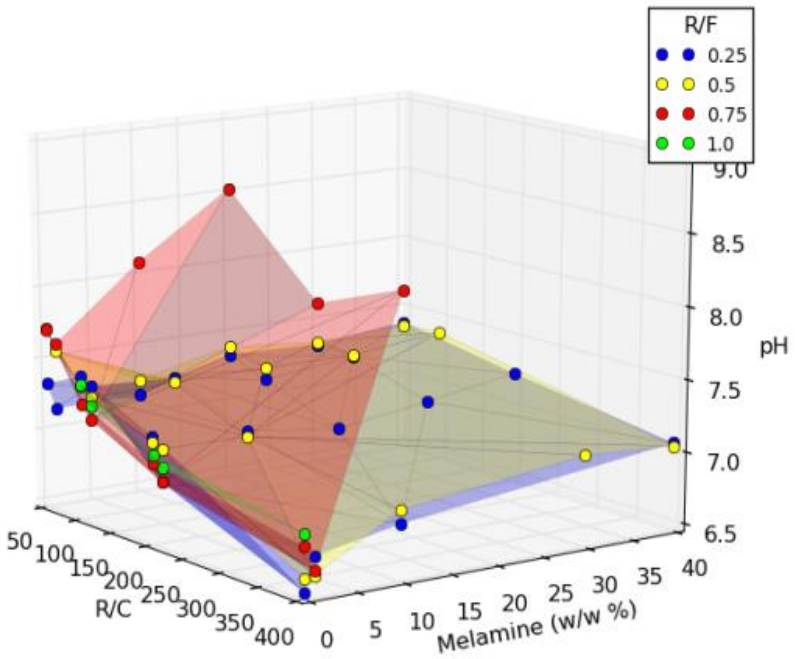

Figure 47: **Initial pH of solution for MRF xerogels synthesised in this study as a result R/C and [M] for different R/F.**

As R/C increases, less carbonate is used and, consequently, pH tends to decrease due to the combined effect of a lower concentration of base in the synthetic system (relatively strong base) and higher resorcinol concentration (weak acid, pK_a 9.15). Consequently, for RF gels, R/C ratio is the main parameter that controls initial solution pH. By comparison, melamine is an organic base, therefore, as its concentration increases so too does pH; hence, for MRF gels the pH is also affected significantly (especially at high R/C) by melamine.

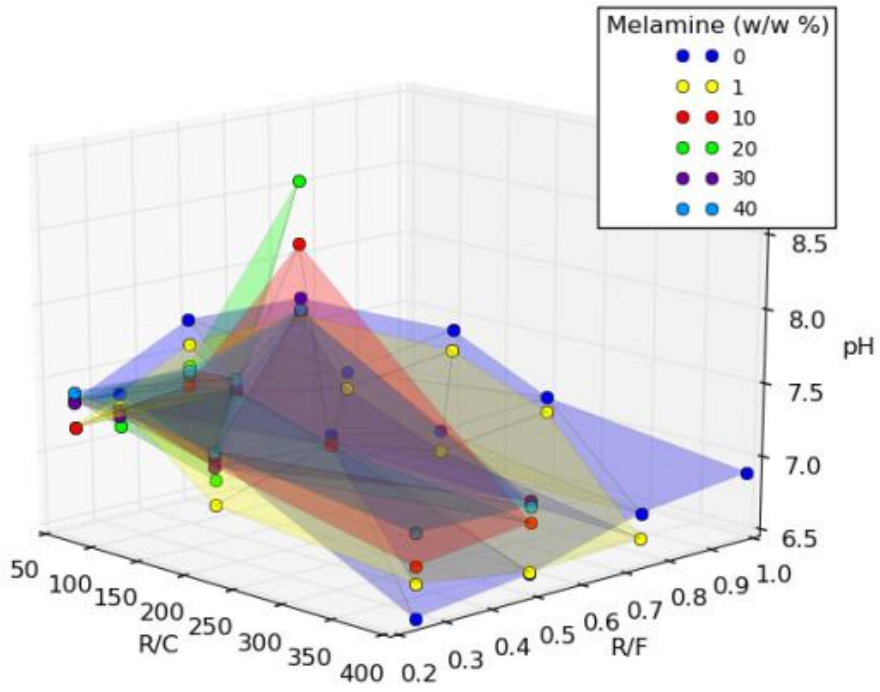

Figure 48: Initial pH of solution for MRF xerogels synthesised in this study as a result R/C and R/F for different [M].

As R/F is increased, the number of formaldehyde molecules available to provide linkages decreases resulting in weaker gels, as a consequence of reduced crosslinking between clusters, however, it is the effect of initial solution pH (and R/C ratio) that ultimately controls the pore structure of the final xerogel [186]. As pH approaches 8.0 and 8.5 for [M] 20 and 10, respectively, pH is generally increased as R/F increases, creating weaker porous structures and, in most cases, gelation fails. It can also be argued that R/F values of 0.75 and 1.0 would produce weaker xerogels, low surfaces area and pore volume as, among other reasons, the high initial solution pH ranges from 7.0 to 8.5 and it is known that initial solution pH has a strong influence on successful gelation. As observed, in this work, for R/F ≥ 0.75, many gels fail to crosslink sufficiently to make further processing possible; such materials are often amorphous non-porous powders and, as a consequence, only those gels

created with R/F 0.25 or 0.5 should be considered for preparation of MRF xerogels when large surface areas, high pore volumes or pore sizes suitable for gas treatment, particularly CO_2 adsorption, are required.

6.6 Surface Functionalities

Fourier transform infrared spectroscopy (FTIR) analysis was used to gain information regarding surface functionalisation of the synthesised gels as FTIR spectroscopy has been routinely applied to probe the chemical structure of carbon materials [171]. In this work, the effect of altering R/C, R/F and [M] on surface group development were examined.

6.6.1 Effect of [M] on Chemical Structure of MRF Xerogels

The suite of MRF materials synthesised in this study were analysed by FTIR, Figure 49 shows a selected group where [M] is increased at constant R/C of 50 and R/F of 0.50. As [M] increases, it is observed that fewer O-H bonds are present, from phenolic groups in the final solid, as supported by the relative decrease in the peak corresponding to the O-H vibration (3200-3500 cm^{-1} [172]) as [M] increases. Comparison of peak depth relative to other key peaks across the same spectra gives an indication of the concentration of each species. For example, it can be seen that as [M] is increased, the proportion of the peaks in the fingerprint region compared to the O-H peak increases considerably. This suggests that the concentration of O-H groups in the MRF40 xerogel is lower compared to the concentration of structural bonds (observed in the fingerprint region) than for the MRF0 sample, for which, the intensities of the O-H peak and the fingerprint region are very similar, indicating the presence of as many O-H bonds as either C-O or C-H structural groups.

It is worth noting that, for pure RF gels, or gels with lower [M] (up to 10%), the O-H peak is broader than for materials with higher [M]. This indicates that, due to the higher concentration of O-H groups, the electrostatic interactions to surrounding hydrogen atoms become important and, therefore, these vibrations occur at wavenumbers close to those for the O-H bond (peak 1 in Figure 49), but sufficiently shifted to result in a broader peak (Figure 50).). At low [M], or for pure RF gels, these interactions become more likely and, therefore, result in a wider peak. Conversely, for higher [M], which means less resorcinol in the recipe (melamine is incorporated as a substitute for resorcinol), and the concentration of O-H groups is expected to be lower, thus, the interactions between them become weaker, resulting in a narrower peak, as the schematic in Figure 50 shows.

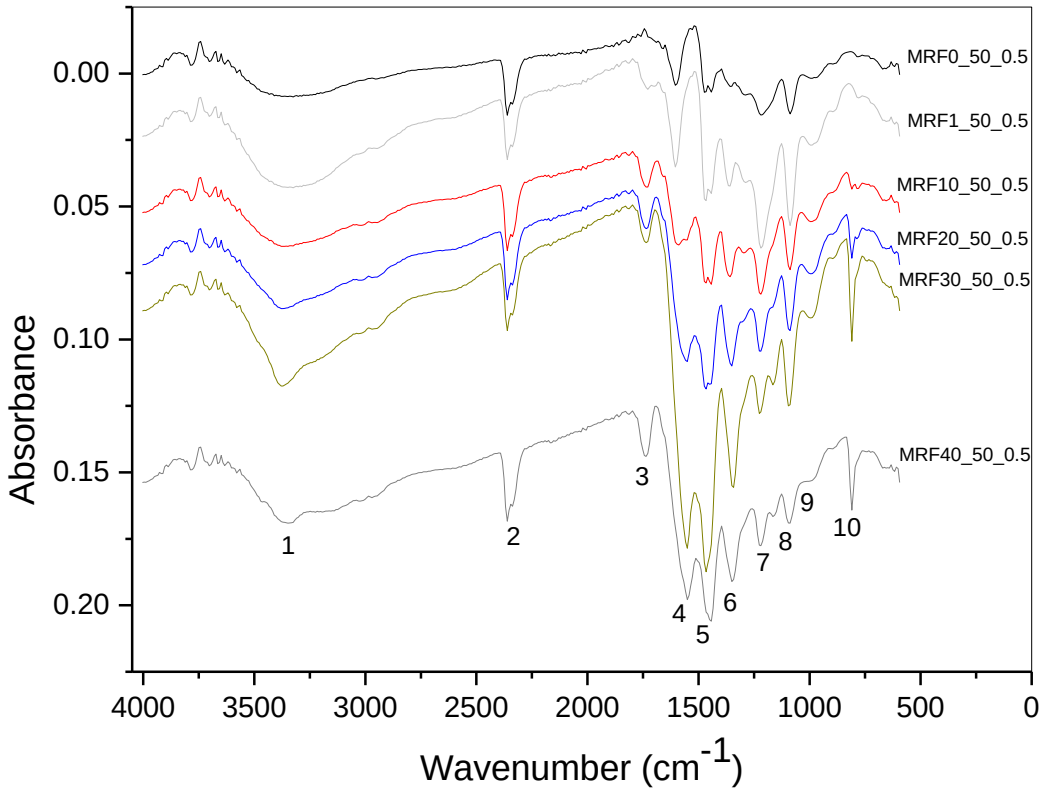

Figure 49: **FTIR spectra for MRF xerogels synthesised in this study varying [M] (0-40 w/w%) for R/C 50 and R/F 0.5.**

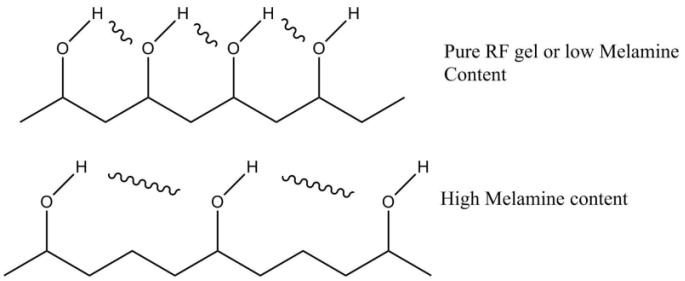

Figure 50: **Schematic of hydrogen interactions with -OH groups at low (high resorcinol) and high (low resorcinol) [M].**

As detailed above, the first peak, at wavenumber 3550-3200 cm^{-1} corresponds to strong O-H vibrations, which is related to resorcinol concentration and intermolecular O-H interactions, while O-H bending (1410-1260 cm^{-1} (s)) and C-OH stretching (1150-1040 cm^{-1} (s)) can be observed in the fingerprint region [172] of MRF xerogels. O-H stretching can mask weaker -NH_2 or =NH stretching vibrations (3500-3300 cm^{-1} (m)); however, these groups also absorb at ~2360 cm^{-1} (peak 2) but, as this peak is also present for MRF0, which

has no nitrogen content, it is more likely to correspond to adsorbed CO_2, which vibrates at 2349 cm^{-1} with a stronger intensity [172]. The peak at 1743 cm^{-1} can be described to carbonyl functionalities (1697 cm^{-1}), formed by nitrogen bonding to two acyl groups via combination with formaldehyde [172]. Conjugated C=O bonds appear at ~1640-1595 cm^{-1}, and peaks 4 and 5 can be related to this effect. However, peak 5 is more likely to be a result of C-H stretching of saturated bonds (1470-1430 cm^{-1}), which can be related to methylene bridge formations (as detailed in Chapter 1) [172]. Peak 4 can be attributed also to primary or secondary amide functionality which vibrates at ~1650 cm^{-1} and 1570-1515 cm^{-1}, respectively [172]

Additionally, in the fingerprint region there are two strong interactions that can produce the peaks observed. Firstly, C-O has strong interaction at frequencies of 1300-1020 cm^{-1}, which suggest that peaks 6, 7 and 8 could be associated to this bond. Secondly, C-H peaks for aromatic groups, have strong interactions at frequencies between 850-700 cm^{-1}, hence, peak 10 and the shoulder observed in peak 9 can be related to this interaction. Overall, the key changes observed for increasing [M], at constant R/C and R/F ratio, are the reduction of O-H stretching vibrations (3550-3200 cm^{-1}), as a consequence of reducing resorcinol concentration, and an increase in imide functionalities (1697 cm^{-1}).

6.6.2 Effect of R/F on Chemical Structure of MRF Xerogels

Figure 51 shows the effect of increasing R/F for a system with constant [M] and R/C. The data represents suites of low, medium and high [M] materials. It can be seen that while O-H stretching bonding (3550-3200 cm^{-1}) is little affected at high [M] (Figure 51c); peaks at 1600-1400 cm^{-1}, ascribed to C=O 1640-1595 cm^{-1}, seems to reduce its intensity as R/F is increased. This decrease may be attributed to the higher degree of crosslinking at lower R/F, as ring substitution increases with higher relative concentrations of formaldehyde in the system. Therefore, the concentration of these bonds is higher for lower R/F and consequently intensity is increased. However, as detailed above, peak 5 (Figure 49), can also result from methylene bridge formation; hence, at lower R/F ratio such bridging should be favoured, particularly at initial solution pH 7-8.

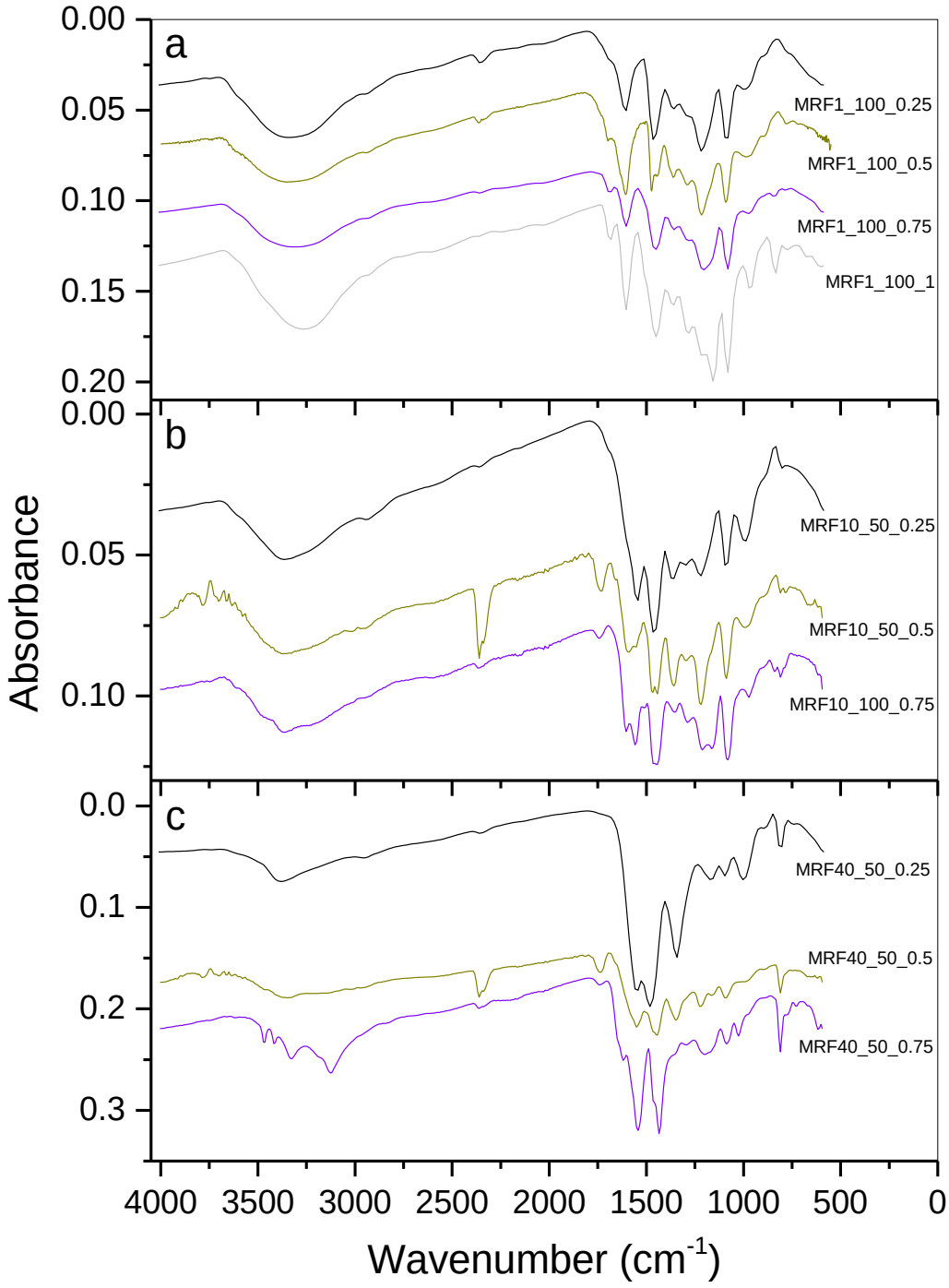

Figure 51: **FTIR spectra for MRF xerogels synthesised in this study varying R/F for three sets of constant (low, medium and high) R/C and [M].**

The main difference between the spectra shown in Figure 51 is [M]; for lower [M], the formaldehyde in solution reacts mainly with resorcinol i.e. in MRF1 there is 99% resorcinol and 1% melamine. As the concentration changes, for example to 60% resorcinol and 40% melamine for MRF40%, more melamine is available for reaction and greater resorcinol

substitution occurs. This means, that for lower [M] (MRF1), all structural bonds (such as C=O and C-H) will be similarly affected by a change in R/F. Instead, for higher [M] (MRF40), C-H bonds, due to methylene bridging, will be affected to a higher degree than C=O, because melamine does not contain these bond types and, also, the crosslinking reaction will involve a higher percentage of melamine, for MRF40, than for MRF1.

6.6.3 Effect of R/C on Chemical Structure of MRF Xerogels

The effect of increasing R/C ratio for constant R/F and [M], is shown in Figure 52, with more evident changes at higher [M]. Increasing R/C impacts more markedly on the region 1600-1250 cm^{-1}, in which higher intensity peaks are observed as [M] increases, but generally the entire fingerprint region is affected. As R/C increases, more resorcinol is present in the initial solution, therefore, crosslinking is enhanced with increased intensities for associated peaks at 1640-1595 cm^{-1} (C=O), 1470-1430 cm^{-1} (C-H methylene bridge), 1300-1020 cm^{-1} (C-O) and 850-700 cm^{-1} (C-H).

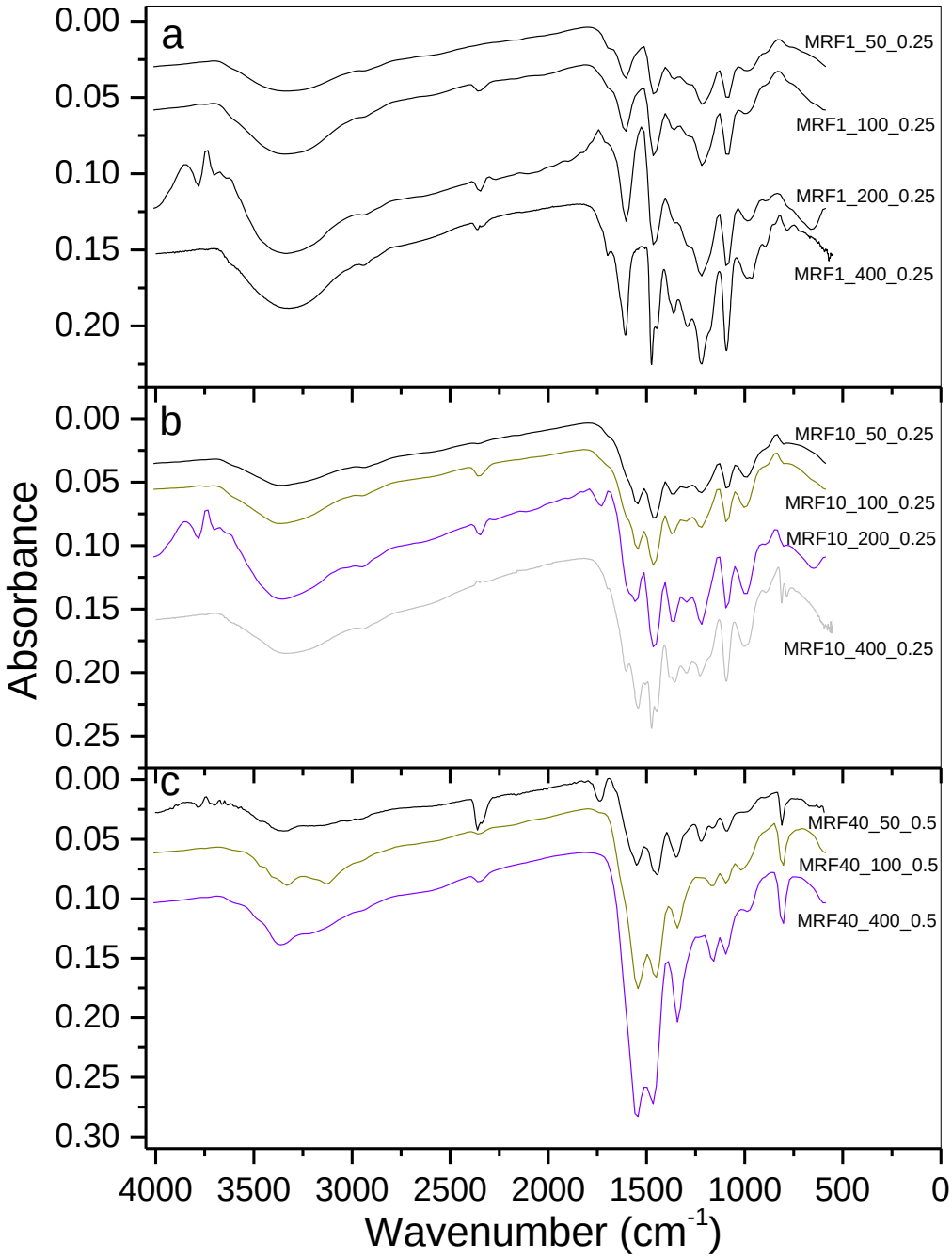

Figure 52: **FTIR spectra for MRF xerogels synthesised in this study varying R/C 50-400 for three sets of constant (low, medium and high) R/F and [M] 1-40 w/w%.**

6.7 Effect of R/C, R/F and [M] on Surface Area

Total surface area can be divided into micropore surface area (pores < 2 nm width) and non-micropore surface area (pores > 2 nm width). It has been observed that R/F values of 0.25 and 0.5 offer better control of xerogel properties than higher R/F. The reason is that lower R/F values permit a higher degree of crosslinking, given that lower R/F offer a larger

number of substitutes available (formaldehyde) to react with the O-H groups of resorcinol or the amine groups of melamine, which leads to a higher rate of crosslinking. It is observed that increasing R/C produces a similar effect as increasing [M] with regards to surface area of MRF xerogels.; this parameter decreases as either R/C and [M] is increased, while a simultaneous increase in both parameters results in a more drastic reduction in surface area (Figure 53).

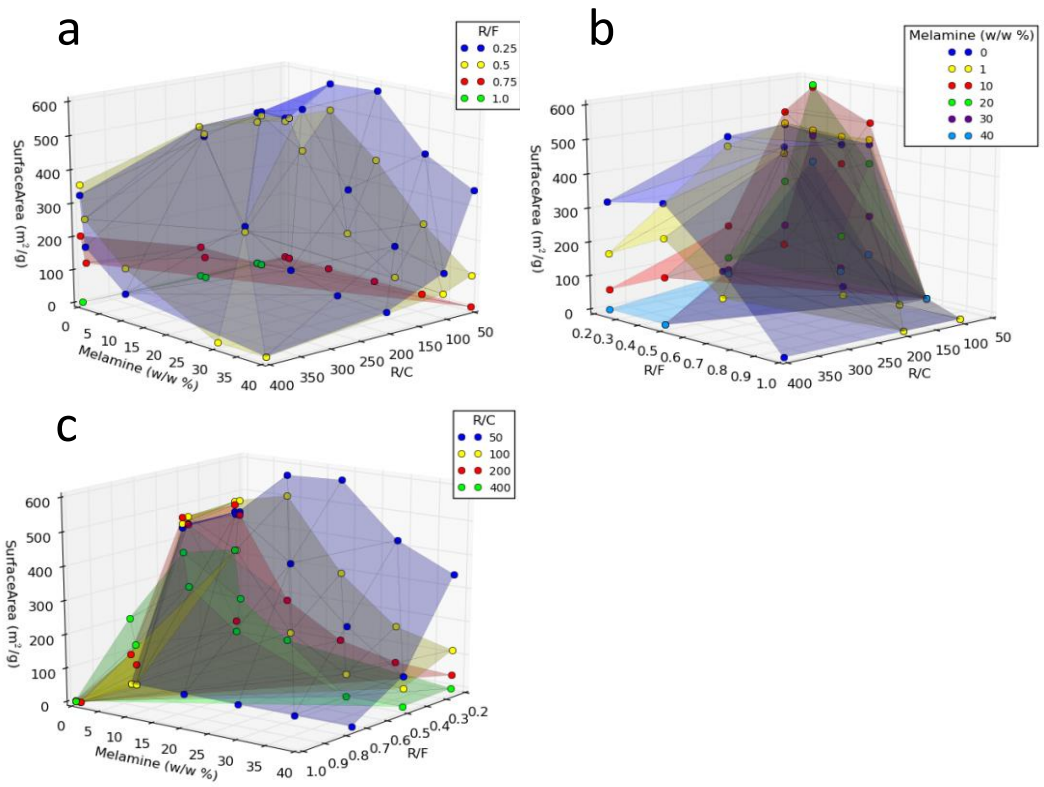

Figure 53: Surface areas obtained for MRF xerogels synthesised in this study using R/F 0.25 and 0.5, R/C 50-400, and [M] 0-40 w/w%.

The highest surface areas (Figure 53) are obtained for MRF 20 and MRF 10; while, MRF 0 and MRF 1 have a similar distribution. However, surface area drops drastically for [M] of 30 and 40. In general, the best performance in terms of surface area is observed for R/F 0.25 and 0.5. As previously stated, R/F > 0.75 produced weaker gels of wide pores and small surface area, therefore, R/F 0.25 and 0.5 are recommended to obtain higher surface areas and pore sizes suitable for gas adsorption in MRF gels. Additionally, as R/C increases the surface area decreases for a certain [M]. However, this decrease occurs at lower R/C as [M] is increased (Figure 53b). This narrows the window available to obtain significant surface area as [M] is increased. For MRF 0 and MRF 1, instead, this behaviour is more stable for

the range of R/C studied (50 to 400), but the decrease starts to be evident for R/C > 200. A similar trend is observed for micropore surface area and non-micropore surface area (Figure 54).

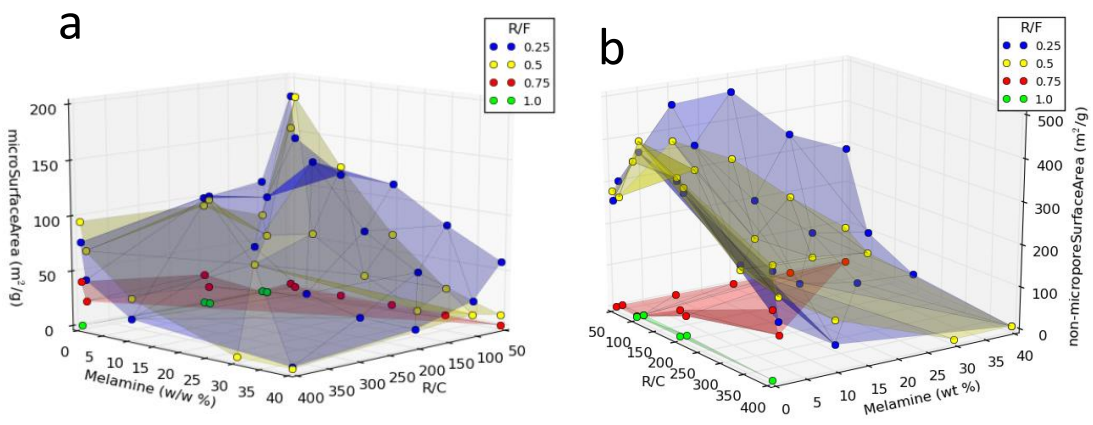

Figure 54: **(a) Micropore surface areas and (b) non-micropore surface areas obtained for MRF xerogels synthesised in this study using [M] 0–40 w/w%, R/C 50–400, and R/F 0.25-1.0.**

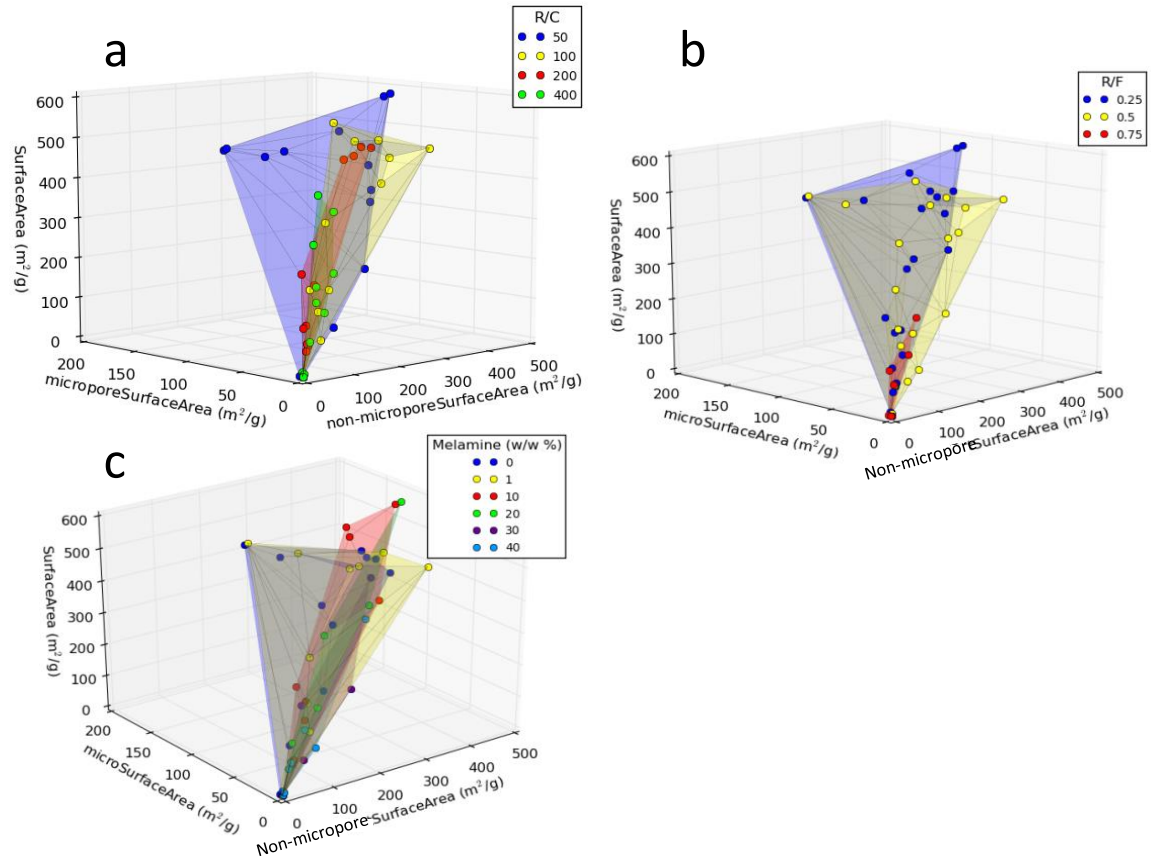

Figure 55: **Microporosities obtained for MRF xerogels synthesised in this study varying (a) R/C, (b) R/F, and (c) [M].**

Microporosity is a very important feature for solid sorbents applied to gas treatment; thus, understanding how varying the parameters of R/F, R/C and [M] affects microporosity formation in solid MRF resins becomes important. It is observed that increasing R/C, R/F or [M] tends to hinder micropore development while simultaneously increasing pore size (Figure 55).

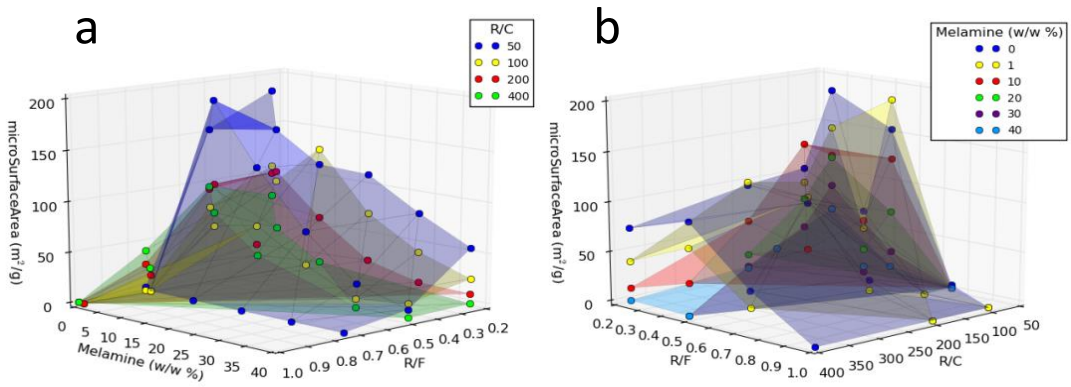

Figure 56: Micropore surface areas obtained for MRF xerogels synthesised in this study using [M] 0–40 w/w%, R/C 50–400, and R/F 0.25-1.0.

R/F values of 0.25 and 0.5 offer a better degree of control when tuning this type of material; this is explained by the fact that it enhances the level of crosslinking during cluster aggregation. R/F directly controls the stoichiometry of the reaction, the number of substitutions occurring in the ring (resorcinol and/or melamine) and, consequently, the level of crosslinking. Therefore, this affects the formation of voids spaces in-between the aggregates or clusters, which impact on pore size and, therefore, the microporosity and non-micropore surface area. R/F between 0.25 and 0.5 results in gels with operational internal area and, instead, higher R/F values result in weak gels with low surface area. As R/C is increased, less resorcinol molecules are activated to react, as fewer sodium carbonate molecules are present in solution. Therefore, this weakens the structure, forming lager pore sizes and quashing microporosity in the material. As shown before, increasing [M] affects pore size in a similar way as increasing R/C, therefore micropore formation is hindered (Figure 56).

6.8 Effect of R/C, R/F and [M] on Total and Micro Pore Volume

Total pore volumes were calculated from the maximum N_2 uptake (which makes them equivalent) at the highest pressure (~0.98 bar), and micropore volume is calculated using the t-plot method. A larger total pore volume is obtained for low [M] (0-20 %) and low R/C

(50-200); there is a significant difference between low R/F (0.25 and 0.5) and higher R/F (Figure 57).

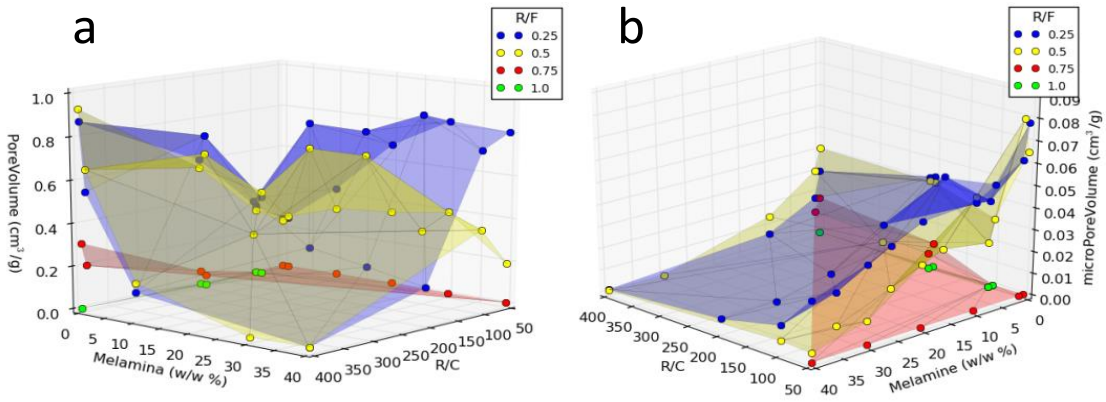

Figure 57: **(a) Pore volumes and (b) micro pore volumes obtained f for MRF xerogels synthesised in this study using [M] 0–40 w/w%, R/C 50–400, and R/F 0.25-1.0.**

As previously explained, micropore volume and micropore surface area are calculated using the t-plot method and both follow the same trend. Microporosity tends to decrease as R/C and [M] are increased; however, significant results are obtained only for low R/F (0.25 and 0.5). Additionally, while R/C 50 and 100 result in gels with high N_2 uptake for materials with surfaces areas of 300-600 m^2/g and 100-500 m^2/g, respectively; R/C 200 and 400, by contrast, exhibit significant N_2 uptake for only a narrow window at low [M]. Increasing [M] does not, therefore, necessarily mean an increase in N_2 uptake. Surface area is a bigger impact than increase in N_2 uptake, which can be tailored controlling R/C and R/F ratio and is maximized at values of 50 and 100 for the former and 0.25 and 0.5 for the latter.

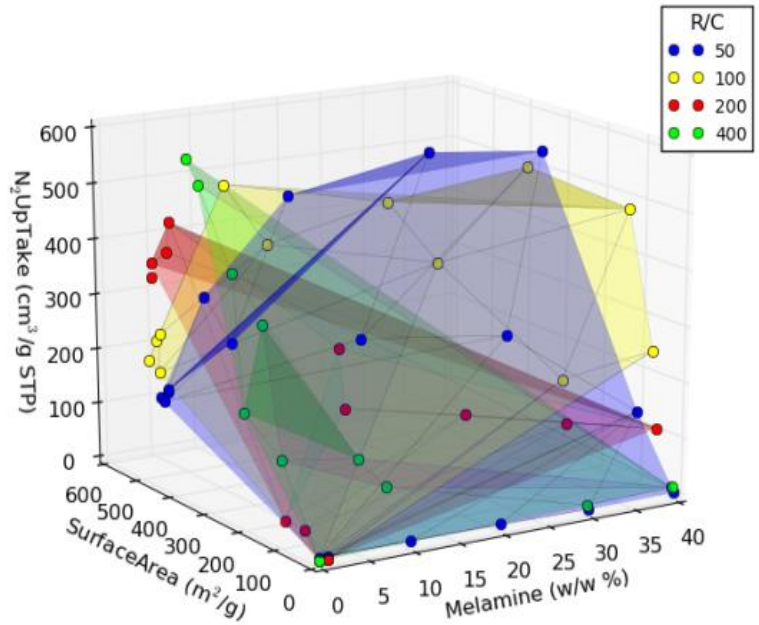

Figure 58: **Nitrogen up take for Melamine-Resorcinol-Formaldehyde xerogels produced using melamine content of 0–40 w/w%, Resorcinol/Catalyst ratio of 50–400, and Resorcinol/Formaldehyde ratio of 0.25-1.0.**

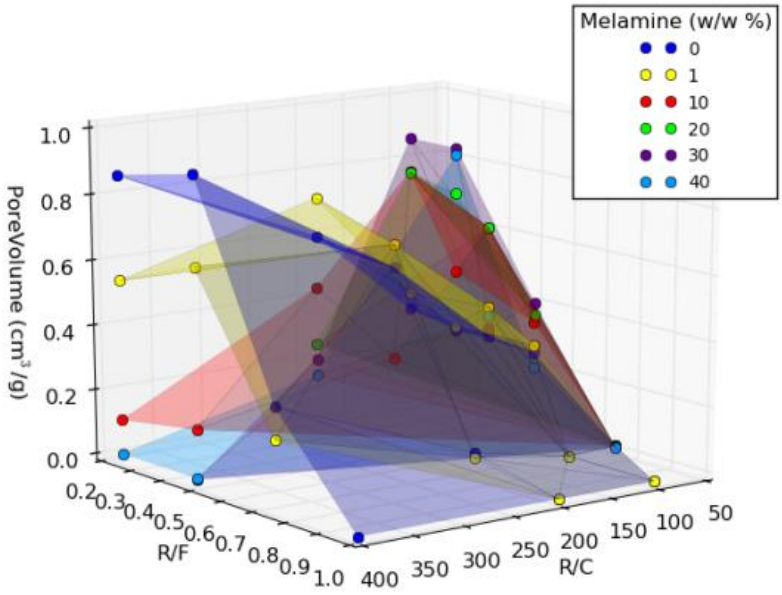

Figure 59: **Pore volumes for MRF xerogels synthesised in this study varying R/F and R/C for different [M].**

Two different behaviours can be distinguished: at low R/C (50 and 100) and high R/C (400) with respect to both pore volume and N_2 uptake (Figure 58 and 59). At high R/C the largest uptake is seen for low [M] (MRF0s) and uptake progressively decreases as [M] increases, while for low R/C the opposite is observed, with higher N_2 uptakes for higher [M] (40 and 30). The higher N_2 uptake is observed for pore sizes between 5-15 nm, with a few

exceptions, for gels with high [M] (30 and 40) and low R/C (50 and 100) even up to 25 nm. There are two maximum pore volumes, at low [M] and high R/C, and at low R/C and high [M]. Nevertheless, micropore volume tends to decrease as R/C, R/F and [M] values are increased, but for low R/F (0.25 and 0.5) this decrease is not as steep. A maximum in micropore volume for each [M] analysed was observed at low R/C (50).

6.9 Effect of R/C, R/F and [M] on Pore Size

Pore size is only controlled at low R/F (0.25 and 0.5), while at higher R/F (0.75 and 1.0) pore size becomes a random parameter with tendency to create large pore sizes because of weak crosslinking and interactions between clusters. The smallest pore sizes are obtained for low R/C (50) for which the amount of catalyst is highest and this enhances crosslinking among clusters, promoting the formation of small voids and pores. For low R/C (50) and R/F (0.25 and 0.5), pore size increases gradually as [M] is increased; in general, low R/C results in smaller pore sizes for low [M], while the opposite occurs for higher R/C.

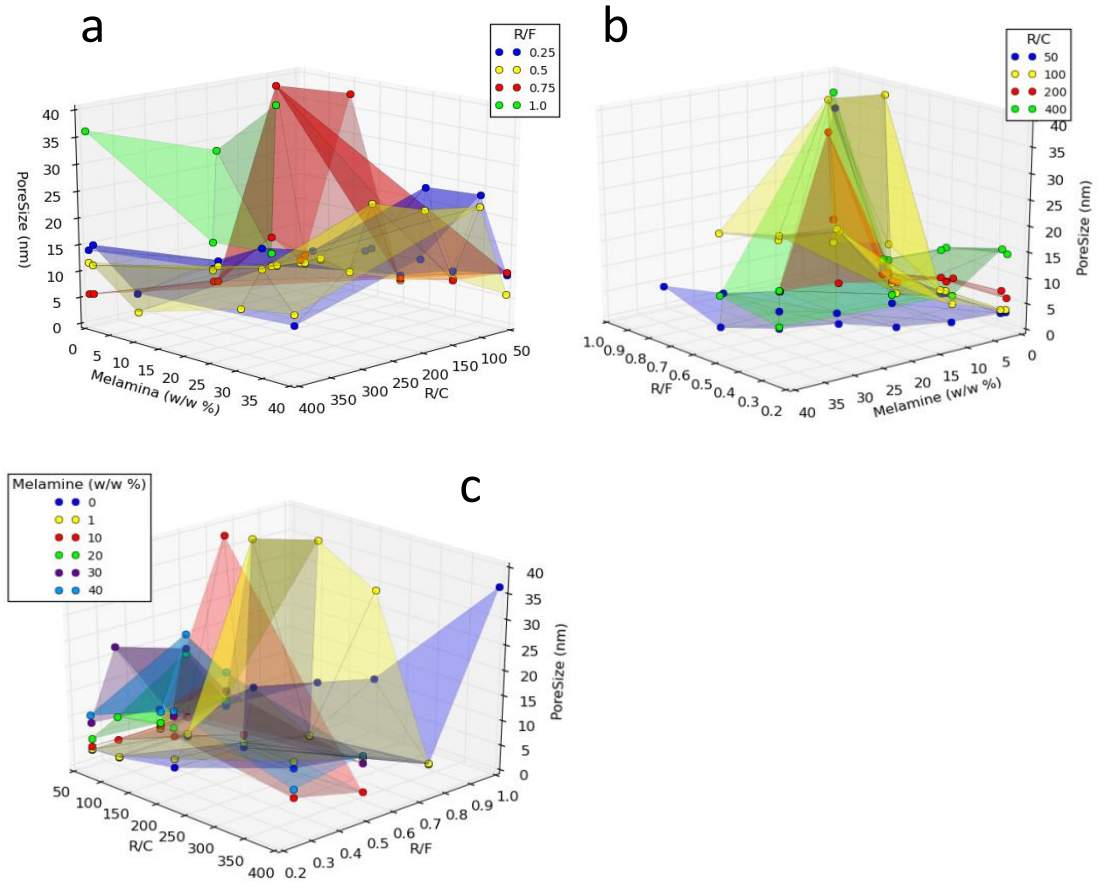

Figure 60: **Pore sizes obtained for MRF xerogels synthesised in this study using R/C 50-400, R/F 0.25-1.0, and [M] 0-40 w/w%.**

6.10 **Key Findings**

During the parametric study, on this chapter, the selected synthesis parameter studied, R/C, R/F and [M], were varied obtaining different recipes. CHN analysis confirmed that N is incorporated into the structure of MRF xerogels. SEM analysis showed that the increasing content of N produces structural changes. N_2 adsorption tests showed that in general N_2 adsorption capacity increases as melamine increased. This is because as [M] increases, pore size becomes larger and therefore pore volume increases. The pore shape is changing from ink bottle like pores to open mesopores as [M] increases, this is explained by the change in hysteresis loops from Type H2 to H1. It was found that increasing [M] result in a similar effect as increasing R/C on structural properties such as pore size, pore volume and surface area. Additionally, low R/F content results in better crosslinking between clusters while high R/F results in weaker structures due to poor crosslinking.

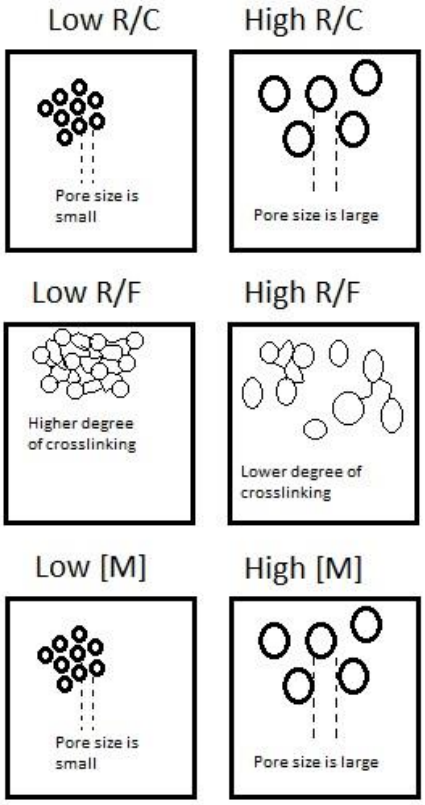

Scheme 2: Effect of R/C, R/F and [M] on gelation and xerogel structure.

Chapter 7
Results Part III

7 Results Part III – Characterization of Selected Samples

This chapter focuses on a study of selected samples, identified from the parametric study in Chapter 6 for further analysis. The incorporation of melamine into resorcinol-formaldehyde xerogel structures modifies the surface chemistry of the final solid material. This modification becomes important in applications such as carbon capture because, by the addition of basic groups (such as amines) on the surface, the number of acid-base interactions (between CO_2 and surface) can be increased and, therefore, CO_2 adsorption capacity can be enhanced. Consequently, it becomes interesting to assess and quantify the degree of surface functionalisation. In a related study, the thermal stability of MRF materials was analysed, while CO_2 adsorption capacities, kinetics of adsorption and regeneration were also studied for these materials.

7.1 Samples Selection

As described previously, materials were selected on the basis of their micropore volume, aiming to provide a suite of samples, with varying nitrogen contents, but similar micropore volumes to allow direct comparison of the observed difference in CO_2 capacity in terms of [M]. This subset of samples was taken from a family of xerogels produced with varying R/C and R/F, as well as [M], which resulted in over 100 samples from which the suite of materials shown in Table 9 were selected and their structural properties are also given for reference.

MRF0_100_0.5, MRF1_400_0.5, MRF10_200_0.25, MRF20_100_0.25, MRF30_50_0.25 and MRF40_50_0.25 all exhibit micropore volumes of ~0.03 cm^3/g, allowing a comparison of their performance in terms of CO_2 adsorption uptake. This provides a basis to observe the effect of increasing nitrogen content on CO_2 adsorption capacity. Other samples were included in the study to observe the impact of increasing R/C for MRF0s and MRF1. Density was measured for the selected MRF xerogel samples, MRF0_50_0.25 exhibits a high density. This combined with its narrow pore size and the smallest pore volume of the samples selected suggests a highly compact structure in this particular sample. In contrast, MRF10_200_0.25 has an even higher value of density than MRF0_50_0.25, but its average pore sixe is 6 times larger and with a total pore volume that is almost double, therefore surface area should be more accessible for adsorption and gas diffusion, suggesting the opposite for MRF0_50_0.25.

Table 9: **Total (BET), non-micropore and micro surface area, total pore and micropore volume and pore size obtained by BET analysis, Rouquerol correction and t-plot method for MRF xerogels synthesised in this study.**

Sample	BET total surface area (m^2/g)	non-micropore surface area (m^2/g)	Micro surface area (m^2/g)	Pore Volume (cm^3/g)	Micropore Volume (cm^3/g)	Pore Size (nm)	Density[1] (cm^3/g)
MRF0_50_0.25	441.8	258.1	183.7	0.239	0.078	2	1.2(±0.1)
MRF0_100_0.25	475.5	369.3	106.2	0.330	0.047	3	0.76(±0.03)
MRF0_200_0.25	464.4	365.4	98.9	0.603	0.042	5	0.81(±0.03)
MRF0_100_0.5	445.8	369.2	73.6	0.308	0.031	3	1.01(±0.06)
MRF1_100_0.25	480.2	388.7	91.6	0.379	0.040	3	0.96(±0.04)
MRF1_400_0.5	256.2	187.2	69.0	0.652	0.030	11	0.79(±0.03)
MRF10_200_0.25	193.6	143.8	61.4	0.441	0.027	12	1.43(±0.09)
MRF20_100_0.25	302.5	228.1	74.4	0.763	0.032	11	1.17(±0.08)
MRF30_50_0.25	427.9	344.6	83.2	0.822	0.036	8	0.65(±0.02)
MRF40_50_0.25	351.3	285.6	57.9	0.804	0.027	10	1.05(±0.06)

7.2 Nitrogen Adsorption Isotherms

Surface areas and porosities were obtained for all samples, using analysis of N_2 sorption, producing isotherms and pore size distributions (Figure 61, grouped by melamine content). The isotherms produced for N_2 adsorption on the MRF xerogels studied here (Figure 61 a, b and c) can all be classified as Type IV **[147]**, which indicates mesoporous solid sorbents. The pore filling mechanism involves initial monolayer coverage followed by multilayer adsorption and, finally, capillary condensation. Hysteresis loops shows two distinct shapes: H1 and H2. H2(a) is observed for low [M] (MRF0s and MRF1_100_0.25); while, MRF1_400_0.5 exhibits a shape closer to H2(b), and samples with higher [M] show a mix of behaviour between H2(b) and H1. The trend in moving from H2(a) to H2(b) and H1 seems to be a general one when increasing [M], but it is arguable that the shape of the hysteresis loops for MRF10, MRF20, MRF30 and MRF40 xerogels (Figure 61**)** correspond to H2(b), H1 or a mix of both.

[1] Density measurements were carried out by James Flannigan during a summer project within the Chemical and Process Engineering department of the University of Strathclyde

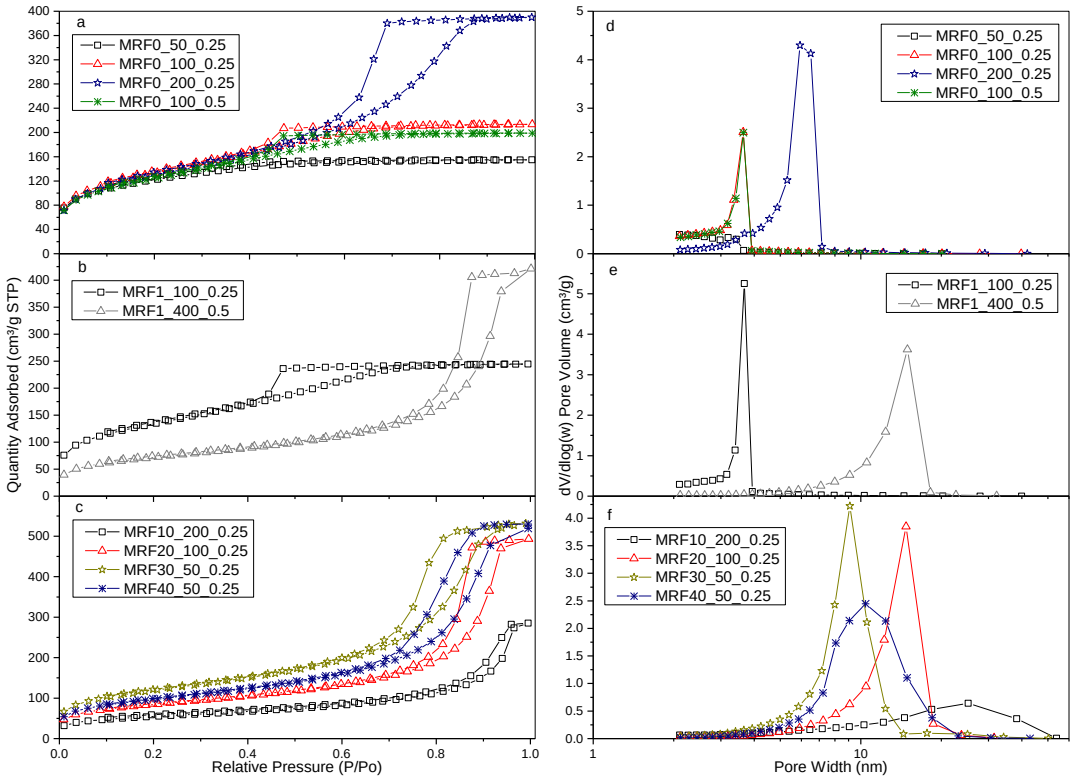

Figure 61: **(a) N_2 adsorption isotherms and (d) pore size distributions for MRF xerogels synthesised in this study using variable R/C and R/F for [M] 0 w/w%; (b) N_2 adsorption isotherms and (e) pore size distributions for MRF xerogels synthesised in this study using variable R/C and R/F for [M] 1 w/w%; (c) N_2 adsorption isotherms and (f) pore size distributions for MRF xerogels synthesised in this study using variable R/C and R/F for [M] 10, 20, 30 and 40 w/w%.**

The pore size distributions (Figure 61d, e and f) show an increase in pore size as melamine content is increased. Figure 61d allows a comparison for increasing R/C with constant R/F and [M]. The samples, MRF0_50_0.25, MRF0_100_0.25 and MRF0_200_0.25, show an increase in pore size, of 2, 3 and 5 nm, respectively, with increasing R/C, which is consistent with the literature [112, 128]. MRF0_100_0.5 exhibits an identical isotherm and pore size distribution as MRF0_100_0.25, suggesting that R/F has little effect at the levels studied. Results are consistent for MRF0_100_0.25 and MRF1_100_0.25 with the same R/C and R/F, and only a minor difference in [M]; therefore, these samples exhibit similar N_2 isotherms and pore size distributions. Average pore size increases as [M] is increased and there is an associated increase in N_2 uptake, of 213.4 cm^3/g STP for MRF0_100_0.25 and 244.6 cm^3/g STP for MRF1_100_0.25. This increase in pore volume does not, however, necessarily translate to an increase in CO_2 uptake, given that not all volume available results in useful interactions with CO_2. MRF1_400_0.5 has a noticeable larger pore size than MRF1_100_0.25, which can be attributed to the higher R/C used. The degree of

crosslinking of RF xerogels decreases as [M] increases, affecting the porous characteristics, as can be seen in Table 9, i.e. addition of melamine into the structure of MRF0_50_0.25 to MRF40_50_0.25, increases the average pore size (from ~2 nm to ~10 nm), reducing the surface area (from ~441 m^2/g to ~351 m^2/g), increasing pore volume (from ~0.24 cm^3/g to ~0.80 cm^3/g) but reducing the proportion of microporosity (from ~0.078 cm^3/g to ~0.027 cm^3/g). Therefore, as discussed in chapter 6, [M] concentration has a significant impact on structure properties of MRF xerogels.

7.3 Elemental Analysis

All samples were analysed using elemental analysis to quantify the compositional percentages of carbon, hydrogen and nitrogen (CHN), and to confirm the level of incorporation of nitrogen into the final xerogel structure. Results are shown in Table 10, and it is evident that there is a direct correlation between nitrogen content determined and melamine concentration used in the xerogel synthesis.

Table 10: Elemental analysis (carbon, hydrogen and nitrogen) of selected MRF xerogels synthesised in this study.

Sample	Carbon (w/w %)	Hydrogen (w/w %)	Nitrogen (w/w %)
MRF0_50_0.25	61.65	5.12	0.00
MRF0_100_0.25	57.00	5.20	0.00
MRF0_200_0.25	59.94	4.78	0.00
MRF0_100_0.5	62.68	4.72	0.00
MRF1_100_0.25	57.52	5.28	0.76
MRF1_400_0.5	61.71	4.89	0.79
MRF10_200_0.25	57.10	5.03	8.84
MRF20_100_0.25	53.07	4.94	16.01
MRF30_50_0.25	50.17	4.84	22.23
MRF40_50_0.25	47.76	4.77	29.37

7.4 Determination of Basic Functionalities on Surface of MRF Xerogels

All samples were analysed by a titration method following the procedure outlined in Section 4.15. This analysis was aimed at gaining information about the change that occurs in the surface of the RF gel by introducing melamine into the structure. Particularly, this surface modification is attributed to the amines groups present in the structure of melamine, which represent basic moieties.

The quantity of carbon basic surface functionalities (Ncsf) groups can be calculated by titrating an acid solution, of known molarity, that was previously in contact with the samples, with a solution of sodium hydroxide (NaOH). The quantity of basic groups on the surface of the xerogels can be calculated using the Equation 63:

$$n_{fg} = [HCl]V_{HCl} - ([NaOH]V_{NaOH})\frac{V_{HCl}}{V_{Aq}} \qquad \text{Equation 63}$$

The results obtained are shown in Figure 62:

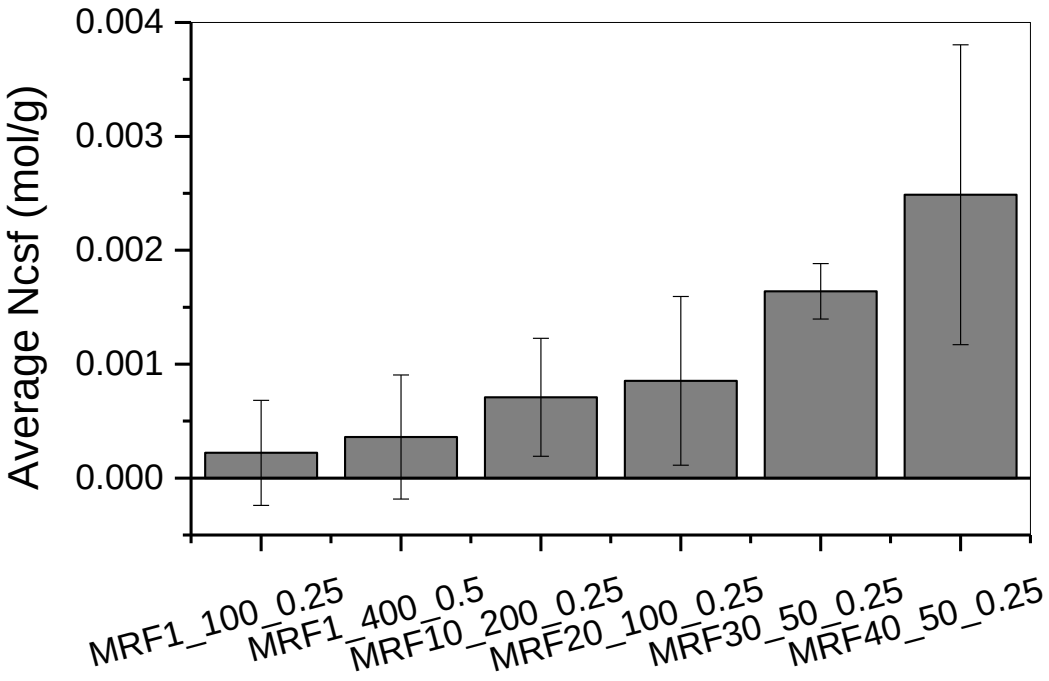

Figure 62: Average carbon surface basic functionalities analysed by titration for (a) MRF0 xerogels and (b) for MRF xerogels containing 1, 10, 20, 30 and 40 % of melamine.

Results obtained for MRF0s xerogels show a small degree of fluctuation around zero, which suggest that no basic functionalities are present in xerogels formed by resorcinol and formaldehyde. Samples were treated with N_2 bubbling prior titration test, as detailed in Section 4.15, to remove as much as possible of CO_2 dissolved in the solution, which would affect the NaOH consumption. However, N_2 bubbling was stopped during titration, which were carried out under room conditions and some CO_2 from air may have dissolved back into the solution during analysis.

Samples containing 1% of melamine and higher show a clear ascending trend in the number of basic carbon functionalities, increasing with increasing melamine content. The trend

observed in Figure 62 shows an increase in carbon basic surface functionalities (Ncsf) as melamine concentration is increased. This confirms the incorporation of melamine into the structure and the surface functionalization by the amines. CO_2 adsorption is expected to be enhanced as the basicity of xerogel surface is increased.

7.5 Fourier Transform Infrared Spectroscopy

As discussed above, samples were tested using Boehm titration and CHN methods to determine the bulk basic character and total nitrogen content; however, the presence of resorcinol, and its associated oxygen groups, results in acidic character, including phenolic species, and this can affect the results obtained from such analysis. It is also imperative to understand the surface character of the materials used as this will be the primary mode of interaction with adsorbed CO_2. Figure 63 shows the FTIR spectra obtained for all MRF xerogels studied here. There are three main acidic frequencies to focus on for these systems and the data suggests that, of these, no lactonic or carboxylic groups are present (absence of peaks at 1765 cm^{-1} and 1690 cm^{-1}, respectively), but does indicate phenolic structures from the O-H stretch at 3550-3200 cm^{-1} (note: if carboxylic/lactonic groups are present, their contribution to the acidic behaviour is insignificant compared to the phenolic groups). Hence, all acidic contributions are assumed to result from phenolic groups.

As melamine concentration increases in the synthetic matrix, less resorcinol is used; hence, the final structures are expected to exhibit fewer phenolic groups in the final materials. The FTIR spectra obtained for all samples show a peak attributed to phenolic functionalities (3200-3500 cm^{-1}) [172], which changes with varying melamine concentration. Comparison of the depth of the peak to others in the same spectra gives an indication of the concentration of the species. For example, It can be seen that as the melamine concentration increases the proportionality of the peaks in the fingerprint region compared to the O-H peak increases considerably, suggesting that the concentration of O-H groups in MRF40_50_0.25 is lower compared to the concentration of the skeletal bonds (observed in the fingerprint region) than for the MRFO samples,. By comparison, the MRF0 xerogels exhibit O-H peak and fingerprint region intensities that are very similar, suggesting as many -OH bonds or groups as C-O or C-H structural groups. The peak observed at ~2350 cm^{-1} likely corresponds to surface absorbed CO_2, which vibrates at 2349 cm^{-1} [172]. While the shoulder between 2950 and 2850 cm^{-1} can be ascribed to C-H stretching vibrations (i.e. CH_2, CH_3 or CH), this is supported by the peak observed at ~1490 cm^{-1}, which would be related

to C-H deformations. The C=O bond gives a peak at 1640-1595 cm^{-1}, however, it could also be attributed to primary or secondary amide functionality which vibrates at ~1650 cm^{-1} and 1570-1515 cm^{-1}, respectively [172]; peak intensity, hence concentration of groups, increases as melamine concentration in increased. The presence of C=O bonding was also analysed by XPS, the results of which are shown in the Section 7.6.

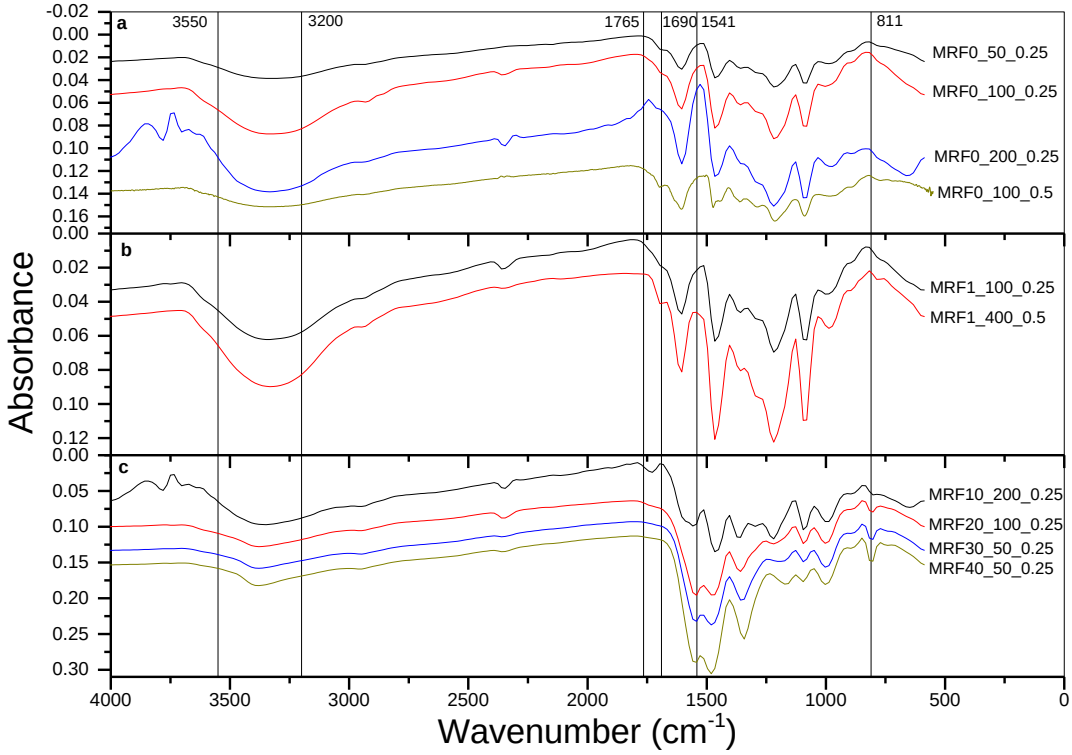

Figure 63: **FTIR spectra for (a) MRF xerogels of variable R/C and R/F for [M] 0 w/w%; (b) MRF xerogels of variable R/C and R/F for [M] 1 w/w% and (c) MRF xerogels of variable R/C and fixed R/F for [M] 10-40 w/w%.**

There is a peak at ~1300 cm^{-1} the intensity of which seems to increase as concentration of melamine is increased. Therefore, this peak is likely associated to the C-N stretching vibration (1360-1080 cm^{-1}) [172], for amine groups related to melamine. Additionally, C-O has a strong interaction at 1300-1020 cm^{-1} [172], hence, the peak observed at ~1150 cm^{-1} is possibly associated with this vibration. Finally, there are strong peaks at 850-700 cm^{-1}, which can be ascribed to C-H peaks for aromatic groups.

7.6 Surface Snalysis by X-ray Photoelectron Spectroscopy

The incorporation of nitrogen into the xerogel structure has also been observed by X-ray Photoelectron Spectroscopy as shown in Figure 64.

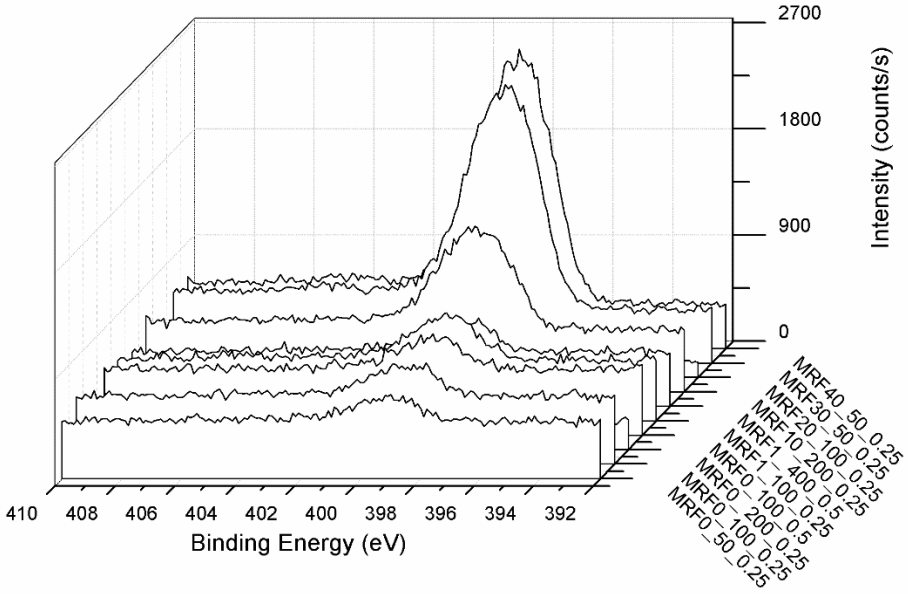

Figure 64: XPS measurement of nitrogen binding energy in MRF xerogel samples.

XPS results confirm the increase of nitrogen content as melamine concentration increases. This also reinforces the assertion that experimental error accounts for the small fluctuations observed when quantifying the number of basic functionalities by titration for MRF0s.

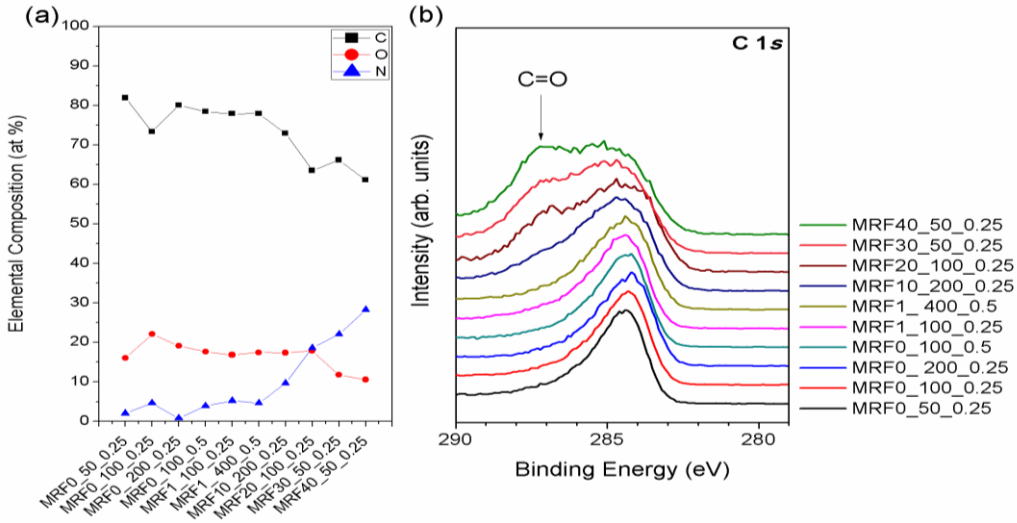

Figure 65: MRF xerogel samples analysed by XPS for (a) elemental analysis and (b) for binding energy for C1s.

Figure 65a shows XPS carbon, oxygen and nitrogen elemental analysis results for the selected MRF samples. It is important to note that XPS is very sensitive to contaminants,

even from within the high vacuum chamber. Therefore, it is probable that some adventitious carbon has also been captured within the XPS measurements that would not be detected by CHN. This is the reason for the observed higher carbon content from XPS analysis in comparison to CHN results.

Figure 65b show an increasing amount of C=O bonding in MRF samples as melamine concentration is increased. This is in agreement with results obtained by FTIR (Figure 63). Different possibilities were considered to explain the occurrence of this increased C=O bonding. Firstly, the possibility that the C=O bond could correspond to the presence of CO_2 molecules adsorbed on the surface of the molecules was considered, as its increasing concentration is expected to increase as a consequence of increasing nitrogen content, as per the underlying hypothesis of this work, therefore, higher interactions would be expected between the surface and CO_2 molecules. However, the fact that all samples were thoroughly degassed, at high vacuum, prior to XPS analysis, suggests that the presence of CO_2 adsorbed molecules is unlikely.

During the synthesis procedure, an oven held at 85 ± 5 °C is used for gelation of MRF resins and, post gelation, most gels exhibited a darker colour on the top layer. Therefore, oxidation was considered as a potential reason for the presence of C=O bonding. However, all resins, including those with no melamine were synthesised by the same procedure, hence, all experienced the same conditions and, importantly, the same interfacial area for oxidation to occur; the observation of an absence of C=O bonds for MRF0 indicates that oxidation is questionable. Given the relationship with increasing additive content, it is possible that oxidation is favoured by increasing melamine concentration. In order to test this theory, FTIR was conducted separately on the two layers obtained from the final gel matrix.

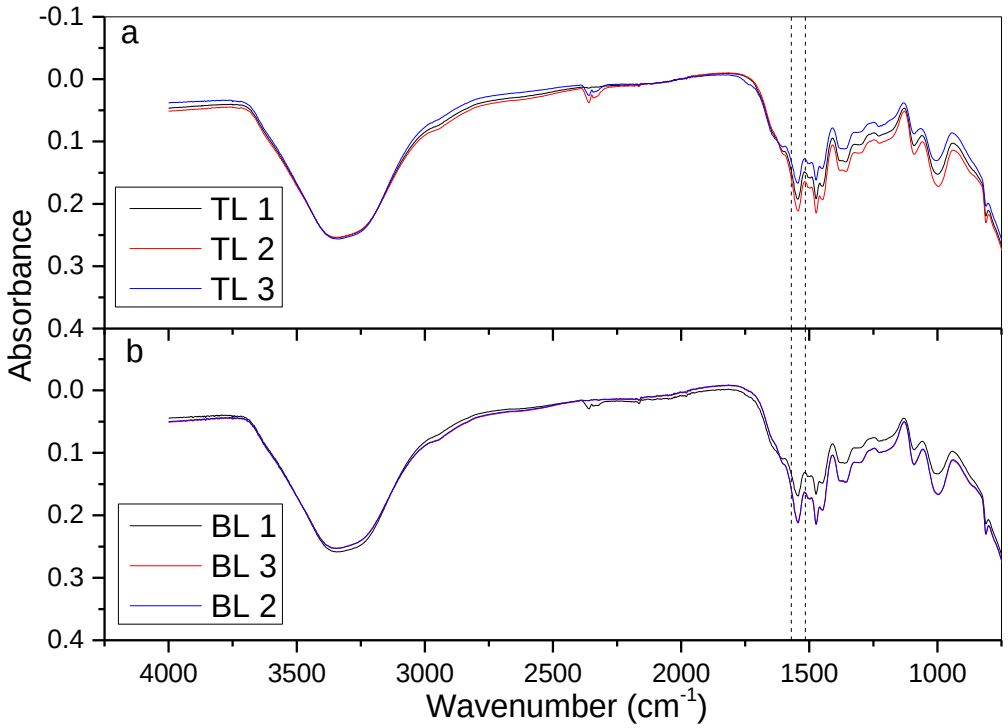

Figure 66: FTIR spectra for MRF20_100_0.25 for three samples of (a) top layer (TL) and (b) bottom layer (BL).

Figure 66 shows FTIR spectra obtained for both the top and bottom layers of a sample of a sample of MRF20_100_0.25. This sample was chosen for its high melamine content, as the peak corresponding to C=O bonding increases as melamine content increases, therefore, it is sensitive to analyse a sample of high melamine content. 30 and 40 % melamine contents were discounted because, at these levels, crosslinking becomes weaker and gelation tends to fail. FTIR spectra obtained for both layers are identical, suggesting a homogeneous composition irrespective of stratification. The large peak observed at ~3500-3100 cm^{-1} corresponds to O-H vibrations, , observed as the gels were 'wet' (hydrogel) during the measurement as, in order to assess only the effect of gelation, the gel did not undergo a drying stage prior to FTIR analysis. The region of interest of these spectra is where the C=O bonds appears at a wavenumber of ~1570-1515 cm^{-1}.

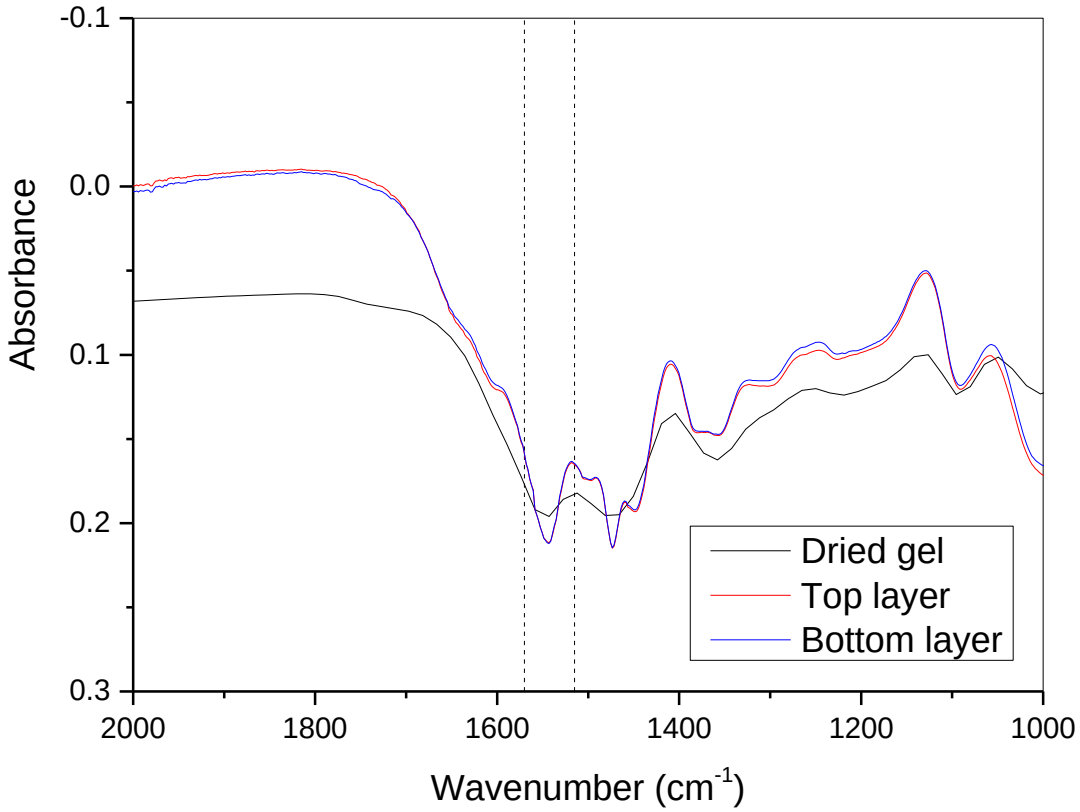

Figure 67: FTIR spectra for MRF20_100_0.25 a dried gel compared to top layer and bottom layer of a 'wet' gel.

Figure 67 shows that the peaks observed in the spectra of a dried MRF20_100_0.25 xerogel coincides with the peaks observed in both the top and bottom layers of a 'wet' gel. This suggests that formation of these moieties is not consequence of oxidation, or drying, but instead this group appears as a consequence of the polymerization reaction occurring during gelation. This supposition is fully supported by the fact that there is no difference what-so-ever between the spectra obtained for the top and bottom layers in these tests. Additionally, as stated above, this peak increases as [M] increases; therefore, this reinforces the hypothesis that these peaks must be a consequence of the polymerization reaction between melamine and formaldehyde.

It was necessary to discard the effect of other stages of the synthesis procedure (solvent exchange and drying). All MRF hydrogels are treated with acetone for solvent exchange, therefore, it was necessary to eliminate the effect of acetone on the surface of the material, either by entrainment or reaction. However, reports of good solubility of melamine in acetone with formaldehyde explains that while acetone is an appropriate solvent for melamine, reaction only occurs between formaldehyde and melamine, under

the conditions used in this study [191, 192]. Nevertheless, a sample of MRF20_100_0.25 hydrogel was treated with acetone prior to FTIR analysis, while another sample underwent direct drying, without solvent exchange, before being analysed by FTIR.

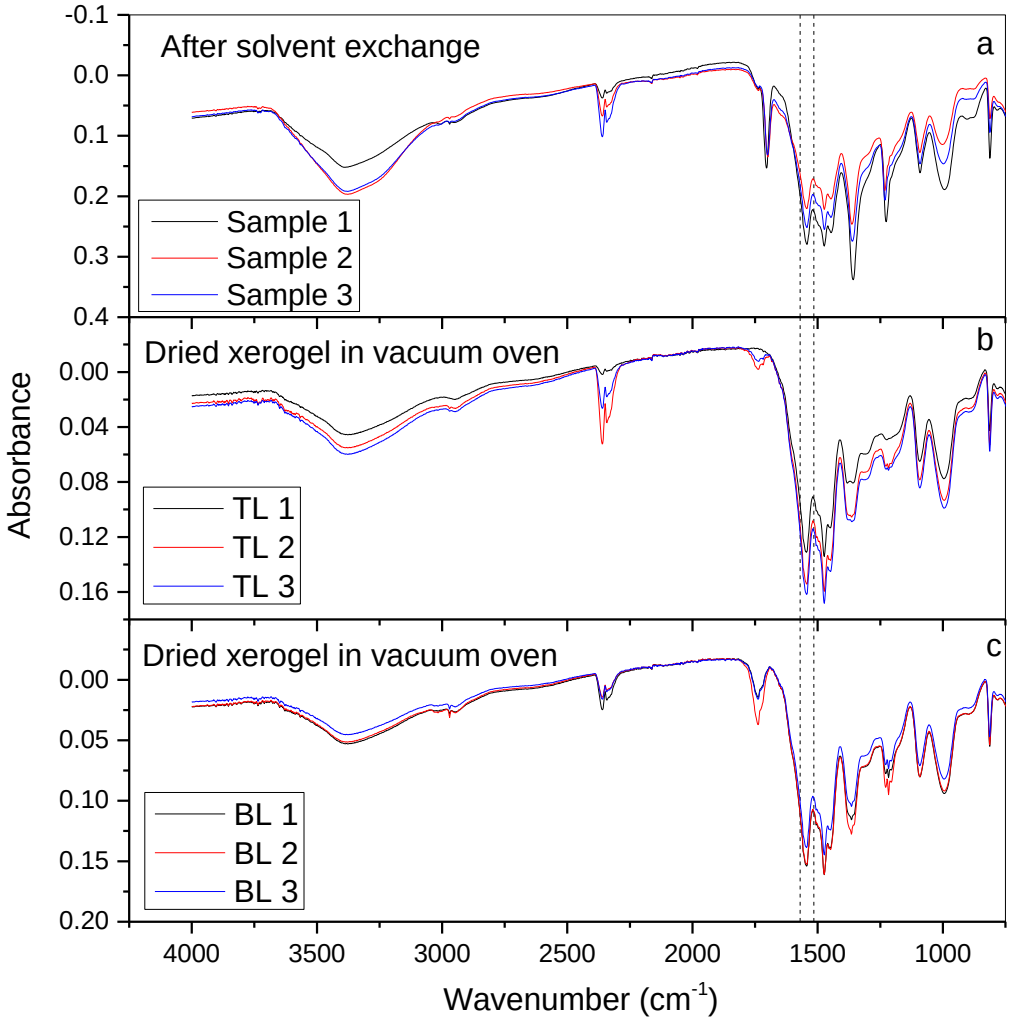

Figure 68: FTIR spectra for MRF20_100_0.25 for three samples (a) after solvent exchange, (b) after drying stage (top layer (TL)) and (c) after drying stage (bottom layer (BL)).

Figure 68 shows that the sample tested after solvent exchange and that analysed after drying only exhibit similar FTIR spectra. Particularly, the region of interest (~1570-1515 cm^{-1}), suggests that neither of these stages invokes chemical changes to the gel network.

As explained above, the increasing amount of C=O bonding must be attributed to the polymerization reaction occurring during gelation. The detailed study of the reaction mechanism exceeds the scope of the current project; however, a preliminary hypothesis is presented in Scheme 3:

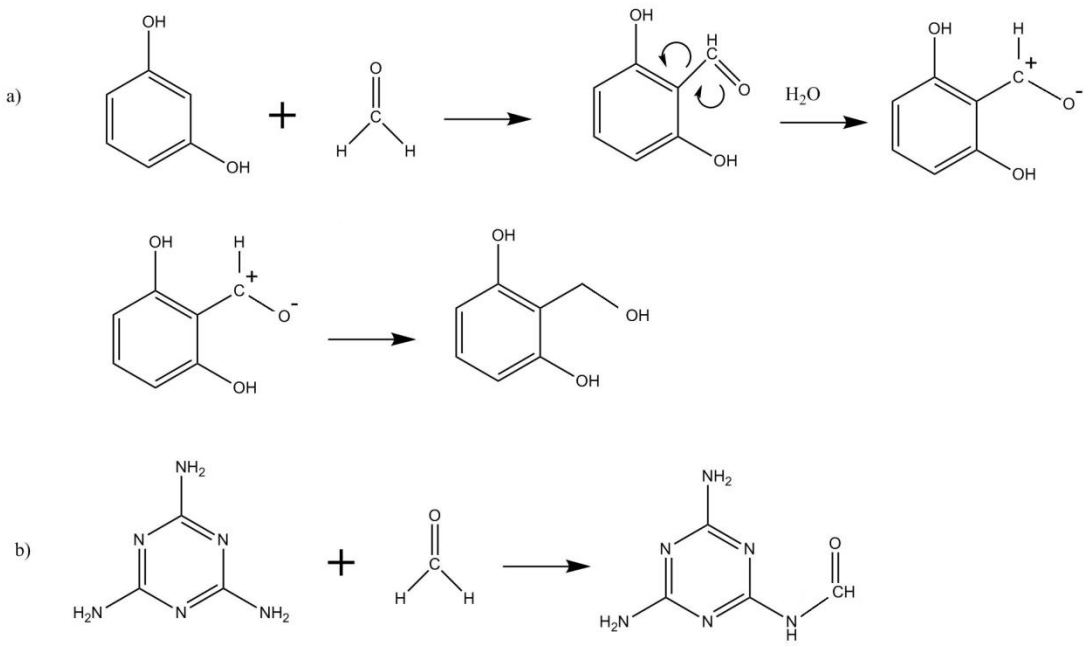

Scheme 3: Reaction of formaldehyde with (a) resorcinol and (b) melamine

The addition of formaldehyde with resorcinol is more favoured than its addition to melamine, due to the higher reactivity of resorcinol than melamine. Therefore, even at higher melamine concentration formaldehyde would probably first consume the available resorcinol than melamine. However, despite that supposition, the occurrence of C=O bonding can be explained by the probable conjugate effect occurring in the melamine molecule (Reaction b in Scheme 3). Additionally, the reaction of resorcinol and formaldehyde produces a compound with no C=O bonding present (Reaction a in Scheme 3), due to the conjugate effect, which would delocalise the charges, resulting in a negatively charged oxygen atom. In contrast, reaction of formaldehyde with melamine would form a compound where the electron density of the C=O double bond would have no mechanism for alternative stabilisation; this is a consequence of the stable 'R-N-C bonds (see product of reaction b in Scheme 3) within the structure, hence, C=O moieties would not be consumed in further reaction (crosslinking) but would tend to be retained within the structure (Reaction b in Scheme 3). This also explains the mechanical weaknesses observed for xerogels with increased melamine concentrations. The intermediate formed by addition of formaldehyde to resorcinol is more likely to react to crosslink the material, strengthening the structure of the gel. By contrast, those intermediates formed by reaction of formaldehyde with melamine would have higher stability, therefore, less 'desire' for further crosslinking, making the gel structure weaker. Moreover, cluster with higher content of melamine would likely be heavier than cluster with higher content of resorcinol. This would

promote a degree of heterogeneity within the final MRF structure due to gravitational effect during cluster growth and gelation.

7.7 Proximate Analysis of MRF Xerogels

Thermogravimetric experiments were conducted to determine the thermal behaviour of MRF xerogels. Curves corresponding to mass change (TG), derivative thermo-gravimetric (DTG) and differential scanning calorimetry (DSC) of MRF samples were obtained under N_2 environment by exposing the samples to ramped temperatures increasing from room temperature to 920 °C, before switching to an air environment at 820 °C (oxygen present). The curves obtained allow the division of the combustion process into three stages. The first stage occurs at ~120 °C and corresponds to the point when moisture evaporates from the samples. The second stage is observed at ~920 °C, at which temperature volatile matter is decomposed. At the third stage, the N_2 flow is replaced with air, allowing oxygen to contact the sample at ~820 °C resulting in combustion of fixed carbon.

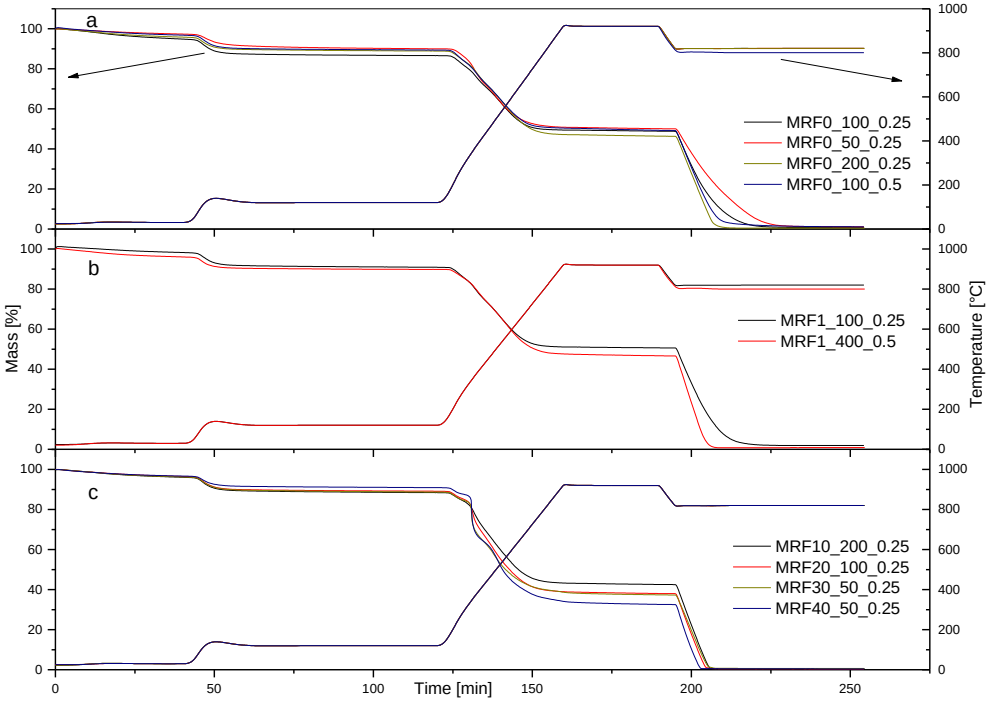

Figure 69: Thermo-gravimetric (TG) analysis of MRF xerogels, mass loss (TG) and temperature programme used. The measurement was carried out in a N_2 atmosphere from room temperature to ~920 °C, then temperature is set to ~820 °C and air is used instead.

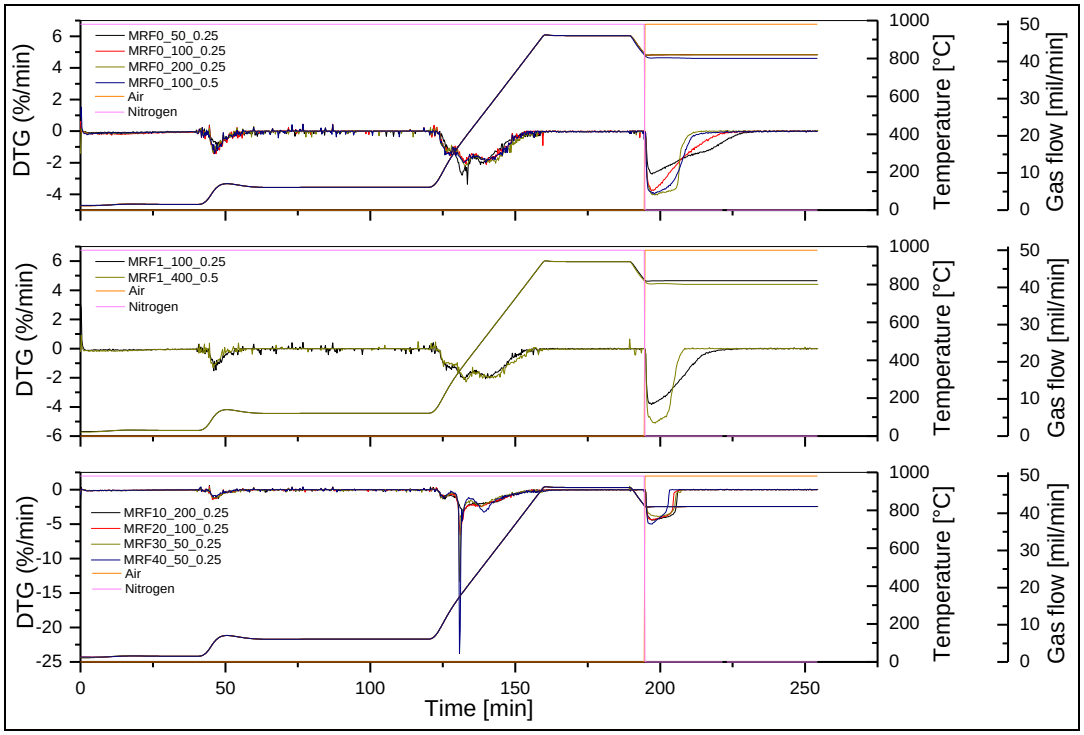

Figure 70: Derivative of mass change with respect to time (DTG) measured for the MRF selected samples. The temperature programme and Gas flows (N_2 and air).

The DTG curve (derivate of mass change with respect to time) indicates the change in weight of material with time (which also corresponds changing temperature as a function of time). Therefore, the three peaks observed indicate the reduction in weight due to loss of moisture, volatile matter and fixed carbon, respectively. The mass loss due to moisture evaporation is approximately 10% for all MRF samples (Figure 72), which corresponds to the first peak observed in the DTG graph (Figure 70) and is similar in all cases, occurring at 80-130 °C. By contrast, the second peak is significantly wide, at ~200-750 °C, and corresponding to the loss of volatile matter, with multiple reactions occurring (peaks) at different temperatures within this range. The intensity of the narrow peak at 345 °C increases markedly as melamine concentration is increased. This peak corresponds to the decomposition of the resin's structure, at the sublimation temperature of melamine (345 °C) [193], simultaneously, formaldehyde, methanol, amines and NH_3 are released. Switching the gas flow to air at 820 °C promotes combustion of fixed carbons (third peak in Figure 70) the content of which decreases as melamine concentration is increased (Figure 72).

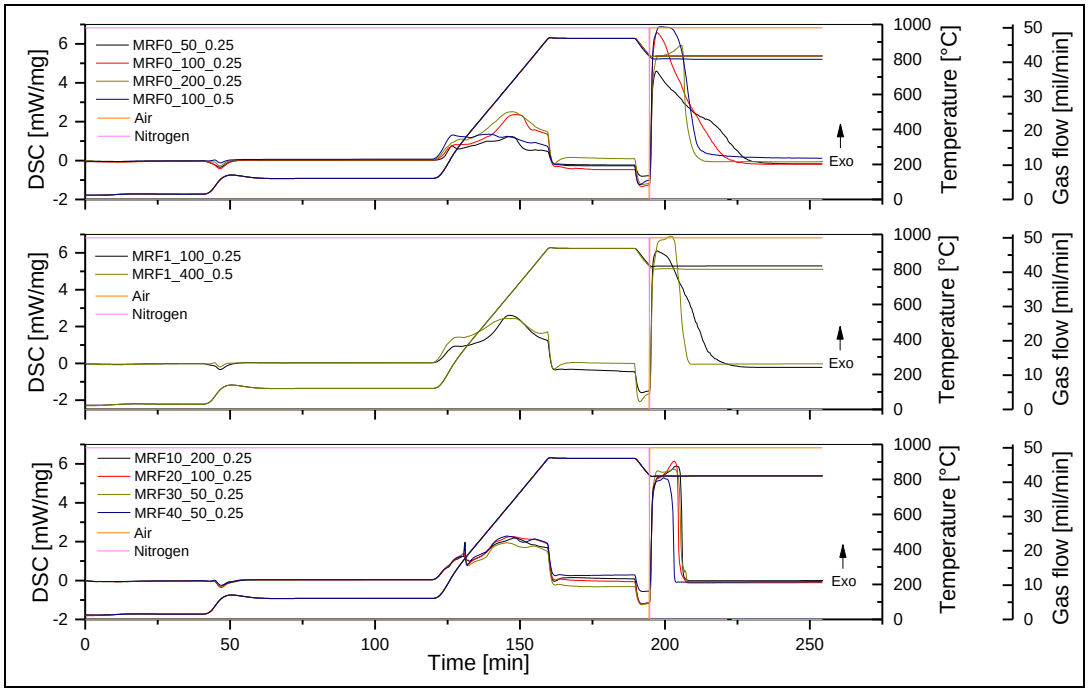

Figure 71: Differential scanning calorimetry (DSC) measured for the MRF selected samples. Temperature programme and Gas flows (N_2 and air).

The DSC curve (differential scanning calorimetry) shows the heat flow, i.e. whether the process occurring (mass loss) is exothermic or endothermic. Thus, DSC monitors the temperature and heat flow during transitions in the sample, which is to say during mass change, as a function of time and temperature under a controlled atmosphere.

The first peak observed for all materials (Figure 71) corresponds to the endothermic loss of physisorbed moisture from the sample. This is analogous to evaporation of confined water molecules from the surface of the xerogel. Instead the loss of volatile mater and fixed carbon are both exothermic processes, these processes imply that some bonds are breaking (endothermic) but others are forming (exothermic), therefore, the energy produced in the formation of new species exceeds the energy consumed for prior breaking of the bonds between these groups and the surface of the xerogel.

As melamine concentration is increased, the percentage of volatile matter is increased while fixed carbon decreases. This confirms the lower level of crosslinking for samples with higher melamine contents, while the reduction of fixed carbon arises from the reduction of carbon in the structure as it is replaced by nitrogen present in melamine (triazine). The

moisture quantity in all samples is ~10 %, which corresponds to water vapour adsorbed from air during storage. The ashes remaining after the combustion stage account for ~1 %.

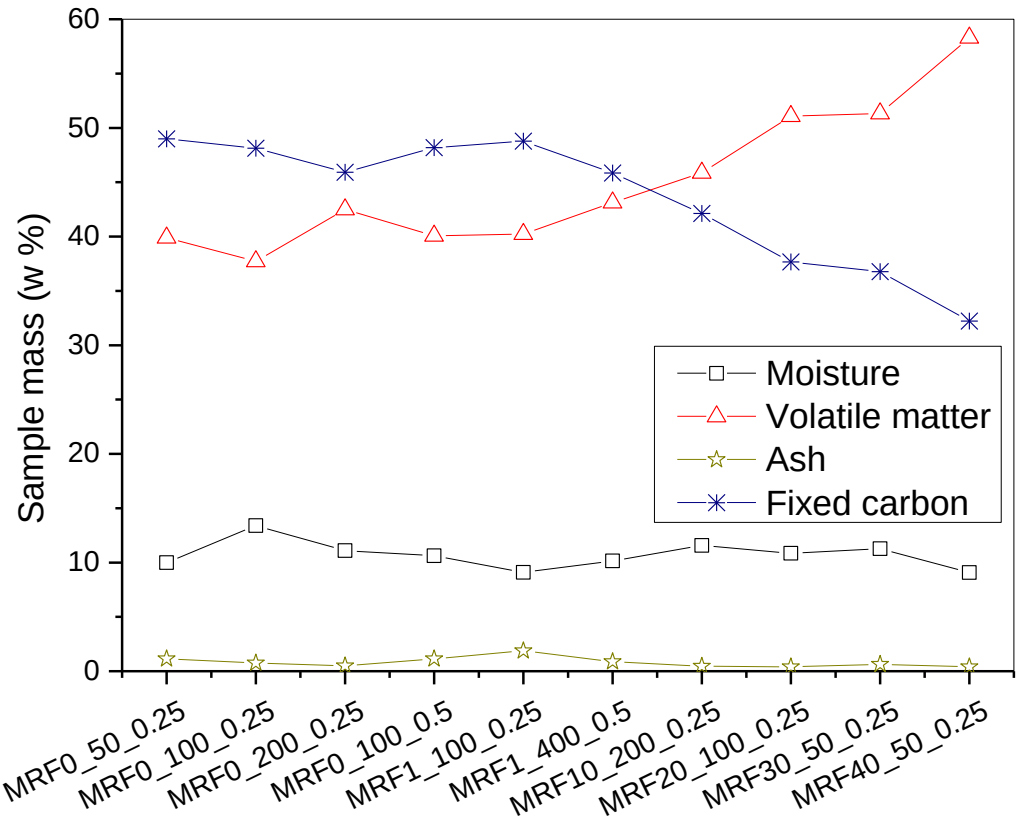

Figure 72: Proximate analysis showing mass percentage composition in MRF xerogel samples analysed.

7.8 Gravimetric CO_2 Adsorption Capacity

CO_2 uptake capacities of xerogels were tested at 0 and 60 °C by static adsorption measurements using an Intelligent Gravimetric Analyser (IGA), supplied by Hiden Isochema Ltd. As expected, the amount of CO_2 adsorbed at 0 °C is significantly higher than at 60 °C; however, an increase in CO_2 adsorption is observed, at each temperature, as [M] is increased. This confirms the expected enhancement of adsorption capacity by incorporation of nitrogen into the structure, which increases adsorption by exploiting the Lewis acid-base interactions between CO_2 molecules (acidic character) and basic functionalized adsorption sites on the surface of the MRF xerogels.

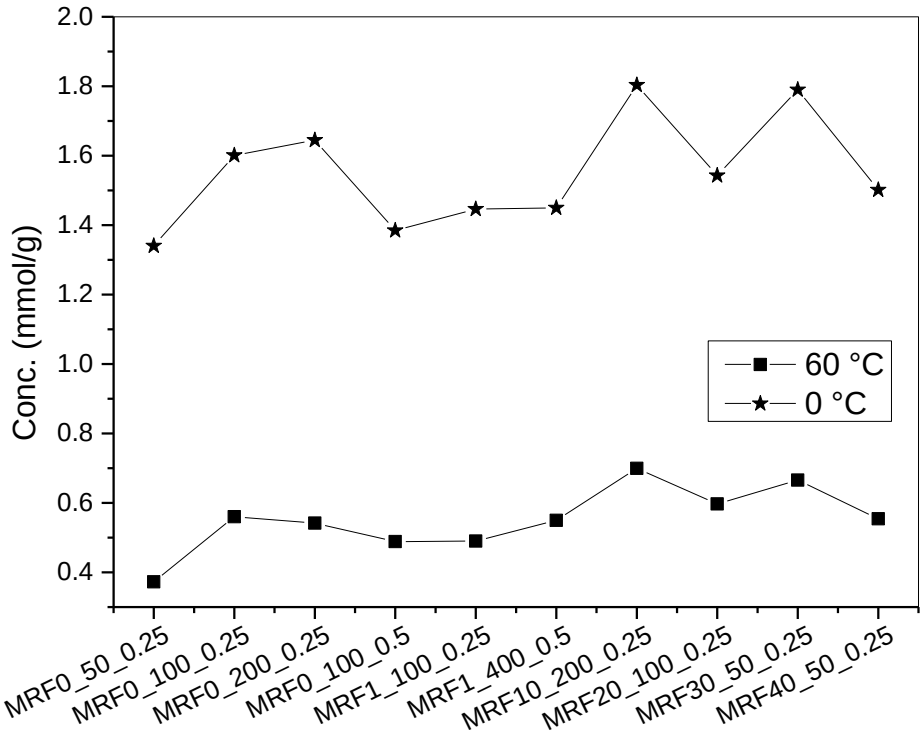

Figure 73: CO_2 adsorption capacity tested at 60 and 0 °C of MRF xerogel of variable R/C, R/F and [M].

CO_2 adsorption capacity decreases significantly at higher temperature, as expected for physical adsorption, which has an exothermic enthalpy associated with the process (ΔH). The CO_2 adsorption isotherms obtained (Figure 74) exhibit Type I character as classified by IUPAC [147], indicative of microporous materials; given the predominantly mesoporous character of the MRF materials tested, it is likely that adsorption of CO_2 is limited, under the conditions used, to the microporous region, hence, the Type I shapes observed.

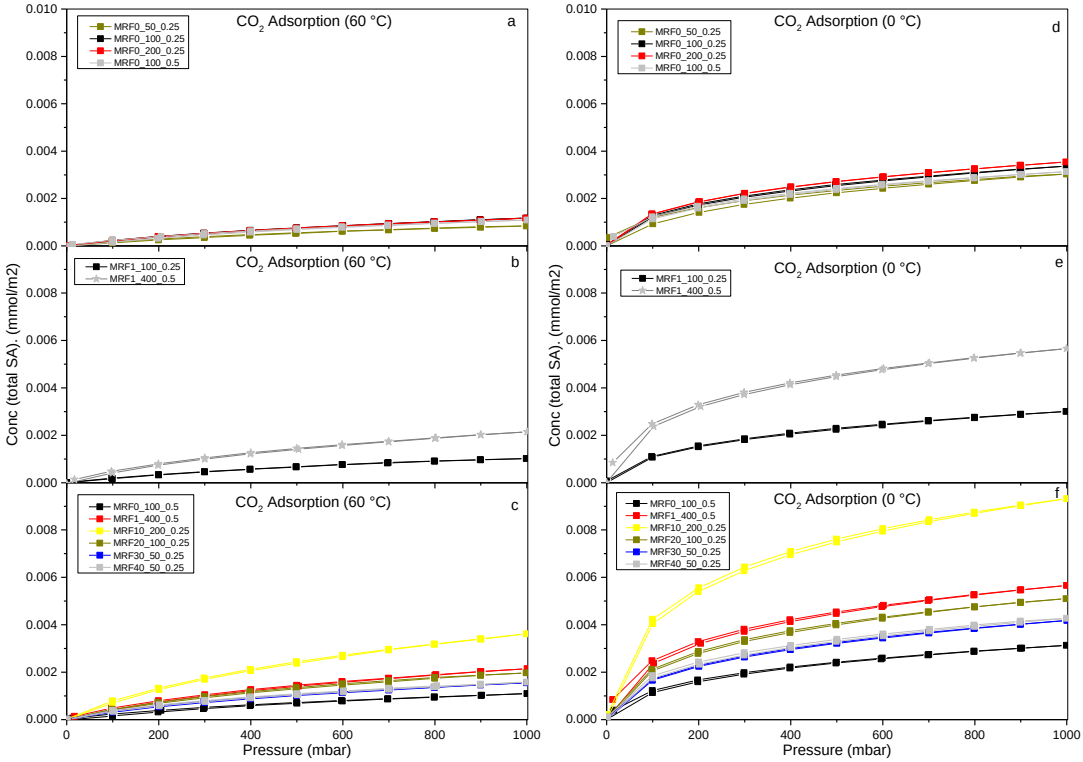

Figure 74: **CO_2 adsorption isotherm of MRF0_50_0.25, MRF0_100_0.25, MRF0_200_0.25 and MRF0_100_0.5 (a) at 60 °C and (d) at 0 °C. CO_2 adsorption isotherm of MRF1_100_0.25 and MRF1_400_0.5 (b) at 60 °C and (e) at 0 °C and CO_2 adsorption isotherm of MRF0_100_0.5, MRF1_400_0.5, MRF10_200_0.25, MRF20_100_0.25, MRF30_50_0.25 and MRF40_50_0.25 all samples of similar micropore volume (~0.03 cm^3/g) (c) at 60 °C and (f) at 0 °C.**

Data presented in Figure 74 has been normalized in reference to the surface area of each material, which has been measured by BET (Table 9). Figure 74 shows a significant increase in CO_2 adsorption at 0 and 60 °C, which is attributed to the effect of nitrogen incorporated into the structure of the MRF xerogel. Surface nitrogen groups enhance the interaction between CO_2 molecules and the xerogel material. The trend observed is independent of temperature; however, capacity drops significantly at higher temperature as adsorptive molecules have greater kinetic energy, which reduces the likelihood of attachment to the surface, and the increased temperature also increases desorption due to the exothermic nature of physisorption.

7.9 Thermodynamics of Adsorption

The isosteric enthalpies (ΔH_i) and entropies (ΔS_i) of adsorption were calculated at constant concentration of CO_2 adsorbed using Equation 64:

$$Ln(p) = \frac{\Delta H_i}{RT} - \frac{\Delta S_i}{R} \qquad \text{Equation 64}$$

where p is the pressure required to adsorb a given molar uptake of gas at temperature T, and R is the gas constant (8.314 J/K mol). The results obtained are shown in Figure 75.

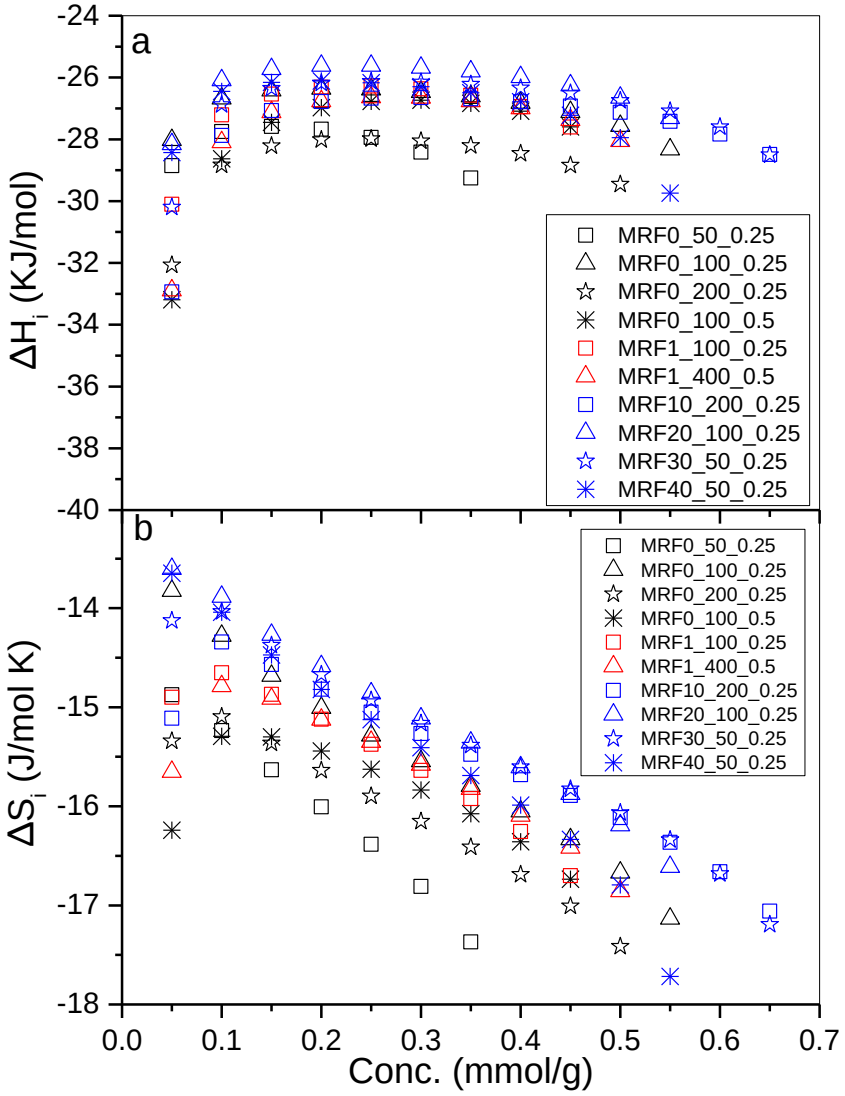

Figure 75: **Variation of (a) enthalpies of adsorption and (b) entropies of adsorption for CO2 adsorption on MRF xerogels.**

The data shows a variation in enthalpy and entropy of adsorption of CO_2 on MRF xerogels with pressure for all materials studied. However, enthalpies of adsorption do not vary significantly with increasing melamine concentration; with only ~1-2 kJ/mol difference for higher melamine contents (10, 20, 30 and 40) compared to the MRF0 series. In all cases, the heat of adsorption falls within the range ~-30 to -25 kJ/mol, which is comparatively higher than the enthalpy of vaporization (15.326 kJ/mol) at -57.5 °C [194]. This indicates that adsorption is controlled by interactions other than condensation of the gas, and the

difference can be attributed to the enhanced adsorption potential offered by the microporous structures of these materials and, for the modified gels, further cooperative effects offered by the nitrogen centres incorporated from melamine. This suggests that the enthalpy of interaction between these two adsorption centres is comparable in strength. Entropies of adsorption in all cases decreases as concentration adsorbed increased; as known from thermodynamic theory, an increasingly negative entropy change indicates increasing order, which would be expected in the adsorption of adsorptive species from the gas phase to confinement in the adsorbed phase, and the associated reduction in degrees of freedom.

One of the drawbacks of using amine scrubbing for CO_2 adsorption is the large regenerative energy required to recover the gas and recycle the amine. Hence, it is desirous to develop, not only materials with a good capacity for CO_2 adsorption but also, materials that do not require the same level of thermal stimulus for gas recovery as existing technologies. The low energy penalty observed for adsorption of CO_2 on the materials studied here suggests such a gain in this case and energies that are comparable with adsorption in microporous voids; the comparatively low energy associated with incorporation of melamine into the xerogel structure, observed by CO_2 adsorption, can be explained by charge delocalisation effects on the melamine ring. The melamine includes two types of nitrogen functionality, the amines bound to the carbon of the ring and the pyridinic nitrogen in the ring. Amines would be less likely to interact with the CO_2 molecules, firstly because they would be consumed during the crosslinking process and secondly adsorption may be hindered for steric reasons. In contrast, pyridinic nitrogens would be more accessible to approaching CO_2 molecules. The heat of adsorption, or energy penalty, might be expected to increase due to this N – CO_2 interaction; however, regeneration has been tested successfully, with only pressure as the driving force. Therefore, the small energy penalty might be explained by this charge delocalisation within the ring, the three nitrogens present in the ring would 'donate' the charge from their lone pairs of electrons to stabilize the ring, therefore reducing the effective charge on these sites, resulting in a weaker interaction with CO_2 molecules and, therefore, a smaller energy penalty.

7.10 Kinetics of CO_2 Adsorption

Kinetics of adsorption were monitored also using an IGA system. The pressure was increased over a set period of time until the desired value was achieved. The pressure at

the set point was controlled by active computer control of the inlet/outlet valves to maintain the required pressure. During this process, mass uptake was monitored as a function of time until equilibrium was achieved, after which the pressure was increased to the next set point, thereby repeating the process. The mass uptake due to adsorption for each pressure step was used to determine the kinetic parameters for adsorption using a set of nested kinetic models, selected on the combined basis of whichever best described the observed behaviour with the fewest variables.

CO_2 adsorption on porous MRF xerogels followed a stretched exponential (SE) mass transfer model in all cases, and kinetic parameters were determined over the relative pressure range up to ~0.98 bar at ~0 °C.

The SE model is described by Equation 65:

$$\frac{M_t}{M_e} = 1 - e^{-kt^{\beta 1}} \qquad \text{Equation 65}$$

where M_t and M_e are the mass uptake at time t and equilibrium, respectively, k is the rate constant and β the exponent of adsorption.

The SE model most appropriately described the behaviour observed for most of the xerogels tested at 0 °C; however, particularly in the case of MRF0_50_0.25, it was more difficult to determine the most suitable model given that the DE (double exponential, Equation 66) model also described the kinetic profiles adequately. Despite the fact that the DE model provided fits that were as good as, or in a few cases better than, the SE model, it is important to remember that, in general, DE would generally fit better than SE by virtue of the introduction of more parameters within the model; therefore, the fitting should be improved but there may not always be a rationale for the increased variables themselves.

$$\frac{M_t}{M_e} = A_1\left(1 - e^{-k_1 t}\right) + (1 - A_1) \cdot \left(1 - e^{k_2 t}\right) \qquad \text{Equation 66}$$

However, in order to determine the mass transfer model that best describes the adsorption behaviour of MRF xerogels, it is important to see the overall results from all materials tested and the trends exhibited therein.

Figure 76 shows fitting residuals for both SE and DE models for MRF0_50_0.25 for an adsorption pressure step between ~100-200 mbar. The DE model fits slightly better than SE, however, it is important to note that this step took the maximum time set for equilibration (180 min), which occurred for most points within this isotherm, suggesting that the mass uptake was not yet fully equilibrated. For this reason, both residual values exceed 0.02% at higher normalised time (n-time).

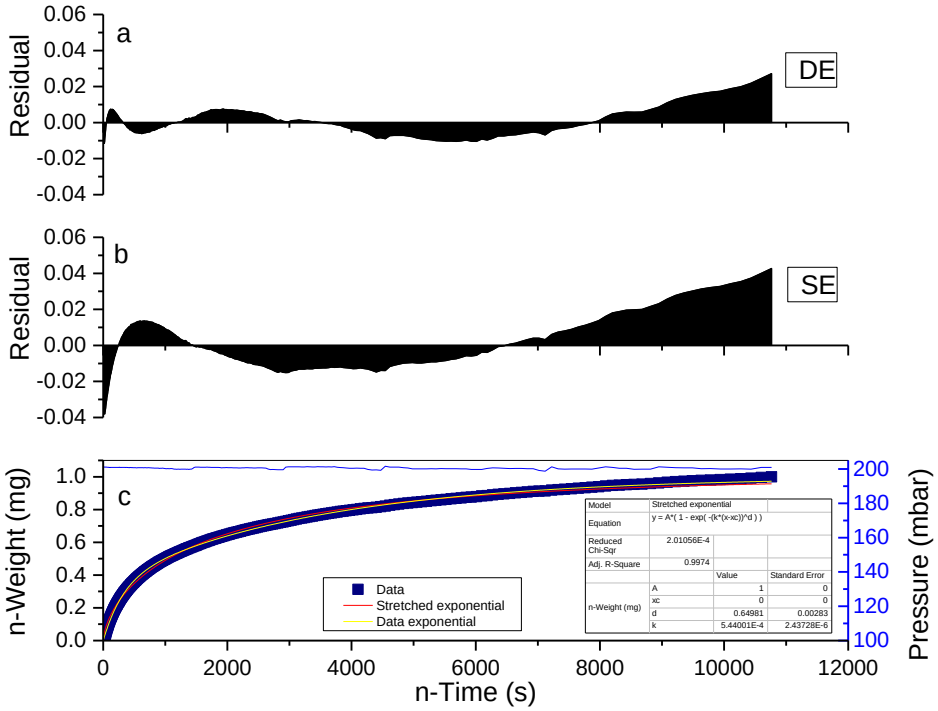

Figure 76: Residual values for (a) DE and (b) SE models across the (c) mass profile for MRF0_50_0.25 for a pressure step from ~100-200 mbar.

A similar behaviour was observed for most of the mass profiles collected at different pressure steps, as shown in Figure 77.

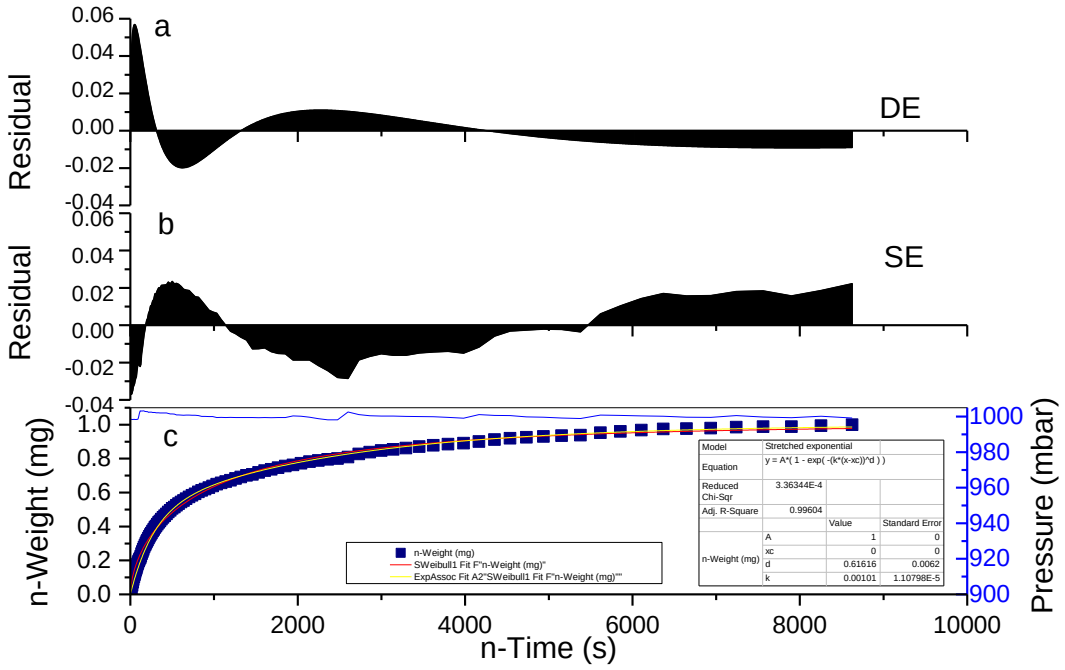

Figure 77: **Residual values for (a) DE and (b) SE models across the (c) mass profile for MRF0_50_0.25 for a pressure step from ~900-1000 mbar.**

Figure 78 shows the calculated rate constant using both DE and SE model for adsorption of CO_2 at 0 °C. The k_2 rate constants of the DE model would dominate adsorption, if described by DE (k_2 being the slowest rate constants). It should be noted that the k_2 values for the DE model are of the same order of magnitude as those singularly obtained from the SE model.

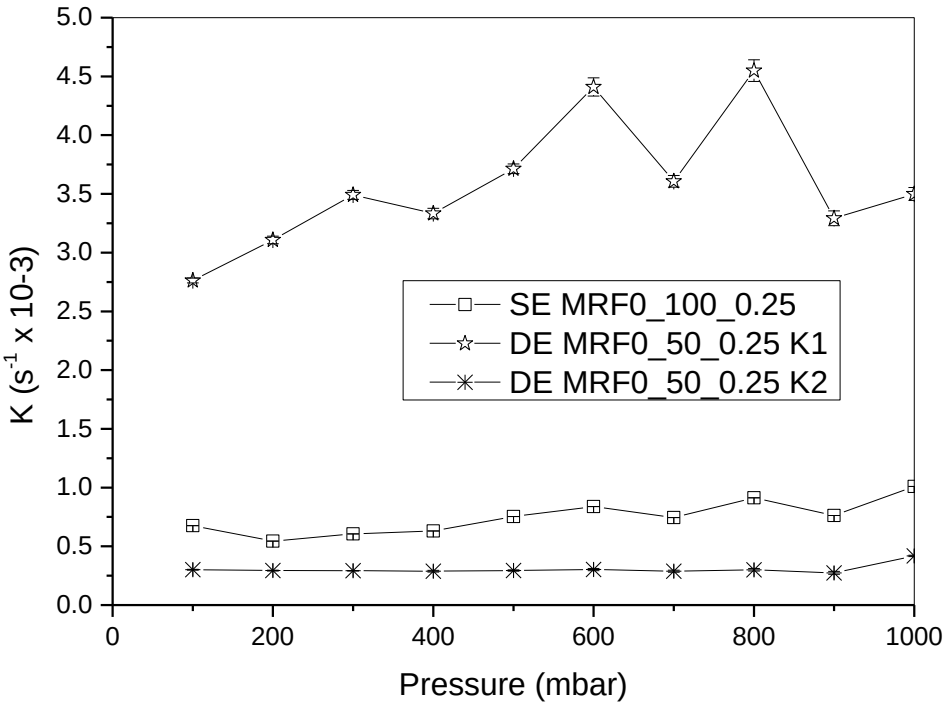

Figure 78: **Rate constants obtained at 0 °C for adsorption of CO_2 from DE and SE model for MRF0_50_0.25.**

Figure 79 to 90 show examples of the mass profiles obtained for all materials tested at 0 °C, fitted using the SE model.

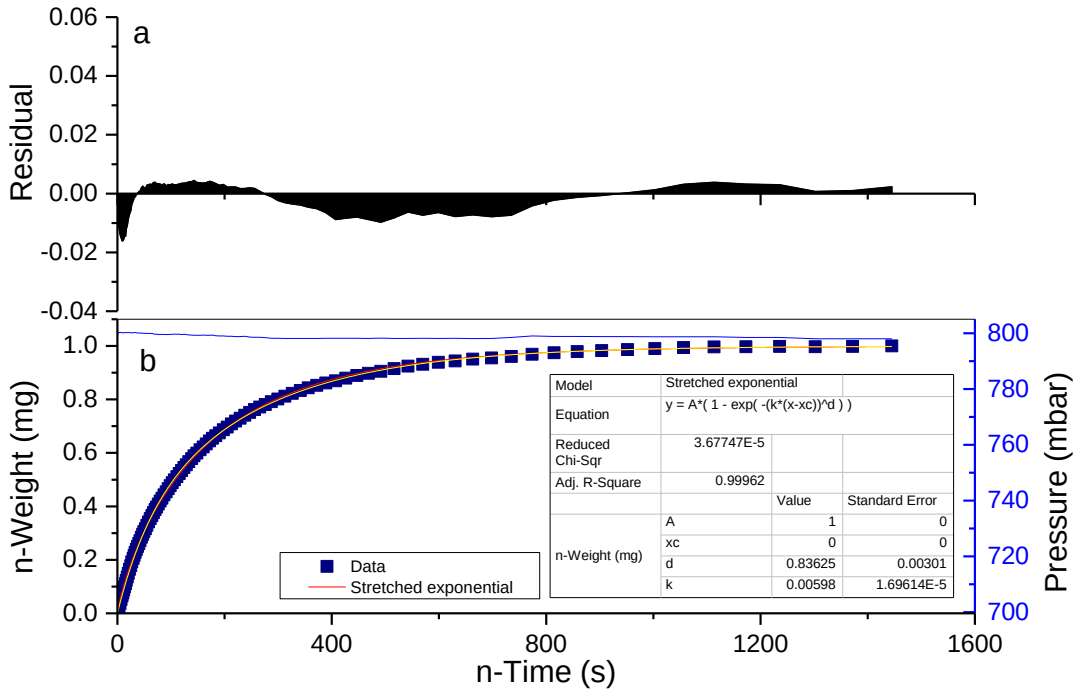

Figure 79: **Residual values for (a) the SE model across the (b) mass profile for MRF0_100_0.25 for a pressure step from ~700-800 mbar.**

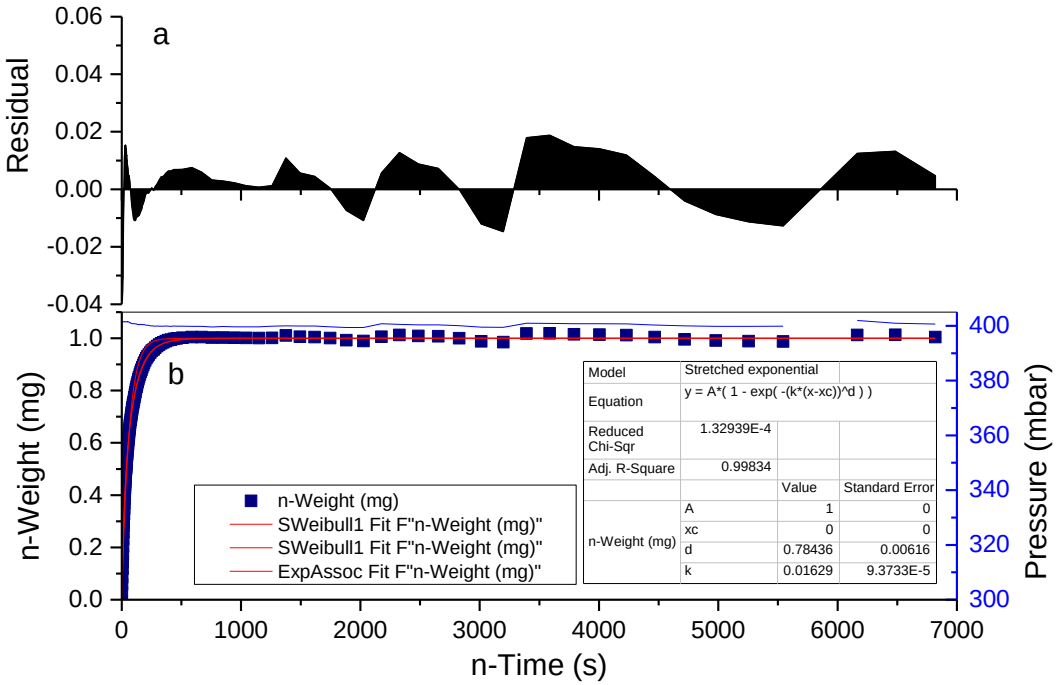

Figure 80: **Residual values for (a) the SE model across the (b) mass profile for MRF0_200_0.25 for a pressure step from ~300-400 mbar.**

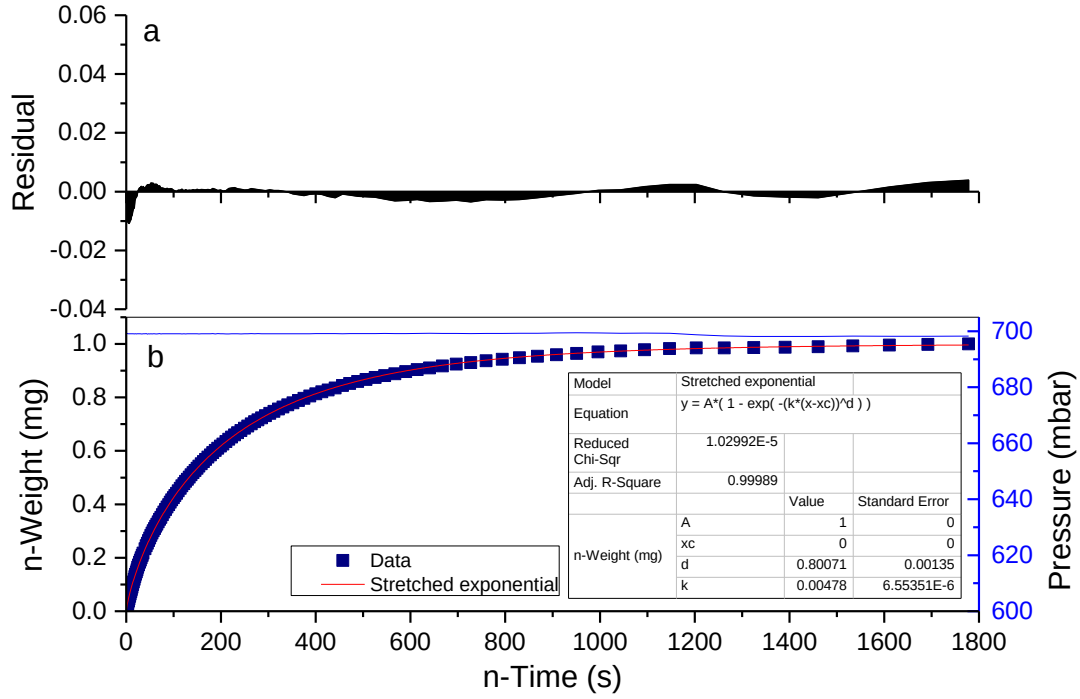

Figure 81: **Residual values for (a) the SE model across the (b) mass profile for MRF0_100_0.5 for a pressure step from ~600-700 mbar.**

Figure 82 summarizes the rate constants obtained from the SE model to describe the kinetics of CO_2 adsorption onto MRF0 xerogels of various R/C and R/F.

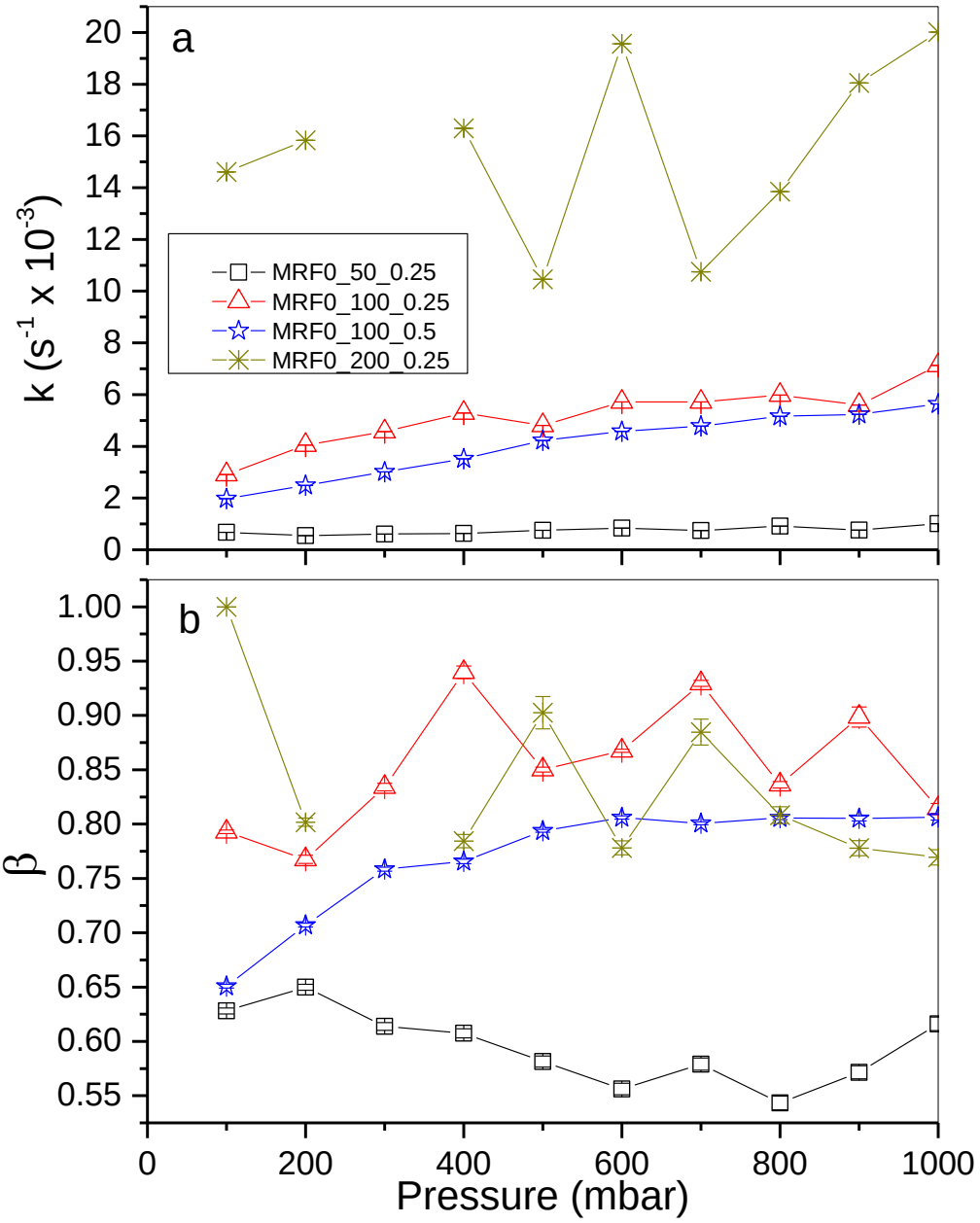

Figure 82: **Kinetic parameters obtained at 0 °C from the SE model: (a) rate constants (k) for adsorption of CO_2 on MRF xerogels and (b) the corresponding exponents (β).**

Figure 82 shows that, as R/C is increased, the kinetics of adsorption become faster; this behaviour is observed for MRF0_50_0.25, MRF0_100_0.25 and MRF0_200_0.25. As R/C increases, average pore size increases from 2, 3 and 5 nm, respectively. Therefore, diffusion of the gas stream should be facilitated as R/C increases. MRF0_100_0.5 shows similar behaviour as MRF0_100_0.25 suggesting that R/F has little effect on the kinetics of

adsorption of CO_2 onto MRF xerogels. As pressure is increased, rate constants tend to increase because adsorption is favoured at higher pressure, which may due to the fact that adsorbate molecules would tend to condense more readily within the pores as pressure is increased and/or molecules would possess more energy to overcome diffusional barriers at pore entrances.

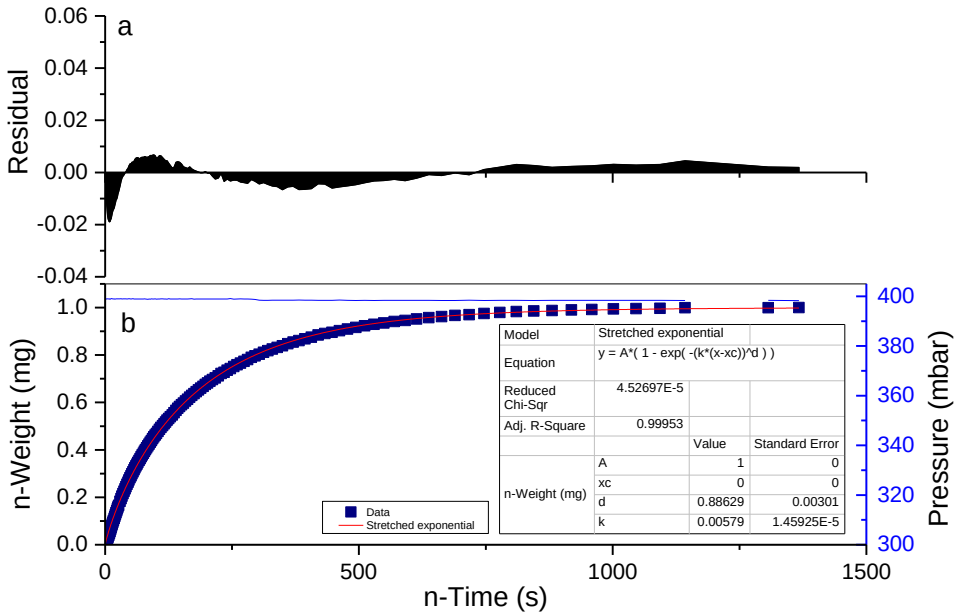

Figure 83: **Residual values for (a) the SE model across the (b) mass profile for MRF1_100_0.25 for a pressure step from ~600-700 mbar.**

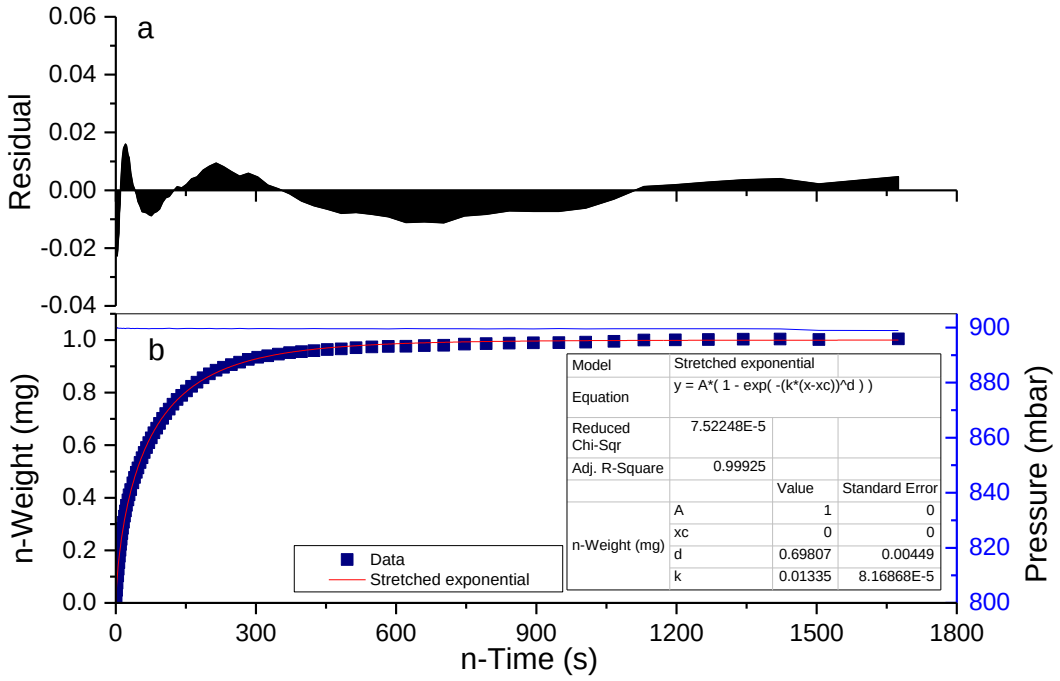

Figure 84: **Residual values for (a) the SE model across the (b) mass profile for MRF1_400_0.5 for a pressure step from ~600-700 mbar.**

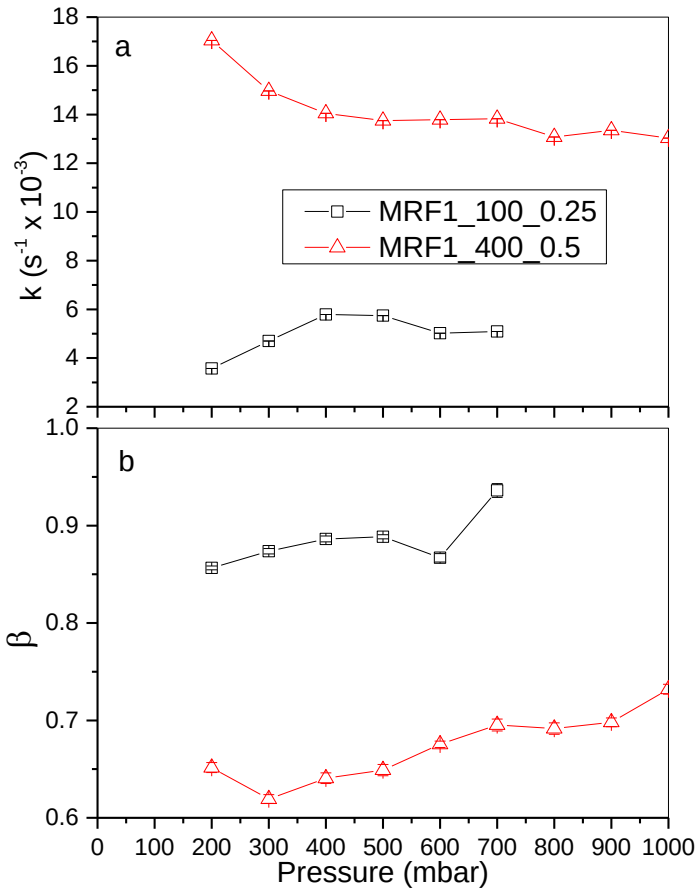

Figure 85: **Kinetic parameters obtained at 0 °C from the SE model: (a) rate constants (k) for adsorption of CO_2 on MRF xerogels and (b) the corresponding exponents (β).**

Figure 85 confirms that, as R/C is increased, higher rate constants are obtained for CO_2 adsorption on MRF xerogels.

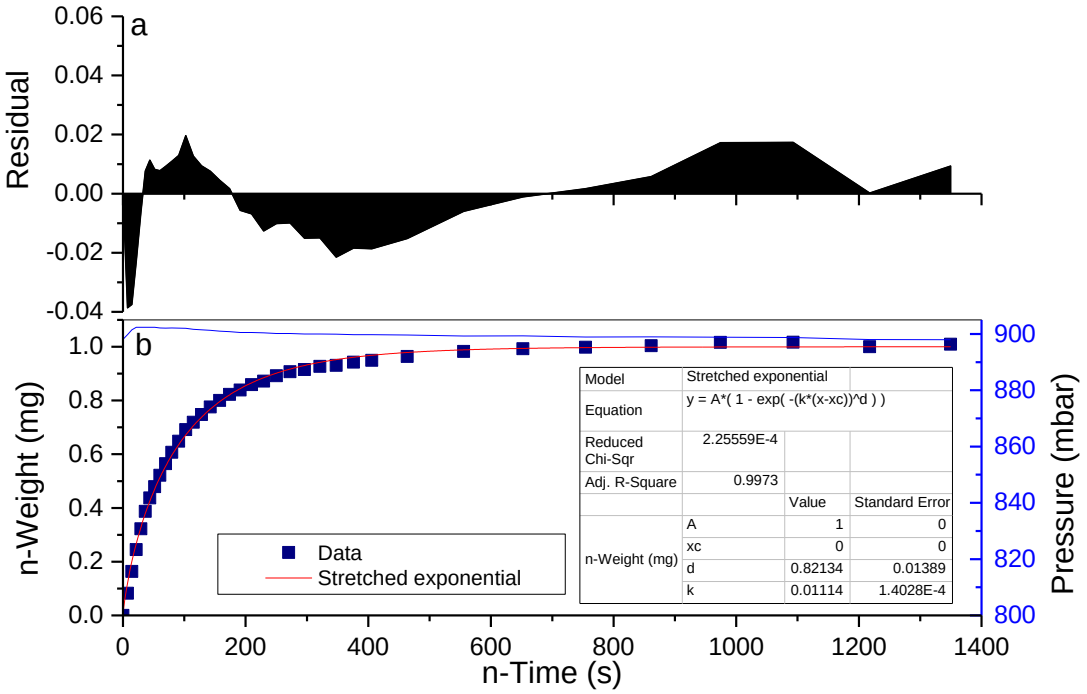

Figure 86: Residual values for (a) the SE model across the (b) mass profile for MRF10_200_0.25 for a pressure step from ~800-900 mbar.

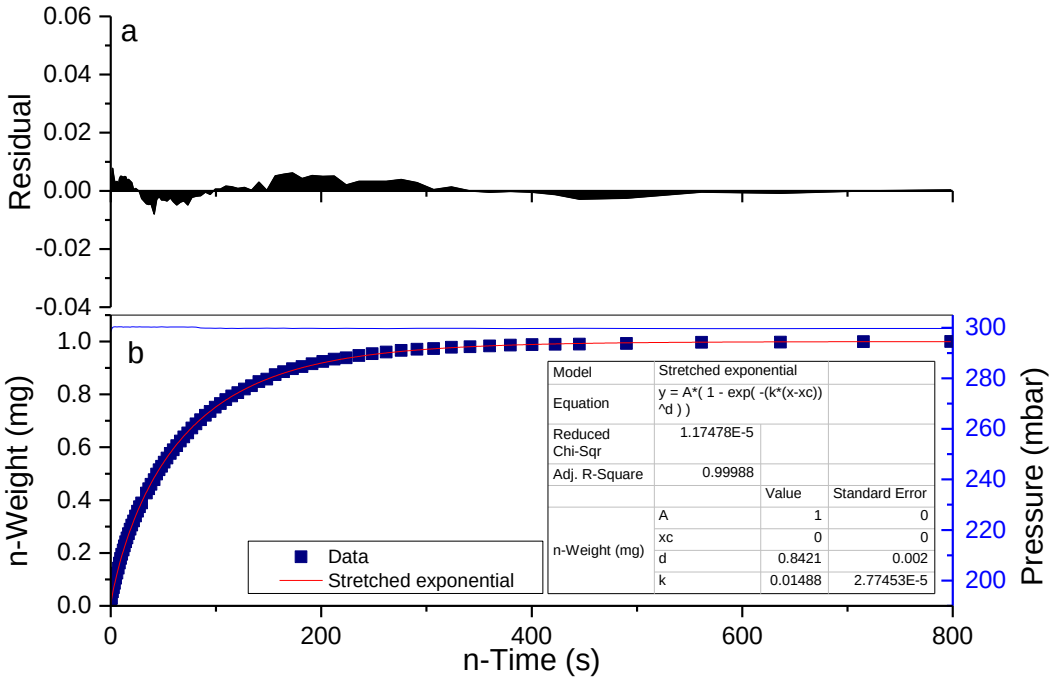

Figure 87: **Residual values for (a) the SE model across the (b) mass profile for MRF20_100_0.25 for a pressure step from ~200-300 mbar.**

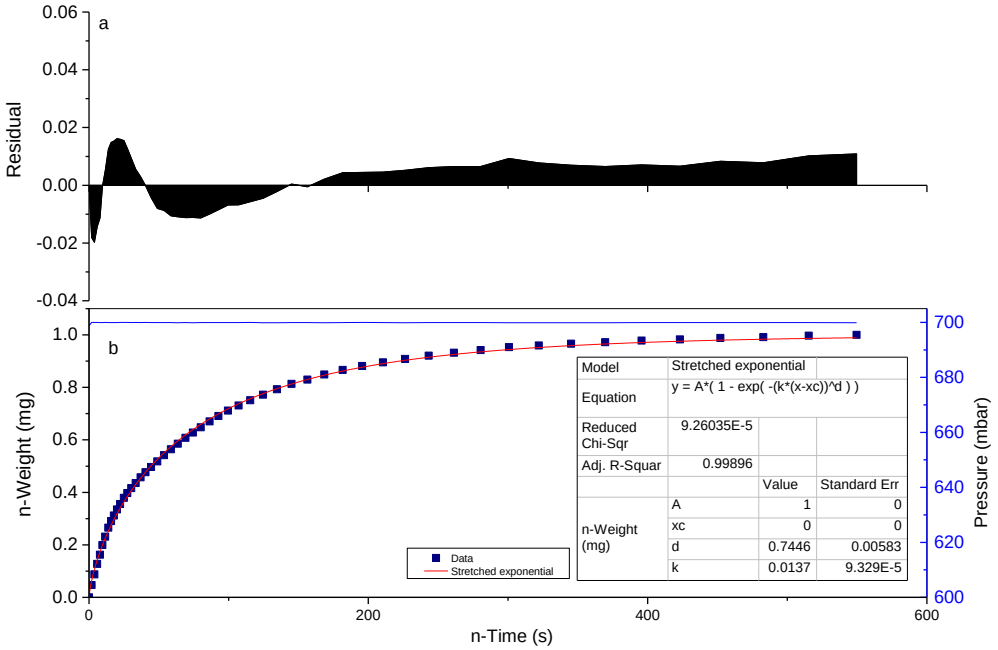

Figure 88: **Residual values for (a) the SE model across the (b) mass profile for MRF30_50_0.25 for a pressure step from ~600-700 mbar.**

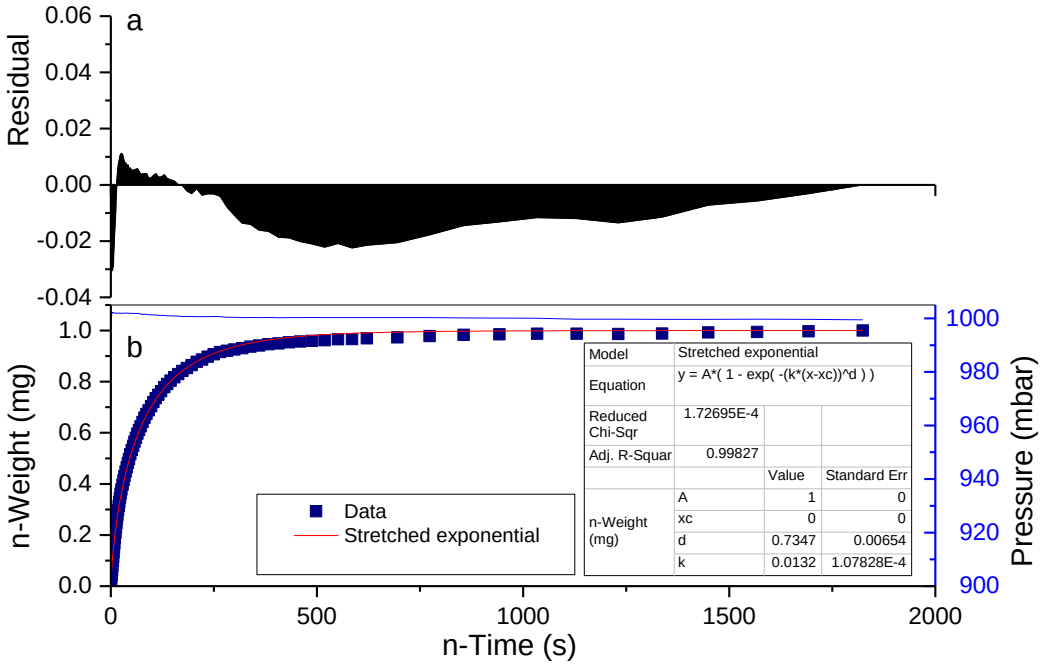

Figure 89: **Residual values for (a) the SE model across the (b) mass profile for MRF40_50_0.25 for a pressure step from ~900-1000 mbar.**

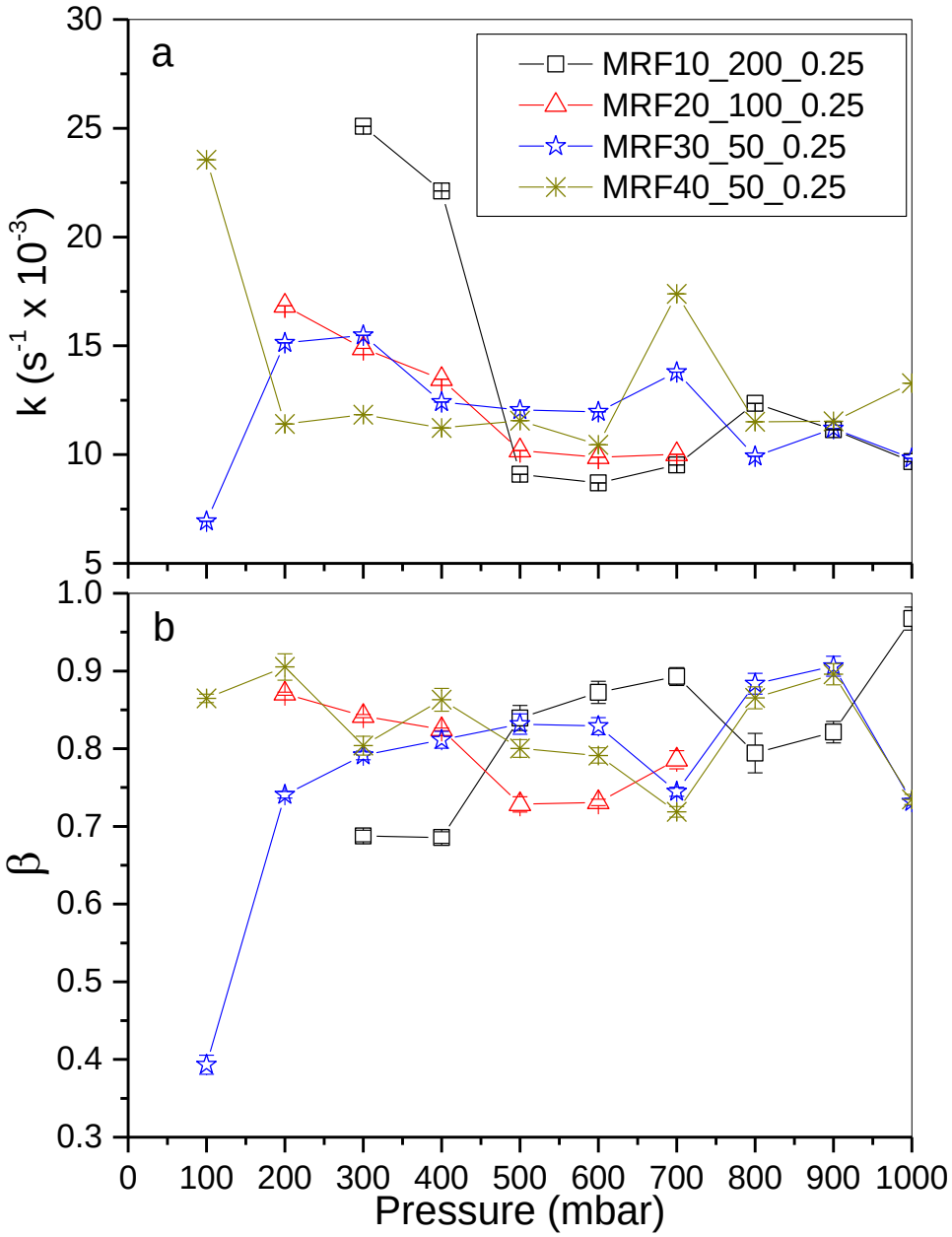

Figure 90: **Kinetic parameters obtained at 0 °C from the SE model: (a) rate constants (k) for adsorption of CO_2 on MRF xerogels and (b) the corresponding exponents (β).**

Adsorption on MRF xerogels involves diffusion through a porous system, which may exhibit different shapes, such as bottle neck-like or spherical characteristics; these differences markedly affect the diffusion of gas molecules through the material network. Adsorption of CO_2 onto the MRF xerogel surface should be enhanced by interactions between the adsorbate and surface functional groups; as [M] is increased, a higher number of interactions between CO_2 molecules and the MRF surface are expected. Rate constants obtained within this study suggest this to be the case; as melamine concentration is

increased from 0 through to 40 %, the rate constants for adsorption also increase. As pressure is increased (Figure 90b), the exponent tends to values closer to 1, suggesting a behaviour 'closer' to the LDF model.

Physical adsorption is an exothermic process, therefore, at high temperatures, such as at 60 °C, it becomes very difficult to assess kinetics of adsorption. The uptake at such high temperatures is reduced while the speed on uptake increases, meaning that equilibrium is achieved within a shorter timescale. Additionally, adsorptive/adsorbate molecules possess higher kinetic energy, therefore, they tend to desorb easily from the xerogel surface. Due to the fit residuals obtained and to maintain a consistent model over the whole pressure range, the rate constants for CO_2 adsorption on the surface of MRF xerogels have been obtained from the SE model. Results are shown in Figure 91 to 93

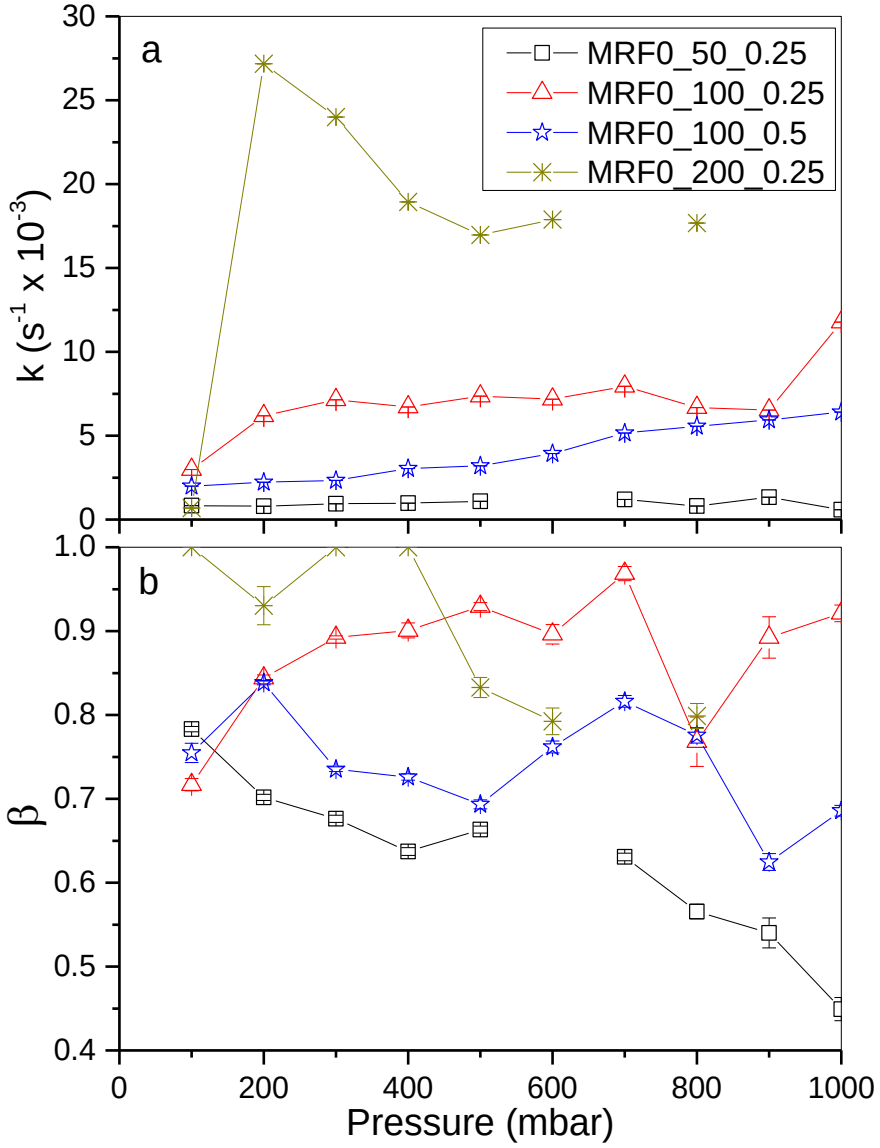

Figure 91: **Kinetic parameters obtained at 60 °C from the SE model: (a) rate constants (k) for adsorption of CO_2 on MRF xerogels and (b) the corresponding exponents (β).**

MRF0 xerogels exhibit rate constants for CO_2 adsorption of the same order of magnitude at both temperatures studied (60 °C: Figure 91 and 0 °C: Figure 82). In contrast, the exponent, *β*, exhibits higher values at higher temperature, suggesting behaviour more aligned with the LDF model at increased temperatures, i.e. a reduction in the width of the rate distribution. It should also be noted that the *β* exponent tends to decrease as pressure is increased and a similar trend is observed for both temperatures. As R/C is increased, (MRF0_50_0.25, MRF0_100_0.25 and MRF0_200_0.25) rate constant increases and the same observation is true for *β*. This trend is influenced by the increase in pore size, and pore volume, as R/C is increased, which facilitates diffusion of gases through the porous

network of the gels. MRF0_100_0.25 and MRF0_100_0.5 follow the same trend, with similar rates, again, suggesting that R/F has very little, or almost negligible, impact on the kinetics of adsorption of CO_2 on MRF xerogels.

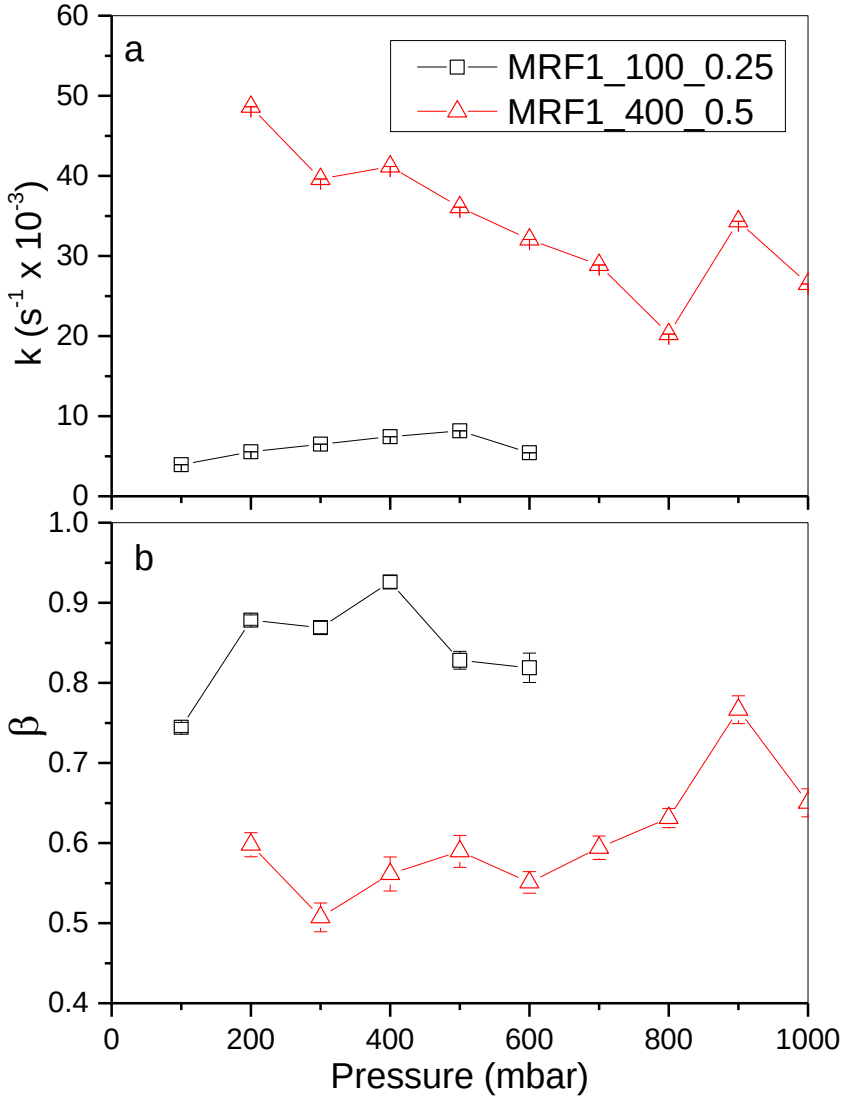

Figure 92: **Kinetic parameters obtained at 60 °C from the SE model: (a) rate constants (k) for adsorption of CO_2 on MRF xerogels and (b) the corresponding exponents (β).**

Similarly, the rate constants obtained for MRF1 xerogels at 60 °C (Figure 92) display behaviour similar to that observed at 0 °C (Figure 85). MRF1_400_0.5 exhibits significantly higher rate constants at 60 °C than at 0 °C, and, at both temperatures, the rate decreases as pressure increases. In contrast, MRF1_100_0.25 exhibits rate constants of similar value at both temperatures, suggesting that the kinetics of gas diffusion through its structure is highly influenced by its narrow pore size distribution and more 'closed' structure in comparison to MRF1_400_0.5.

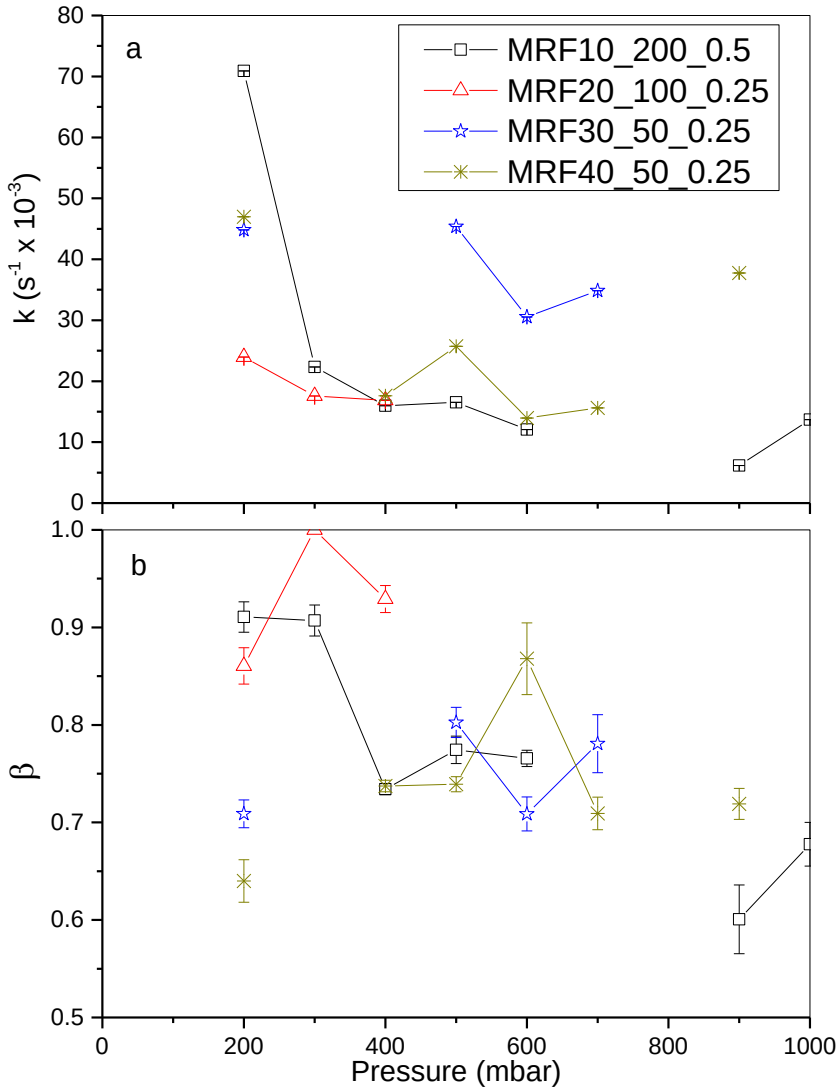

Figure 93: **Kinetic parameters obtained at 60 °C from the SE model: (a) rate constants (k) for adsorption of CO_2 on MRF xerogels and (b) the corresponding exponents (β).**

The behaviour observed for MRF of higher melamine contents (10, 20, 30 and 30 %) differs significantly at 60 °C compared with 0 °C. Observing the exponent, it can be stated that at 0 °C increasing the pressure results in *β* tending to unity (LDF model), while at 60 °C the opposite is true. As detailed above, at higher temperatures, the uptake is reduced and adsorbate/adsorptive molecules have greater kinetic energy, therefore, they tend not to adsorb as easily onto the xerogel surface given the exothermic nature of physisorption. Rate constants at 60 °C are significantly higher than those at 0 °C. However, at 0 °C they tend to decrease while at 60 °C they tend to increase. However, given the difficulty in obtaining rate constants at higher temperatures it was not possible to assess the full range of pressure (0-1000 mbar) in all cases.

7.11 Adsorption Activation Energies

The barriers to diffusion for adsorption of CO_2 over the pressure range ~0-1000 mbar were calculated for pressures steps of ~100 mbar using the Arrhenius equation, Equation 67.

$$k = Ae^{\frac{-Ea}{RT}} \qquad \text{Equation 67}$$

where *k* is the rate constants calculated from the SE kinetic model in this study, *A* is the pre-exponential factor, *Ea* is the activation energy, *R* is the universal gas constant and *T* is the temperature of adsorption.

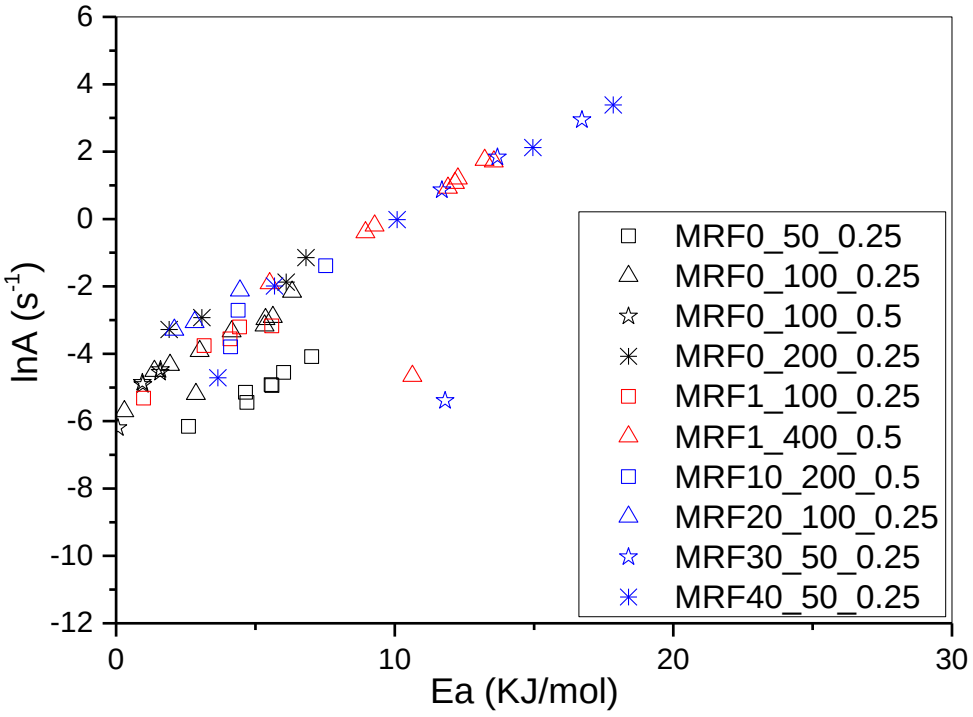

Figure 94: Variation of ln (pre-exponential factor) (ln(A)) with activation energy (Ea) for adsorption of CO_2 on MRF xerogels.

Figure 94 shows the relationship between ln(A) and Ea, which is in agreement with results reported for carbon based materials [195-197]. The data presented can be split into 3 subsets, the MRF0 series, MRF1 samples and higher [M] xerogels. As [M] increases, activation energies tend to larger values, suggesting an increase in the strength of barriers of diffusion. There may be several contributions to the increase in diffusional barriers for these materials, such as charge effects, steric effects or CO_2 alignment onto adsorption sites. The charge effect refers to possible polarization or partial charges on the MRF surface, which might interact with the CO_2 molecule. However, there is, a more likely, and

larger contribution from steric effects as a result of functional groups, such as amines from melamine, present on the surface. These groups might block, or partially block, the entrance of pores. Additionally, these groups would have thermal mobility; therefore, they would vibrate, especially at higher temperatures, which would result in potentially greater blockage of pore entrances. This contrasts, with the pore size increasing as melamine increases, which should minimize the aforementioned steric effect. However, as [M] is increased, pore volume and pore size also increase, while surface area decreases. Therefore, it can be said that the increase in pore volume does not necessarily result in an increase of 'useful' pore volume for CO_2 adsorption. For instance, the average pore size is observed to increase from ~2 nm (MRF0_50_0.25) to ~12 nm (MRF10_200_0.25); for these larger pores diffusion would not be affected by diffusional barriers, instead it can be considered as 'free diffusion'. Therefore, the activation energy measured would be more likely related to diffusion through small pores present in these materials, i.e. pore diameters close to the molecular dimensions of the probe gas (3.189 Å x 3.339 Å x 5.361 Å) [198]. These small pores would suffer from the same potential steric effects as the larger counterparts with increasing melamine concentration and, therefore, an increase in activation energy would be observed.

In addition to steric effects, alignment of CO_2 molecules onto specific adsorption sites may also affect kinetic energies. CO_2 molecules would interact differently with MRF0 (RF) than with a MRF xerogel synthesised with melamine, as a consequence of the chemical moieties present. While, CO_2 can adsorb on the graphitic basal planes of the gels, particularly in the micropores, there would be specific directionality onto the surface of a modified xerogel, when melamine is present, driven by the nitrogen group position. A CO_2 molecule would tend to be attracted to nitrogen, because of its free lone pair of electrons, which interact with the partial positive charge on the carbon of CO_2, induced as a result of the electronegativity of oxygen. As a consequence, the carbon atom would need to align with the nitrogen, which suggests that not all collisions would be successful in resulting in adsorption.

The ten materials tested in this study have similar micropore volumes (~0.03 cm^3/g), therefore, considering an adsorbed density of 1.023 g/cm^3 and molecular weight of 44.01 g/mol for CO_2, the maximum liquid capacity of the micropores would be ~0.698 mmol/g. The CO_2 uptake at 60 °C never exceeds, with only MRF10_200_0.25 equalling the uptake at

maximum pressure, however, the isotherm has not levelled off by this point indicating that the volume would be exceeded at a high enough pressure. Contrastingly, at 0 °C, the CO_2 adsorption uptake exceeds the CO_2 micropore volume in all cases, therefore, the adsorption uptake is beyond the micropore volume, potentially as a result of enhanced interactions with the material surface i.e. nitrogen functionalities. This accounts for the increase in uptake as [M] increases; the increased uptake at lower temperature is ascribed to the exothermic nature of physisorption in the micropores and onto the nitrogen groups within the walls of the larger pores (meso and macro). The activation energies observed here, in conjunction with the low energy penalty observed for those MRF of higher melamine content, suggests that CO_2 adsorption on MRF xerogels would be kinetically rather than thermodynamically controlled.

7.12 CO_2 Cycling

A series of CO_2 adsorption-desorption cycling tests were performed to assess the long-term working capacities, and stabilities, of the 10 samples studied in this chapter. Most samples underwent 90 cycles (charge and discharge) and one sample (MRF1_100_0.25) was exposed to 500 cycles. Results of these cycling studies show that MRF xerogels have the ability to retain their reversible storage capacity during the cycle interval tested, suggesting long term stability in terms of uptake and the samples themselves. This is complementary to the thermal stability results obtained by thermo-gravimetric analysis. Adsorption capacity can be measured as the difference between the charge and discharge cycles. Results obtained are shown in Figure 95 to 97.

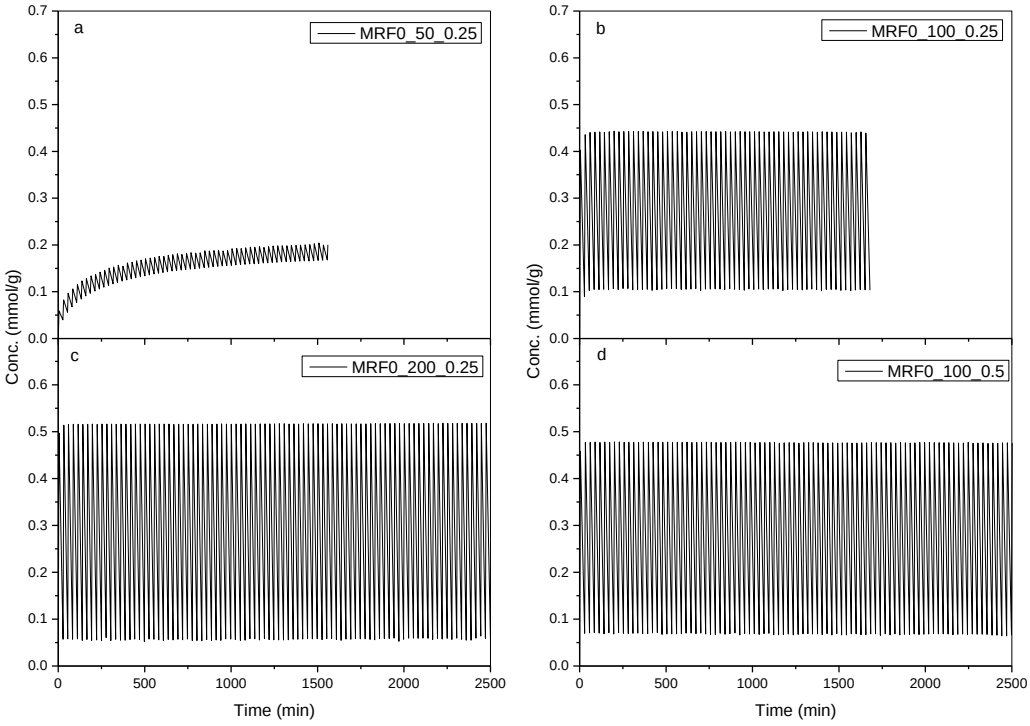

Figure 95: CO_2 adsorption capacities for (a) MRF0_50_0.25 over 60 cycles; (b) MRF0_100_0.25 over 60 cycles; (c) MRF0_200_0.25 over 90 cycles and (d) MRF0_100_0.5 over 90 cycles.

Figure 95 shows a significant increase in adsorption capacity for samples MRF0_50_0.25, MRF0_100_0.25 and MRF0_200_0.25. This enhanced capacity can be directly linked with the increase in R/C. As R/C increases so does pore size (2, 3, and 5 nm, respectively) and pore volume (0.239, 0.330 and 0.603 cm^3/g, respectively) as shown in Table 9. Therefore, the increase in adsorption capacity can be attributed to the larger pore volume, which can be accessed more easily for larger pore sizes. MRF0_100_0.5 (pore volume of 0.308 cm^3/g and pore size of 3 nm) exhibits an adsorption capacity slightly larger than MRF0_100_0.25, suggesting that, contrastingly, R/F has no significant impact on capacity.

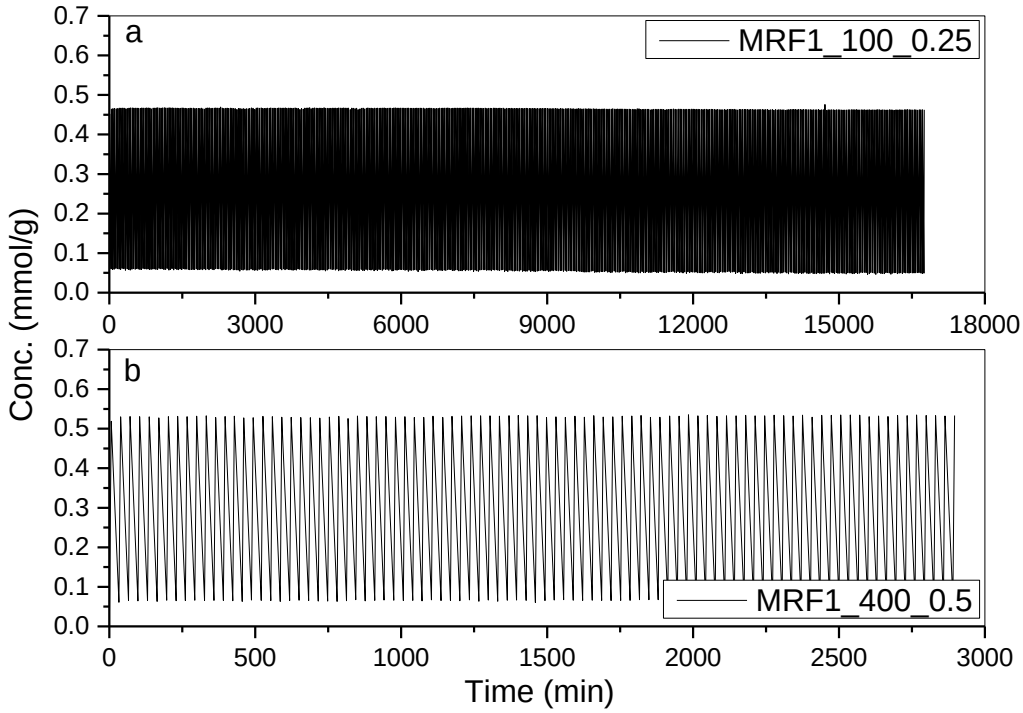

Figure 96: CO_2 adsorption capacities for (a) MRF1_100_0.25 over 500 cycles and (b) MRF1_400_0.5 over 90 cycles.

MRF1_400_0.5 shows an enhanced adsorption capacity compared to MRF1_100_0.25, which, as previously observed, can be attributed to the larger value of R/C used. It is important to note that the adsorption capacity of MRF1_400_0.5 has been observed to be stable up to 500 cycles, suggesting the high regenerative ability of this material.

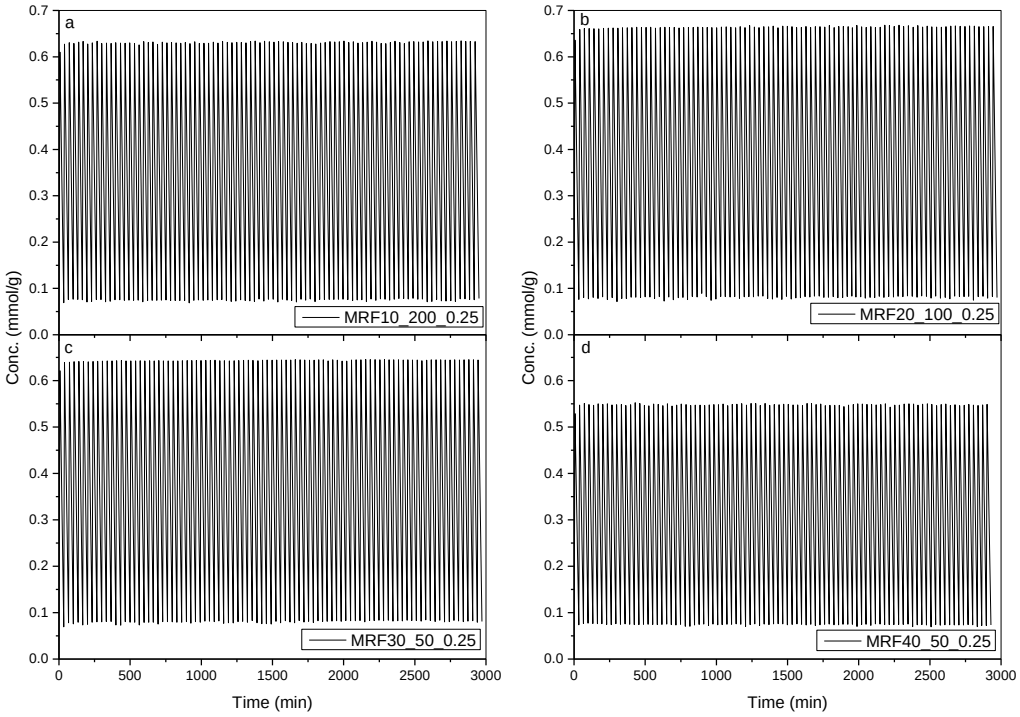

Figure 97: CO_2 adsorption capacities for (a) MRF10_200_0.25 over 90 cycles; (b) MRF20_100_0.25 over 90 cycles; (c) MRF30_50_0.25 over 90 cycles and (d) MRF40_50_0.5 over 90 cycles.

The reversible quantity of CO_2 (or any adsorbate) adsorbed between the lower and upper operating pressures (at a given temperature) of a system is more important industrially than the single maximum adsorption capacity. Adsorption isotherm shape defines the pressure range in which most of the reversible uptake occurs, however, the rate of adsorption/desorption will affect this property due to kinetic limitations. The shapes of the adsorption isotherms obtained for CO_2 on the MRF xerogels studied here are Type I (microporous), therefore, the storage adsorption capacity will be defined by the lowest range of pressure selected. The amount of CO_2 adsorbed per unit mass of material defines the gravimetric storage capacity which is shown in Figure 98. The storage capacity clearly increases as [M] is increased, with a maximum observed for MRF20_100_0.25, after which storage capacity falls despite the increase in [M]. This final reduction is likely due to the proportion of melamine in the synthetic matrix impinging on the ability of the gel network to successfully crosslink, producing a weaker gel, which may impact on accessibility of nitrogen functionalities within the material.

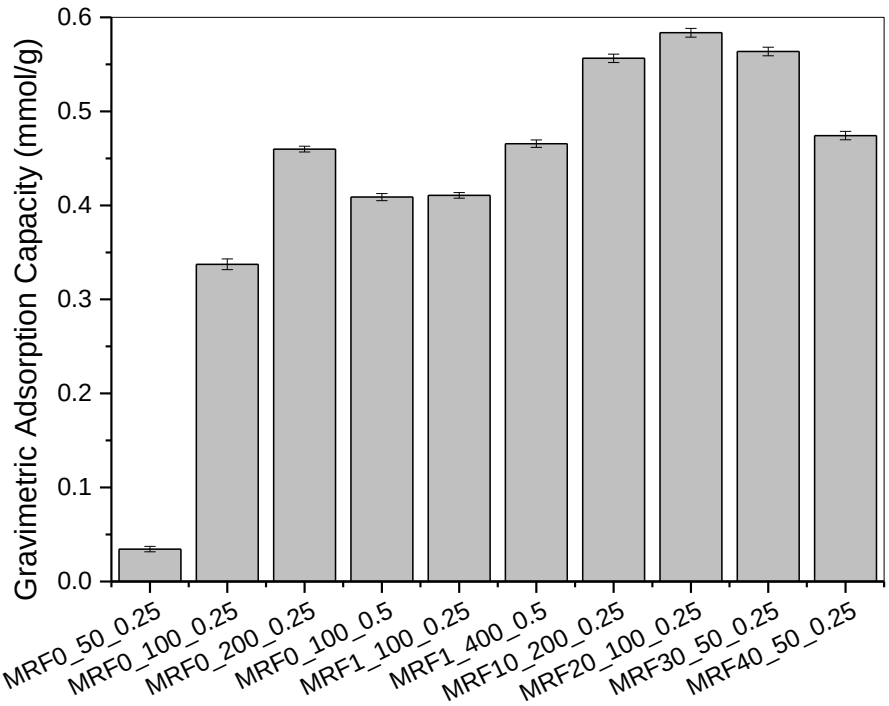

Figure 98: Gravimetric adsorption capacities of MRF xerogels of variable R/C, R/F and [M].

Grouping those materials with similar synthesis parameters allows the evaluation of the effect of nitrogen content on the adsorption capacity of MRF xerogels. The increase of nitrogen content in xerogels enhances CO_2 adsorption capacity as observed by comparison of gravimetric adsorption capacities of MRF0_100_0.25 (0.337 mmol/g), MRF1_100_0.25 (0.411 mmol/g) and MRF20_100_0.25 (0.584 mmol/g). A similar trend is observed for MRF0_200_0.25 (0.460 mmol/g) and MRF10_200_0.25 (0.556 mmol/g). However, it is also observed that this increase is limited at some level, as occurs for MRF0_50_0.25, MRF30_50_0.25 and MRF40_50_0.25. There is a significant increase in adsorption capacity when the melamine content increases up to 30 %, however, increasing again to 40 % actually results in deterioration of the adsorption capacity.

7.13 **Key Findings**

In this chapter, 10 samples were selected from the materials generated in Chapter 6. The selection was based on their micropore volume and N content. Boehm titration showed an increase in carbon basic surface functionalities (Ncsf) as [M] increases, reducing the concentration of phenolic groups. C=O bonding was observed to increase using FTIR and XPS, it was demonstrated that this bond appears as a consequence of the polymerisation reaction, a hypothesis was presented for this occurrence. Thermal stability was tested by

proximate analysis, and MRF xerogels exhibited high thermal stability, however it was found that volatile matter increases as [M] increases. CO_2 adsorption was tested both at 0 and 60 °C allowing not only to measure CO_2 capacity but also its kinetics of adsorption, which was observed to be fast at both temperature. MRF10_200_0.25 has exhibited the largest CO_2 adsorption capacity of the samples tested. This can be attributed to a 'balance effect', that is to say that, as [M] increases, so does pore volume and pore size, allowing an easier gas diffusion through the network of MRF xerogels. However, as pore size increases, microporosity is sacrificed, but this is compensated with the increase of successful interaction of CO_2 molecules with the surface of MRF xerogels. The working capacity was also determined from a series of cycling studies on the MRF selected samples. The working capacity was observed to increase with [M]. The measured heat of adsorption demonstrated that incorporation of nitrogen functionalities results in a low energy penalty, which demonstrates that the adsorption mechanism is still driven by physical forces even with the incorporation of the nitrogen groups. This is an important result in terms of regeneration of MRF xerogels.

Chapter 8
Results Part IV

8 Results Part IV – Competitive Analysis

This chapter reports results obtained from selectivity studies on the MRF xerogels used in this study, demonstrating the potential for selective adsorption of CO_2 from various gas mixtures. Three gas mixtures have been used: CO_2-N_2, CO_2-CH_4 and CO_2-H_2; these mixtures were chosen because all represent important gas separation applications in industry, such as CO_2 removal from flue gases from power plants (separation of CO_2-N_2), sour gas sweetening where hydrogen sulphide (H_2S) is a key component but CO_2 is also present requires separation (CO_2-CH_4 mixture) and separating species in the water-gas shift reaction (separation of CO_2-H_2).

8.1 Selection of MRF Xerogels

The xerogel materials used in this section were selected as being representative of three melamine concentrations used in the synthesis of the suite MRF xerogels produced in this work, herein classified as zero, low and high. Four materials were selected from those analysed in Chapter 7:

- MRF0_100_0.25
- MRF0_200_0.25
- MRF1_400_0.5
- MRF10_200_0.25

All MRF xerogels tested in Chapter 7 demonstrated high thermal stabilities and regenerative abilities; however, MRF0_50_0.25 exhibited low adsorption capacity during cycling (Figure 95), hence, it was not selected for further study. MRF0_100_0.25 and MRF0_200_0.25 are essentially RF xerogels, as no melamine was included in the synthetic matrix; they are selected here as they exhibited the highest CO_2 adsorption capacities from the four MRF0 samples studied in Chapter 7 (Figure 73 and 41). MRF0_100_0.25 and MRF0_100_0.5 demonstrated very similar nitrogen uptakes, pore size distributions (average diameter ~3 nm) and total pore volumes (0.330 and 0.308 cm^3/g, respectively), indicating that they have similar structures, hence, R/F ratio has very little influence on final gel properties in such systems (Table 9 and Figure 61). It is notable, however, that MRF0_100_0.25 exhibited a slightly higher CO_2 uptake (Figure 73), perhaps as a consequence of its larger micropore volume (~0.047 cm^3/g) than MRF0_100_0.5 (~0.031 cm^3/g). Additionally, rate constants for adsorption of CO_2 at both temperatures probed are

faster for both MRF0_100_0.25 and MRF0_200_0.25 (Figure 82 and Figure 91) than the other MRF0 samples.

Similarly, MRF1_400_0.5 exhibits a greater CO_2 adsorption capacity than MRF1_100_0.25 (Figure 73) despite its smaller micropore volume (~0.030 and 0.040 cm^3/g, respectively); however, the larger pore volume measured for MRF1_400_0.5 (~0.652 cm3/g) compared to MRF1_100_0.25 (~0.379 cm3/g), combined with a larger average pore size (~11 and 3 nm, respectively) can result in in a faster rate of diffusion (Figure 85 and 59). Both materials exhibit stable behaviour throughout cycling studies (Figure 96), however, the CO_2 working capacity was higher for MRF1_400_0.5 (Figure 98).

MRF10_200_0.5 was chosen as representative of the high melamine content MRF xerogels; this material had the smallest surface area of the ten materials studied in Chapter 7 (Table 9). However, it exhibited the largest CO_2 adsorption uptake (Figure 73 and 41) at both temperatures, and also exhibited fast adsorption kinetics (Figure 90 and 60), possibly helped by the increase in pore size at higher melamine concentrations, which facilitates gas diffusion through the MRF network. This material also exhibited stable behaviour during cycling (Figure 97). MRF20_100_0.25 gave a larger adsorption capacity during cycling than MRF10_200_0.25 (Figure 98), however, as previously described, increasing melamine content results in weaker crosslinking of the gel structures. This is supported by proximate analysis results, which show that volatile matter exceeds fixed carbon content for [M] >20% (Figure 72).

8.2 Selectivity of Adsorption for Mixture of CO_2-N_2

As explained in Chapter 1, power plants are one of the major contributors to CO_2 pollution; flue gases from power plants have varied compositions depending on the type of fuel used, but typically CO_2 levels will be 7-14 % for coal fired and 4 % for gas fired [23], sources. The remaining gas balance is composed mainly of N_2 and small quantities of other components. Flue gases from power plants are usually treated with a series of chemical processes and scrubbers to remove pollutants, while fabric filters or electrostatic precipitators are used to remove solid particles, specific units are used to remove sulphur dioxide (SO_2), which is typically a by-product when burning coal. CCS technologies have been developed to remove CO_2 from these pre-treated flue gases before they are released to the atmosphere. Nowadays, most CO_2 removal processes use liquid absorbents such as amines to clean CO_2 from exhaust gases.

Within the design of these experiments, it is important to recall that flue gases are a mixture of different species, depending on fuel used and plant configuration, such as NO_X, SO_X, CO, CO_2, N_2 and solid particles. As stated above, NO_X and SO_X, and solid particles, are generally filtered out by ceramic filters, catalysed filters or dry scrubbers [199-202]; however, this still leaves multiple components in the stream to be treated. Competitive adsorption studies cannot simply transition from single to more than two components, therefore, it is necessary to develop an understanding of the processes occurring by considering competing mixtures of two components that have each already been studied as single species. Consequently, in the studies undertaken here, CO_2 is present at a fixed proportion and the balance is composed of N_2, allowing the selectivity of the tested MRF gels, towards CO_2 over N_2, to be determined.

The mixture of gases used for CO_2 and N_2 competitive adsorption was 15 and 85 %, respectively. This concentration is closer to the higher end of the range of CO_2 concentrations in flue gases but should allow more accurate determination of the effect of competition given that a higher CO_2 concentration will result in a smaller margin of error in the adsorption isotherm of the gas mixture.

All adsorption tests presented in this chapter have been performed at 60 °C; at this temperature the adsorption of N_2 is expected to be very low, or nearly negligible. N_2 possesses a quadrupole but no defined charge moments, and the fluctuations of this quadrupole will increase with temperature, meaning that its adsorption potential, by physisorption, is very low. Contrastingly, CO_2 molecules are linear and the two oxygen atoms attract electron density from the covalent bonds with carbon, creating diploes within the molecules, by virtue of their comparative electronegativity. This will enhance interaction with the xerogel surface, while the incorporation of nitrogen in the xerogel structure, especially those in the ring (melamine), would provide additional interaction sites for CO_2 as acid-base interactions enhance adsorption. For the reasons mentioned above, it is expected that very low N_2 uptake would be observed at this temperature, in favour of CO_2.

Figure 99 to 102 show the adsorption isotherms obtained for both the pure components and gas mixtures described above. It is important to note that the concentrations presented in these graphs have been normalized by dividing through by available surface area (m^2) for the tested material (Table 9). Gravimetric adsorption measurements have

been corrected for the fact that they are conducted using gas flow rather than static environments, using the calibrations outlined in Chapter 4. These calibrations allow weight values to be obtained, which account for the uplift generated at specific pressures. It is important to note that such corrections could be performed using mass spectrometry of the outlet concentration, which is compared to the inlet concentration, allowing the quantity adsorbed to be calculated from the difference. The required equipment was not available for this study; hence, the previously described calibration test was developed to assess the adsorption uptake for flowing measurements conducted on the IGA.

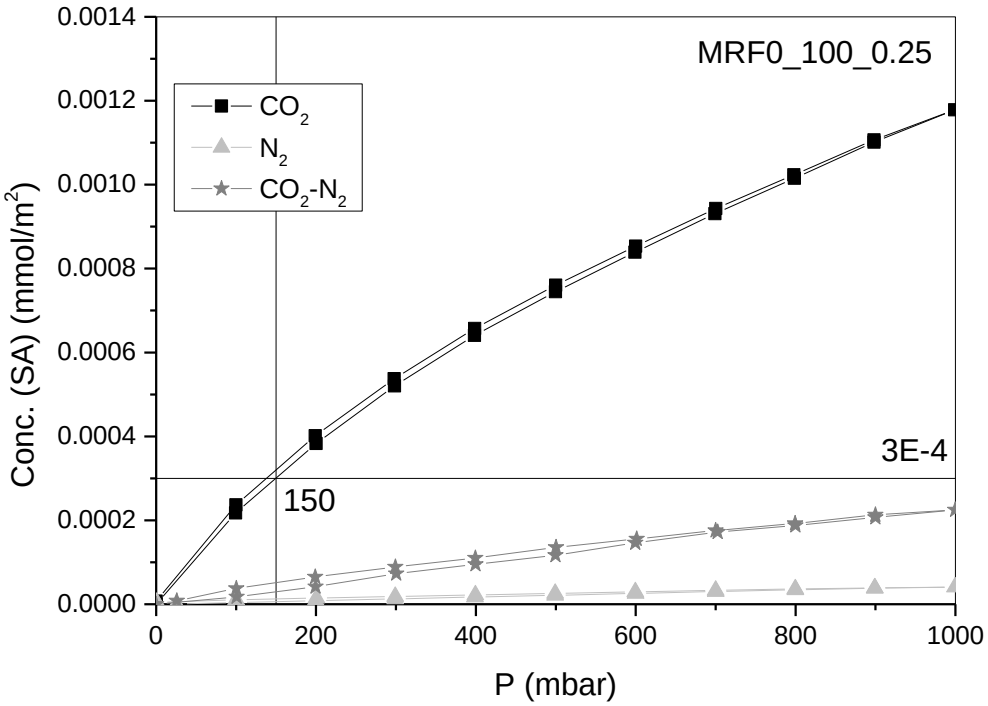

Figure 99: Gas adsorption uptake of CO_2, N_2 and mixture CO_2-N_2 (15-85 %) tested with intelligent gravimetric analyser (IGA) at 60 °C under flow conditions of 200 cm^3 min^{-1} for MRF0_100_0.25.

The vertical line at pressure 150 mbar and the horizontal line at the intersection of the vertical line with the pure CO_2 isotherm curve gives the concentration of pure CO_2 adsorbed at that pressure. This data is relevant because it corresponds to the concentration of CO_2 chosen in the binary mixture (15 %). Therefore, at 1000 mbar of the mixture the partial concentration of CO_2 is 150 mbar.

Figure 99 shows the uptake capacity of MRF0_100_0.25 tested with both pure CO_2 and N_2, and the mixture (15%:85%, respectively). As expected, by the temperature used (60 °C), the pure N_2 uptake is very low compared to that of pure CO_2. Therefore, it is expected that the xerogel selectively adsorbs CO_2 from the mixture. It is also important to note that the

maximum uptake obtained from the mixture is lower than that observed at ~150 mbar for pure CO_2, which is the CO_2 concentration at ~1 bar in the mixture. Additionally, there is no evidence of N_2 adsorption being enhanced by the presence of CO_2.

The equilibration time of the pure CO_2 adsorption isotherm for MRF0_100_0.25 took an average of ~10-20 min per pressure step to reach the plateau on the mass profile. This can be compared to the equilibration times of the mixture (CO_2-N_2), and while it is important to note that this equilibration time might be slightly shorter because of the low concentration of CO_2 (15%), the times observed are of a similar order, averaging ~10-12 min for most pressure steps. This suggests that CO_2 is being adsorbed selectively on the xerogel in a timeframe similar to the pure gas, which has positive implications for commercial use of such materials.

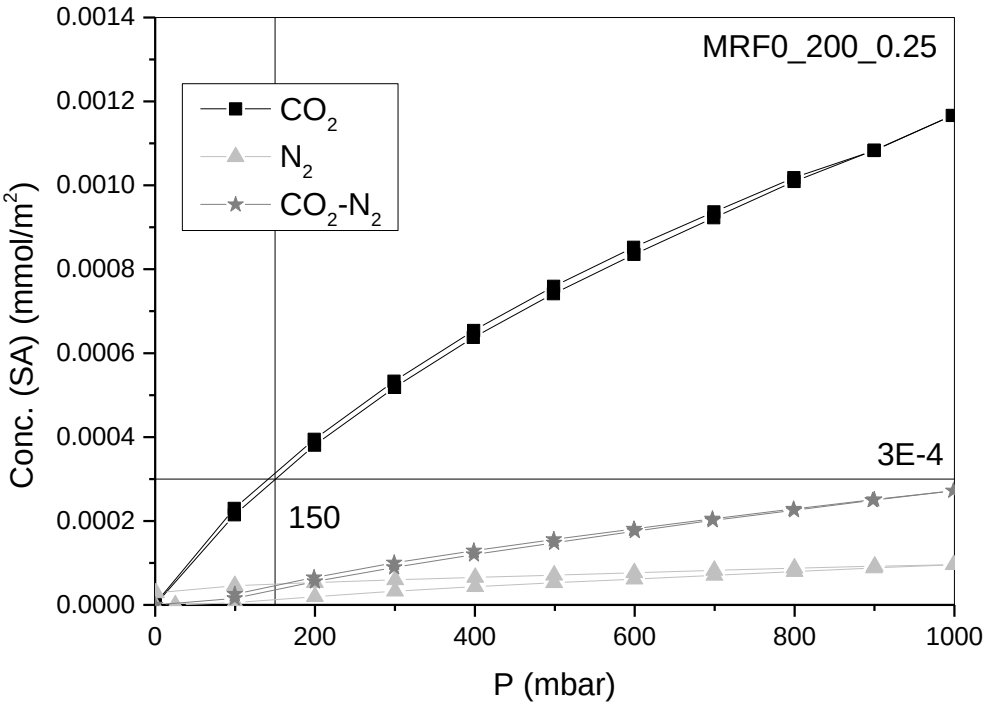

Figure 100: Gas adsorption uptake of CO_2, N_2 and mixture CO_2-N_2 (15-85 %) tested with intelligent gravimetric analyser (IGA) at 60 °C under flow conditions of 200 cm^3 min^{-1} for MRF0_200_0.25.

Figure 100 shows that the total uptake at 1000 mbar of the gas mixture again corresponds to a similar mass to that of the pure gas at 150 mbar. It was observed that N_2 adsorption data, particularly that for the desorption branch, did not equilibrate fully at low pressure, hence, hysteresis is observed for this isotherm. The results do suggest that, for this material, while N_2 adsorption is small, there may be kinetic limitations that mean it is

retained once adsorbed in a timescale beyond that which would be useful for cycling systems. Again, comparison of the equilibration times of the pure isotherm and those obtained for the mixture shows similar behaviour for MRF0_200_0.25. The pure CO_2 isotherm equilibrates averagely in under ~3 min for most pressure points, while the isotherm of the mixture achieves equilibrium in an even shorter timescale (~2 min). This might be explained by observing the equilibration times for the pure CO_2, and for pressures below 300 mbar the equilibration time is ~1 min. Therefore, given that at ~1 bar the pressure of CO_2 is only ~150 mbar, then fast equilibration is expected. This is also applicable for the other materials studied.

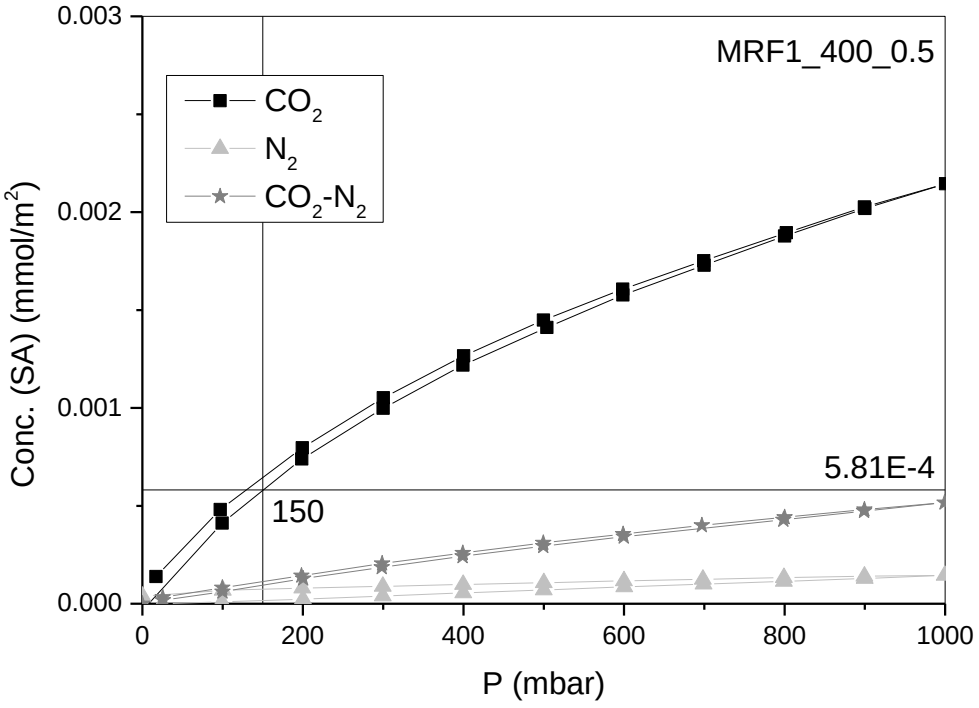

Figure 101: Gas adsorption uptake of CO_2, N_2 and mixture CO_2-N_2 (15-85 %) tested with intelligent gravimetric analyser (IGA) at 60 °C under flow conditions of 200 cm^3 min^{-1} for MRF1_400_0.5.

The incorporation of 1% melamine in MRF1_400_0.5, helped by the fast kinetics of adsorption, increases the concentration of CO_2 adsorbed to double that of MRF0_100_0.25 and MRF0_200_0.25. It can be assumed that the gas adsorbed from the mixture is mostly CO_2, due to the limiting quantity being comparable to the pure system. The equilibration times for both the pure CO_2 isotherm and the mixture are similar. The pure CO_2 isotherm equilibrates for most of the pressure steps in an average time of less than ~4 min, while the mixture does so in less than 2 min. The low concentration of CO_2 in the mixture may be the main reason for the, slightly, faster equilibration observed, as detailed above.

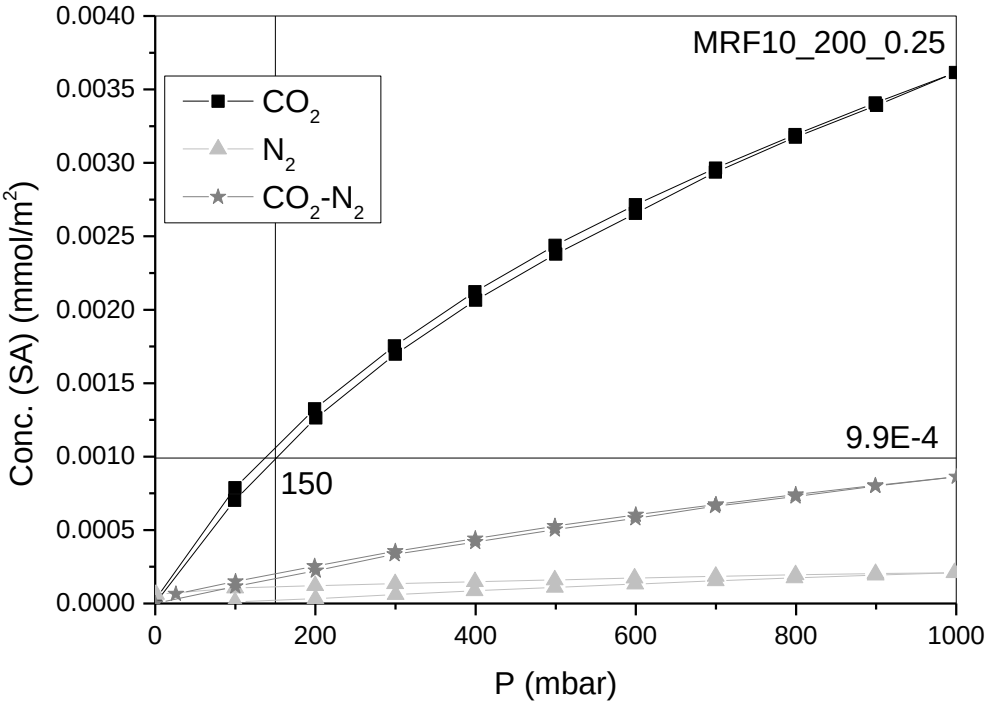

Figure 102: Gas adsorption uptake of CO_2, N_2 and mixture CO_2-N_2 (15-85 %) tested with intelligent gravimetric analyser (IGA) at 60 °C under flow conditions of 200 cm^3 min^{-1} for MRF10_200_0.25.

The CO_2 uptake for MRF10_200_0.25 is approximately three times larger compared than that for the MRF0 xerogels. In all cases, the materials exhibit an uptake close to that of the pure CO_2 isotherm. Therefore, is important to note that MRF xerogels are still selective for CO_2 even in the presence of high concentrations of N_2. Equilibration times for both the pure and mixture isotherms are again very similar, averaging less than ~3 min for CO_2 and ~1 to 2 min for the mixture. Again, the N_2 equilibration time was observed to be ~180 min in average, which is constant over all samples studied.

8.2.1 Thermodynamic Analysis by Ideal Adsorbed Solution Theory

As detailed above, the adsorption uptakes for the gas mixture, at 150 mbar of CO_2 in a balance of N_2 are similar to the pure CO_2 results. Combined with the fact that nitrogen is expected to exhibit a low uptake at 60 °C, an argument can be made for assuming that CO_2 is selectively adsorbed from the gas stream. However, this needs to be proven categorically, hence, Ideal Adsorbed Solution Theory (IAST), which relates the compositions of the adsorbed phase and the bulk gas phase for binary systems was used to confirm selectivity in these systems. IAST gives useful information about selectivity of a given adsorbent in separating a desired component from a binary mixture; the model predicts the composition of the adsorbed phase in equilibrium, based on the thermodynamics of the process.

The pure N_2 adsorption isotherms have been fitted to the Langmuir isotherm in its linear form:

$$\frac{P}{C} = \frac{P}{C_m} + \frac{1}{KC_m} \qquad \text{Equation 68}$$

where *P* is the pressure at which the concentration (*C*) of gas adsorbed, *K* is the equilibrium constant of adsorption and C_m is the concentration adsorbed within the monolayer.

IAST was not applicable for MRF0_100_0.25 and MRF1_400_0.5 due to their significantly low N_2 uptake and, as a consequence, the data did not fit the Langmuir isotherm well. Therefore, *K* and C_m could not been determined and IAST could not be applied.

The pure N_2 isotherm for MRF0_200_0.25 was fitted with Equation 68 (obtaining a reasonable R^2 of 0.998). The *K* and C_m values obtained were 0.2394 bar^{-1} and 0.2304 mmol/g, respectively. Similarly, the pure CO_2 isotherm for this material was fitted using the same equation (R^2=0.998), and the *K* and C_m values obtained were 1.071 bar^{-1} and 0.9946 mmol/g, respectively. The system temperature was 60 °C, the mixture composition was 15% CO_2 and 85 % N_2. IAST was applied using the data obtained from the pure systems and using the parameters of the mixed adsorption measurement, allowing the equilibrium concentration at a system pressure of 1 bar to be obtained.

The amount of CO_2 and N_2 adsorbed at equilibrium, using IAST, were 0.127 and 0.27 mmol/g, respectively. Normalizing this value per m^2 of MRF0_200_0.25 surface area (464.4 m^2/g), the concentrations were 5.8 x 10^{-5} mmol/m^2 for N_2 and 2.73 x 10^{-4} mmol/m^2 for CO_2. It is worth noting that the concentration calculated using IAST agrees with the CO_2 concentration calculated from the adsorption isotherm of the mixture, which was 2.72 x 10^{-4} mmol/m^2. The concentration of N_2 at equilibrium is very small, ~17.4% of the total adsorbed, which suggests that separation is also favoured thermodynamically, giving a selectivity for CO_2 of 26.5 %, and a mole fraction in the adsorbed phase of 0.824 for CO_2 and 0.176 for N_2.

By contrast, IAST with MRF10_200_0.25 gives an adsorbed phase with mole fractions of 0.902 for CO_2 and 0.098 for N_2, and a selectivity of 52.2 %. This shows, not only, that increasing melamine results in an increase of CO_2 uptake, but also that MRF xerogels are

potential materials for CO_2 separation from gas mixtures given their enhanced selectivity both kinetically and thermodynamically.

8.3 Selectivity of Adsorption for Mixture of CO_2-CH_4

The separation of CO_2 from CH_4 is generally related to the separation of H_2S as well. The process of separating H_2S from a gas stream is called gas sweetening, as H_2S is considered the sour gas; however, separation of CO_2 is also required in such systems. Therefore, sour gas sweetening requires separation of hydrogen sulphide (H_2S) and CO_2 from CH_4. MRF xerogels could potentially be applied to such separations, analogously to liquid amines sorbents, which are applied to separation of both CO_2 and H_2S. Current sour gas sweetening processes requires solvents with specific characteristics, including high selectivity for CO_2, H_2S and other sulphur compounds, low uptake of hydrocarbons, thermal stability, low energy penalty for regeneration, non-corrosive, and low solvent vapour pressure to minimize solvent losses. MRF xerogels possess many of the mentioned requirements:

- Non-corrosive
- Thermally stable
- Easy to regenerate
- Low energy for regeneration (pressure swing)
- Mainly physisorption, which is reinforced by the low heat of condensation (ΔH) of CO_2 on MRF xerogels
- Solid sorbents, which would minimize material losses, compared to liquid solvents
- Minimized toxicity of waste compared to liquid amine sorbents (highly toxic)

There are three main features that need to be determined for the MRF xerogels in order to fully evaluate their potential for carbon capture. The adsorption capacity for H_2S and sulphur compounds could be a key parameter requiring further analysis, however, it is beyond the scope of the current project. It is worth noting that, as H_2S is chemically similar to CO_2, both having acidic character, it could be expected that MRF xerogels with an affinity for CO_2 would adsorb H_2S as well. Previous research has demonstrated that H_2S can be removed using liquid amine sorbents, on which most of the sour gas sweetening processes are based [76, 203-205]. Therefore, by incorporating amines (melamine) into the RF structure, it can be said that MRF xerogels may be potentially applied to the removal of H_2S, akin to liquid amine sorbents.

MRF xerogel CO_2 capacities were reported in Chapter 7, and the hydrocarbon (CH_4) uptakes were also tested here, as it is additionally of interest to test its selectivity for CO_2 in a gas mixture with CH_4. The affinity of MRF xerogels for CH_4 is expected to be low, given its non-polar character.

Figure 103-106 show a comparison of adsorption uptakes for pure CO_2, pure CH_4 and a mixture of 15% CO_2 and 85% CH_4. Firstly, it is important to note that CH_4 uptake is low in all cases, which is a beneficial characteristic for a sorbent to be used for gas sweetening. The adsorption uptake, in all cases, has been normalised on the basis of available surface area (m^2) to allow direct comparison between materials (Table 9).

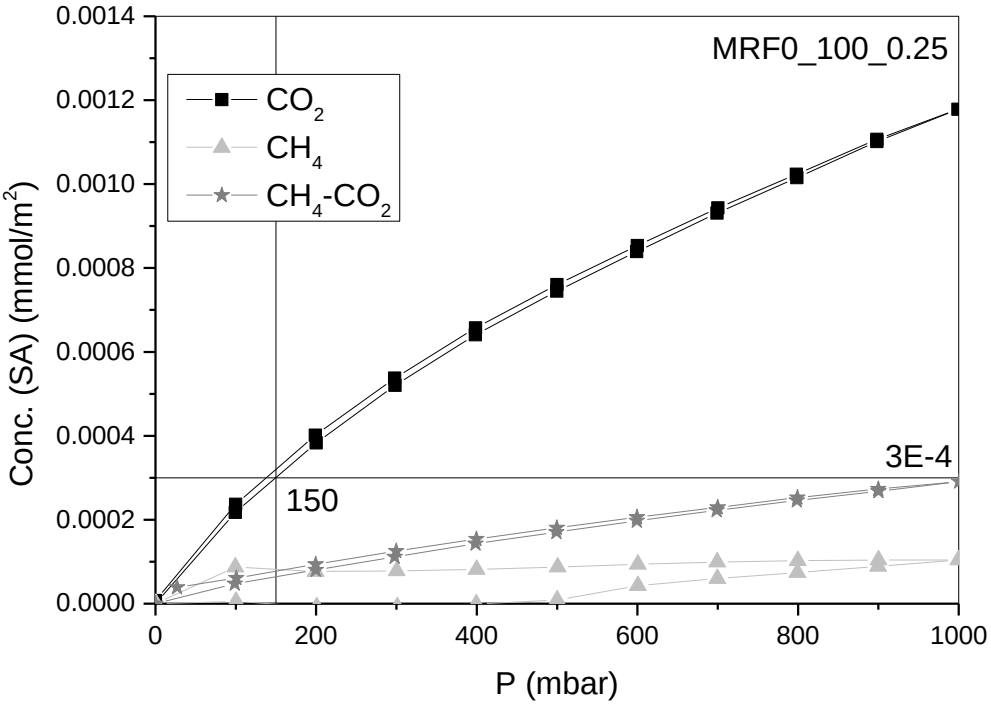

Figure 103: Gas adsorption uptake of CO_2, CH_4 and mixture CO_2-CH_4 (15-85 %) tested with intelligent gravimetric analyser (IGA) at 60 °C under flow conditions of 200 cm^3 min^{-1} for MRF0_100_0.25.

Figure 103 shows adsorption uptakes for MRF0_100_0.25 of the pure components, CO_2 and CH_4, and the mixture, 15%:85%, respectively. The uptake at ~1000 mbar of the gas mixture adsorption isotherm is, practically, the same as that observed at 150 mbar of the pure component (CO_2). Additionally, the equilibration times for both pure CO_2 and the gas mixture are very similar, being on average ~10-20 min for both systems. In contrast, the average equilibration time for pure CH_4 was ~35 min. Therefore, the uptake observed at ~1000 mbar, combined with the negligible CH_4 uptake (pure), and the similarity of the equilibration times, suggest that mainly CO_2 is selectively adsorbed.

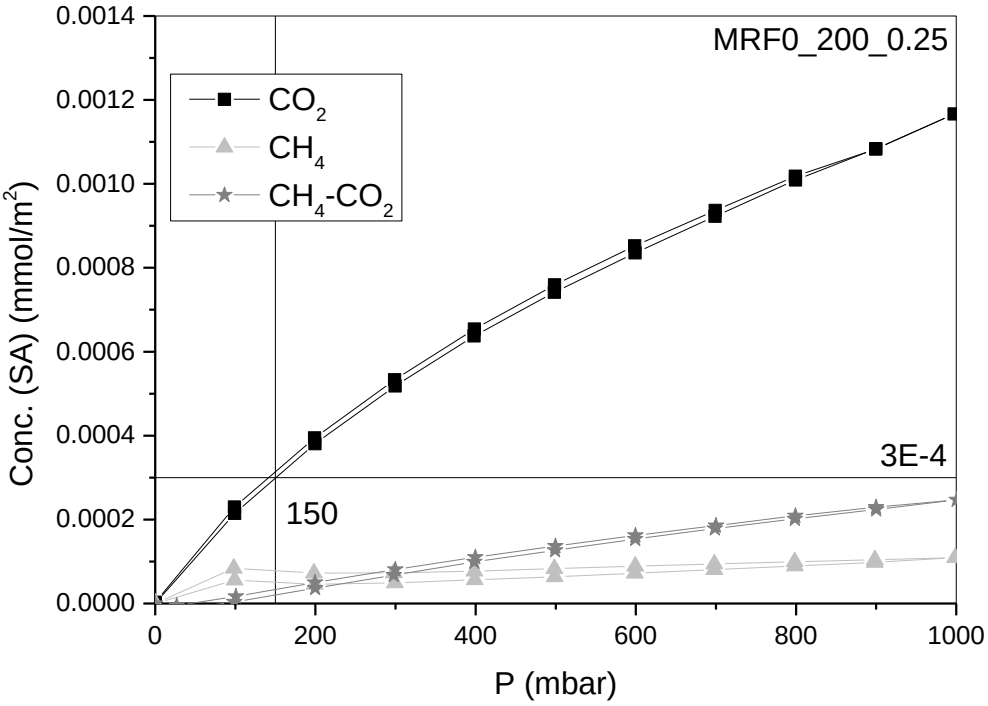

Figure 104: Gas adsorption uptake of CO_2, CH_4 and mixture CO_2-CH_4 (15-85 %) tested with intelligent gravimetric analyser (IGA) at 60 °C under flow conditions of 200 cm^3 min^{-1} for MRF0_200_0.25.

Figure 104 shows the uptake at 1000 mbar of the mixture is again significantly close to the uptake at 150 mbar of the pure CO_2 isotherm. CH_4 adsorption, in the pure stream, has been observed to be negligible. Comparison of equilibration times for the pure isotherm compared to those of the mixture show similar behaviour is observed for MRF0_200_0.25. The pure CO_2 isotherm equilibrates on average in under ~3 min, while the isotherm of the mixture does so in ~1 min. This contrasts with an average time of ~180 min for pure CH_4 to equilibrate. The kinetics of adsorption of pure CH_4 are very slow compared to pure CO_2 and, the mixture behaves in a very similar way kinetically to pure CO_2, suggesting that separation of CO_2 from CH_4 is favoured.

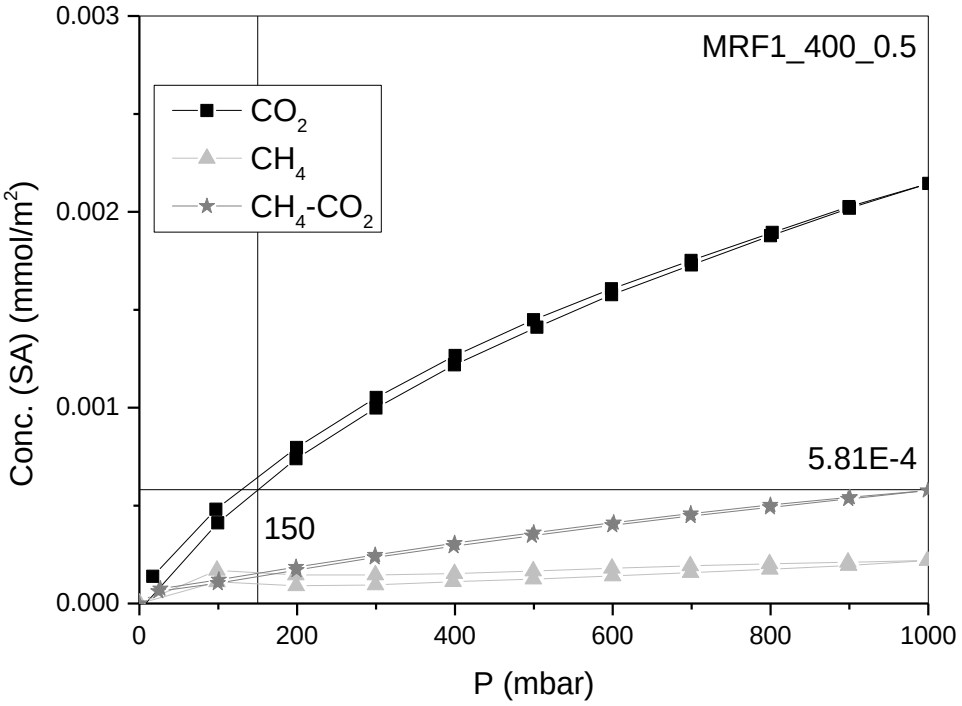

Figure 105: Gas adsorption uptake of CO_2, CH_4 and mixture CO_2-CH_4 (15-85 %) tested with intelligent gravimetric analyser (IGA) at 60 °C under flow conditions of 200 cm^3 min^{-1} for MRF1_400_0.5.

The uptake of the gas mixture isotherm for MRF1_400_0.5 in Figure 105 is approximately double that observed for the MRF0 samples. This is very similar to the behaviour observed for the CO_2-N_2 mixture, the similar equilibration times observed for both pure CO_2 and the gas mixture isotherms, ~4 min and ~2 min, respectively, suggest that CO_2 is mainly adsorbed from the mixture. Additionally, the CH_4 equilibration time was ~180 min, similar to that for MRF0_200_0.25.

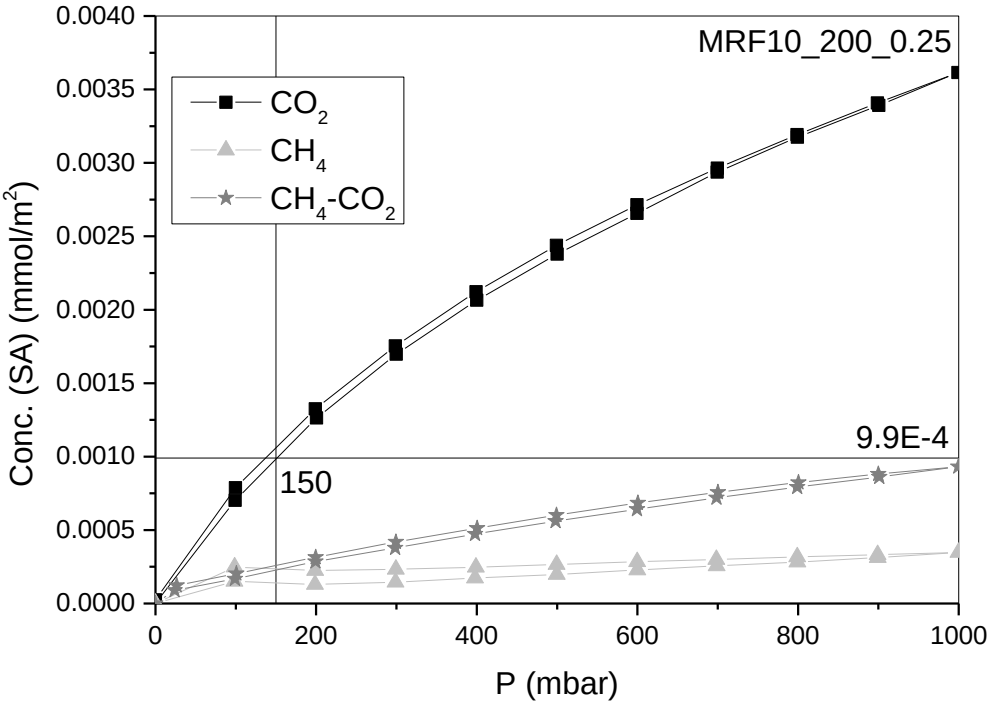

Figure 106: Gas adsorption uptake of CO_2, CH_4 and mixture CO_2-CH_4 (15-85 %) tested with intelligent gravimetric analyser (IGA) at 60 °C under flow conditions of 200 cm^3 min^{-1} for MRF10_200_0.25.

Figure 106 shows that the total uptake of the mixture (at ~1000 mbar) is the same, or very close, to that observed for the CO_2-N_2 mixture, which suggest that CO_2 is being selectively adsorbed from the mixture in both cases. The equilibration times of both the pure CO_2 and CO_2-CH_4 mixture are again similar. The average time for equilibration for pure CO_2 was ~3 min, while for the mixture it was ~1 min; CH_4 equilibration time was observed to be ~180 min, similar to the previous samples.

Thermodynamic analysis by IAST was attempted for the mixture of CO_2-CH_4, but failed due to the low CH_4 uptake compared to CO_2 at the conditions tested. The fitting of MRF0_100_0.25 and MRF1_400_0.5 CH_4 adsorption data with the Langmuir isotherm was unsuccessful, again as a consequence of the low CH_4 uptake. Despite these negative results, it was possible to determine k and C_m for MRF0_200_0.25 and MRF10_200_0.25. CH_4 isotherms, analysed using the Langmuir model, gave C_m values of 1.13 x 10^{-4} and 6.52 x 10^{-4} mmol/g, for MRF0_200_0.25 and MRF10_200_0.25, respectively. In contrast, C_m values for CO_2 adsorption on these materials were 0.995 and 1.046 mmol/g, respectively. It is important to note that the CO_2 uptake is >8000 times that for CH_4 on MRF0_200_0.25 and ~2000 times for MRF10_200_0.25. This large difference, therefore, makes the vapour pressure for CH_4 very large (Equation 55 and 56), which means that CH_4 would tend to stay

in the gas bulk phase and not condense. Thus, due to its relatively higher condensate concentration from IAST, CO_2 would tend to condense on MRF xerogels, while CH_4 would tend to remain in the gas phase. Given that the uptake from the CO_2-CH_4 mixture is similar to that for the CO_2-N_2 mixture, for each material, there are likely similar selective effects in both systems, which would be expected to increase as [M] increases as demonstrated for CO_2-N_2; however a higher MRF xerogel affinity for CH_4 can be expected compared to either N_2 or H_2.

8.4 Selectivity of Adsorption for Mixture of CO_2-H_2

The separation of CO_2 from H_2 is very common in gasification or steam reforming processes. This is based on treating the fuel, natural gas or coal, prior to combustion, as explained in Chapter 1. The final stage of this process is the reaction known as water-gas shift, which aims to oxidized CO to CO_2 using steam, giving a product gas stream rich in CO_2 (over 20 %) and H_2. CO_2 is, therefore, required to be separated from H_2 before this stream is fed to gas turbines (integrated gasification combined cycle). Despite the need to capture CO_2 prior to combustion, the water-gas shift reaction is the major source of H_2 for industrially important applications, such as the Haber process (also called Haber-Bosch process) [206-208], which uses atmospheric nitrogen and H_2 to produce ammonia (NH_3) in a catalysed reaction at high temperature (400-500 °C) and pressure (150-250 bar), with an overall conversion of 97 %. One of its main applications nowadays is the production of fertilizers.

One of the major drawbacks of the technologies available for CO_2 separation from H_2 is the high energy requirements for regeneration of sorbents [14]. MRF xerogels have demonstrated easy regeneration abilities (Chapter 7), fast kinetics of CO_2 adsorption, low energy penalties, and thermal stability. It is necessary that the MRF sorbent exhibit low affinity for H_2 to accomplish a good degree of separation.

Figure 107 and 108 show a comparison of uptakes for pure CO_2, pure H_2 and a mixture of 15% CO_2 and 85% H_2. It is important to note that the H_2 adsorption uptake at 60 °C and ~1 bar is expected to be very low. In order to probe the effect of additive concentration, it was decided to focus on the two limits of no melamine present (MRF0_100_0.25) and high [M] (MRF10_200_0.25). In this way, the adsorption gravimetric analysis could be allowed to equilibrate for longer time periods, due to time constraints in the total adsorption time. Additionally, observations from the data presented for the other two mixtures tested, suggest that the higher [M] content will increase selectivity for CO_2. The adsorption uptake,

in all cases, has been normalised to account for the available surface area (m^2) for each material (Table 9).

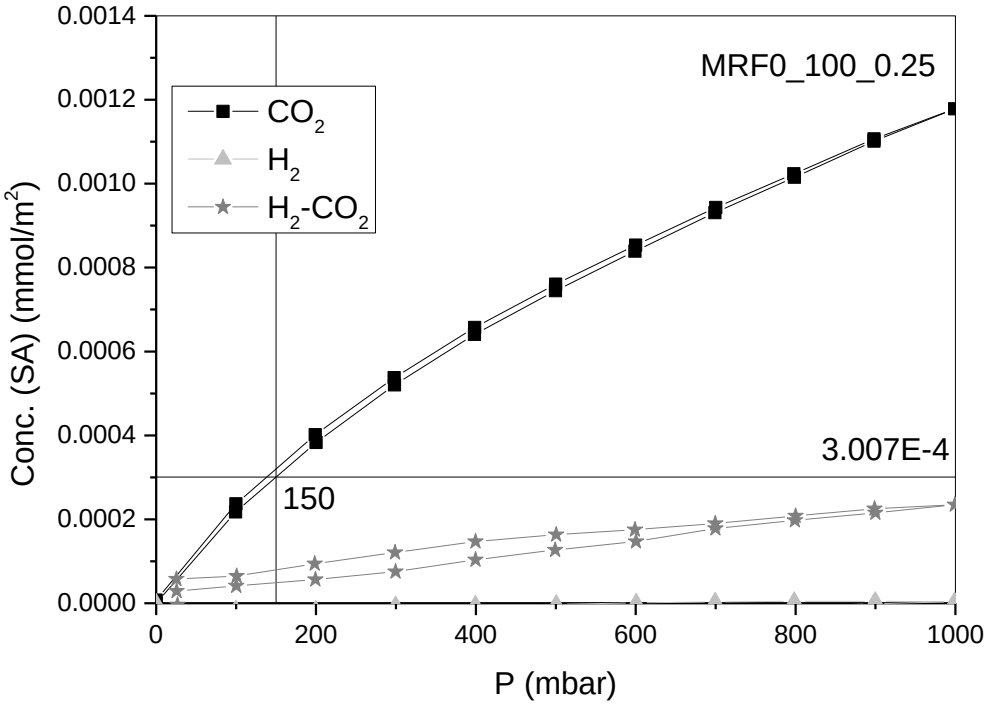

Figure 107: Gas adsorption uptake of CO_2, H_2 and mixture CO_2-H_2 (15-85 %) tested with intelligent gravimetric analyser (IGA) at 60 °C under flow conditions of 200 cm^3 min^{-1} for MRF0_100_0.25.

Figure 107 shows the adsorption uptake on MRF0_100_0.25 for the pure components, CO_2 and H_2, and the mixture. The uptake at ~1000 mbar of the gas mixture adsorption isotherm is close to that observed at 150 mbar of the pure component (CO_2). Additionally, the equilibration times for both pure CO_2 and the mixture are very similar, ~10-20 min for both systems. Therefore, the uptake observed at ~1000 mbar, combined with the negligible H_2 uptake (pure), and the similarity of the equilibration times, suggests that CO_2 is mainly adsorbed selectively by this material.

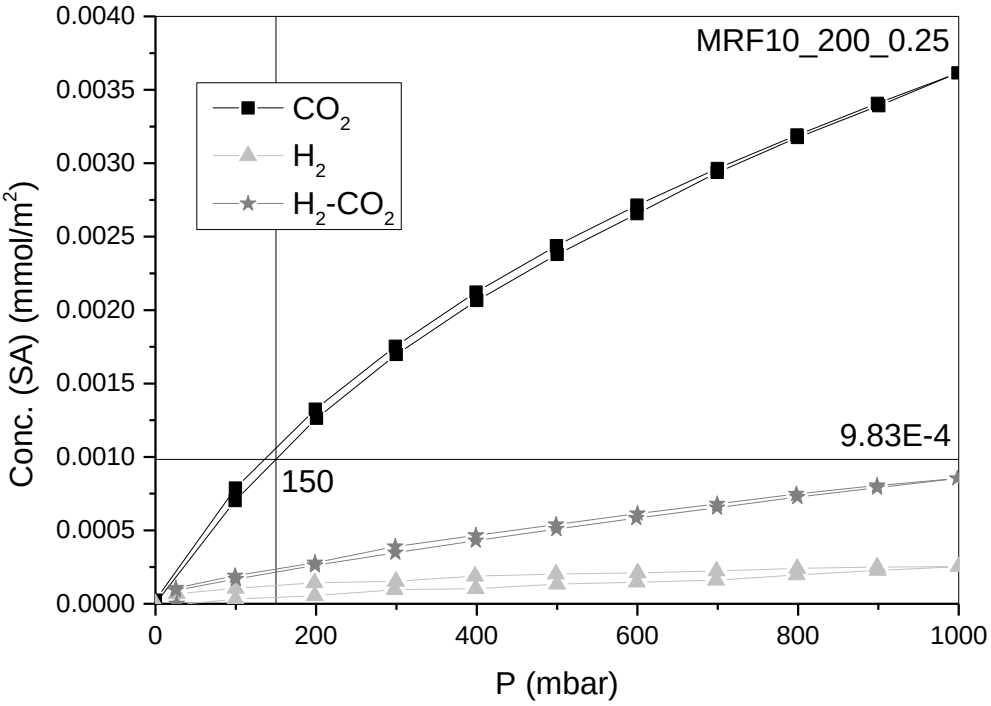

Figure 108: Gas adsorption uptake of CO_2, H_2 and mixture CO_2-H_2 (15-85 %) tested with intelligent gravimetric analyser (IGA) at 60 °C under flow conditions of 200 cm^3 min^{-1} for MRF10_200_0.25.

Figure 108 shows that the total uptake of the mixture (at ~1000 mbar) is the same, or very close, to that observed for the CO_2-H_2 mixture, which suggests that CO_2 is being selectively adsorbed from the mixture. The equilibration times of both pure CO_2 and the mixture are again similar. The average time for equilibration of pure CO_2 was ~3 min, while for the mixture it was ~1 min, while the H_2 equilibration time was observed to be ~240 min on average.

Thermodynamic analysis by IAST was attempted for the mixture of CO_2-H_2, but, similarly to the CO_2-CH_4 mixture, IAST failed because of the low H_2 uptake. The fitting of MRF0_100_0.25 and MRF10_200_0.25 H_2 adsorption data with the Langmuir isotherm also failed because of the low uptake of H_2 at these conditions. Therefore, the parameters *k* and C_m could not be determined and IAST could not been applied. However, the uptake of the CO_2-H_2 mixture for both materials gave quantities comparable to the uptake of these materials with CO_2-CH_4 and CO_2-N_2. Therefore, selectivity can be assumed to increase as [M] increases, in a manner similar to that demonstrated for CO_2-N_2.

8.5 Key Findings

The selectivity of MRF xerogels for CO_2 in binary mixtures with N_2, CH_4 and H_2 was tested. It was found that, as [M] increases, MRF xerogels increase the selectivity for CO_2 from the binary mixtures. Experimental results were contrasted with IAST for the CO_2-N_2 mixture, MRF0_200_0.25 exhibited a selectivity of 26.5% for CO_2 while MRF10_200_0.25 showed a selectivity of 52.2%. Results obtained from this system were compared to CO_2-CH_4 and CO_2-H_2 mixtures, which showed similar results. However, CH_4 a higher affinity of MRF xerogels for CH_4 can be expected compared to N_2 or H_2.

Table 11: Summary of results for CO_2 selectivity from binary systems with N_2, CH_4 and H_2.

Sample	Pure CO_2 uptake expected at 150 mbar (mmol/m^2)	Uptake from CO_2-N_2 (mmol/m^2)	IAST thermodynamic prediction for CO_2 uptake from CO_2-N_2 (mmol/m^2)	Uptake from CO_2-CH_4 (mmol/m^2)	Uptake from CO_2-H_2 (mmol/m^2)
MRF0_100_0.25	3E-4	2.2E-4	-	3E-4	2.3E-4
MRF0_200_0.25	3E-4	2.72E-4	2.73E-4	2.47E-4	-
MRF1_400_0.5	5.81E-4	5.16E-4	-	5.77E-4	-
MRF10_200_0.25	9.9E-4	8.6E-4	9.09E-4E-4	9.3E-4	8.5E-4

Chapter 9
Conclusions

9 Conclusions

Several samples of varying R/C, R/F and [M] were synthesised in order to study the influence of these parameters on the final textural properties of the resulting MRF xerogels and their ability to adsorb CO_2. The synthesis procedure was altered to incorporate melamine successfully into the MRF xerogel structure and to obtain repeatability between different batches. The MRF xerogel properties were characterised by a range of techniques, including nitrogen adsorption, FTIR, proximate analysis, Boehm titration, XPS and gravimetric adsorption measurements. The data gathered allowed determination of trends between the variables studied and the resulting structural properties. The kinetics and thermodynamics of adsorption for CO_2 were also studied, as well as CO_2 cycling by pressure swing. MRF xerogels were also tested for CO_2 selectivity using binary mixtures of N_2-CO_2, CH_4-CO_2 and H_2-CO_2.

9.1 Synthesis Method: Repeatability

The first stage of this research was study of the effects of incorporating melamine into the RF synthetic matrix. A total of 55 gels of varying compositions (MRF1, MRF7, MRF10 and MRF20, all with R/C 100 and R/F 0.5) were produced. 27 of these gels were produced with the standard synthesis method, of which, 7 were produced by varying the size of the jar used, which affected the thickness of the gel. The remaining 28 samples were produced with a pre-heating method.

The pre-hating synthesis method was found to be more suitable for synthesis of MRF materials due to the low solubility of melamine at room temperature and pressure. Therefore, solutions were pre-heated to 50 °C, thereby, increasing the solubility of melamine. It was demonstrated that melamine was successfully incorporated into the MRF xerogel structure for concentrations up to 40% [M]. CHN elemental analysis showed identical compositions in the different layers observed for the xerogels produced. Additionally, repeatability was observed for different batches of MRF xerogels analysed by nitrogen adsorption measurements, which showed identical N_2 isotherms between different batches analysed. The isotherms observed were of Type IV in all cases with characteristic hysteresis loops, which are representative of capillary condensation within mesoporous. As melamine concentration increases, the closure of the hysteresis loop

occurred at higher relatives pressures, which was attributed to the material rather than the adsorptive.

9.2 Parametric Study of MRF Synthesis

The effect of varying R/C, R/F and [M] on MRF final textural properties was studied. Different levels for each variable were selected, which gave 100 different combination and resulting MRF xerogels. Hysteresis loops, observed for N_2 adsorption isotherms, were observed to vary from Type H2 (low [M]) to Type H1 (high [M]). Pore sizes were observed to increase as [M] increases, changing the pore shape from ink bottle like pores (narrow neck and wide body) to open mesopores. As R/F was increased, the hysteresis loop transition changed to a transition between the closely related H2(a) to H2(b). Pore widening is evident for all R/C values, increasing as [M] increases, indicating greater influence of [M] when less catalyst is present. It was found that increasing R/C and [M] resulted in a reduction in N_2 adsorption capacity. As R/C is increased, the onset of this reduction occurs at lower [M], suggesting that, for a given R/C (and R/F), there is a maximum level of [M] that can be incorporated, before the pore size becomes so large that surface area decreases drastically. As [M] increases, the xerogels become softer and weaker, suggesting a lower level of crosslinking. The total surface area and N_2 uptake increases with [M] up to a maximum, which was usually MRF10, and MRF20 or 30 for low R/C and R/F. In general, pore volume increases as [M] increases, because of the larger pores that are present. In contrast, increasing R/F did not significantly change pore size, however, a decrease in N_2 uptake was observed. As R/C increased to 200 and 400 gelation failed more often at higher levels of [M]. This is a result of reduced catalyst concentration, which results in fewer resorcinol anions being activated and, therefore, crosslinking is weaker. This effect is more pronounced as R/F increases, because of the lower concentration of formaldehyde that is present.

CHN elemental analysis results confirmed melamine incorporation into the MRF xerogel structure, and N concentration increased linearly, in all cases, as [M] increased. The pH of the initial solution was recorded for all samples, and this allowed comparisons between the different MRF compositions. R/C is the main parameter controlling pH, which decreases as R/C increases, due to the lower concentration of catalyst used (relatively strong base). As R/F increases, less formalin solution (pH of 2.8 to 4.0) was used; therefore, pH tends to increase because of less acidic influence from formalin. Thus, as R/F increases, gels were

weaker because crosslinking between clusters is reduced. R/F 0.75 and 1.0 produce weaker gels and many times gelation fails, instead R/F 0.25 and 0.5 are recommended for MRF xerogel preparation. As [M] (weak organic base) increases so does pH, however, the greater influence comes from R/C. The effect of the initial pH (and R/C) ultimately controls the pore structure; however, when pH approaches 8 to 8.5 gelation often fails.

The impact of R/C, R/F and [M] on surface functional groups was studied by FTIR. It was observed that concentration of O-H bonds changed as [M] increased, for constant R/C and R/F. As [M] increased, the interaction between neighbouring O-H becomes weaker, therefore this peak becomes narrower. Also, C=O functionalities were observed to increase with [M]. For constant R/C and [M], at low R/F methylene bridges should be favoured, particularly when initial pH is 7 to 8.

Surface area decreases with increasing [M] or increasing R/C, and this parameter reduces drastically if both variables are increased simultaneously. The largest surface areas were obtained by MRF20 and MRF10 (with R/F 0.25 and 0.5). As [M] is higher, the decrease in surface area with increasing R/C occurs at lower R/C. Larger pore volumes were obtained at low [M] (0-20 %), low R/C (50-200) and low R/F (0.25 and 0.5). Increasing [M] does not translate to an increase in N_2 uptake (pore volume), generally, surface area has a greater impact. The pore size is only controlled at low R/F (0.25 and 0.5), while at larger R/F (0.75 and 1.0) it essentially becomes a random parameter, with a tendency for larger pores to form. The smallest pore sizes were obtained for low R/C (50). Increasing [M] increases pore size, in a similar way as increasing R/C. Increasing R/C, R/F and/or [M] tends to hinder micropore development.

9.3 Optimisation of CO_2 Adsorption in Modified Xerogels

Ten materials were selected from the 100 samples produced during the parametric study. These samples were analysed and characterised for CO_2 adsorption. Samples were chosen in basis of their micropore volume and varying N content. 6 samples had very similar micropore volume with different levels of nitrogen content (0, 1, 10, 20, 30 and 40), while 3 MRF0 samples with increasing R/C (50, 100 and 200) and 1 additional MRF1 sample with high R/C (400) were also chosen. The 10 selected samples allowed evaluation of increasing R/C, increasing [M] and comparison between R/F (0.25 and 0.5).

Boehm titration analysis showed an increase in carbon basic surface functionalities (Ncsf) as [M] increases. This agrees with the reduction of acidic contributions from phenolic groups as melamine increases, as determined by FTIR. However, C=O bonding was found to increase as [M] concentration increases, both from FTIR and XPS, and it was demonstrated that this bond must be a result of the polymerization reaction of MRF xerogels during gelation. Thermal stability of MRF xerogels was analysed by proximate analysis, which showed an increase in volatile matter as [M] increased, while fixed carbon decreased. Volatile matter was determined to be greater than fixed carbon for [M] of 20% and higher. This confirms the weakness observed as [M] increases in MRF xerogels as a result of weaker crosslinking, which is linked to increasing C=O concentration from a reduction in the degree of crosslinking.

CO_2 adsorption capacities were measured at 0 and 60 °C, and the uptakes were observed to decrease with temperature due to the exothermic nature of physisorption. CO_2 adsorption capacity increases, at both temperatures, as [M] increases. MRF10_200_0.25 exhibited the highest CO_2 capacity. The enthalpy and entropy of adsorption were, also, assessed. Heat of adsorption (enthalpy) does not vary significantly with increasing [M], being within the range ∼-30 to -25 kJ/mol. As expected, entropy decreases as the amount adsorbed increases, due to the lower degrees of freedom of adsorbed molecules compared to the bulk gas. The low enthalpy of adsorption suggests that MRF xerogels would be easy to regenerate, particularly compared to liquid amine sorbents. The low enthalpy is attributed to the fact that the CO_2 molecule tends to interact with the N located in the ring, rather than the amine groups, these being weaker in their intensity of interaction, but sufficiently strong to enhance CO_2 adsorption compared to RF xerogels. The kinetics of adsorption, at 0 and 60 °C, were described in all cases by a stretched exponential method, with increasing rate constants of adsorption, *k*, as [M] increases. As R/C increases, so does pore size, which should facilitate gas diffusion through the network of MRF xerogels, for this reason *k* increases as R/C increases. Rate constants tend to increase with pressure for MRF0 xerogels and MRF1_100_0.25, while MRF1_400_0.5 showed a small decrease at low pressure and then k tends to constant values, which was also the case for MRF xerogels with 10 and higher [M] %. Generally, rate constant increases as [M] increases, and with temperature. Activation energies were generally low (0-20 kJ/mol) and increase with increasing [M]. CO_2 regeneration ability was tested by CO_2 cycling (pressure swing) for MRF xerogels; in all cases, adsorption capacity increases as [M] increases.

9.4 Selectivity Analysis

Selectivity of selected MRF xerogels, for CO_2 from binary mixtures with N_2, CH_4 and H_2, was tested. It was found that in the three cases studied, selectivity for CO_2 was favoured. N_2, CH_4 and H_2 all exhibit low uptakes at the conditions tested (60 °C and ~1 bar). The uptake was favoured kinetically in all cases, given the faster approach to equilibrium for CO_2 than the other gases. IAST was used to predict the selectivity thermodynamically, and CO_2 was shown to be selectively adsorbed from a N_2-CO_2 mixture at 26.5% for MRF0_200_0.25, increasing to 52.2 % for MRF10_200_0.25. Therefore, the increase of [M] not only increases the CO_2 adsorption uptake, but also its selectivity.

9.5 Applicability of MRF Xerogels for CCS

It has been demonstrated that incorporating nitrogen functionalities into the structure of RF xerogels enhances their CO_2 adsorption capacities. Therefore, this reduces the amount of sorbent required for a given uptake, and consequently reduces the volume of equipment and vessels. The selectivity for CO_2 adsorption, in comparison to any other gas present in the flue stream, is a key parameter. N_2 is in large concentration in flue gases, results show that MRF xerogels have high selectivity for CO_2 from the binary mixture. Additionally, it is a requirement that materials exhibit fast adsorption and desorption kinetics, which is the case for MRF xerogels at both 0 and 60 °C, and during cycling/regeneration analysis. The materials, and the related adsorption behaviour, are benefitted by the moderate heats of adsorption, and low activation energies, as well as high thermal stability.

Chapter 10

Future Work

10 Future Work

In order to apply MRF xerogels for CCS, it is necessary to further enhance the CO_2 adsorption capacity to be able to compete with liquid amine sorbents. Therefore, CO_2 adsorption capacities of MRF xerogels need to be developed further for this specific application. Similarly, there are other aspects of ideal sorbents that require additional analysis such as:

- Selectivity in ternary, quaternary and more complex gas mixtures, including NO_X, SO_X, H_2O vapour, etc.
- Chemical stability of MRF xerogels in the presence of impurities and contaminants such as NO_X, SO_X and heavy metals.
- Mechanical strength of MRF xerogels is an important parameter because the sorbent in a CCS system would be exposed to vibrations, high flow rates of gases, and varied operating conditions (pressures and temperature).
- Analysis of sorbent cost, which implies the scaled up manufacture of MRF xerogels in an appropriate production process.

Additionally, there are aspects of MRF polymerisation reactions that have not been fully understood yet. Polymerisation reactions are very complex and include a high number of intermediate species and reactions. A better description of MRF polymerisation reactions could lead to potential opportunities to tune further the MRF xerogel properties to match desired requirements for given applications. The occurrence of C=O bonding in MRF xerogels must be further studied. This thesis presented a hypothesis for this occurrence, however, this must further developed.

The study of other synthesis parameters that affect MRF textural properties would be necessary, such as solids content. Initial pH could also be controlled within optimal ranges for MRF gelation, however, the inclusion of new species (cations and anions from the pH altering species) may alter the sol-gel process, hence, the benefits and drawbacks should be assessed.

Similarly, the incorporation of melamine, or similar additives, would likely have an impact on other properties of RF xerogels, such as conductivity and heat transfer. This may alter the current applications of RF xerogel in these matters and/or present alternatives for future use.

The scale up of MRF xerogels materials must be assessed and studied in order to bring possible routes for production. This would be a key factor to determine the possible application of this material in industrial processes, particularly for carbon capture and storage. Another important parameter for industrial usages of MRF xerogels is to determine their statistical variance among difference batches of material produced. This must be done once the scale up stage has been developed.

Appendixes

Appendix A Hydrogel Reaction Composition for R/C of 50

This appendix details the weights of resorcinol, formaldehyde, catalyst (sodium carbonate) and Melamine for each gel produced.

The calculations are based on fixed total mass of solids of 6 g in each case, and a solids content of 20% in deionized water.

A1 R/C of 50 and R/F of 0.25

Table 12: MRF0_50_0.25 composition.

	Equivalent Moles	Moles	Mass (g)	Percentage Mass (%)	Percentage Moles (%)
Resorcinol	1	0.0258	2.8432	47.3867	19.9203
Formaldehyde	4	0.1033	3.1021	51.7010	79.6813
Sodium carbonate	0.02	0.0005	0.0547	0.9123	0.3984
Melamine		0	0	0	0
Total		0.1296	6	100	100

Table 13: MRF1_50_0.25 composition

	Equivalent Moles	Moles	Mass (g)	Percentage Mass (%)	Percentage Moles (%)
Resorcinol	1	0.0256	2.8148	46.9128	19.8467
Formaldehyde	4	0.1023	3.0710	51.1840	79.3870
Sodium carbonate	0.02	0.0005	0.0542	0.9032	0.3969
Melamine		0.0005	0.06	1	0.3693
Total		0.1288	6	100	100

Table 14: MRF10_50_0.25 composition

	Equivalent Moles	Moles	Mass (g)	Percentage Mass (%)	Percentage Moles (%)
Resorcinol	1	0.0232	2.5589	42.6480	19.1399
Formaldehyde	4	0.0930	2.7918	46.5309	76.5595
Sodium carbonate	0.02	0.0005	0.0493	0.8211	0.3828
Melamine		0.0048	0.6000	10	3.9178
Total		0.1214	6.0000	100	100

Table 15: MRF20_50_0.25 composition.

	Equivalent Moles	Moles	Mass (g)	Percentage Mass (%)	Percentage Moles (%)
Resorcinol	1	0.0207	2.2746	37.9093	18.2463
Formaldehyde	4	0.0826	2.4816	41.3608	72.9852
Sodium carbonate	0.02	0.0004	0.0438	0.7299	0.3649
Melamine		0.0095	1.2	20	8.4035
Total		0.1132	6	100	100

Table 16: MRF30_50_0.25 composition.

	Equivalent Moles	Moles	Mass (g)	Percentage Mass (%)	Percentage Moles (%)
Resorcinol	1	0.0181	1.9902	33.1707	17.2131
Formaldehyde	4	0.0723	2.1714	36.1907	68.8524
Sodium carbonate	0.02	0.0004	0.0383	0.6386	0.3443
Melamine		0.0143	1.8	30	13.5903
Total		0.1050	6	100	100

Table 17: MRF40_50_0.25 composition.

	Equivalent Moles	Moles	Mass (g)	Percentage Mass (%)	Percentage Moles (%)
Resorcinol	1	0.0155	1.7059	28.4320	16.0047
Formaldehyde	4	0.0620	1.8612	31.0206	64.0188
Sodium carbonate	0.02	0.0003	0.0328	0.5474	0.3201
Melamine		0.0190	2.4000	40	19.6564
Total		0.0968	6.0000	100	100

A2 R/C of 50 and R/F of 0.5

Table 18: MRF0_50_0.5 composition.

	Equivalent Moles	Moles	Mass (g)	Percentage Mass (%)	Percentage Moles (%)
Resorcinol	1	0.0348	3.8344	63.9069	33.1126
Formaldehyde	2	0.0697	2.0918	34.8627	66.2252
Sodium carbonate	0.02	0.0007	0.0738	1.2304	0.6623
Melamine		0	0	0	0
Total		0.1052	6	100	100

Table 19: MRF1_50_0.5 composition.

	Equivalent Moles	Moles	Mass (g)	Percentage Mass (%)	Percentage Moles (%)
Resorcinol	1	0.0345	3.7961	63.2679	32.9620
Formaldehyde	2	0.0690	2.0708	34.5140	65.9240
Sodium carbonate	0.02	0.0007	0.0731	1.2181	0.6592
Melamine		0.0005	0.06	1	0.4548
Total		0.1046	6	100	100

Table 20: MRF10_50_0.5 composition.

	Equivalent Moles	Moles	Mass (g)	Percentage Mass (%)	Percentage Moles (%)
Resorcinol	1	0.0313	3.4510	57.5162	31.5280
Formaldehyde	2	0.0627	1.8826	31.3764	63.0561
Sodium carbonate	0.02	0.0006	0.0664	1.1074	0.6306
Melamine		0.0048	0.6	10	4.7853
Total		0.0994	6	100	100

Table 21: MRF20_50_0.5 composition.

	Equivalent Moles	Moles	Mass (g)	Percentage Mass (%)	Percentage Moles (%)
Resorcinol	1	0.0279	3.0675	51.1255	29.7486
Formaldehyde	2	0.0557	1.6734	27.8901	59.4972
Sodium carbonate	0.02	0.0006	0.0591	0.9843	0.5950
Melamine		0.0095	1.2	20	10.1593
Total		0.0937	6	100	100

Table 22: MRF30_50_0.5 composition.

	Equivalent Moles	Moles	Mass (g)	Percentage Mass (%)	Percentage Moles (%)
Resorcinol	1	0.0244	2.6841	44.7349	27.7359
Formaldehyde	2	0.0488	1.4642	24.4039	55.4718
Sodium carbonate	0.02	0.0005	0.0517	0.8613	0.5547
Melamine		0.0143	1.8	30	16.2376
Total		0.0879	6	100	100

Table 23: MRF40_50_0.5 composition.

	Equivalent Moles	Moles	Mass (g)	Percentage Mass (%)	Percentage Moles (%)
Resorcinol	1	0.0209	2.3006	38.3442	25.4409
Formaldehyde	2	0.0418	1.2551	20.9176	50.8818
Sodium carbonate	0.02	0.0004	0.0443	0.7382	0.5088
Melamine		0.0190	2.4	40	23.1684
Total		0.0821	6	100	100

A3 R/C of 50 and R/F of 0.75

Table 24: MRF0_50_0.75 composition.

	Equivalent Moles	Moles	Mass (g)	Percentage Mass (%)	Percentage Moles (%)
Resorcinol	1	0.0394	4.3386	72.3100	42.4929
Formaldehyde	1.33	0.0525	1.5779	26.2978	56.6572
Sodium carbonate	0.02	0.0008	0.0835	1.3922	0.8499
Melamine		0	0	0	0
Total		0.0927	6	100	100

Table 25: MRF1_50_0.75 composition.

	Equivalent Moles	Moles	Mass (g)	Percentage Mass (%)	Percentage Moles (%)
Resorcinol	1	0.0390	4.2952	71.5869	42.2739
Formaldehyde	1.33	0.0520	1.5621	26.0348	56.3651
Sodium carbonate	0.02	0.0008	0.0827	1.3783	0.8455
Melamine		0.0005	0.06	1	0.5155
Total		0.0923	6	100	100

Table 26: MRF10_50_0.75 composition.

	Equivalent Moles	Moles	Mass (g)	Percentage Mass (%)	Percentage Moles (%)
Resorcinol	1	0.0355	3.9047	65.0790	40.2014
Formaldehyde	1.33	0.0473	1.4201	23.6680	53.6019
Sodium carbonate	0.02	0.0007	0.0752	1.2530	0.8040
Melamine		0.0048	0.6	10	5.3927
Total		0.0882	6	100	100

Table 27: MRF20_50_0.75 composition.

	Equivalent Moles	Moles	Mass (g)	Percentage Mass (%)	Percentage Moles (%)
Resorcinol	1	0.0315	3.4709	57.8480	37.6626
Formaldehyde	1.33	0.0420	1.2623	21.0382	50.2169
Sodium carbonate	0.02	0.0006	0.0668	1.1138	0.7533
Melamine		0.0095	1.2	20	11.3673
Total		0.0837	6	100	100

Table 28: MRF30_50_0.75 composition.

	Equivalent Moles	Moles	Mass (g)	Percentage Mass (%)	Percentage Moles (%)
Resorcinol	1	0.0276	3.0370	50.6170	34.8343
Formaldehyde	1.33	0.0368	1.1045	18.4085	46.4457
Sodium carbonate	0.02	0.0006	0.0585	0.9745	0.6967
Melamine		0.0143	1.8	30	18.0233
Total		0.0792	6	100	100

Table 29: MRF40_50_0.75 composition.

	Equivalent Moles	Moles	Mass (g)	Percentage Mass (%)	Percentage Moles (%)
Resorcinol	1	0.0236	2.6032	43.3860	31.6638
Formaldehyde	1.33	0.0315	0.9467	15.7787	42.2184
Sodium carbonate	0.02	0.0005	0.0501	0.8353	0.6333
Melamine		0.0190	2.4	40	25.4845
Total		0.0747	6	100	100

A4 R/C of 50 and R/F of 1.0

Table 30: MRF0_50_1.0 composition.

	Equivalent Moles	Moles	Mass (g)	Percentage Mass (%)	Percentage Moles (%)
Resorcinol	1	0.0422	4.6439	77.3985	49.5049
Formaldehyde	1	0.0422	1.2667	21.1113	49.5049
Sodium carbonate	0.02	0.0008	0.0894	1.49016	0.9901
Melamine		0	0	0	0
Total		0.0852	6	100	100

Table 31: MRF1_50_1.0 composition.

	Equivalent Moles	Moles	Mass (g)	Percentage Mass (%)	Percentage Moles (%)
Resorcinol	1	0.0418	4.5975	76.6245	49.2273
Formaldehyde	1	0.0418	1.2540	20.9002	49.2273
Sodium carbonate	0.02	0.0008	0.0885	1.4753	0.98455
Melamine		0.0005	0.06	1	0.5608
Total		0.0848	6	100	100

Table 32: MRF10_50_1.0 composition.

	Equivalent Moles	Moles	Mass (g)	Percentage Mass (%)	Percentage Moles (%)
Resorcinol	1	0.0380	4.1795	69.6587	46.6130
Formaldehyde	1	0.03780	1.1400	19.0002	46.6130
Sodium carbonate	0.02	0.0007	0.0805	1.3412	0.9323
Melamine		0.0048	0.6	10	5.8416
Total		0.0814	6	100	100

Table 33: MRF20_50_1.0 composition.

	Equivalent Moles	Moles	Mass (g)	Percentage Mass (%)	Percentage Moles (%)
Resorcinol	1	0.033743	3.715129	61.91882	43.44096
Formaldehyde	1	0.033743	1.013343	16.88905	43.44096
Sodium carbonate	0.02	0.000675	0.071528	1.192131	0.868819
Melamine		0.009515	1.2	20	12.24927
Total		0.077676	6	100	100

Table 34: MRF30_50_1.0 composition.

	Equivalent Moles	Moles	Mass (g)	Percentage Mass (%)	Percentage Moles (%)
Resorcinol	1	0.0295	3.2507	54.1790	39.9459
Formaldehyde	1	0.0295	0.8867	14.7779	39.9459
Sodium carbonate	0.02	0.0006	0.0626	1.0431	0.7989
Melamine		0.0143	1.8	30	19.3092
Total		0.0739	6	100	100

Table 35: MRF40_50_1.0 composition.

	Equivalent Moles	Moles	Mass (g)	Percentage Mass (%)	Percentage Moles (%)
Resorcinol	1	0.0253	2.7863	46.4391	36.0759
Formaldehyde	1	0.0253	0.7600	12.6668	36.0759
Sodium carbonate	0.02	0.0005	0.0536	0.89410	0.7215
Melamine		0.0190	2.4	40	27.1267
Total		0.0701	6	100	100

A5 Quantities Used for R/C of 50

Table 36: Quantities required for R/C of 50 and R/F of 1.0 for various additives concentrations.

R/C = 50	R/F = 1				
Melamine (wt%)	**Resorcinol (g)**	**Formaldehyde (ml)**	**Na_2CO_3 (g)**	**H_2O (ml)**	**Melamine (g)**
0	4.6439	3.14	0.0894	3.41	0
1	4.5975	3.11	0.0885	3.43	0.06
10	4.1795	2.83	0.0805	3.57	0.6
20	3.7151	2.51	0.0715	3.73	1.2
30	3.2507	2.20	0.0626	3.89	1.8
40	2.7863	1.88	0.0536	4.05	2.4

Table 37: Quantities required for R/C of 50 and R/F of 0.75 for various additives concentrations.

R/C = 50	R/F = 0.75				
Melamine (wt%)	**Resorcinol (g)**	**Formaldehyde (ml)**	**Na_2CO_3 (g)**	**H_2O (ml)**	**Melamine (g)**
0	4.3386	3.91	0.0835	3.02	0
1	4.2952	3.87	0.0827	3.04	0.06
10	3.9047	3.52	0.0752	3.22	0.6
20	3.4709	3.13	0.0668	3.42	1.2
30	3.0370	2.74	0.0585	3.62	1.8
40	2.6032	2.35	0.0501	3.81	2.4

Table 38: Quantities required for R/C of 50 and R/F of 0.5 for various additives concentrations.

R/C = 50	R/F = 0.5				
Melamine (wt%)	**Resorcinol (g)**	**Formaldehyde (ml)**	**Na_2CO_3 (g)**	**H_2O (ml)**	**Melamine (g)**
0	3.8344	5.19	0.0738	2.38	0
1	3.7961	5.13	0.0731	2.41	0.06
10	3.4510	4.67	0.0664	2.64	0.6
20	3.0675	4.15	0.0591	2.90	1.2
30	2.6841	3.63	0.0517	3.17	1.8
40	2.3006	3.11	0.0443	3.43	2.4

Table 39: Quantities required for R/C of 50 and R/F of 0.25 for various additives concentrations.

R/C = 50	R/F = 0.25				
Melamine (wt%)	**Resorcinol (g)**	**Formaldehyde (ml)**	**Na_2CO_3 (g)**	**H_2O (ml)**	**Melamine (g)**
0	2.8432	7.69	0.0547	1.11	0
1	2.8148	7.61	0.0542	1.15	0.06
10	2.5589	6.92	0.0493	1.50	0.6
20	2.2746	6.15	0.0438	1.89	1.2
30	1.9902	5.38	0.0383	2.28	1.8
40	1.7059	4.62	0.0328	2.67	2.4

Appendix B Hydrogel Reaction Composition for R/C of 100

This appendix details the weights of resorcinol, formaldehyde, catalyst (sodium carbonate) and Melamine for each gel produced.

The calculations are based on fixed total mass of solids of 6 g in each case, and a solids content of 20% in deionized water.

B1 R/C of 100 and R/F of 0.25

Table 40: MRF0_100_0.25 composition.

	Equivalent Moles	Moles	Mass (g)	Percentage Mass (%)	Percentage Moles (%)
Resorcinol	1	0.0259	2.85623	47.60384	19.96008
Formaldehyde	4	0.1038	3.116274	51.9379	79.84032
Sodium carbonate	0.01	0.0002	0.027496	0.458261	0.199601
Melamine		0	0	0	0
Total		0.1300	6	100	100

Table 41: MRF1_100_0.25 composition.

	Equivalent Moles	Moles	Mass (g)	Percentage Mass (%)	Percentage Moles (%)
Resorcinol	1	0.0257	2.8277	47.1278	19.8865
Formaldehyde	4	0.1027	3.0851	51.4185	79.5461
Sodium carbonate	0.01	0.0003	0.0272	0.45368	0.1989
Melamine		0.0005	0.06	1	0.3684
Total		0.1291	6	100	100

Table 42: MRF10_100_0.25 composition.

	Equivalent Moles	Moles	Mass (g)	Percentage Mass (%)	Percentage Moles (%)
Resorcinol	1	0.0233	2.5706	42.8434	19.1800
Formaldehyde	4	0.0934	2.8046	46.7441	76.7201
Sodium carbonate	0.01	0.0002	0.0247	0.4124	0.1918
Melamine		0.0048	0.6	10	3.9081
Total		0.1217	6	100	100

Table 43: MRF20_100_0.25 composition.

	Equivalent Moles	Moles	Mass (g)	Percentage Mass (%)	Percentage Moles (%)
Resorcinol	1	0.0207	2.2850	38.0831	18.2867
Formaldehyde	4	0.0830	2.4930	41.5503	73.1467
Sodium carbonate	0.01	0.0002	0.0220	0.3666	0.1829
Melamine		0.0095	1.2	20	8.3837
Total		0.1135	6	100	100

Table 44: MRF30_100_0.25 composition.

	Equivalent Moles	Moles	Mass (g)	Percentage Mass (%)	Percentage Moles (%)
Resorcinol	1	0.0182	1.9994	33.3227	17.2535
Formaldehyde	4	0.0726	2.1814	36.3565	69.0139
Sodium carbonate	0.01	0.0002	0.0193	0.3208	0.1725
Melamine		0.0143	1.8	30	13.5600
Total		0.1052	6	100	100

Table 45: MRF40_100_0.25 composition.

	Equivalent Moles	Moles	Mass (g)	Percentage Mass (%)	Percentage Moles (%)
Resorcinol	1	0.015565	1.713735	28.56228	16.04477
Formaldehyde	4	0.062261	1.869761	31.16272	64.17906
Sodium carbonate	0.01	0.000156	0.016497	0.274957	0.160448
Melamine		0.019029	2.4	40.00005	19.61573
Total		0.097011	5.999993	100	100

B2 R/C of 100 and R/F of 0.5

Table 46: MRF0_100_0.5 composition.

	Equivalent Moles	Moles	Mass (g)	Percentage Mass (%)	Percentage Moles (%)
Resorcinol	1	0.0350	3.8581	64.3025	33.2226
Formaldehyde	2	0.0701	2.1047	35.0785	66.4452
Sodium carbonate	0.01	0.0003	0.0371	0.6190	0.3322
Melamine		0	0	0	0
Total		0.1055	6	100	100

Table 47: MRF1_100_0.5 composition.

	Equivalent Moles	Moles	Mass (g)	Percentage Mass (%)	Percentage Moles (%)
Resorcinol	1	0.0347	3.8196	63.6595	33.0719
Formaldehyde	2	0.0694	2.0837	34.7277	66.1438
Sodium carbonate	0.01	0.0003	0.0368	0.6128	0.3307
Melamine		0.0005	0.06	1	0.4535
Total		0.1049	6	100	100

Table 48: MRF10_100_0.5 composition.

	Equivalent Moles	Moles	Mass (g)	Percentage Mass (%)	Percentage Moles (%)
Resorcinol	1	0.0315	3.4723	57.8723	31.6371
Formaldehyde	2	0.0631	1.8942	31.5706	63.2742
Sodium carbonate	0.01	0.0003	0.0334	0.5571	0.3164
Melamine		0.0048	0.6	10	4.7723
Total		0.0997	6	100	100

Table 49: MRF20_100_0.5 composition.

	Equivalent Moles	Moles	Mass (g)	Percentage Mass (%)	Percentage Moles (%)
Resorcinol	1	0.0280	3.0865	51.4420	29.8561
Formaldehyde	2	0.0561	1.6838	28.0628	59.7121
Sodium carbonate	0.01	0.0003	0.0297	0.4952	0.2986
Melamine		0.0095	1.2	20	10.1332
Total		0.0939	6	100	100

Table 50: MRF30_100_0.5 composition.

	Equivalent Moles	Moles	Mass (g)	Percentage Mass (%)	Percentage Moles (%)
Resorcinol	1	0.0245	2.7007	45.0118	27.8409
Formaldehyde	2	0.0491	1.4733	24.5549	55.6819
Sodium carbonate	0.01	0.0002	0.0260	0.4333	0.2784
Melamine		0.0143	1.8	30	16.1988
Total		0.0881	6	100	100

Table 51: MRF40_100_0.5 composition.

	Equivalent Moles	Moles	Mass (g)	Percentage Mass (%)	Percentage Moles (%)
Resorcinol	1	0.0210	2.3149	38.5815	25.5423
Formaldehyde	2	0.0420	1.2628	21.0471	51.0846
Sodium carbonate	0.01	0.0002	0.0223	0.3714	0.2554
Melamine		0.0190	2.4	40	23.1177
Total		0.0823	6	100	100

B3 R/C of 100 and R/F of 0.75

Table 52: MRF0_100_0.75 composition.

	Equivalent Moles	Moles	Mass (g)	Percentage Mass (%)	Percentage Moles (%)
Resorcinol	1	0.0397	4.3690	72.8169	42.6742
Formaldehyde	1.33	0.0529	1.5889	26.4821	56.8990
Sodium carbonate	0.01	0.0004	0.0421	0.7010	0.4267
Melamine		0	0	0	0
Total		0.0930	6	100	100

Table 53: MRF1_100_0.75 composition.

	Equivalent Moles	Moles	Mass (g)	Percentage Mass (%)	Percentage Moles (%)
Resorcinol	1	0.0393	4.3253	72.0887	42.4549
Formaldehyde	1.33	0.0524	1.5730	26.2173	56.6065
Sodium carbonate	0.01	0.0004	0.0416	0.6997	0.4245
Melamine		0.0005	0.06	1	0.5141
Total		0.0925	6	100	100

Table 54: MRF10_100_0.75 composition.

	Equivalent Moles	Moles	Mass (g)	Percentage Mass (%)	Percentage Moles (%)
Resorcinol	1	0.0357	3.9321	65.5352	40.3789
Formaldehyde	1.33	0.0476	1.4300	23.8340	53.8385
Sodium carbonate	0.01	0.0004	0.0378	0.6309	0.4038
Melamine		0.0048	0.6	10	5.3788
Total		0.0884	6	100	100

Table 55: MRF20_100_0.75 composition.

	Equivalent Moles	Moles	Mass (g)	Percentage Mass (%)	Percentage Moles (%)
Resorcinol	1	0.0317	3.4952	58.2535	37.8351
Formaldehyde	1.33	0.0423	1.2711	21.1857	50.4468
Sodium carbonate	0.01	0.0003	0.0336	0.5608	0.3783
Melamine		0.0095	1.2	20	11.3398
Total		0.0839	6	100	100

Table 56: MRF30_100_0.75 composition.

	Equivalent Moles	Moles	Mass (g)	Percentage Mass (%)	Percentage Moles (%)
Resorcinol	1	0.0278	3.0583	50.9718	35.0001
Formaldehyde	1.33	0.0370	1.1122	18.5375	46.6668
Sodium carbonate	0.01	0.0003	0.0294	0.4907	0.3500
Melamine		0.0143	1.8	30	17.9831
Total		0.0794	6	100	100

Table 57: MRF40_100_0.75 composition.

	Equivalent Moles	Moles	Mass (g)	Percentage Mass (%)	Percentage Moles (%)
Resorcinol	1	0.0239	2.6214	43.6901	31.8210
Formaldehyde	1.33	0.0317	0.9533	15.8893	42.4280
Sodium carbonate	0.01	0.0002	0.0252	0.4206	0.3182
Melamine		0.0190	2.4	40	25.4328
Total		0.0748	6	100	100

B4 R/C of 100 and R/F of 1.0

Table 58: MRF0_100_1.0 composition.

	Equivalent Moles	Moles	Mass (g)	Percentage Mass (%)	Percentage Moles (%)
Resorcinol	1	0.0425	4.6788	77.9795	49.7512
Formaldehyde	1	0.0425	1.2762	21.2698	49.7512
Sodium carbonate	0.01	0.0004	0.0450	0.7507	0.4975
Melamine		0	0	0	0
Total		0.0854	6	100	100

Table 59: MRF1_100_1.0 composition.

	Equivalent Moles	Moles	Mass (g)	Percentage Mass (%)	Percentage Moles (%)
Resorcinol	1	0.0421	4.6320	77.1997	49.4729
Formaldehyde	1	0.0421	1.2634	21.0571	49.4729
Sodium carbonate	0.01	0.0004	0.0446	0.7432	0.4947
Melamine		0.0005	0.06	1.0	0.5594
Total		0.0850	6	100	100

Table 60: MRF10_100_1.0 composition.

	Equivalent Moles	Moles	Mass (g)	Percentage Mass (%)	Percentage Moles (%)
Resorcinol	1	0.0382	4.2109	70.1816	46.8518
Formaldehyde	1	0.0382	1.1486	19.1428	46.8518
Sodium carbonate	0.01	0.0004	0.0405	0.6756	0.4685
Melamine		0.0048	0.6	10	5.8278
Total		0.0816	6	100	100

Table 61: MRF20_100_1.0 composition.

	Equivalent Moles	Moles	Mass (g)	Percentage Mass (%)	Percentage Moles (%)
Resorcinol	1	0.0340	3.7430	62.3836	43.6705
Formaldehyde	1	0.0340	1.0209	17.0158	43.6705
Sodium carbonate	0.01	0.0003	0.0360	0.6005	0.43670
Melamine		0.0095	1.2	20	12.2222
Total		0.0778	6	100	100

Table 62: MRF30_100_1.0 composition.

	Equivalent Moles	Moles	Mass (g)	Percentage Mass (%)	Percentage Moles (%)
Resorcinol	1	0.0297	3.2751	54.5857	40.1641
Formaldehyde	1	0.0297	0.8933	14.8888	40.1641
Sodium carbonate	0.01	0.0003	0.0315	0.5255	0.4016
Melamine		0.0143	1.8	30	19.2701
Total		0.0741	6	100	100

Table 63: MRF40_100_1.0 composition.

	Equivalent Moles	Moles	Mass (g)	Percentage Mass (%)	Percentage Moles (%)
Resorcinol	1	0.0255	2.8073	46.7877	36.2801
Formaldehyde	1	0.0255	0.7657	12.7619	36.2801
Sodium carbonate	0.01	0.0002	0.0270	0.4504	0.3628
Melamine		0.0190	2.4	40	27.0770
Total		0.0703	6	100	100

B5 Quantities Used for R/C of 100

Table 64: Quantities required for R/C of 100 and R/F of 1.0 for various additives concentrations.

R/C = 100	R/F = 1				
Melamine (wt%)	**Resorcinol (g)**	**Formaldehyde (ml)**	**Na_2CO_3 (g)**	**H_2O (ml)**	**Melamine (g)**
0	4.6788	3.16	0.0450	3.40	0
1	4.6320	3.13	0.0446	3.42	0.06
10	4.2109	2.85	0.0405	3.56	0.6
20	3.7430	2.53	0.0360	3.72	1.2
30	3.2751	2.22	0.0315	3.88	1.8
40	2.8073	1.90	0.0270	4.04	2.4

Table 65: Quantities required for R/C of 100 and R/F of 0.75 for various additives concentrations.

R/C = 100	R/F = 0.75				
Melamine (wt%)	**Resorcinol (g)**	**Formaldehyde (ml)**	**Na_2CO_3 (g)**	**H_2O (ml)**	**Melamine (g)**
0	4.3690	3.94	0.0421	3.01	0
1	4.3253	3.90	0.0416	3.03	0.06
10	3.9321	3.55	0.0379	3.21	0.6
20	3.4952	3.15	0.0336	3.41	1.2
30	3.0583	2.76	0.0294	3.61	1.8
40	2.6214	2.36	0.0252	3.81	2.4

Table 66: Quantities required for R/C of 100 and R/F of 0.5 for various additives concentrations.

R/C = 100	R/F = 0.5				
Melamine (wt%)	**Resorcinol (g)**	**Formaldehyde (ml)**	**Na_2CO_3 (g)**	**H_2O (ml)**	**Melamine (g)**
0	3.8582	5.22	0.0371	2.36	0
1	3.8196	5.17	0.0368	2.39	0.06
10	3.4723	4.70	0.0334	2.63	0.6
20	3.0865	4.17	0.0297	2.89	1.2
30	2.7007	3.65	0.0260	3.15	1.8
40	2.3149	3.13	0.0223	3.42	2.4

Table 67: Quantities required for R/C of 100 and R/F of 0.25 for various additives concentrations.

R/C = 100	R/F = 0.25				
Melamine (wt%)	**Resorcinol (g)**	**Formaldehyde (ml)**	**Na_2CO_3 (g)**	**H_2O (ml)**	**Melamine (g)**
0	2.8562	7.73	0.0275	1.10	0
1	2.8277	7.65	0.0272	1.14	0.06
10	2.5706	6.95	0.0247	1.49	0.6
20	2.2850	6.18	0.0220	1.88	1.2
30	1.9994	5.41	0.0192	2.27	1.8
40	1.7137	4.64	0.0165	2.66	2.4

Appendix C Hydrogel Reaction Composition for R/C of 100

This appendix details the weights of resorcinol, formaldehyde, catalyst (sodium carbonate) and Melamine for each gel produced.

The calculations are based on fixed total mass of solids of 6 g in each case, and a solids content of 20% in deionized water.

C1 R/C of 200 and R/F of 0.25

Table 68: MRF0_200_0.25 composition.

	Equivalent Moles	Moles	Mass (g)	Percentage Mass (%)	Percentage Moles (%)
Resorcinol	1	0.0260	2.8628	47.7132	19.9800
Formaldehyde	4	0.1040	3.1234	52.0572	79.9201
Sodium carbonate	0.005	1.30E-4	0.0138	0.2297	0.0999
Melamine		0	0	0	0
Total		0.1301	6	100	100

Table 69: MRF1_200_0.25 composition.

	Equivalent Moles	Moles	Mass (g)	Percentage Mass (%)	Percentage Moles (%)
Resorcinol	1	0.0257	2.8342	47.2360	19.9065
Formaldehyde	4	0.1030	3.0922	51.5366	79.6261
Sodium carbonate	0.005	1.29E-4	0.0136	0.2274	0.0995
Melamine		0.0005	0.06	1.0	0.3679
Total		0.1293	6	100	100

Table 70: MRF10_200_0.25 composition.

	Equivalent Moles	Moles	Mass (g)	Percentage Mass (%)	Percentage Moles (%)
Resorcinol	1	0.0234	2.5765	42.9418	19.2001
Formaldehyde	4	0.0936	2.8111	46.8515	76.8006
Sodium carbonate	0.005	1.17E-4	0.0124	0.2067	0.0960
Melamine		0.0048	0.6	10	3.9032
Total		0.1219	6	100	100

Table 71: MRF20_200_0.25 composition.

	Equivalent Moles	Moles	Mass (g)	Percentage Mass (%)	Percentage Moles (%)
Resorcinol	1	0.0208	2.2902	38.1705	18.3069
Formaldehyde	4	0.0832	2.4988	41.6458	73.2278
Sodium carbonate	0.005	1.04E-4	0.0110	0.1837	0.0915
Melamine		0.0095	1.2	20	8.3738
Total		0.1136	6	100	100

Table 72: MRF30_200_0.25 composition.

	Equivalent Moles	Moles	Mass (g)	Percentage Mass (%)	Percentage Moles (%)
Resorcinol	1	0.0182	2.0040	33.3992	17.2737
Formaldehyde	4	0.0728	2.1864	36.4400	69.0950
Sodium carbonate	0.005	9.1E-05	0.0096	0.1608	0.0864
Melamine		0.0143	1.8	30	13.5449
Total		0.1054	6	100	100

Table 73: MRF40_200_0.25 composition.

	Equivalent Moles	Moles	Mass (g)	Percentage Mass (%)	Percentage Moles (%)
Resorcinol	1	0.0156	1.717677	28.62792	16.06489
Formaldehyde	4	0.0624	1.874062	31.23433	64.25954
Sodium carbonate	0.005	7.8E-05	0.008268	0.137794	0.080324
Melamine		0.019029	2.4	39.99996	19.59525
Total		0.097113	6.000006	100	100

C2 R/C of 200 and R/F of 0.5

Table 74: MRF0_200_0.5 composition.

	Equivalent Moles	Moles	Mass (g)	Percentage Mass (%)	Percentage Moles (%)
Resorcinol	1	0.0351	3.8701	64.5022	33.2779
Formaldehyde	2	0.0703	2.1112	35.1874	66.5557
Sodium carbonate	0.005	1.76E-4	0.0186	0.3105	0.1664
Melamine		0	0	0	0
Total		0.1056	6	100	100

Table 75: MRF1_200_0.5 composition.

	Equivalent Moles	Moles	Mass (g)	Percentage Mass (%)	Percentage Moles (%)
Resorcinol	1	0.0348	3.8314	63.8571	33.1272
Formaldehyde	2	0.0696	2.0901	34.8355	66.254
Sodium carbonate	0.005	1.74E-4	0.0184	0.30736	0.1656
Melamine		0.0005	0.06	1	0.4529
Total		0.1050	6	100	100

Table 76: MRF10_200_0.5 composition.

	Equivalent Moles	Moles	Mass (g)	Percentage Mass (%)	Percentage Moles (%)
Resorcinol	1	0.0316	3.4831	58.0519	31.6919
Formaldehyde	2	0.0633	1.9001	31.6686	63.3838
Sodium carbonate	0.005	1.58E-4	0.0168	0.2794	0.1585
Melamine		0.0048	0.6	10	4.7658
Total		0.0998	6	100	100

Table 77: MRF20_200_0.5 composition.

	Equivalent Moles	Moles	Mass (g)	Percentage Mass (%)	Percentage Moles (%)
Resorcinol	1	0.0281	3.0961	51.6017	29.9101
Formaldehyde	2	0.0562	1.6890	28.1499	59.8202
Sodium carbonate	0.005	1.41E-4	0.0149	0.2484	0.1495
Melamine		0.0095	1.2	20	10.1201
Total		0.0940	6	100	100

Table 78: MRF30_200_0.5 composition.

	Equivalent Moles	Moles	Mass (g)	Percentage Mass (%)	Percentage Moles (%)
Resorcinol	1	0.0246	2.7091	45.1515	27.8938
Formaldehyde	2	0.0492	1.4779	24.6312	55.7875
Sodium carbonate	0.005	1.23E-4	0.0130	0.2173	0.1395
Melamine		0.0143	1.8	30	16.1793
Total		0.0882	6	100	100

Table 79: MRF40_200_0.5 composition.

	Equivalent Moles	Moles	Mass (g)	Percentage Mass (%)	Percentage Moles (%)
Resorcinol	1	0.0211	2.3221	38.7013	25.5933
Formaldehyde	2	0.0422	1.2667	21.1124	51.1866
Sodium carbonate	0.005	1.05E-4	0.0112	0.1863	0.1280
Melamine		0.0190	2.4	40	23.0921
Total		0.0824	6	100	100

C3 R/C of 200 and R/F of 0.75

Table 80: MRF0_200_0.75 composition.

	Equivalent Moles	Moles	Mass (g)	Percentage Mass (%)	Percentage Moles (%)
Resorcinol	1	0.0398	4.3844	73.0730	42.7655
Formaldehyde	1.33	0.0531	1.5945	26.5753	57.0207
Sodium carbonate	0.005	1.99E-4	0.0211	0.3517	0.2138
Melamine		0	0	0	0
Total		0.0931	6	100	100

Table 81: MRF1_200_0.75 composition.

	Equivalent Moles	Moles	Mass (g)	Percentage Mass (%)	Percentage Moles (%)
Resorcinol	1	0.0394	4.3405	72.3423	42.5459
Formaldehyde	1.33	0.0526	1.5786	26.3095	56.7279
Sodium carbonate	0.005	1.97E-4	0.0209	0.3482	0.2127
Melamine		4.76E-5	0.06	1	0.5134
Total		0.0927	6	100	100

Table 82: MRF10_200_0.75 composition.

	Equivalent Moles	Moles	Mass (g)	Percentage Mass (%)	Percentage Moles (%)
Resorcinol	1	0.0358	3.9459	65.7657	40.4682
Formaldehyde	1.33	0.0478	1.4351	23.9178	53.9576
Sodium carbonate	0.005	1.79E-4	0.0190	0.3165	0.2023
Melamine		0.0048	0.6	10	5.3718
Total		0.0886	6	100	100

Table 83: MRF20_200_0.75 composition.

	Equivalent Moles	Moles	Mass (g)	Percentage Mass (%)	Percentage Moles (%)
Resorcinol	1	0.0319	3.5075	58.4584	37.9219
Formaldehyde	1.33	0.0425	1.2756	21.2602	50.5625
Sodium carbonate	0.005	1.59E-4	0.0169	0.2814	0.1896
Melamine		0.0095	1.2	20	11.3260
Total		0.0840	6	100	100

Table 84: MRF30_200_0.75 composition.

	Equivalent Moles	Moles	Mass (g)	Percentage Mass (%)	Percentage Moles (%)
Resorcinol	1	0.0279	3.0691	51.1511	35.0836
Formaldehyde	1.33	0.0372	1.1162	18.6027	46.7782
Sodium carbonate	0.005	1.39E-4	0.0148	0.2462	0.1754
Melamine		0.0143	1.8	30	17.9628
Total		0.0794	6	100	100

Table 85: MRF40_200_0.75 composition.

	Equivalent Moles	Moles	Mass (g)	Percentage Mass (%)	Percentage Moles (%)
Resorcinol	1	0.0239	2.6306	43.8438	31.9002
Formaldehyde	1.33	0.0319	0.9567	15.9452	42.5336
Sodium carbonate	0.005	1.19E-4	0.0127	0.2110	0.1595
Melamine		0.0190	2.4	40	25.4067
Total		0.0749	6	100	100

C4 R/C of 200 and R/F of 1.0

Table 86: MRF0_200_1.0 composition.

	Equivalent Moles	Moles	Mass (g)	Percentage Mass (%)	Percentage Moles (%)
Resorcinol	1	0.0427	4.6964	78.2733	49.8753
Formaldehyde	1	0.0427	1.2810	21.3500	49.8753
Sodium carbonate	0.005	2.13E-4	0.0226	0.3767	0.2494
Melamine		0	0	0	0
Total		0.0855	6	100	100

Table 87: MRF1_200_1.0 composition.

	Equivalent Moles	Moles	Mass (g)	Percentage Mass (%)	Percentage Moles (%)
Resorcinol	1	0.0422	4.6494	77.4906	49.5967
Formaldehyde	1	0.0422	1.2682	21.1364	49.5967
Sodium carbonate	0.005	2.11E-4	0.0224	0.3730	0.2480
Melamine		4.76E-4	0.06	1	0.5587
Total		0.0851	6	100	100

Table 88: MRF10_200_1.0 composition.

	Equivalent Moles	Moles	Mass (g)	Percentage Mass (%)	Percentage Moles (%)
Resorcinol	1	0.0384	4.2268	70.4460	46.9721
Formaldehyde	1	0.0384	1.1529	19.2149	46.9721
Sodium carbonate	0.005	1.92E-4	0.0203	0.3391	0.2349
Melamine		0.0048	0.6	10	5.8209
Total		0.0817	6	100	100

Table 89: MRF20_200_1.0 composition.

	Equivalent Moles	Moles	Mass (g)	Percentage Mass (%)	Percentage Moles (%)
Resorcinol	1	0.0341	3.7571	62.6187	43.7862
Formaldehyde	1	0.0341	1.0248	17.0799	43.7862
Sodium carbonate	0.005	1.71E-4	0.0181	0.3014	0.2189
Melamine		0.0095	1.2	20	12.2086
Total		0.0779	6	100	100

Table 90: MRF30_200_1.0 composition.

	Equivalent Moles	Moles	Mass (g)	Percentage Mass (%)	Percentage Moles (%)
Resorcinol	1	0.0299	3.2875	54.7913	40.2741
Formaldehyde	1	0.0299	0.8967	14.9449	40.2741
Sodium carbonate	0.005	1.49E-4	0.0158	0.2637	0.2014
Melamine		0.0143	1.8	30	19.2504
Total		0.0741	6	100	100

Table 91: MRF40_200_1.0 composition.

	Equivalent Moles	Moles	Mass (g)	Percentage Mass (%)	Percentage Moles (%)
Resorcinol	1	0.0256	2.8178	46.9640	36.3831
Formaldehyde	1	0.0256	0.7686	12.8100	36.3831
Sodium carbonate	0.005	1.28E-4	0.0136	0.2260	0.1819
Melamine		0.0190	2.4	40	27.0519
Total		0.0703	6	100	100

C5 Quantities Used for R/C of 200

Table 92: Quantities required for R/C of 200 and R/F of 1.0 for various additives concentrations.

R/C = 200	R/F = 1				
Melamine (wt%)	**Resorcinol (g)**	**Formaldehyde (ml)**	**Na_2CO_3 (g)**	**H_2O (ml)**	**Melamine (g)**
0	4.6964	3.18	0.0226	3.40	0
1	4.6494	3.14	0.0224	3.41	0.06
10	4.2268	2.86	0.0203	3.56	0.6
20	3.7571	2.54	0.0181	3.72	1.2
30	3.2875	2.22	0.0158	3.88	1.8
40	2.8178	1.91	0.0136	4.04	2.4

Table 93: Quantities required for R/C of 200 and R/F of 0.75 for various additives concentrations.

R/C = 200	R/F = 0.75				
Melamine (wt%)	**Resorcinol (g)**	**Formaldehyde (ml)**	**Na_2CO_3 (g)**	**H_2O (ml)**	**Melamine (g)**
0	4.3844	3.95	0.0211	3.00	0
1	4.3405	3.91	0.0209	3.02	0.06
10	3.9459	3.56	0.0190	3.20	0.6
20	3.5075	3.16	0.0169	3.40	1.2
30	3.0691	2.77	0.0148	3.60	1.8
40	2.6306	2.37	0.0127	3.80	2.4

Table 94: Quantities required for R/C of 200 and R/F of 0.5 for various additives concentrations.

R/C = 200	R/F = 0.5				
Melamine (wt%)	**Resorcinol (g)**	**Formaldehyde (ml)**	**Na_2CO_3 (g)**	**H_2O (ml)**	**Melamine (g)**
0	3.8701	5.23	0.0186	2.36	0
1	3.8314	5.18	0.0184	2.38	0.06
10	3.4831	4.71	0.0168	2.62	0.6
20	3.0961	4.19	0.0149	2.88	1.2
30	2.7091	3.66	0.0130	3.15	1.8
40	2.3221	3.14	0.0112	3.41	2.4

Table 95: Quantities required for R/C of 200 and R/F of 0.25 for various additives concentrations.

R/C = 200	R/F = 0.25				
Melamine (wt%)	**Resorcinol (g)**	**Formaldehyde (ml)**	**Na_2CO_3 (g)**	**H_2O (ml)**	**Melamine (g)**
0	2.8628	7.74	0.0138	1.09	0
1	2.8342	7.67	0.0136	1.13	0.06
10	2.5765	6.97	0.0124	1.48	0.6
20	2.2902	6.20	0.0110	1.87	1.2
30	2.0040	5.42	0.0096	2.26	1.8
40	1.7177	4.65	0.0083	2.65	2.4

Appendix D Hydrogel Reaction Composition for R/C of 400

This appendix details the weights of resorcinol, formaldehyde, catalyst (sodium carbonate) and Melamine for each gel produced.

The calculations are based on fixed total mass of solids of 6 g in each case, and a solids content of 20% in deionized water.

D1 R/C of 400 and R/F of 0.25

Table 96: MRF0_400_0.25 composition.

	Equivalent Moles	Moles	Mass (g)	Percentage Mass (%)	Percentage Moles (%)
Resorcinol	1	0.0260	2.8661	47.7680	19.9900
Formaldehyde	4	0.1041	3.1270	52.1170	79.9600
Sodium carbonate	0.0025	6.51E-5	0.0069	0.1150	0.0500
Melamine		0	0	0	0
Total		0.1302	6	100	100

Table 97: MRF1_400_0.25 composition.

	Equivalent Moles	Moles	Mass (g)	Percentage Mass (%)	Percentage Moles (%)
Resorcinol	1	0.0258	2.8374	47.2903	19.9165
Formaldehyde	4	0.1031	3.0957	51.5959	79.6660
Sodium carbonate	0.0025	6.44E-5	0.0068	0.1138	0.0498
Melamine		4.76E-4	0.06	1	0.3677
Total		0.1294	6	100	100

Table 98: MRF10_400_0.25 composition.

	Equivalent Moles	Mass (g)	Percentage Mass (%)	Percentage Moles (%)	Equivalent Moles
Resorcinol	1	0.0234	2.5795	42.9912	19.2102
Formaldehyde	4	0.0937	2.8143	46.9053	76.8409
Sodium carbonate	0.0025	5.86E-5	0.0062	0.1035	0.0480
Melamine		0.0048	0.6	10	3.9008
Total		0.1220	6	100	100

Table 99: MRF20_400_0.25 composition.

	Equivalent Moles	Mass (g)	Percentage Mass (%)	Percentage Moles (%)	Equivalent Moles
Resorcinol	1	0.0208	2.2929	38.2144	18.3171
Formaldehyde	4	0.0833	2.5016	41.6936	73.2683
Sodium carbonate	0.0025	5.21E-5	0.0055	0.0920	0.0458
Melamine		0.0095	1.2	20	8.3688
Total		0.1137	6	100	100

Table 100: MRF30_400_0.25 composition.

	Equivalent Moles	Mass (g)	Percentage Mass (%)	Percentage Moles (%)	Equivalent Moles
Resorcinol	1	0.0182	2.0063	33.4376	17.2839
Formaldehyde	4	0.0729	2.1889	36.4819	69.1356
Sodium carbonate	0.0025	4.56E-5	0.0048	0.0805	0.0432
Melamine		0.0143	1.8	30	13.5373
Total		0.1054	6	100	100

Table 101: MRF40_400_0.25 composition.

	Equivalent Moles	Mass (g)	Percentage Mass (%)	Percentage Moles (%)	Equivalent Moles
Resorcinol	1	0.0156	1.7196	28.6608	16.0750
Formaldehyde	4	0.0625	1.8762	31.2702	64.2998
Sodium carbonate	0.0025	3.9E-5	0.0041	0.0690	0.0402
Melamine		0.0190	2.4	40	19.5850
Total		0.0972	6	100	100

D2 R/C of 400 and R/F of 0.5

Table 102: MRF0_400_0.5 composition.

	Equivalent Moles	Mass (g)	Percentage Mass (%)	Percentage Moles (%)	Equivalent Moles
Resorcinol	1	0.0352	3.8761	64.6024	33.3056
Formaldehyde	2	0.0704	2.1145	35.2421	66.6112
Sodium carbonate	0.0025	8.8E-5	0.0093	0.1555	0.0833
Melamine		0	0	0	0
Total		0.1057	6	100	100

Table 103: MRF1_400_0.5 composition.

	Equivalent Moles	Mass (g)	Percentage Mass (%)	Percentage Moles (%)	Equivalent Moles
Resorcinol	1	0.0348	3.8374	63.9564	33.1548
Formaldehyde	2	0.0697	2.0934	34.8896	66.3097
Sodium carbonate	0.0025	8.71E-5	0.0092	0.1539	0.0829
Melamine		4.76E-4	0.06	1	0.4525
Total		0.1051	6	100	100

Table 104: MRF10_400_0.5 composition.

	Equivalent Moles	Mass (g)	Percentage Mass (%)	Percentage Moles (%)	Equivalent Moles
Resorcinol	1	0.031685	3.488536	58.14221	31.7194
Formaldehyde	2	0.06337	1.903074	31.71787	63.43879
Sodium carbonate	0.0025	7.92E-05	0.008396	0.139927	0.079298
Melamine		0.004757	0.6	10	4.762514
Total		0.099892	6.000006	100	100

Table 105: MRF20_400_0.5 composition.

	Equivalent Moles	Mass (g)	Percentage Mass (%)	Percentage Moles (%)	Equivalent Moles
Resorcinol	1	0.0282	3.1009	51.6820	29.9372
Formaldehyde	2	0.0563	1.6916	28.1937	59.8744
Sodium carbonate	0.0025	7.04E-5	0.0075	0.1244	0.0748
Melamine		0.0095	1.2	20	10.1136
Total		0.0941	6	100	100

Table 106: MRF30_400_0.5 composition.

	Equivalent Moles	Mass (g)	Percentage Mass (%)	Percentage Moles (%)	Equivalent Moles
Resorcinol	1	0.0246	2.7133	45.2217	27.9202
Formaldehyde	2	0.0493	1.4802	24.6695	55.8405
Sodium carbonate	0.0025	6.16E-5	0.0065	0.1088	0.0698
Melamine		0.0143	1.8	30	16.1695
Total		0.0883	6	100	100

Table 107: MRF40_400_0.5 composition.

	Equivalent Moles	Mass (g)	Percentage Mass (%)	Percentage Moles (%)	Equivalent Moles
Resorcinol	1	0.0211	2.3257	38.7615	25.6189
Formaldehyde	2	0.0422	1.2687	21.1453	51.2378
Sodium carbonate	0.0025	5.28E-5	0.0056	0.0933	0.0640
Melamine		0.0190	2.4	40	23.0793
Total		0.0824	6	100	100

D3 R/C of 400 and R/F of 0.75

Table 108: MRF0_400_0.75 composition.

	Equivalent Moles	Mass (g)	Percentage Mass (%)	Percentage Moles (%)	Equivalent Moles
Resorcinol	1	0.0399	4.3921	73.2017	42.8113
Formaldehyde	1.33	0.0532	1.5973	26.6221	57.0817
Sodium carbonate	0.0025	9.97E-5	0.0106	0.1762	0.1070
Melamine		0	0	0	0
Total		0.0932	6	100	100

Table 109: MRF1_400_0.75 composition.

	Equivalent Moles	Mass (g)	Percentage Mass (%)	Percentage Moles (%)	Equivalent Moles
Resorcinol	1	0.0395	4.3482	72.4697	42.5916
Formaldehyde	1.33	0.0527	1.5813	26.3559	56.7888
Sodium carbonate	0.0025	9.87E-5	0.0105	0.1744	0.1065
Melamine		4.76E-4	0.06	1	0.5131
Total		0.0927	6	100	100

Table 110: MRF10_400_0.75 composition.

	Equivalent Moles	Mass (g)	Percentage Mass (%)	Percentage Moles (%)	Equivalent Moles
Resorcinol	1	0.0359	3.9529	65.8815	40.5130
Formaldehyde	1.33	0.0479	1.4376	23.9599	54.0174
Sodium carbonate	0.0025	8.98E-5	0.0095	0.1585	0.1013
Melamine		0.0048	0.6	10	5.3683
Total		0.0886	6	100	100

Table 111: MRF20_400_0.75 composition.

	Equivalent Moles	Mass (g)	Percentage Mass (%)	Percentage Moles (%)	Equivalent Moles
Resorcinol	1	0.0319	3.5137	58.5614	37.9654
Formaldehyde	1.33	0.0425	1.2779	21.2977	50.6206
Sodium carbonate	0.0025	7.98E-5	0.0085	0.1409	0.0949
Melamine		0.0095	1.2	20	11.3190
Total		0.0841	6	100	100

Table 112: MRF30_400_0.75 composition.

	Equivalent Moles	Mass (g)	Percentage Mass (%)	Percentage Moles (%)	Equivalent Moles
Resorcinol	1	0.0279	3.0745	51.2412	35.1255
Formaldehyde	1.33	0.0372	1.1181	18.6355	46.8340
Sodium carbonate	0.0025	6.98E-5	0.0074	0.1233	0.0878
Melamine		0.0143	1.8	30	17.9526
Total		0.0795	6	100	100

Table 113: MRF40_400_0.75 composition.

	Equivalent Moles	Mass (g)	Percentage Mass (%)	Percentage Moles (%)	Equivalent Moles
Resorcinol	1	0.0239	2.6353	43.9211	31.9399
Formaldehyde	1.33	0.0319	0.9584	15.9733	42.5866
Sodium carbonate	0.0025	5.98E-5	0.0063	0.1057	0.0798
Melamine		0.0190	2.4	40	25.3936
Total		0.0749	6	100	100

D4 R/C of 400 and R/F of 1.0

Table 114: MRF0_400_1.0 composition.

	Equivalent Moles	Mass (g)	Percentage Mass (%)	Percentage Moles (%)	Equivalent Moles
Resorcinol	1	0.0427	4.7053	78.4210	49.9376
Formaldehyde	1	0.0427	1.2834	21.3902	49.9376
Sodium carbonate	0.0025	1.07E-4	0.0113	0.1887	0.1248
Melamine		0	0	0	0
Total		0.0856	6	100	100

Table 115: MRF1_400_1.0 composition.

	Equivalent Moles	Mass (g)	Percentage Mass (%)	Percentage Moles (%)	Equivalent Moles
Resorcinol	1	0.0423	4.6582	77.6368	49.6587
Formaldehyde	1	0.0423	1.2706	21.1763	49.6587
Sodium carbonate	0.0025	1.06E-4	0.0112	0.1868	0.1241
Melamine		4.76E-4	0.06	1	0.5584
Total		0.0852	6	100	100

Table 116: MRF10_400_1.0 composition.

	Equivalent Moles	Mass (g)	Percentage Mass (%)	Percentage Moles (%)	Equivalent Moles
Resorcinol	1	0.0385	4.2347	70.5790	47.0325
Formaldehyde	1	0.0385	1.1551	19.2512	47.0325
Sodium carbonate	0.0025	9.62E-5	0.0102	0.1699	0.1176
Melamine		0.0048	0.6	10	5.8174
Total		0.0818	6	100	100

Table 117: MRF20_400_1.0 composition.

	Equivalent Moles	Mass (g)	Percentage Mass (%)	Percentage Moles (%)	Equivalent Moles
Resorcinol	1	0.0342	3.764215	62.7369	43.8443
Formaldehyde	1	0.0342	1.026732	17.1122	43.8443
Sodium carbonate	0.0025	8.55E-5	0.009059	0.1510	0.1096
Melamine		0.0095	1.2	20	12.2018
Total		0.0780	6	100	100

Table 118: MRF30_400_1.0 composition.

	Equivalent Moles	Mass (g)	Percentage Mass (%)	Percentage Moles (%)	Equivalent Moles
Resorcinol	1	0.0299	3.2937	54.8948	40.3294
Formaldehyde	1	0.0299	0.8984	14.9732	40.3294
Sodium carbonate	0.0025	7.48E-5	0.0079	0.1321	0.1008
Melamine		0.0143	1.8	30	19.2404
Total		0.0742	6	100	100

Table 119: MRF40_400_1.0 composition.

	Equivalent Moles	Mass (g)	Percentage Mass (%)	Percentage Moles (%)	Equivalent Moles
Resorcinol	1	0.0256	2.8232	47.0527	36.4348
Formaldehyde	1	0.0256	0.7700	12.8341	36.4348
Sodium carbonate	0.0025	6.41E-5	0.0068	0.1132	0.09109
Melamine		0.0190	2.4	40	27.0393
Total		0.0704	6.000006	100	100

C5 Quantities Used for R/C of 400

Table 120: Quantities required for R/C of 400 and R/F of 1.0 for various additives concentrations.

R/C = 400	R/F = 1				
Melamine (wt%)	**Resorcinol (g)**	**Formaldehyde (ml)**	**Na_2CO_3 (g)**	**H_2O (ml)**	**Melamine (g)**
0	4.7053	3.18	0.0113	3.39	0
1	4.6582	3.15	0.0112	3.41	0.06
10	4.2347	2.86	0.0102	3.55	0.6
20	3.7642	2.55	0.0091	3.71	1.2
30	3.2937	2.23	0.0079	3.87	1.8
40	2.8232	1.91	0.0068	4.04	2.4

Table 121: Quantities required for R/C of 400 and R/F of 0.75 for various additives concentrations.

R/C = 400	R/F = 0.75				
Melamine (wt%)	**Resorcinol (g)**	**Formaldehyde (ml)**	**Na_2CO_3 (g)**	**H_2O (ml)**	**Melamine (g)**
0	4.3921	3.96	0.0106	3.00	0
1	4.3482	3.92	0.0105	3.02	0.06
10	3.9529	3.56	0.0095	3.20	0.6
20	3.5137	3.17	0.0085	3.40	1.2
30	3.0745	2.77	0.0074	3.60	1.8
40	2.6353	2.38	0.0063	3.80	2.4

Table 122: Quantities required for R/C of 400 and R/F of 0.5 for various additives concentrations.

R/C = 400	R/F = 0.5				
Melamine (wt%)	**Resorcinol (g)**	**Formaldehyde (ml)**	**Na_2CO_3 (g)**	**H_2O (ml)**	**Melamine (g)**
0	3.8762	5.24	0.0093	2.35	0
1	3.8374	5.19	0.0092	2.38	0.06
10	3.4885	4.72	0.0084	2.62	0.6
20	3.1009	4.19	0.0075	2.88	1.2
30	2.7133	3.67	0.0065	3.15	1.8
40	2.3257	3.15	0.0056	3.41	2.4

Table 123: Quantities required for R/C of 400 and R/F of 0.25 for various additives concentrations.

R/C = 400	R/F = 0.25				
Melamine (wt%)	**Resorcinol (g)**	**Formaldehyde (ml)**	**Na_2CO_3 (g)**	**H_2O (ml)**	**Melamine (g)**
0	2.8661	7.75	0.0069	1.08	0
1	2.8374	7.68	0.0068	1.12	0.06
10	2.5795	6.98	0.0062	1.47	0.6
20	2.2929	6.20	0.0055	1.87	1.2
30	2.0063	5.43	0.0048	2.26	1.8
40	1.7197	4.65	0.0041	2.65	2.4

Appendix E SEM Images

R/C=50 and R/F0.75.

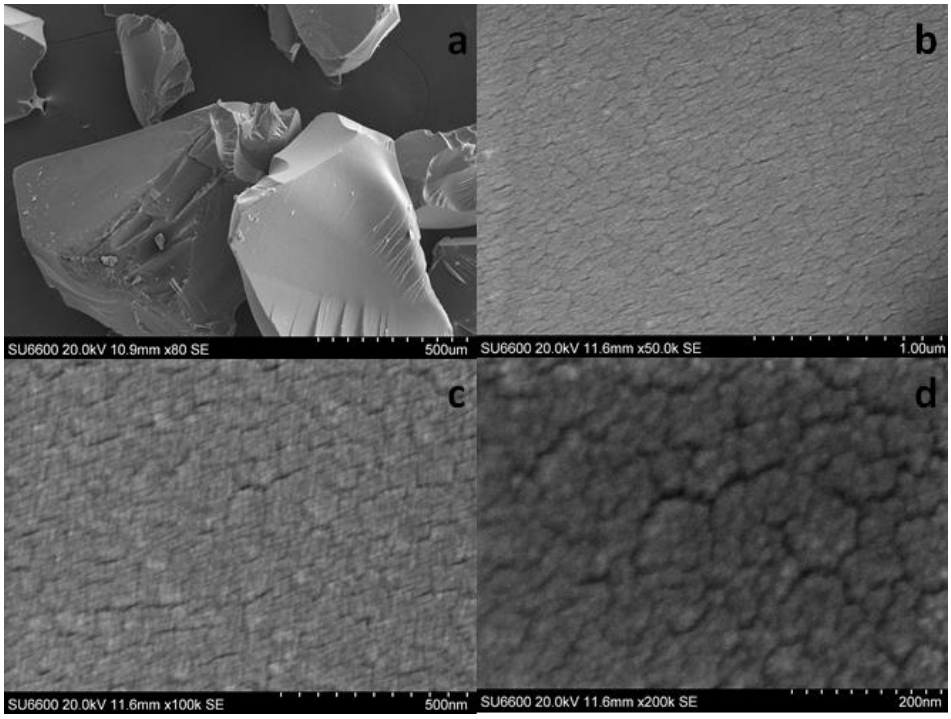

Figure 109: SEM images of MRF0_50_0.75 at a) 80 SE, b) 50.0K SE, c) 100.0K SE and d)200.0K SE.

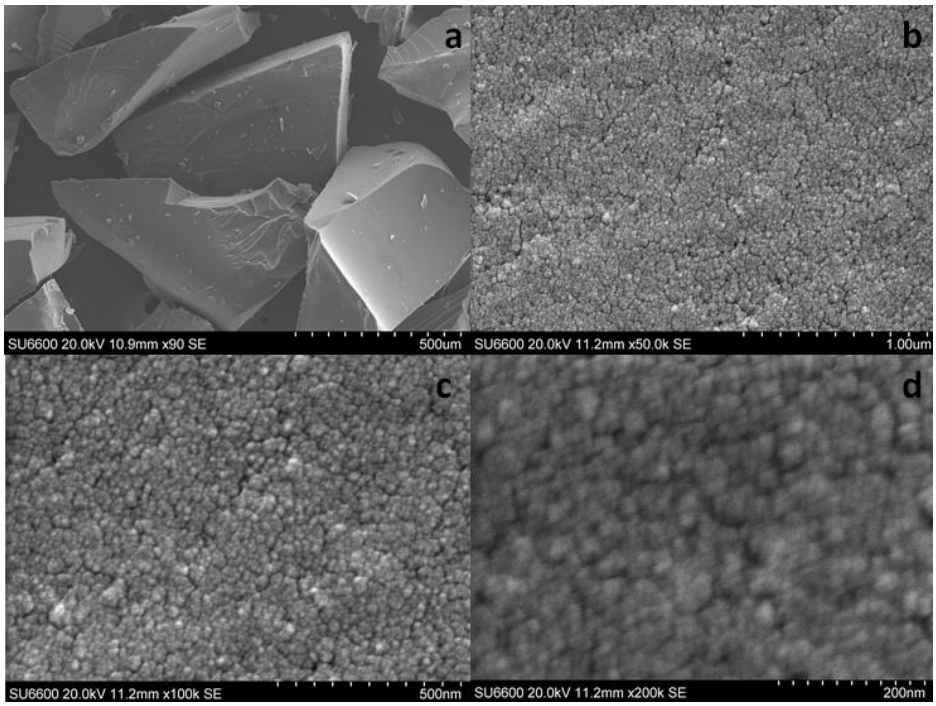

Figure 110: SEM images of MRF10_50_0.75 at a) 90 SE, b) 50.0K SE, c) 100.0K SE and d)200.0K SE.

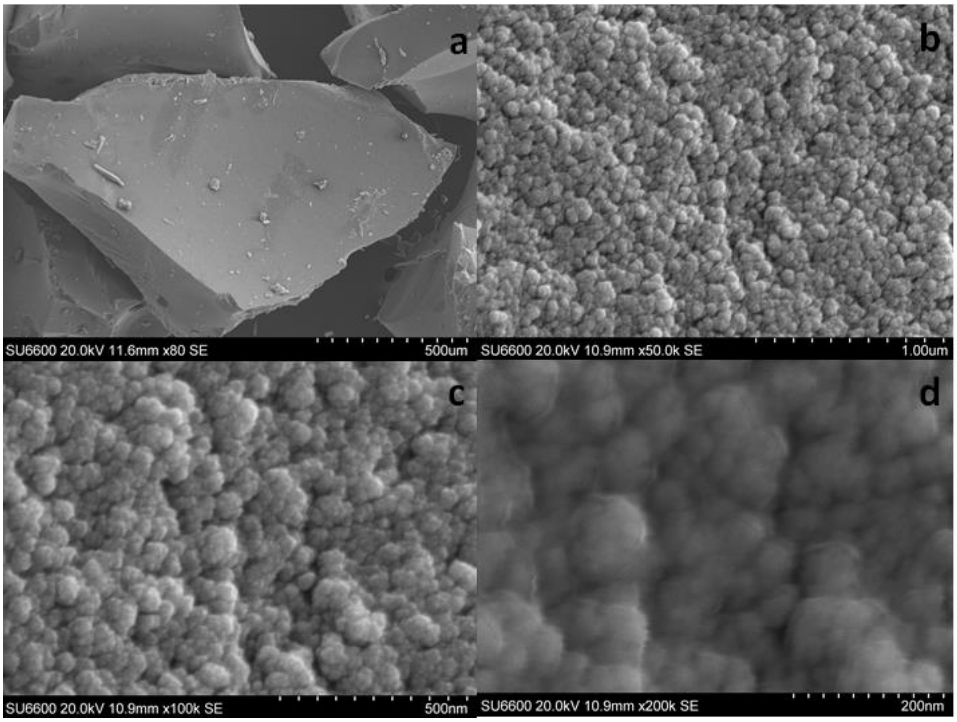

Figure 111: SEM images of MRF20_50_0.75 at a) 80 SE, b) 50.0K SE, c) 100.0K SE and d)200.0K SE.

R/C=50 and R/F0.5

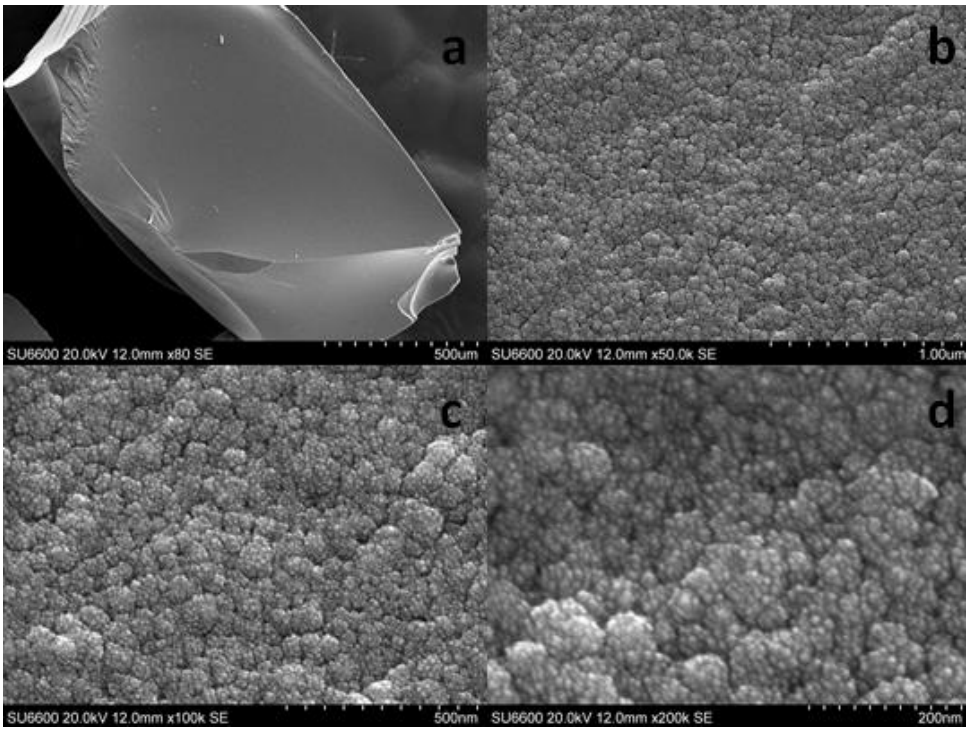

Figure 112: SEM images of MRF0_50_0.5 at a) 80 SE, b) 50.0K SE, c) 100.0K SE and d)200.0K SE.

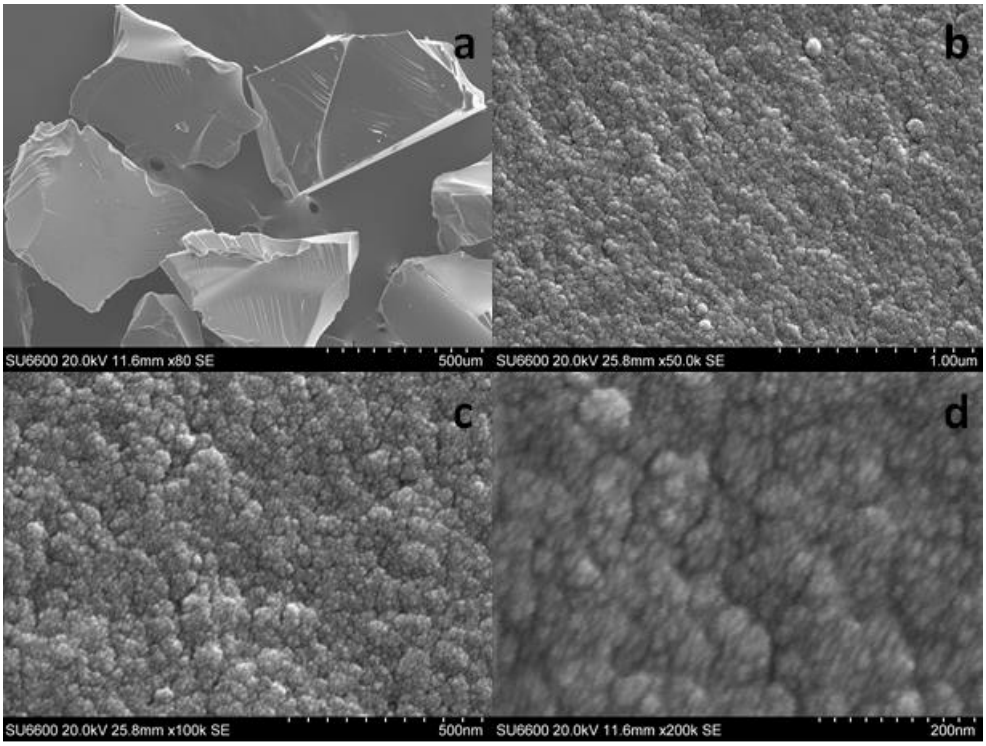

Figure 113: **SEM images of MRF1_50_0.5 at a) 80 SE, b) 50.0K SE, c) 100.0K SE and d)200.0K SE.**

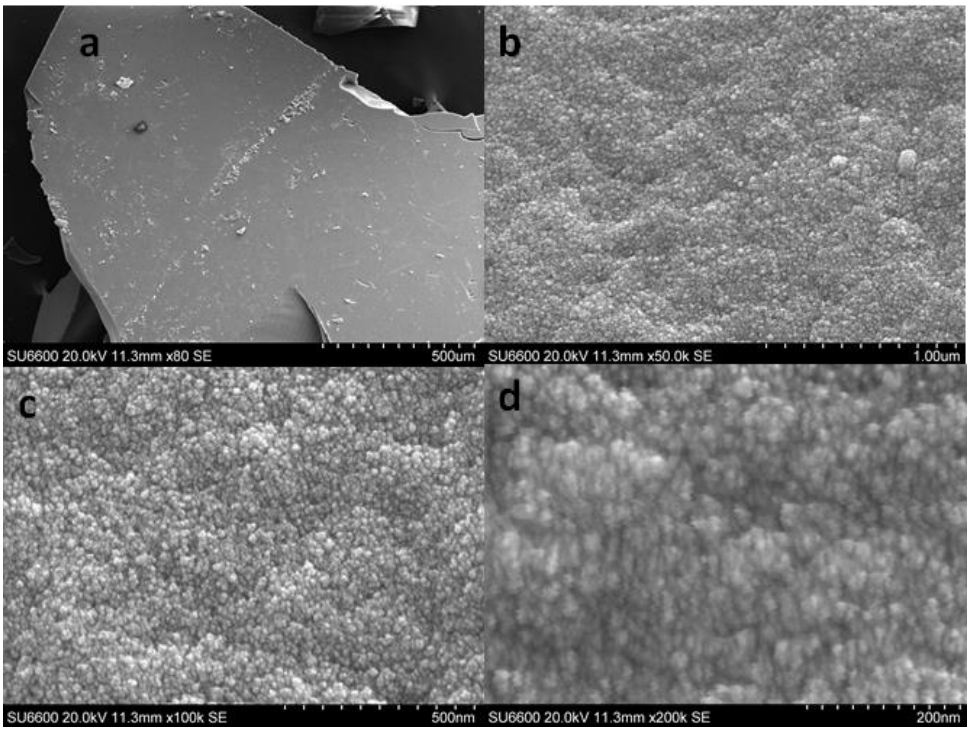

Figure 114: **SEM images of MRF10_50_0.5 at a) 80 SE, b) 50.0K SE, c) 100.0K SE and d)200.0K SE.**

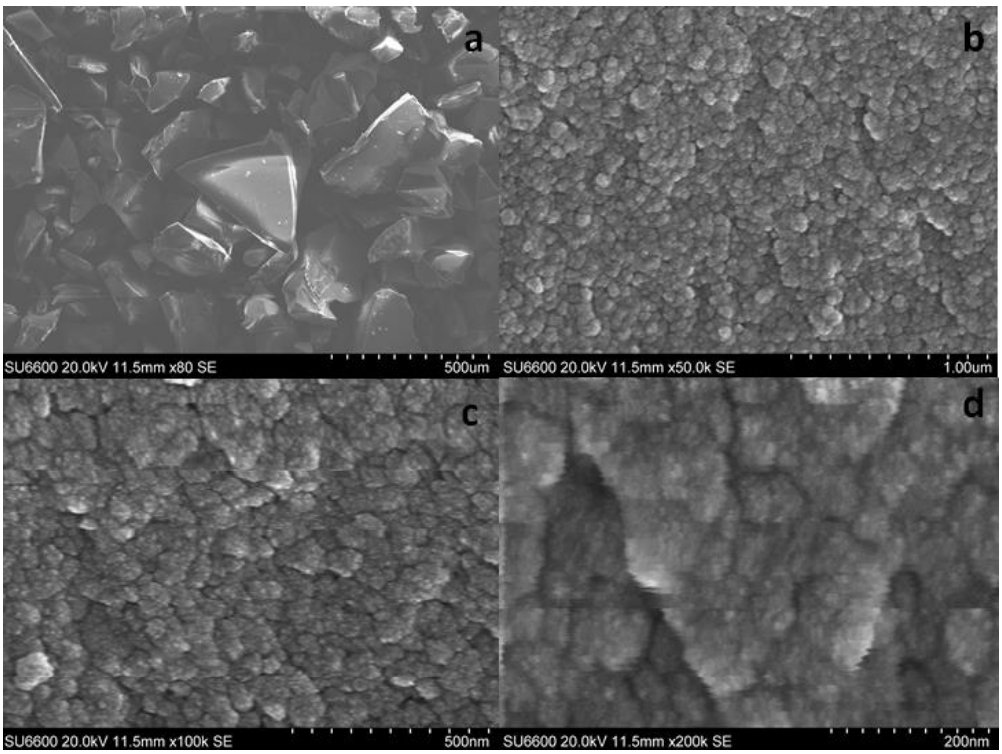

Figure 115: SEM images of MRF20_50_0.5 at a) 80 SE, b) 50.0K SE, c) 100.0K SE and d)200.0K SE.

Appendix F Catalyst Group II for RF Xerogels

F1 Comparison of $BaCO_3$ and $Ba(OH)_2$

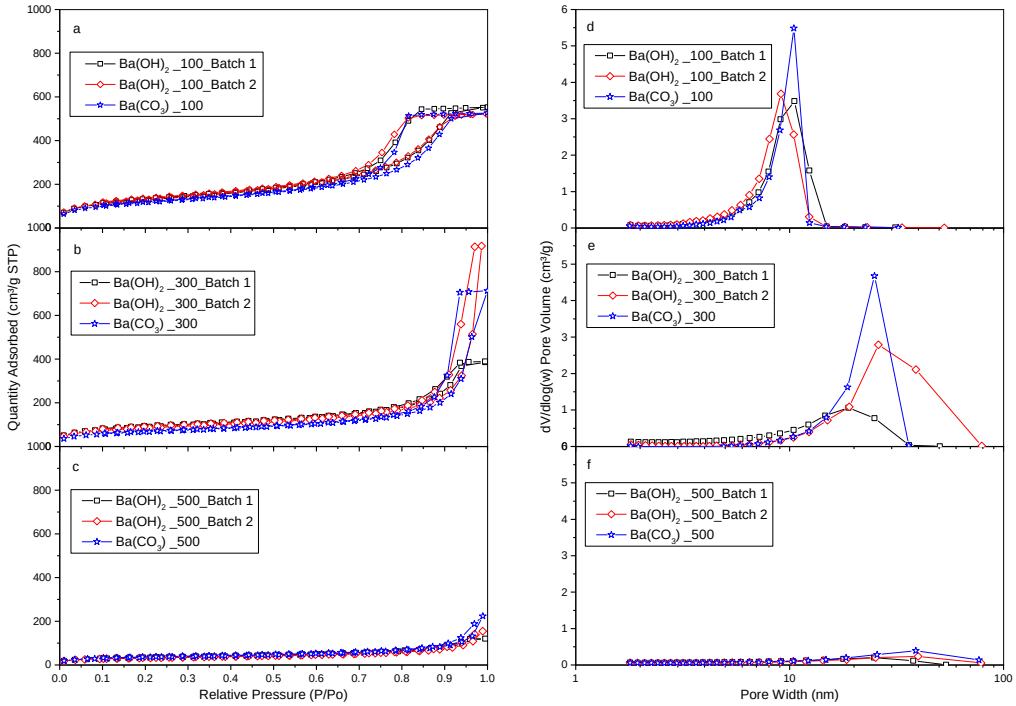

Figure 116: **(a) N_2 adsorption isotherms and (d) pore size distributions for RF xerogels synthesised in this study using $Ba(OH)_2$ and $BaCO_3$ as a catalyst and an R/C of 100; (b) N_2 adsorption isotherms and (e) pore size distributions for RF xerogels synthesised in this study using $Ba(OH)_2$ and $BaCO_3$ as a catalyst and an R/C of 300; (c) N_2 adsorption isotherms and (f) pore size distributions for RF xerogels synthesised in this study using $Ba(OH)_2$ and $BaCO_3$ as a catalyst and an R/C of 500.**

F2 Comparison of $CaCO_3$ and $Ca(OH)_2$

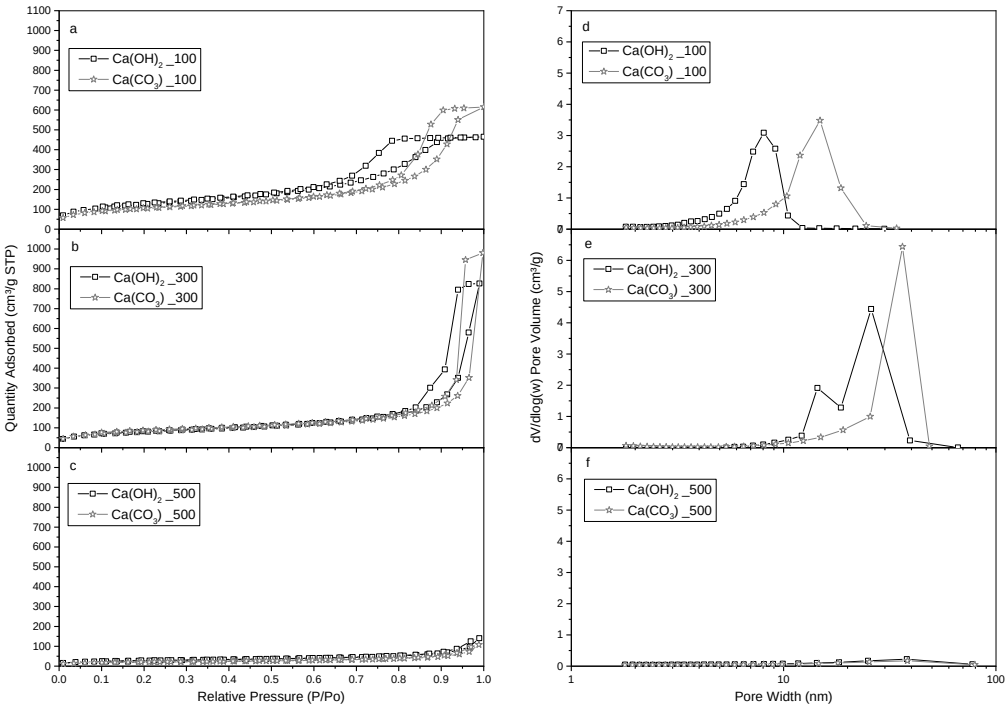

Figure 117: (a) N_2 adsorption isotherms and (d) pore size distributions for RF xerogels synthesised in this study using $Ca(OH)_2$ and $CaCO_3$ as a catalyst and an R/C of 100; (b) N_2 adsorption isotherms and (e) pore size distributions for RF xerogels synthesised in this study using $Ca(OH)_2$ and $CaCO_3$ as a catalyst and an R/C of 300; (c) N_2 adsorption isotherms and (f) pore size distributions for RF xerogels synthesised in this study using $Ca(OH)_2$ and $CaCO_3$ as a catalyst and an R/C of 500.

F3 Comparison $MgCO_3$ and $Mg(OH)_2$

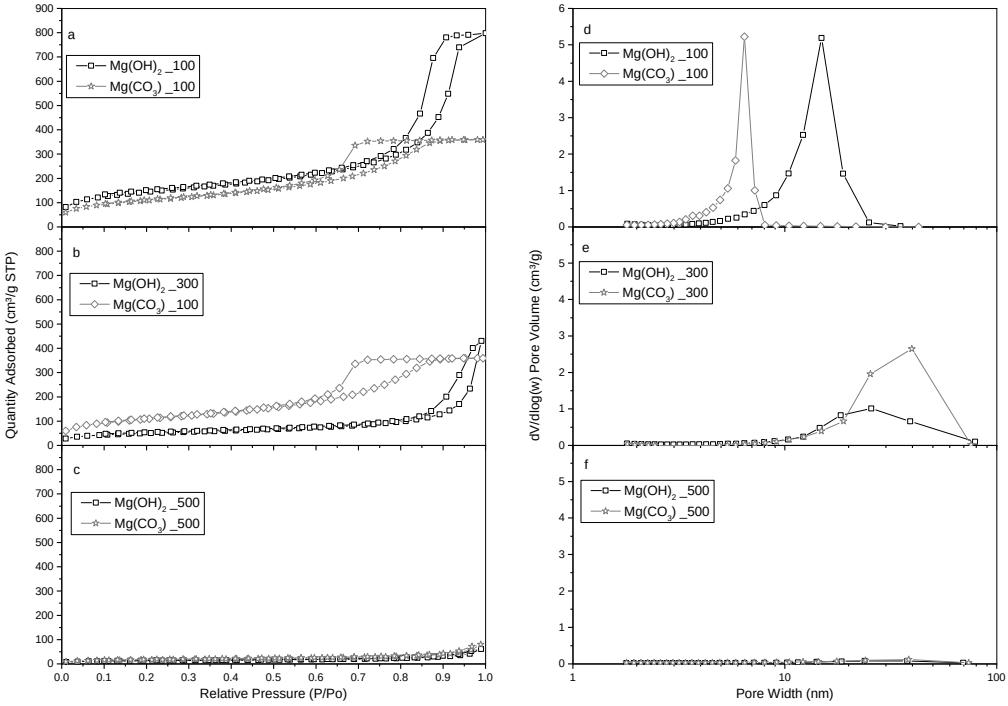

Figure 118: (a) N_2 adsorption isotherms and (d) pore size distributions for RF xerogels synthesised in this study using $Mg(OH)_2$ and $MgCO_3$ as a catalyst and an R/C of 100; (b) N_2 adsorption isotherms and (e) pore size distributions for RF xerogels synthesised in this study using $Mg(OH)_2$ and $MgCO_3$ as a catalyst and an R/C of 300; (c) N_2 adsorption isotherms and (f) pore size distributions for RF xerogels synthesised in this study using $Mg(OH)_2$ and $MgCO_3$ as a catalyst and an R/C of 500.

F4 Comparison $SrCO_3$ and $Sr(OH)_2$

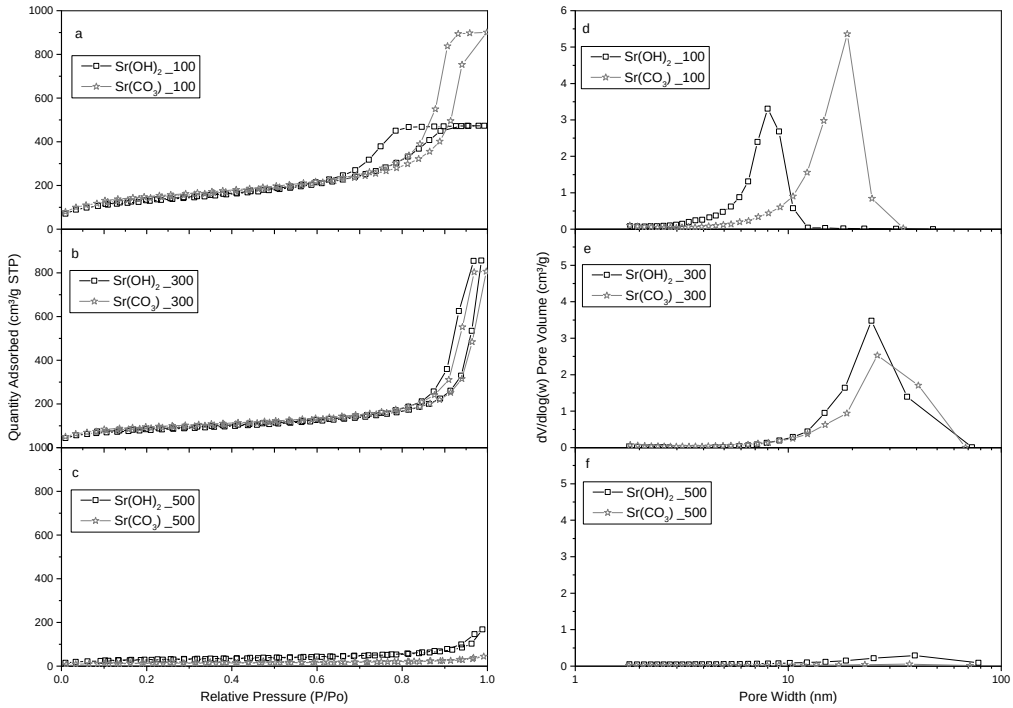

Figure 119: (a) N_2 adsorption isotherms and (d) pore size distributions for RF xerogels synthesised in this study using $Sr(OH)_2$ and $SrCO_3$ as a catalyst and an R/C of 100; (b) N_2 adsorption isotherms and (e) pore size distributions for RF xerogels synthesised in this study using $Sr(OH)_2$ and $SrCO_3$ as a catalyst and an R/C of 300; (c) N_2 adsorption isotherms and (f) pore size distributions for RF xerogels synthesised in this study using $Sr(OH)_2$ and $SrCO_3$ as a catalyst and an R/C of 500.

F5 Comparison Carbonates Group II

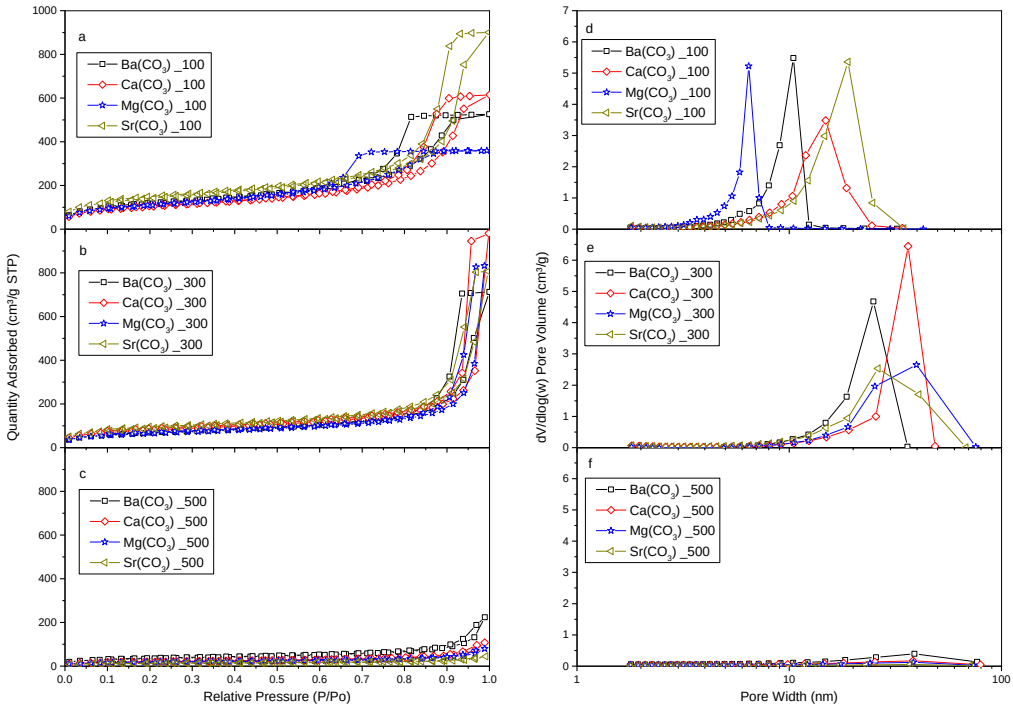

Figure 120: **(a) N_2 adsorption isotherms and (d) pore size distributions for RF xerogels synthesised in this study using $BaCO_3$, $CaCO_3$, $MgCO_3$ and $SrCO_3$ as a catalyst and an R/C of 100; (b) N_2 adsorption isotherms and (e) pore size distributions for RF xerogels synthesised in this study using $BaCO_3$, $CaCO_3$, $MgCO_3$ and $SrCO_3$ as a catalyst and an R/C of 300; (c) N_2 adsorption isotherms and (f) pore size distributions for RF xerogels synthesised in this study using $BaCO_3$, $CaCO_3$, $MgCO_3$ and $SrCO_3$ as a catalyst and an R/C of 500.**

F6 Comparison Hydroxides group II

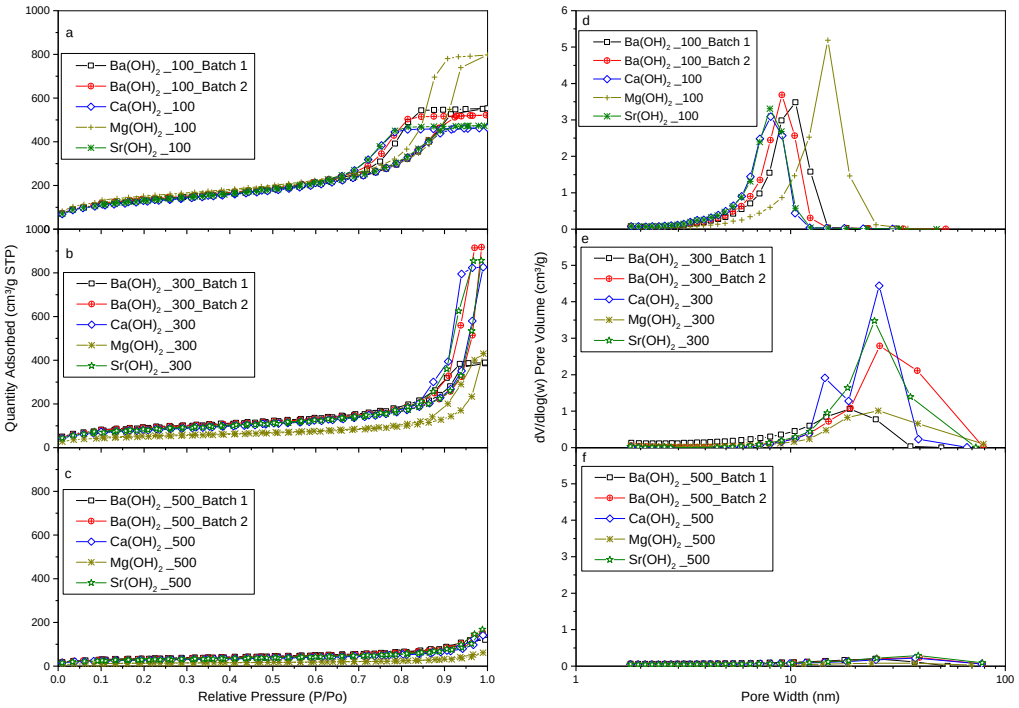

Figure 121: **(a) N_2 adsorption isotherms and (d) pore size distributions for RF xerogels synthesised in this study using $Ba(OH)_2$, $Ca(OH)_2$, $Mg(OH)_2$ and $Sr(OH)_2$ as a catalyst and an R/C of 100; (b) N_2 adsorption isotherms and (e) pore size distributions for RF xerogels synthesised in this study using $Ba(OH)_2$, $Ca(OH)_2$, $Mg(OH)_2$ and $Sr(OH)_2$ as a catalyst and an R/C of 300; (c) N_2 adsorption isotherms and (f) pore size distributions for RF xerogels synthesised in this study using $Ba(OH)_2$, $Ca(OH)_2$, $Mg(OH)_2$ and $Sr(OH)_2$ as a catalyst and an R/C of 500.**

Appendix G Ammeline-N_2 and CO_2 Adsorption

G1 N_2 Adsorption – BET

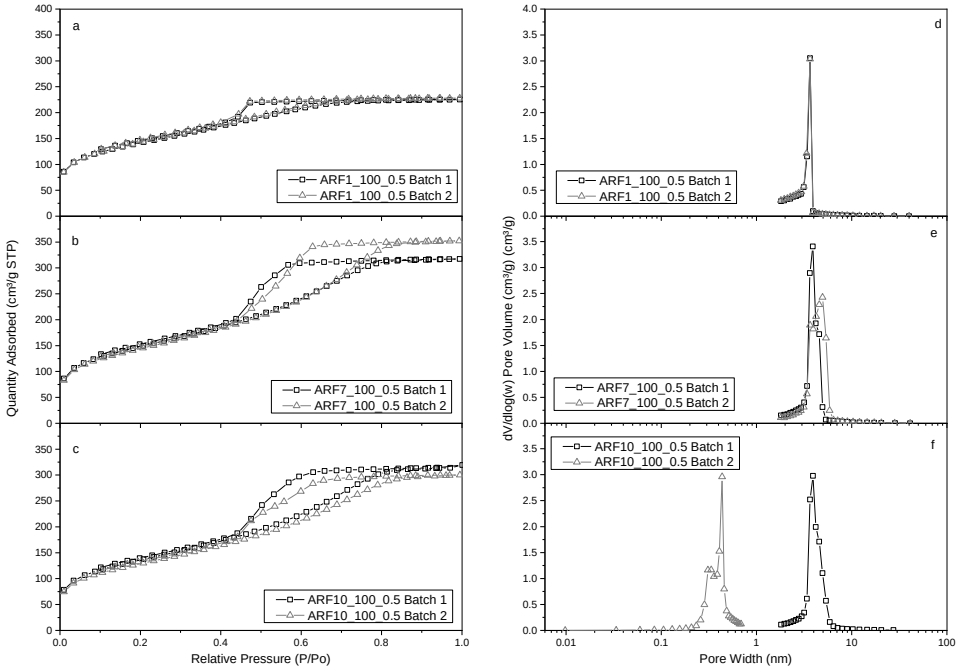

Figure 122: (a) N_2 adsorption isotherms and (d) pore size distributions for ARF1_100_0.5 xerogels synthesised using Na_2CO_3 as catalyst; (b) N_2 adsorption isotherms and (e) pore size distributions for ARF7_100_0.5 xerogels synthesised using Na_2CO_3 as catalyst; (c) N_2 adsorption isotherms and (f) pore size distributions for ARF10_100_0.5 xerogels synthesised using Na_2CO_3 as catalyst.

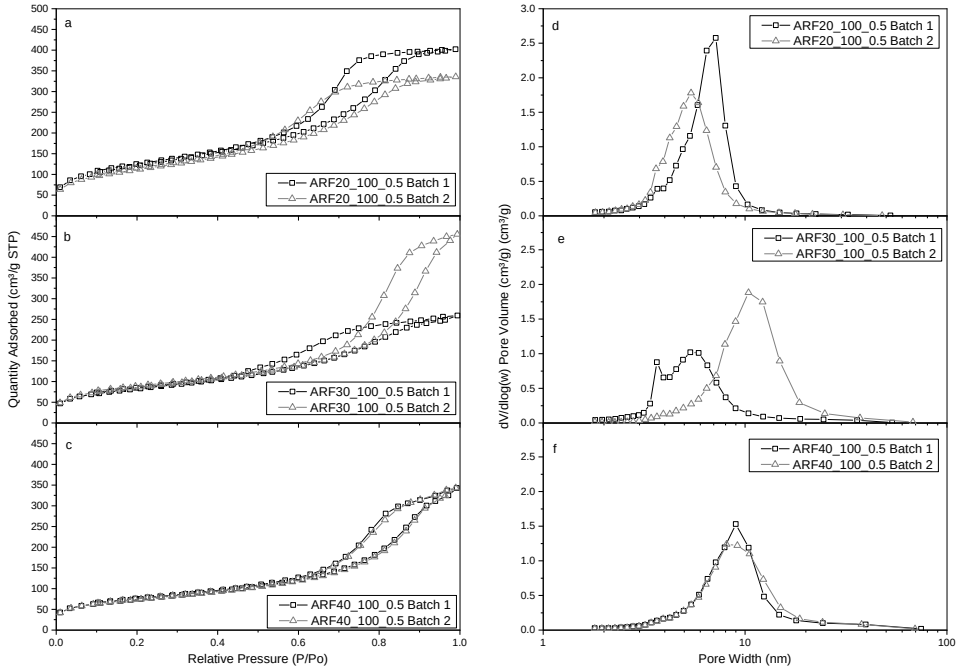

Figure 123: (a) N_2 adsorption isotherms and (d) pore size distributions for ARF20_100_0.5 xerogels synthesised using Na_2CO_3 as catalyst; (b) N_2 adsorption isotherms and (e) pore size distributions for ARF30_100_0.5 xerogels synthesised using Na_2CO_3 as catalyst; (c) N_2 adsorption isotherms and (f) pore size distributions for ARF40_100_0.5 xerogels synthesised using Na_2CO_3 as catalyst.

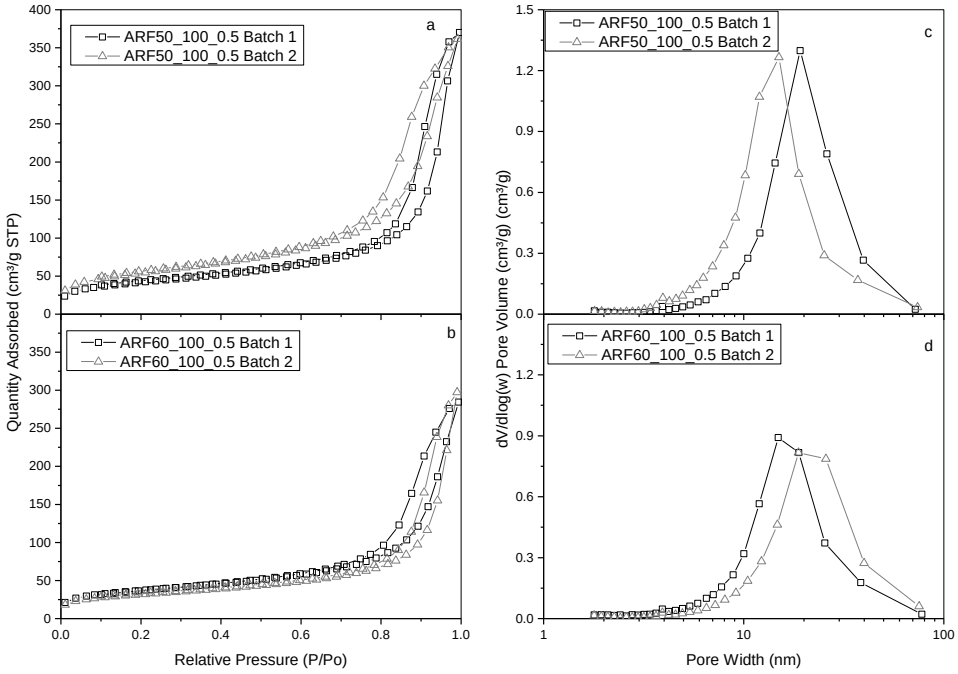

Figure 124: (a) N_2 adsorption isotherms and (c) pore size distributions for ARF50_100_0.5 xerogels synthesised using Na_2CO_3 as catalyst; (b) N_2 adsorption isotherms and (d) pore size distributions for ARF60_100_0.5 xerogels synthesised using Na_2CO_3 as catalyst.

G2 CO_2 Adsorption – IGA

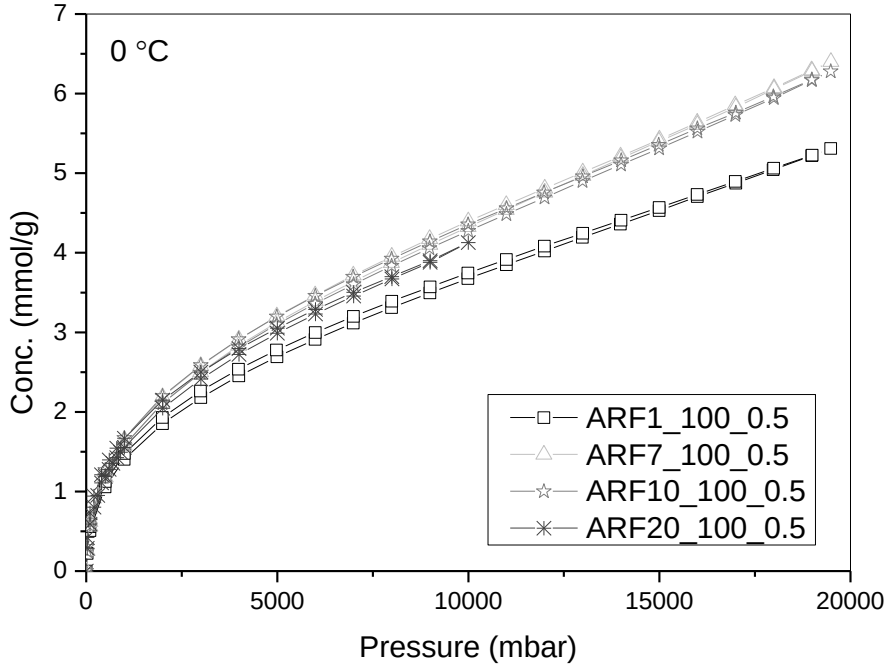

Figure 125: CO_2 adsorption isotherm of ARF1_100_0.5, ARF7_100_0.5, ARF10_100_0.5 and ARF20_100_0.5 at 0 °C.

Appendix H Parametric Study on MRF Xerogels

As a continuation of the parametric study shown in Chapter 6, more MRF xerogels were synthesised within the values of interest for R/C and [M]. The best performance of MRF xerogel was observed for the ranges of R/C of 50 to 200, [M] of 0 to 20 and R/F of 0.25 and 0.5.

Table 124: MRF synthesis variables studied in this work, R/C ratio, R/F ratio and [M], and levels selected for each[2].

R/F	0.25	0.5				
R/C	50	75	100	150	200	
[M]	0	1	5	10	15	20

H1 N_2 Adsorption

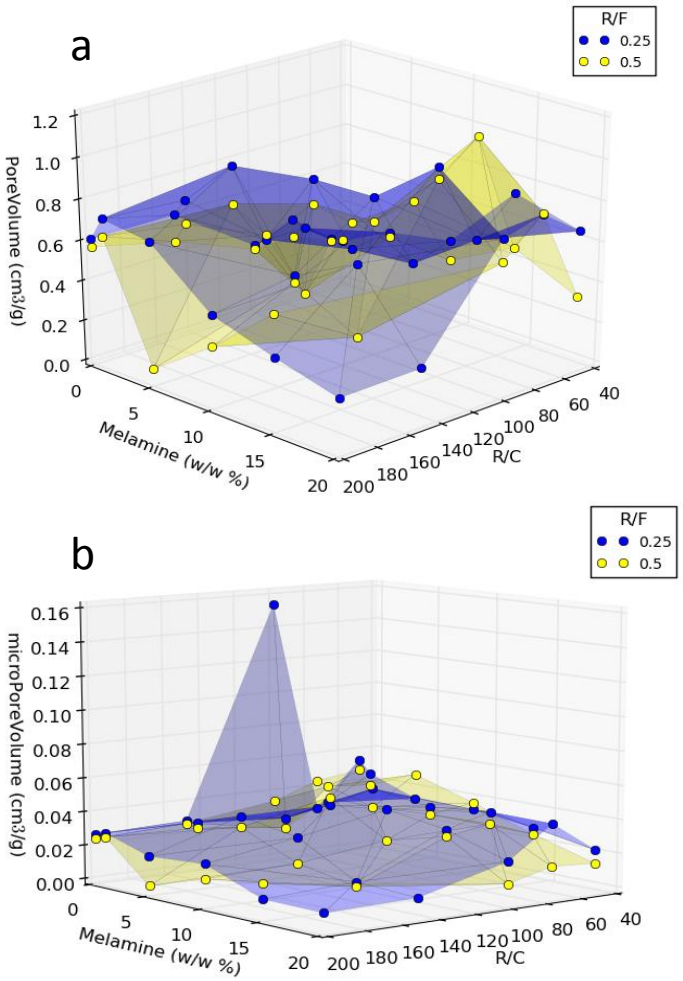

Figure 126: (a) Pore volume and (b) micropore volume for MRF xerogels of variable R/C (50, 75, 100, 150 and 200), R/F (0.25 and 0.5) and [M] (0, 1, 5, 10, 15 and 20).

[2] MRF Samples of R/C 75 and 150 and MRF xerogels containing [M] of 5 and 15 for the ratios of R/C 50, 100 and 200 (a total of 40 xerogels) were synthesised and tested for N_2 adsorption by Caio Ledingham during his MSc final project.

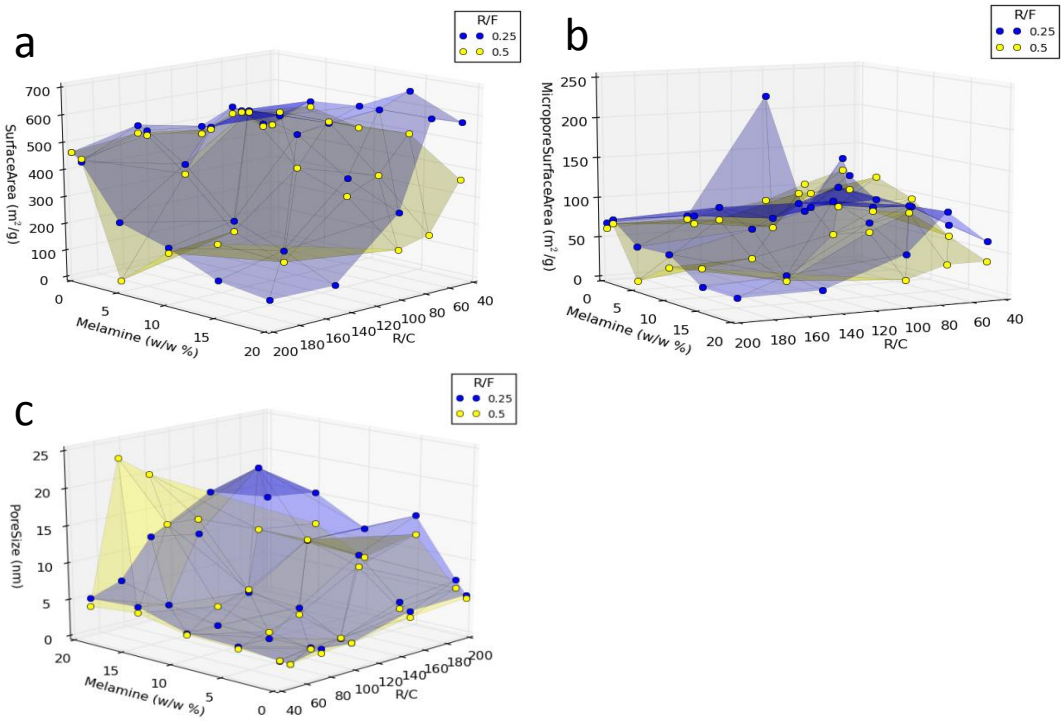

Figure 127: (a) Surface area, (b) micropore surface area and (c) pore size distribution for MRF xerogels of variable R/C (50, 75, 100, 150 and 200), R/F (0.25 and 0.5) and [M] (0, 1, 5, 10, 15 and 20).

H2 CO_2 Adsorption – IGA

Three xerogel were selected from the 60 MRF xerogel samples analysed in this study. These samples were chosen based on their micropore volume aiming for a value of ~0.03 cm^3/g, so results would be comparable to those shown in Figure 74.

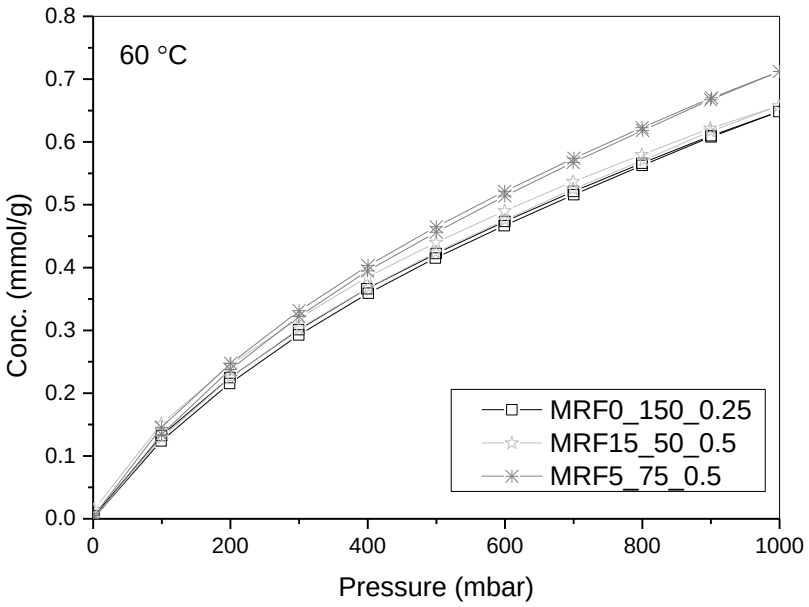

Figure 128: CO_2 adsorption isotherm of MRF0_150_0.25, MRF15_50_0.5 and MRF5_75_0.5 at 60 °C. Micropore volumes were 0.028, 0.026 and 0.033 cm^3/g, respectively.

Appendix I RF Xerogel Doped with Melamine, Ammeline and Cyanuric Acid

A series of xerogel produced both with ammeline (ARF) or cyanuric acid (CRF), as additives, was produced to be compared to the MRF xerogels.

Table 125: MRF synthesis variables studied in this work, R/C ratio, R/F ratio and [Additive] (melamine, ammeline or cyanuric acid), and levels selected for each[3].

R/F	0.25	0.5				
R/C	50	200				
[Additive]	0	1	5	10	15	20

The materials produced were tested for N2 adsorption, obtaining the following results:

I1 Melamine

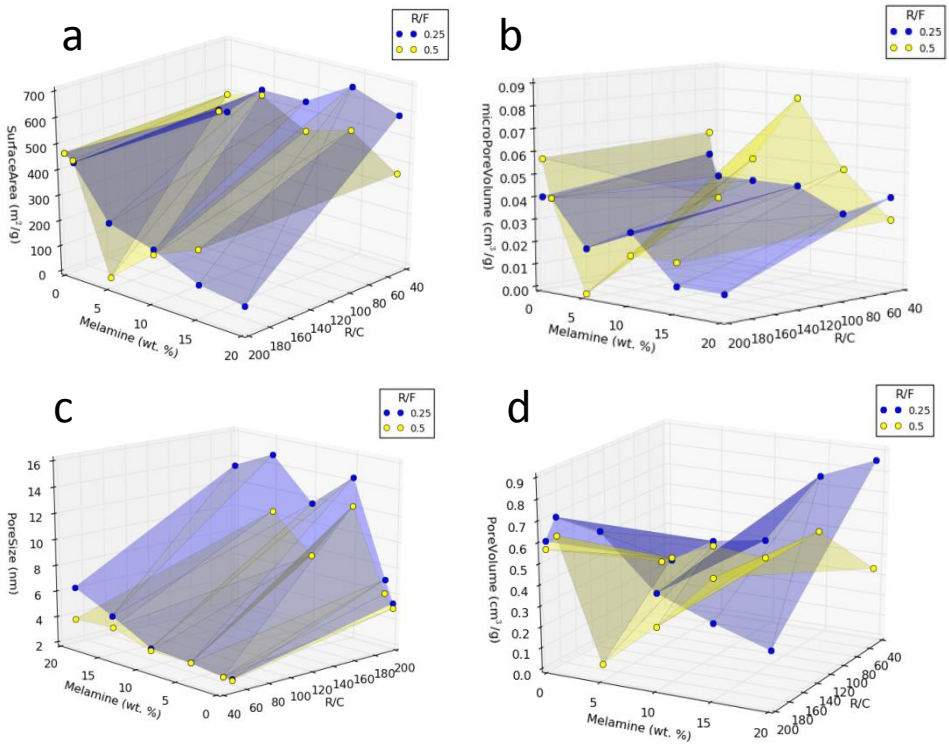

Figure 129: (a) Surface area, (b) micropore volume, (c) pore size and (d) total pore volume for MRF xerogels of variable R/C (50 and 200), R/F (0.25 and 0.5) and [M] (0, 1, 5, 10, 15 and 20).

[3]MRF, ARF and CRF Samples (a total of 71 xerogels) were synthesised and tested for N_2 adsorption by Abdelkarim Altoumi during his MSc final project.

I2 Ammeline

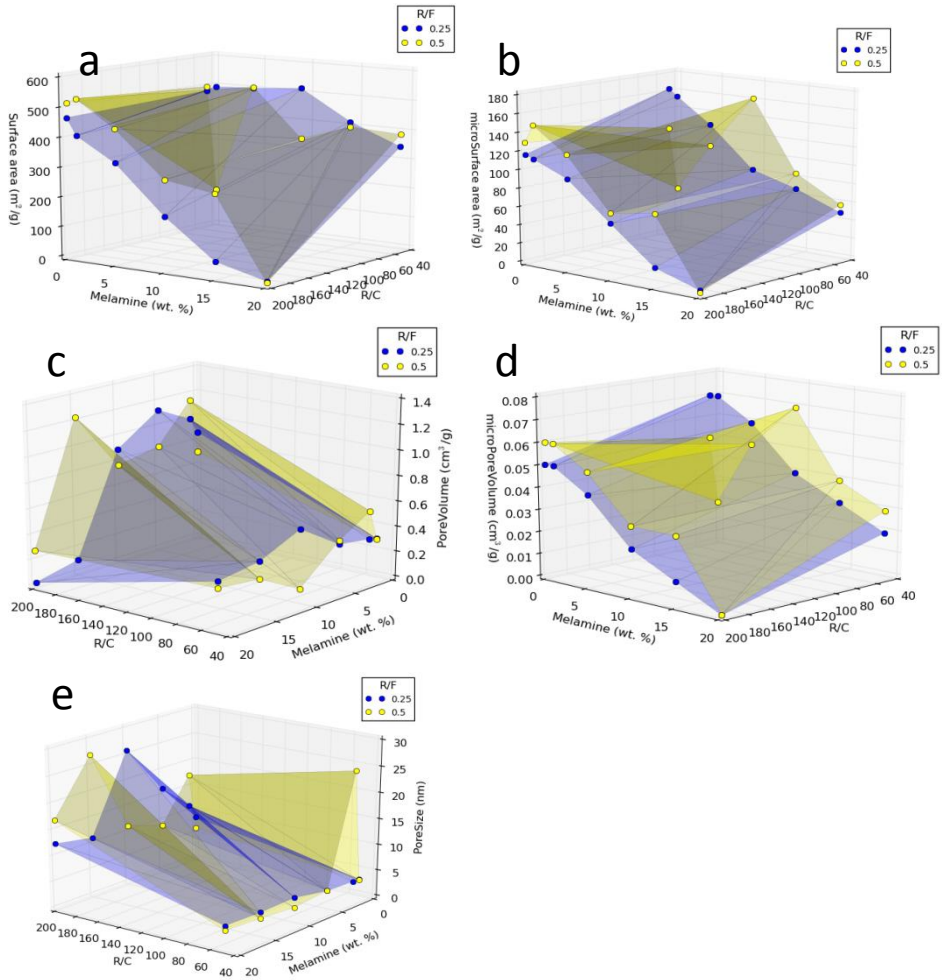

Figure 130: **(a) Surface area, (b) micropore surface area, (c) total pore volume, (d) micropore volume and (e) pore size for ARF xerogels of variable R/C (50 and 200), R/F (0.25 and 0.5) and [M] (0, 1, 5, 10, 15 and 20).**

I3 Cyanuric Acid

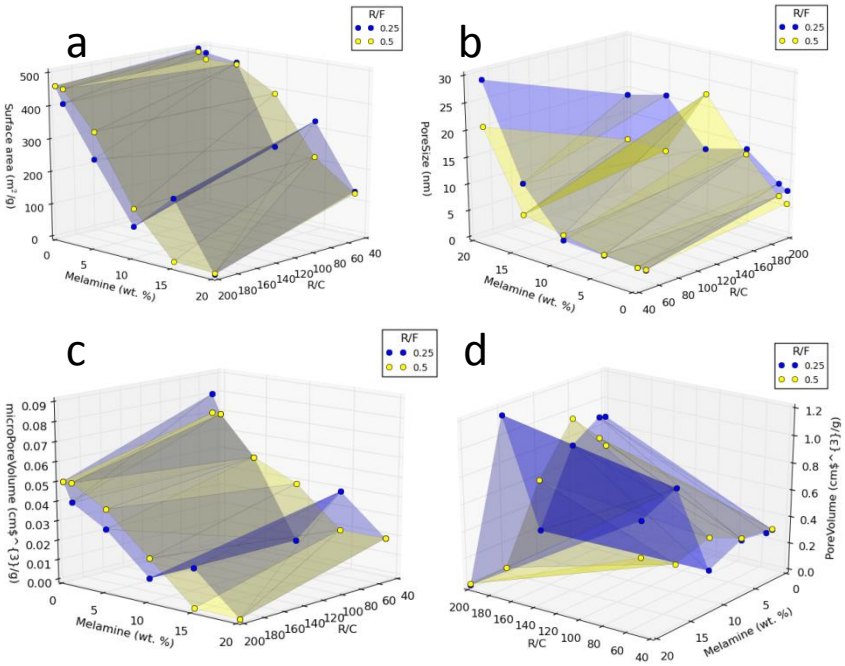

Figure 131: **(a) Surface area, (b) pore size, (c) micropore volume and (d) total pore volume for CRF xerogels of variable R/C (50 and 200), R/F (0.25 and 0.5) and [M] (0, 1, 5, 10, 15 and 20).**

I4 CO_2 Adsorption

Representatives material produced with the different additives were chosen to be compared. These samples were chosen based on their micropore volume aiming for a value of ~0.03 cm^3/g, so results would be comparable to those shown in Figure 74.

Table 126: **MRF, ARF and CRF xerogel samples selected for CO_2 adsorption based on micropore volume.**

Sample	BET total surface area (m^2/g)	External surface area (m^2/g)	Micro surface area (m^2/g)	Pore Volume (cm^3/g)	Micropore Volume (cm^3/g)	Pore Size (nm)
MRF0_100_0.5	445.8	369.2	73.6	0.308	0.031	3
MRF10_200_0.25	193.6	143.8	61.4	0.441	0.027	12
ARF10-200-0.5	295	227	68	0.76	0.03	11
ARF10_200_0.25	174	117	57	0.89	0.02	26
CRF15_50_0.25	332	250	82	0.91	0.04	12

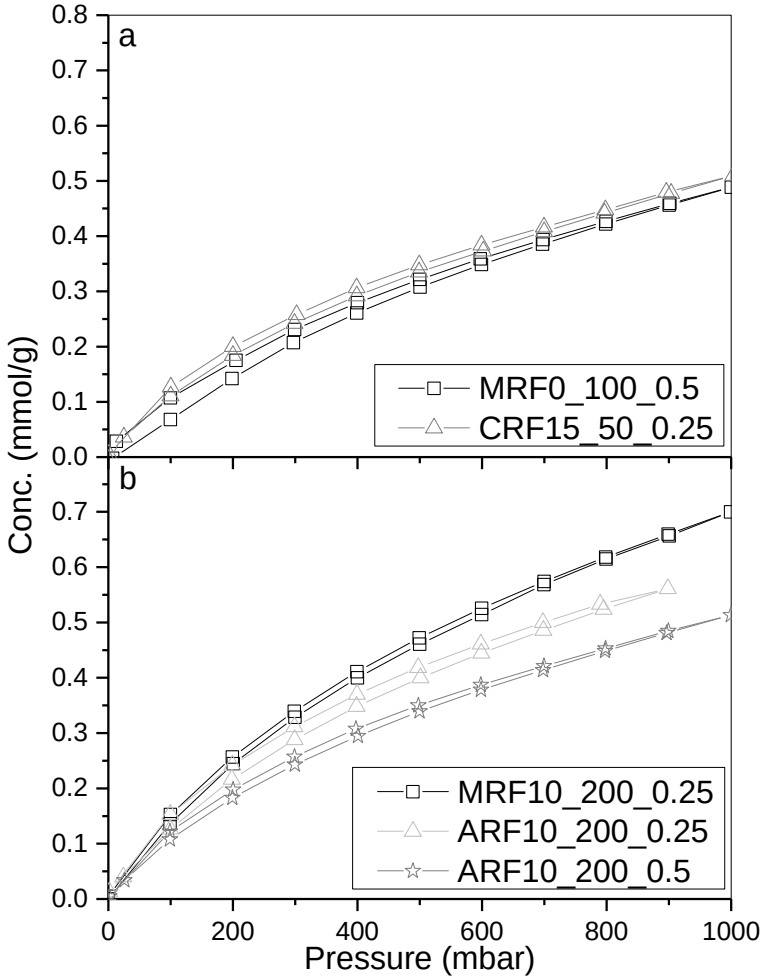

Figure 132: CO2 adsorption at 60 °C for (a) MRF0_100_0.5 and CRF15_50_0.25; and (b) MRF10_200_0.25, ARF10_200_0.25 and ARF10_200_0.5.

Appendix J Raman Analysis

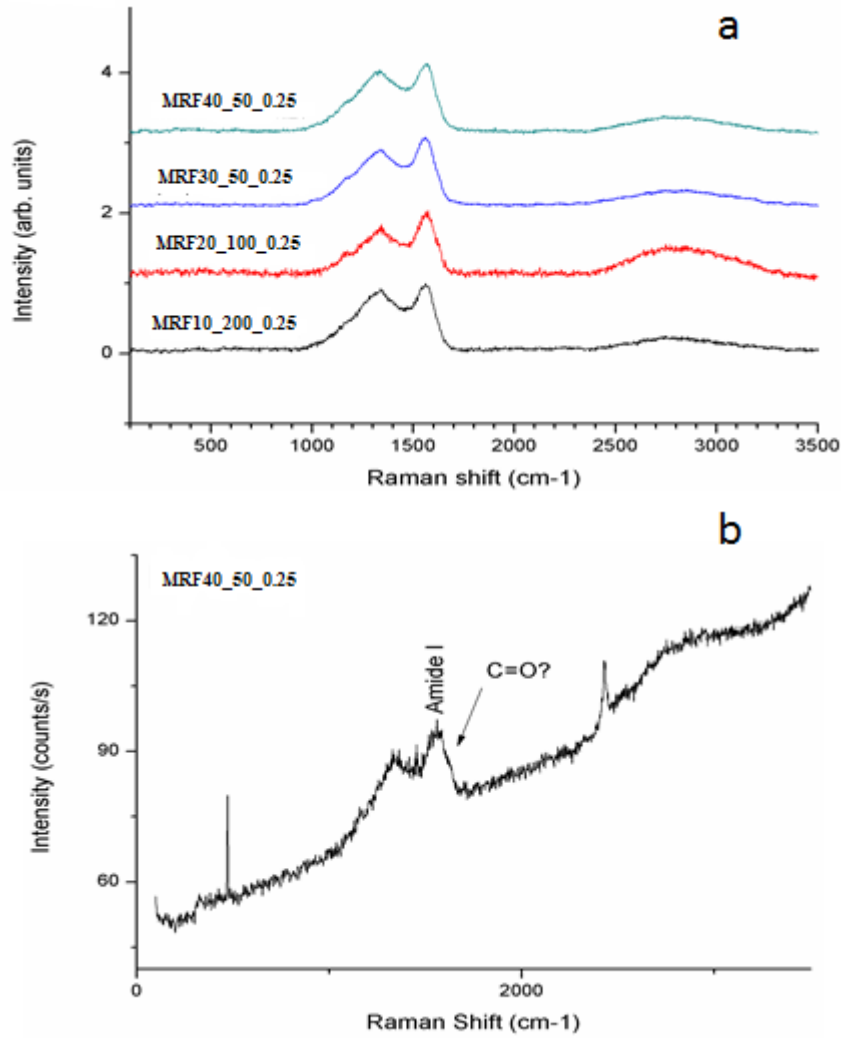

Figure 133: Raman spectroscopy of MRF xerogels, (a) MRF10_200_0.25, MRF20_100_0.25, MRF30_50_0.25 and MRF40_50_0.25 and (b) MRF40_50_0.25[4].

[4] Raman spectroscopy analysis tests were carried out by Dr Billy Murdoch of NEXUS Team in the Stephenson Building of Newcastle University.

Appendix K Summary of Gels Compositions and Gelation Success

Table 127: Summary of gels composition and gelation state for R/C 50 and 100.

R/C	R/F	[M] wt%	Gelation	R/C	R/F	[M] wt%	Gelation
50	1	100	Failed	100	1	100	Failed
50	0,25	0	geled	100	0,25	0	geled
50	0,25	1	geled	100	0,25	1	geled
50	0,25	10	geled	100	0,25	10	geled
50	0,25	20	geled	100	0,25	20	geled
50	0,25	30	geled	100	0,25	30	geled
50	0,25	40	geled	100	0,25	40	geled
50	0,5	0	geled	100	0,5	0	geled
50	0,5	1	geled	100	0,5	1	geled
50	0,5	10	geled	100	0,5	10	geled
50	0,5	20	geled	100	0,5	20	geled
50	0,5	30	geled	100	0,5	30	geled
50	0,5	40	geled	100	0,5	40	geled
50	0,75	0	geled	100	0,75	0	geled
50	0,75	1	geled	100	0,75	1	geled
50	0,75	10	geled	100	0,75	10	Failed
50	0,75	20	geled	100	0,75	20	Failed
50	0,75	30	geled	100	0,75	30	Failed
50	0,75	40	geled	100	0,75	40	Failed
50	1	0	Failed	100	1	0	geled
50	1	1	Failed	100	1	1	geled
50	1	10	Failed	100	1	10	Failed
50	1	20	Failed	100	1	20	Failed
50	1	30	Failed	100	1	30	Failed
50	1	40	Failed	100	1	40	Failed

Table 128: Summary of gels composition and gelation state for R/C 200 and 400.

R/C	R/F	[M] wt%	Gelation	R/C	R/F	[M] wt%	Gelation
200	1	100	Failed	400	1	100	Failed
200	0,25	0	geled	400	0,25	0	geled
200	0,25	1	geled	400	0,25	1	geled
200	0,25	10	geled	400	0,25	10	geled
200	0,25	20	geled	400	0,25	20	geled
200	0,25	30	geled	400	0,25	30	geled
200	0,25	40	geled	400	0,25	40	geled
200	0,5	0	geled	400	0,5	0	geled
200	0,5	1	geled	400	0,5	1	geled
200	0,5	10	geled	400	0,5	10	geled
200	0,5	20	geled	400	0,5	20	geled
200	0,5	30	Failed	400	0,5	30	Failed
200	0,5	40	Failed	400	0,5	40	Failed
200	0,75	0	geled	400	0,75	0	geled
200	0,75	1	geled	400	0,75	1	geled
200	0,75	10	Failed	400	0,75	10	Failed
200	0,75	20	Failed	400	0,75	20	Failed
200	0,75	30	Failed	400	0,75	30	Failed
200	0,75	40	Failed	400	0,75	40	Failed
200	1	0	geled	400	1	0	geled
200	1	1	geled	400	1	1	geled
200	1	10	Failed	400	1	10	Failed
200	1	20	Failed	400	1	20	Failed
200	1	30	Failed	400	1	30	Failed
200	1	40	Failed	400	1	40	Failed

Appendix L Publications

L1 Paper Submitted to Materials Today Chemistry Journal Under Revision.

Parametric study of factors affecting melamine-resorcinol-formaldehyde xerogels properties.

Ivan A. Principe and Ashleigh J. Fletcher

Department of Chemical and Process Engineering, University of Strathclyde, Glasgow G1 1XJ, UK.

Highlights

- Systematic study of three main synthesis variables: R/C, R/F and melamine content.
- Successful incorporation of nitrogen onto resorcinol-formaldehyde xerogels.
- Optimum R/F ratios determined as 0.25 and 0.5.
- Increasing R/C ratios, decreases surface area, pore volume and microporosity.
- Increasing melamine concentration has same effect as increasing R/C ratio.

Abstract

Resorcinol-Formaldehyde (RF) xerogels are organic materials have been widely studied due to their industrially relevant characteristics, such as high surface area, useful pore size and pore volume on which target species can be adsorbed; additionally, RF gels have significant potential to be tailored to specific applications, including catalysis, thermal insulation, filtration, energy storage, and gas treatment. Xerogel properties have been tailored, within this study, by altering the synthetics procedure with a focus on monomer concentrations and catalyst to monomer ratio, thereby incorporation nitrogen into the structure to additionally affect the chemical properties of the final gel. Melamine (M) is used in order to incorporate Nitrogen (N) into the gel structure; and partially replace the Resorcinol (R) typically used, resulting in a Melamine-Resorcinol-Formaldehyde (MRF) gel, the formation of which is often facilitated by a sodium carbonate catalyst (C). R/C and R/F molar ratios, and M concentration ([M]), were chosen for in-depth analysis as they have previously been shown to markedly influence sol-gel formation. The MRF gels produced were subsequently characterized to determine porous structure and chemical functionality. The results indicate that, texturally, increasing [M] produces a similar effect as increasing R/C values: increasing pore size, while decreasing surface area. Pore volume tends to increase when R/C or M increase individually but pore volume and surface area decrease drastically when both variables increase concurrently. Microporosity also tends to increase as R/C decreases, and as the concentration of M is decreased. The results obtained suggest new synthetic modification that may help tailor xerogel properties for specific applications.

Keywords

Catalyst; FTIR; surface area; pore volume; pore size; microporosity; mesoporosity; gelation.

1. Introduction

The design of materials for applications such as carbon capture, solid sorbents, catalyst supports, membranes and hydrogen storage require the control and capability of tuning the porous structure of such systems, including surface area, pore size and distribution, microporosity, and pore volume. Such materials may be formed from gels, including Resorcinol- Formaldehyde (RF) resins, which are a type of organic material that have attracted attention due to their potential application in many processes, such as, catalysis, thermal insulation, carbon capture, filtration, energy storage and as precursor of electrically conducting carbon materials.

RF gels, generally, exhibit a high pore volume, low density, large surface area and an amorphous structure. These parameters can be controlled and tailored as a function of the synthesis procedure [1], thereby making RF gels very attractive for a number of applications. Several factors, such as solvent, temperature, chemical reaction, time, catalyst (C), and agitation, influence sol-gel chemistry, however, base catalysed synthesis is most affected by the concentration of monomers and catalyst, and the initial pH of the sol, as described below.

Initial sol pH: It is generally understood that increasing pH increases surface area [2-5]. For higher values of pH, the formation of hydroxymethyl derivatives of resorcinol is favoured, producing highly branched clusters. This leads to more unstable structures, which produce a larger number of particles and smaller interconnections between them [6]. In contrast, when the pH is lower the effect is reversed. Thus, the formation of resorcinol anion is less favoured which, as a consequence, leads to fewer branched structures, therefore polymerization would take longer and the particles formed would be larger. Consequently, the nucleation regime controls the size of the pores and voids in between the particles of the polymer, thus controlling the mesoporosity of the gel; therefore, lower pH tends to produce larger pore sizes, while higher pH favours crosslinking of the gel, reducing the pore size [4].

Resorcinol–Formaldehyde (R/F) molar ratio: The stoichiometric ratio for R/F is typically set at 1:2. However, the relative quantities can be varied to affect the degree of crosslinking, hence, the density and structure of the final gel.

Resorcinol – Catalyst (R/C) molar ratio: The R/C ratio is one of the most important factors dominating gel physical properties. R/C ratio has a direct impact on density, surface area, and mechanical strength of R-F materials. In general, as R/C ratio decreases so too does pore diameter, while density is increased [7, 8]. Previous work indicate that using lower R/C values, i.e. higher catalyst content, results in gels with smaller particles (3 – 5 nm diameter)

and large neck size (fibrous appearance). On the other hand, higher R/C ratio (lower catalyst content) leads to larger particle sizes (11 – 14 nm) and a 'string of pearls' morphology [7, 9]. This structural difference is related to shrinkage of the gel during the drying stage. For instance, colloidal gels incur little shrinkage during supercritical drying, which affords them with lower surface areas and weaker structures than polymeric gels [6]. Low R/C values (high catalyst content) lead to the formation of small particles, creating microporosity, while high R/C values (low catalyst content) result in mesoporosity. The different shrinkage rates also impact the density of RF gels, for instance, at constant R/F ratio, decreasing R/C ratio increases the density [10]. Despite this, a comparison of gels with similar densities showed that polymeric gels (R/C = 50) were three times stiffer than colloidal material (R/C = 200), demonstrating the impact of neck particles on final mechanical properties [6]. During the polycondensation reaction between R and R, highly cross-linked particles are formed. The R/C ratio is the main parameter controlling the size of interconnected particles and, consequently, the final pore size [9]. Additionally, other authors have shown that R/C ratio is also the most influencing parameter controlling the surface area, pore volume and mechanical properties [1]. Mirzaeian et al. showed, that for the same RF gel system, increasing R/C ratio leads to an increase in the volume of N2 adsorbed [1]. Additionally, Yamamoto et al. showed that the pore size distribution increases with increasing R/C ratio for a constant ratio of R to water (W) [8].

Catalyst (C): The catalyst plays a key role in gel formation, altering gelation time and the physical characteristics of the gel. A comparison of group I catalysts showed that Li, Na, K have similar abilities to stabilize RF colloidal suspensions, by destabilizing the oligomers, thereby increasing their solubility and leading to small clusters [11]. By contrast, Cs is less able to stabilize colloidal suspensions, hence oligomers becomes less soluble, which leads to larger clusters [11]. This means that gels produced with Li, Na or K as catalyst could be applied to gas phase separations, while gels created using Cs as catalyst are better suited to aqueous phase processes.

Total solid content: Increasing solids content means less solvent in the mix, therefore, the density of the final RF gel is increased, as observed by Fairen-Jimenez et al. [12]. Increasing density leads to smaller pore sizes due to the increase in reactant quantity for a given volume [13], which also influences the pore size distribution where high solids content results in monodisperse pores, while low solid content exhibits a heterogeneous polydisperse porosity [9].

Melamine content (M): This parameter is less well studied, however, previous work shows that increasing M/R ratio decreases particle size significantly [14]. Given its basic character, increasing [M] should accelerate the polymerization reaction between R and F, thereby increasing crosslinking density and the molecular weight of polymers. However, the steric hindrance observed for larger chain structures increases their incompatibility with water, which, in turn, increases nucleation rates but decreases the time for cluster growth; overall, increasing [M] results in smaller microspheres.

RF gel formation has been well studied and can be summarized by the following steps [6, 9]:

1. Hydroxymethylated R is formed by reaction of R with F.

2. Formation of nanometer-sized clusters occurs by condensation of these hydroxymethyl groups; thus a gel is formed by crosslinking of clusters.

3. In any sol-gel process, the formation and growth of clusters is influenced by typical sol-gel parameters such as solution pH, temperature and monomer concentration.

Primary studies produced RF gel by polymerization of R and F, using sodium carbonate as catalyst (C) [2, 7, 15], while several other researchers studied the analogous production of aerogels from phenol (P) and F [16, 17] in PF gel synthesis. Methylene ether (-CH2OCH2-) or methylenes (-CH2-) are the two main typical groups bonding the aromatic moieties in the synthesis of phenolic resins. Similarly, for RF gels, the linkages of the different aromatic groups are facilitated by the presence of the aforementioned groups. The concentration of those groups depends on a number of parameters, such as pH, catalyst and monomer concentration. RF gels can be synthetized under either basic or acid conditions and R reacts with F, via a similar route as P does. However, the ability of R to crosslink, forming clusters, is higher than for P because R can bond up to three F groups; with these additions producing mainly ether bridges.

The RF reaction generally occurs in aqueous system at room temperature, the reaction of R and F is favoured, however, it is very slow. For this reason, a catalyst is typically added to accelerate the rate of reaction, where it is consumed and not recoverable after the reaction. For basic catalysis, sodium carbonate is most commonly used as C, which is representative of Group I species (Li, Na, K and Cs) [11]. For gels synthesised under basic conditions, gelation is slow and requires a high temperature. Instead, for gels created under acidic conditions, gelation occurs at room temperature and is faster, often only a few hours [18]. The catalyst used in acidic synthesis is usually acetic, perchloric or hydrochloric acid. Base-catalysed gelation was used exclusively throughout this study, for several reasons, including the fact that acid catalysed gel often exhibit reduced porosity (higher density), which is an important parameter in gas treatment [19]; also industrially, it is usual to avoid the use of acids to reduce risks, and associated costs. As mentioned above, in a basic environment, R is deprotonated to its anionic form and the increased electron density at the 4 or 6 position enhances attachment of a –CH2OH group, as shown in Scheme 1. The addition of one molecule of F results in hydroxymethylation, activating a second position to add another –CH2OH group, giving rise to the dihydroxymethyl (8). Subsequently, the basic catalyst allows formation of the o-quinone intermediate due to deprotonation of hydroxymethylated R to form a methylene bridge (-CH2-) with another R molecule, via condensation reaction, which results in crosslinking within the structure [20].

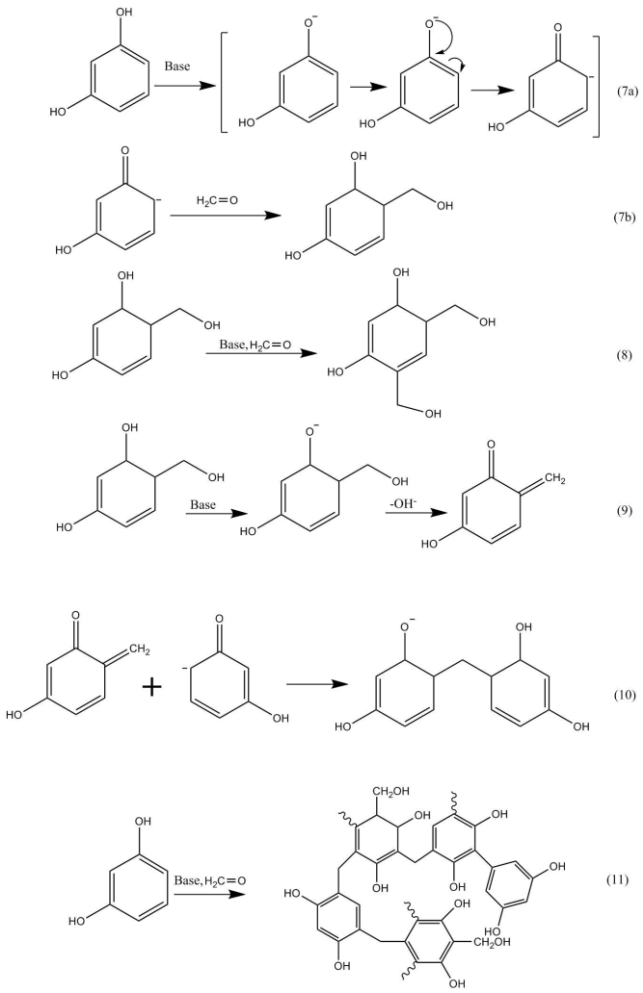

Scheme 1: Mechanism of the base-catalysed RF sol-gel synthesis, based on reaction mechanism of catalysed RF sol-gels [6].

M and F undergo a reaction similar to R and F, with the production of stable polymeric resins, which indeed have a very similar synthesis procedure and chemistry compared to phenolic resins [14].

The reaction of M and F produces six possible products, of which the most stable is the hexamethylolmelamine [21]. Hoodgind et al. stated that this compound can be produced in two ways, either by heating M with an excess of neutral F at 90 °C or by allowing M to react with F at room temperature for a prolonged period of time (15 to 18 h) [21]. The first of those options is similar to the conditions used in this research. MF gel production, and the properties of the resulting materials, is controlled by the same parameters as for RF gels, i.e. ratio of monomers, catalyst, time of reaction and temperature [21, 22]. The MF reaction can be divided into two stages: formation of methylolmelamines (Scheme 2) and condensation (Scheme 3). F in the solution reacts with dissolved M, but M has a low solubility at room temperature in water (0.5 g/100 mL at 298 K and 5 g/100 mL at 373 K); hence, the methylolmelamine formed as a result of that reaction is more soluble than M, so the solution rapidly changes from a suspension to a clear solution.

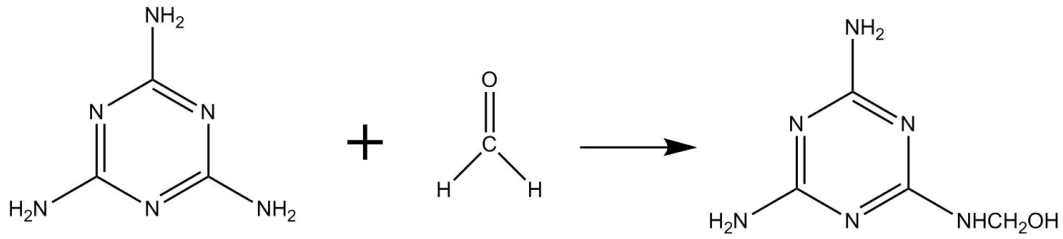

Scheme 2: Formation of methylolmelamines via reaction of melamine and formaldehyde.

Crosslinking of methylolmelamines cluster happens by two types of linkages: ether or methylene bridges [22], dependent on solution pH. At low pH (7 – 8) methylene bridges are favoured, while at pH ≥ 9 ether bridges are predominant [23], see Scheme 3.

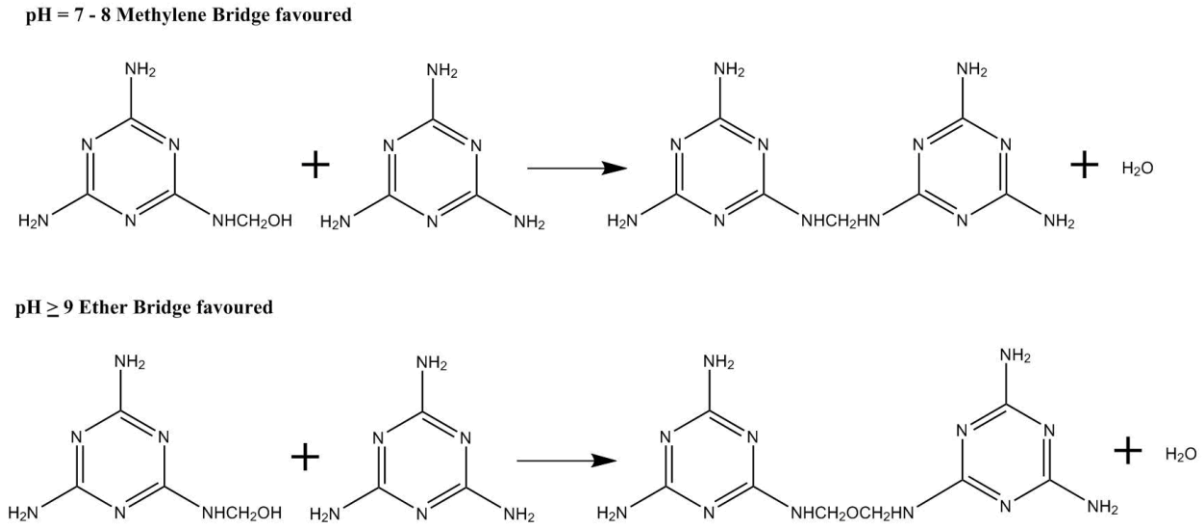

Scheme 3: Methylene and ether bridge formation depending on the solution pH during reactin of melamine and formaldehyde.

Zhou et al. showed that both systems described above, RF and MF, can produce large microspheres of polymer under hydrothermal conditions, even without catalyst [14], and condensation of MF into an RF system can produce a homogeneous MRF microsphere network. The crosslinking reaction between MF and RF microspheres would be facilitated by methylene and ether bridges of hydroxymethyl groups, forming small clusters, which in turn act as nucleation sites trapping inside sufficient unreacted particles to continue the reaction and consequently grow clusters. This process is comparable with the Stöber process, where nucleation is fast before clusters formation, without the need of new nucleation sites [24, 25].

2. Experimental

Materials and Synthesis. Resorcinol (ReagentPlus, 99%), aqueous formaldehyde solution (37 wt% F, stabilized with 10 – 15 % methanol, pH 2.8 – 4.0), sodium carbonate (anhydrous, ≥

99.5%), melamine (99%) and acetone (ACS reagent, ≥99.5%) were all purchased from Sigma-Aldrich.

Compositions of MRF solutions were calculated using the molar ratios of R/F and R/C, sodium carbonate was used as catalyst for all samples. Solution volume was fixed at 30 mL and total solid content (i.e. R, M, F and carbonate) was fixed at 20% w/v, which corresponds to a solid content of 6 g. The chosen parameters of study, R/C, R/F and [M], were varied as shown in Table 1.

Table 1:Melamine-Resorcinol-Formaldehyde synthesis variables studied in this work (Resorcinol/Catalyst ratio, Resorcinol/Formaldehyde ratio and melamine content) and levels selected for each.

R/C	50	100	200	400		
R/F	0	0.25	0.5	0.75	1.0	
[M]	0	1	10	20	30	40

For each chosen R/C, R/F and [M], the required M was weighed out and placed in a sealable 500 mL jar with 25 mL of deionized water, produced in house (Millipore Elix 5 system). The M solution was heated up to ≈323 K and stirred magnetically until completely dissolved. Then, the required R and carbonate were weighed out and added to the solution while it was continuously stirred, until completely dissolved. The required volume of F solution was added to the jar, together with the additional water make the volume up to 30 mL, the jar was sealed and stirred for 30 min. Once the stirring period was complete, the pH of the solution was recorded using a Hanna pH 20 meter, fitted with an H1-1110B pH electrode, before sealing the jar and placing it in a pre-heated oven at 358 ± 5 K, as used in previous works [15]. The solution was left to gel for 3 d. Upon gelation, water contained within the pores of the network was removed through solvent exchange. The cured gel and 90 mL of acetone were shaken for 3 d at room temperature. The wet gel, after solvent exchange, was placed in a vacuum oven at a temperature of 363 K in order to remove any remaining solvent from the gel pores.

Xerogel Characterization. A Micromeretics ASAP 2420 system was used to obtain surface area and porosity by nitrogen adsorption/desorption equilibrium measurements at 77 K, using ~0.5 g sample. The sample was first degassed, at 393 K for 120 min, before testing the nitrogen adsorption capacity. Surface areas were calculated by applying the Brunauer-Emmett-Teller (BET) theory [26] combined with Rouquerol correction for BET application to microporous materials [27]. Pore volume was calculated from the equilibrium measurement of nitrogen adsorbed at ~0.98 bar (i.e. the saturation vaporous pressure of N2 at 77K). The pore size distribution and average pore size were obtained by application of the Barret-Joyner-Halenda (BJH) method [28], while the t-plot method [29] was used to calculate the micropore volume and micropore surface area of samples. Elemental analysis was used to quantify the concentration of carbon, nitrogen and hydrogen. All samples were

analysed by Fourier transform infrared spectroscopy (FTIR) for surface moiety characterization.

3. Results and Discussion

Textural and chemical properties were determined for all 100 gels produced from the possible synthetic parameter combinations used in this study. Results obtained for CHN analysis were as expected (see supporting information). Due to their chemical compositions, both R and M contribute to the total carbon content of each sample but the relative contributions vary due to their individual carbon proportions (carbon contents of 65.5% and 28.6%, respectively). Therefore, as R is substituted by M, the C content decreases, while N comes only from M, therefore, N content increases linearly with [M] (Figure 1). H content is not significantly different for R and M, only a small decrease is observed as M substitutes R and these results are confirmed by CHN analysis for all samples produced in this study.

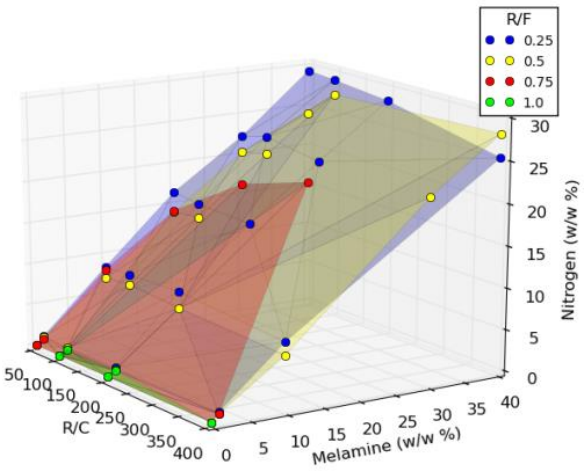

Figure 1: Nitrogen contents for Melamine-Resorcinol-Formaldehyde xerogels synthesised using Resorcinol/Catalyst ratio of 50-400; Resorcinol/Formaldehyde ratio of 0.25-1 for melamine content of 0-40 w/w%.

FTIR analysis was used to gain information regarding surface functionalisation of the synthesised gels as FTIR spectroscopy has been routinely applied to probe the chemical structure of carbon materials [30]. In this work, the effect of altering R/C, R/F and [M] on surface group development was examined. The suite of MRF materials were analysed by FTIR; Figure 2 shows a selected group where [M] is increased at constant R/C (50) and R/F (0.50). An increase in [M] results in fewer OH- bonds, from phenolic groups, in the final solid, as supported by the relative decrease in the peak corresponding to O-H vibration (3200-3500 cm-1 [31]) as [M] increases. Comparison of peak depth relative to other peaks across the spectra gives an indication of the concentration of the species. For example, it can be seen that as [M] increases, the proportionality of the peaks in the fingerprint region compared to the O-H peak increases considerably. This suggests that the concentration of O-H groups in MRF40 is lower compared to the concentration of the structural bonds

(observed in the fingerprint region) than for the MRF0 sample, for which, the intensities of the O-H peak and fingerprint region are very similar, suggesting as many O-H bonds as C-O or C-H structural groups. It is worth noting that for pure RF gels, or gels with lower concentrations of M (up to 10%), the O-H peak is wider than for materials with higher [M]. This indicates that, due to the higher concentration of O-H groups, the electrostatic interactions to surrounding hydrogen atoms become more important and these vibrations occur at wavenumbers close to the O-H bond, but sufficiently shifted to result in a wider peak (Figure 3). Conversely, increasing [M] reduces the concentration of O-H groups, therefore, the interactions between them weakens resulting in a narrower peak (Figure 3).

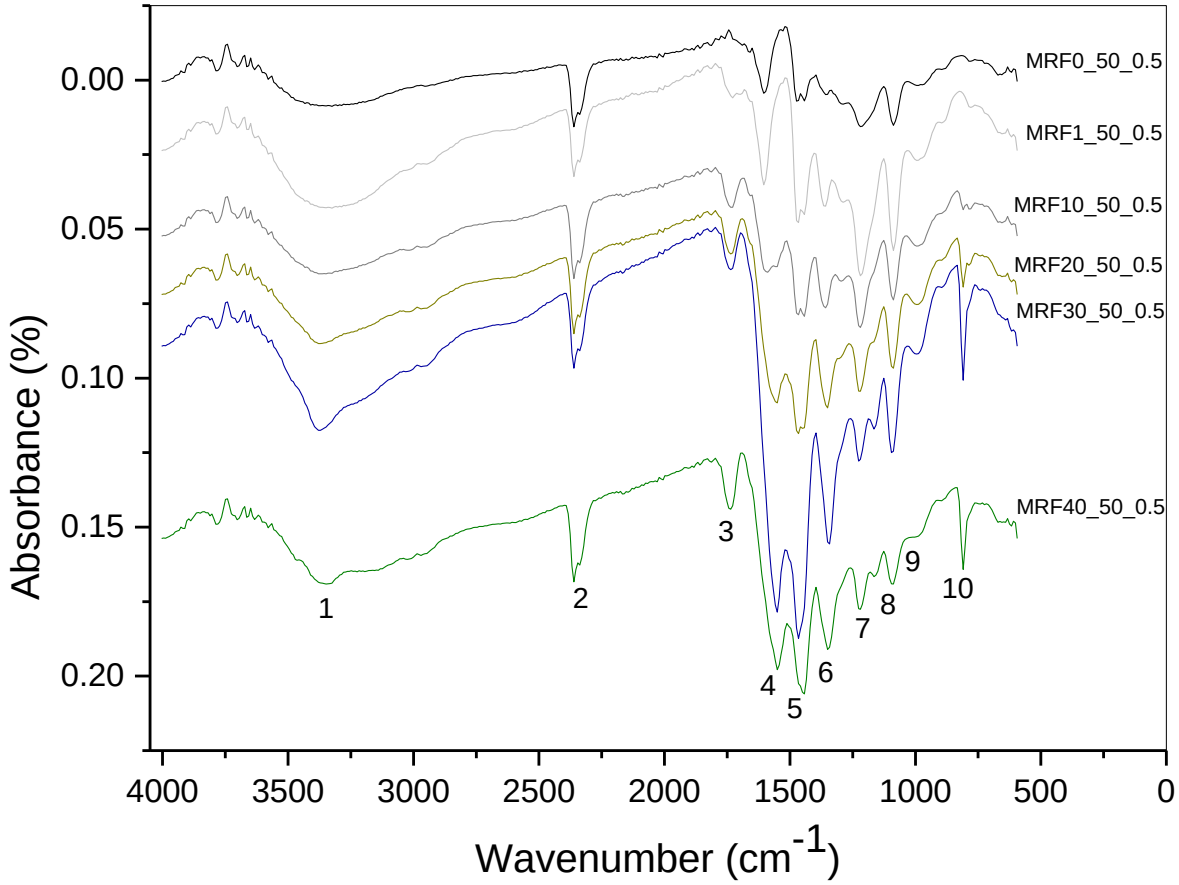

Figure 2: FTIR spectra of varying melamine content of 0-40 w/w% for a constant Resorcinol/Catalyst ratio of 50 and Resorcinol/Formaldehyde ratio of 0.5.

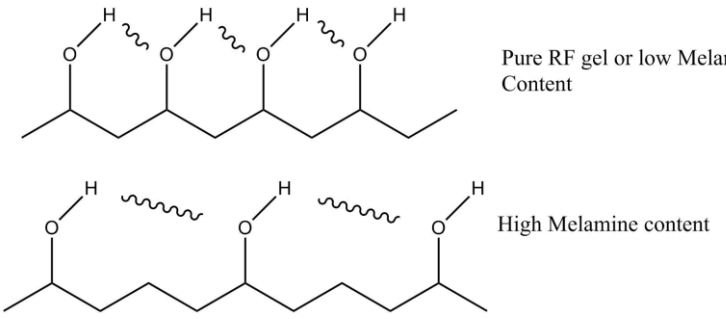

Figure 3: Schematic of hydrogen interactions with OH- groups at low (high resorcinol) and high (low resorcinol) melamine content.

As detailed above, the peak at 3550-3200 cm-1 corresponds to strong O-H bonding, related to R concentration and intermolecular O-H bonds, while O-H bending (1410-1260 cm-1 (s)) and C-OH stretching (1150-1040 cm-1 (s)) can be observed in the fingerprint region [31]. The O-H stretch can mask weaker -NH2 or =NH stretching vibrations (3500-3300 cm-1 (m)); these groups also absorb around 2360 cm-1 but, as this peak is also present for MRF0, which has no nitrogen content, it is more likely to correspond to CO2 which vibrates at 2349 cm-1, with a stronger intensity [31]. While the peak at 1743 cm-1 could be ascribed to carbonyl functionalities, this peak is not present in MRF0 and its intensity increases as nitrogen content is increased. This suggests that the peak more likely results from imide functionalities (1697 cm-1), formed by nitrogen bonding to two acyl groups via combination with F [31]. Conjugated C=O bonds appear at ~1640-1595 cm-1, and C-H stretching of saturated bonds (1470-1430 cm-1), can be related to methylene bridge formation (Scheme 1 and Scheme 3) [31]. Additional peaks in the fingerprint region can be ascribed to C-O (1300-1020 cm-1 (s)), and aromatic group C-H peaks at 850-700 cm-1 (s) [31]. The key changes observed for increasing [M], at constant R/C and R/F ratio, are the reduction of O-H stretching vibrations (3550-3200 cm-1), as a consequence of reducing R concentration, and an increase in imide functionalities (1697 cm-1).

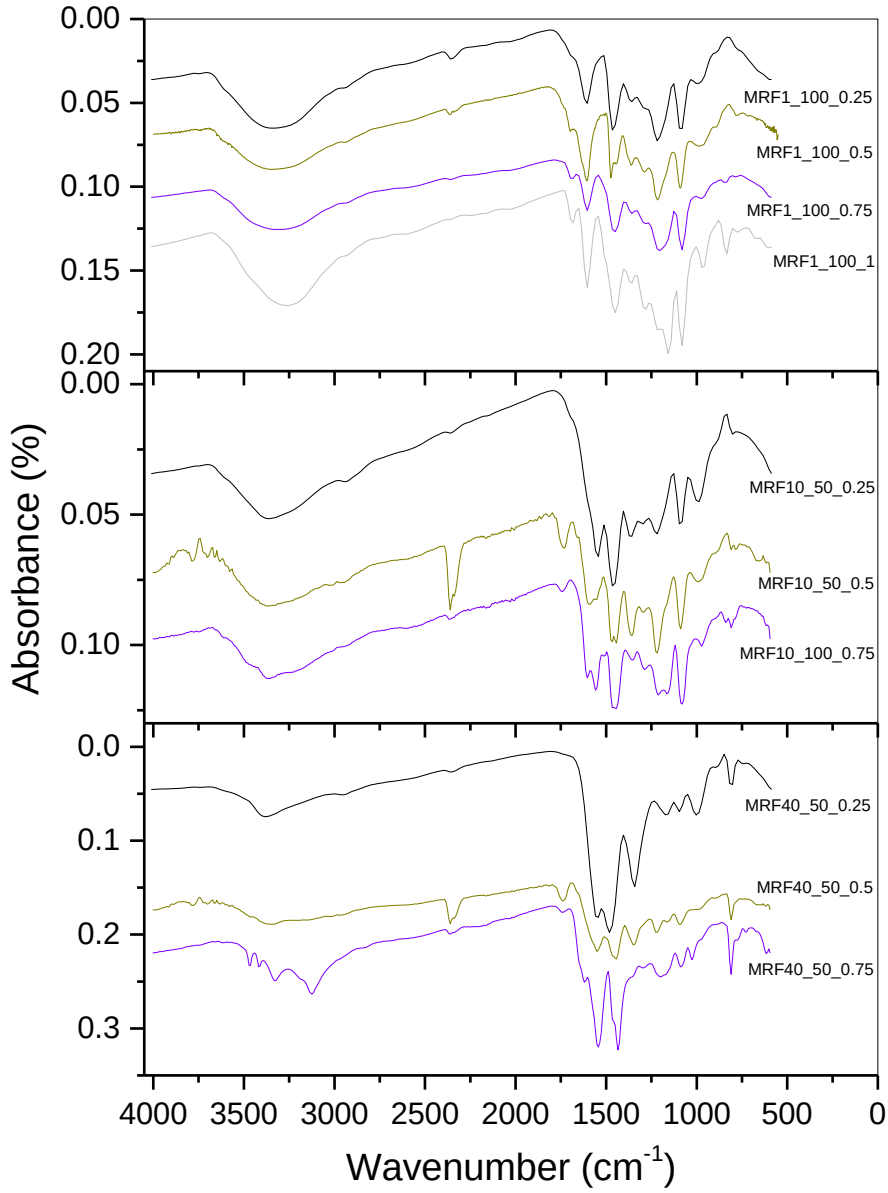

Figure 4: FTIR spectra of varying Resorcinol/Formaldehyde ratio for three sets of constant (low, medium and high) Resorcinol/Catalyst ratio and melamine content.

Figure 4 shows the effect of increasing R/F ratio for a system with constant [M] and R/C ratio. The data represents suites of low, medium and high [M] materials. It can be seen that while O-H stretching (3550 – 3200 cm-1) is little affected at high [M]; peaks at 1600-1400 cm-1, ascribed to C=O groups, seem to reduce in intensity as R/F increases. This decrease may be attributed to the higher degree of cross-linking at low R/F, as ring substitution increases with higher relative concentrations of F. As detailed above, the 1600-1400 cm-1 peak can also result from methylene bridge formation; hence, at low R/F such bridging should be favoured, particularly at initial solution pH 7-8. Similar results are observed for increasing R/C ratio for constant R/F and [M], with more evident changes at higher [M] (see Supporting Information). Increasing R/C impacts more markedly on the region 1600 – 1250

cm-1, with higher intensity peaks as [M] increases, but generally affects the entire fingerprint region. As R/C increases, more R is present in the initial solution, therefore, crosslinking is enhanced with increased intensities for associated peaks at 1640-1595 cm-1 (C=O), 1470-1430 cm-1 (C-H methylene bridge), 1300-1020 cm-1 (C-O) and 850-700 cm-1 (C-H).

Surface areas and porosities were determined for all samples; selected N2 adsorption/desorption isotherms with associated pore size distributions are shown in Figure 5 and Figure 6. In general, it can be seen that increasing R/C significantly reduces the adsorption capacity of the gels. Increasing [M] in MRF gels also produces a decrease in adsorption capacity; however, as R/C is increased the onset of this reduction occurs at lower [M], suggesting that, for a given R/C (and R/F), there is a maximum level of [M] that can be successfully incorporated into the gel matrix before the pore size becomes so large that surface area falls drastically and adsorption capacity is notably reduced. The isotherms obtained can be classified as Type IV, indicative of mesoporous adsorbents; initial monolayer coverage and micropore filling is followed by multilayer adsorption and capillary condensation in pores. The latter phenomenon is often accompanied by a hysteresis loop, the closure point of which, in the case of N2 adsorption at 77 K, occurs for pores wider than 4nm [32]. Data obtained for samples made using R/C 50 and R/F 0.25 (Figure 5) show an increase in average pore size from 2.4 to 9.5 nm, and the gradual opening of the hysteresis loop across this same series. Similarly, in the series with R/C 50 and R/F 0.5, the loops become appreciably open as [M] increases (see Supporting Information).

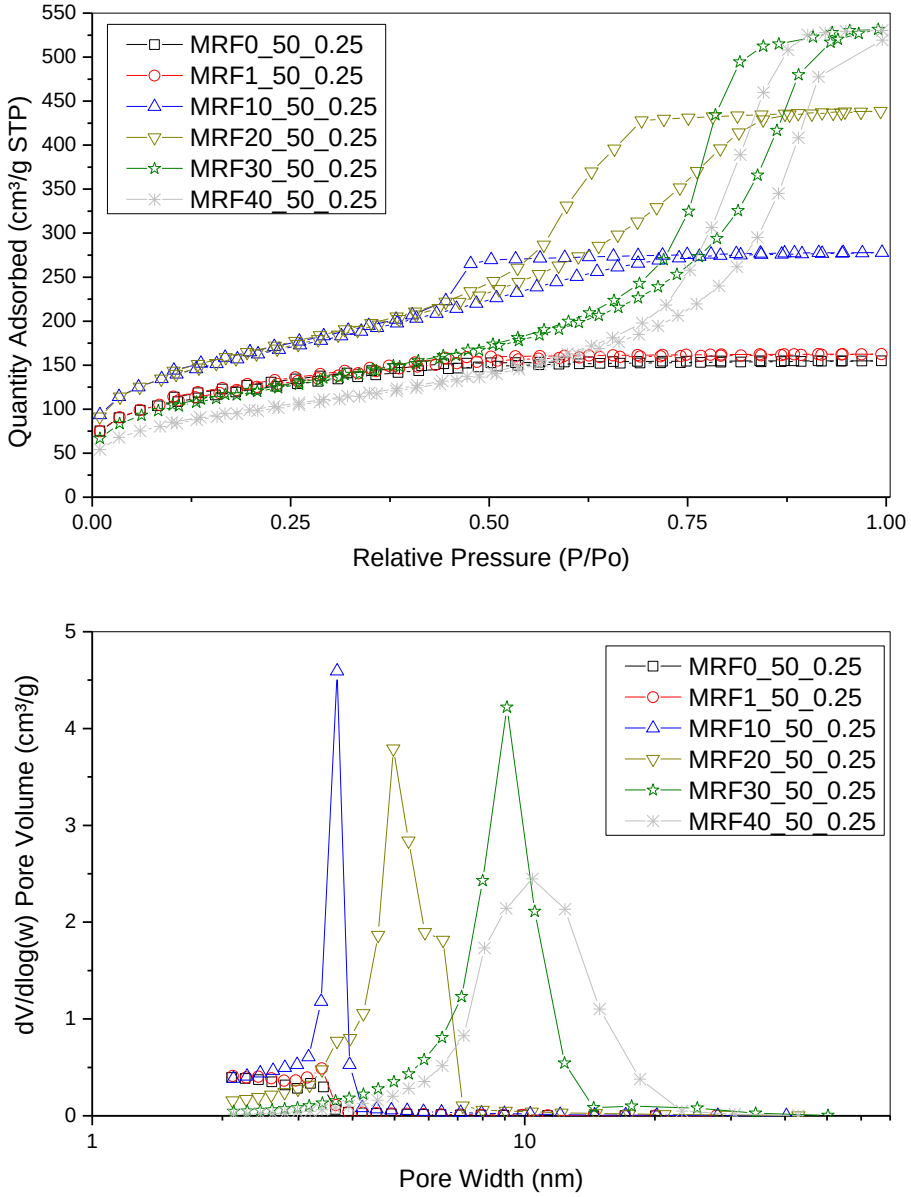

Figure 5: (a) Nitrogen adsorption isotherms and (b) Pore size distributions for a family of Melamine-Resorcinol-Formaldehyde xerogels synthesised using Resorcinol/Catalyst ratio of 50, Resorcinol/Formaldehyde ratio of 0.25 and melamine content of 0-40 w/w%.

The hysteresis loops observed can be classified as Type H1 or H2 depending on the synthetic parameters; at low [M], the hysteresis loops tend to be Type H2(a) before shifting to Type H2(b) for intermediate [M] and, finally, to Type H1 for higher [M]. Type H2 loops indicate complex structures where network effects becomes important, the steep desorption branch is associated with pore-blocking or percolation in narrow pore necks or to cavitation due to the effect of lowering the pressure, therefore, suggesting ink bottle like pores (narrow neck and wide body). Type H1 loops, on the other hand, are often found for ordered mesoporous carbons [32]. This suggests a transition from pores with restricted

access to open mesopores as [M] increases, potentially the result of a decrease in crosslinking. Such changes are not observed for all gel series, however, and for higher values of R/F there is only a transition from H2(a) to H2(b), likely due to the lack of F and again the associated impact this has on crosslinking of the materials. The widening of the pores is evident across all R/C values as [M] increases; however, as R/C increases, the shift from H2(a) to H2(b) loops occurs at lower [M], which indicates that the influence of [M] is greater when less catalyst is present in the system (Figure 6).

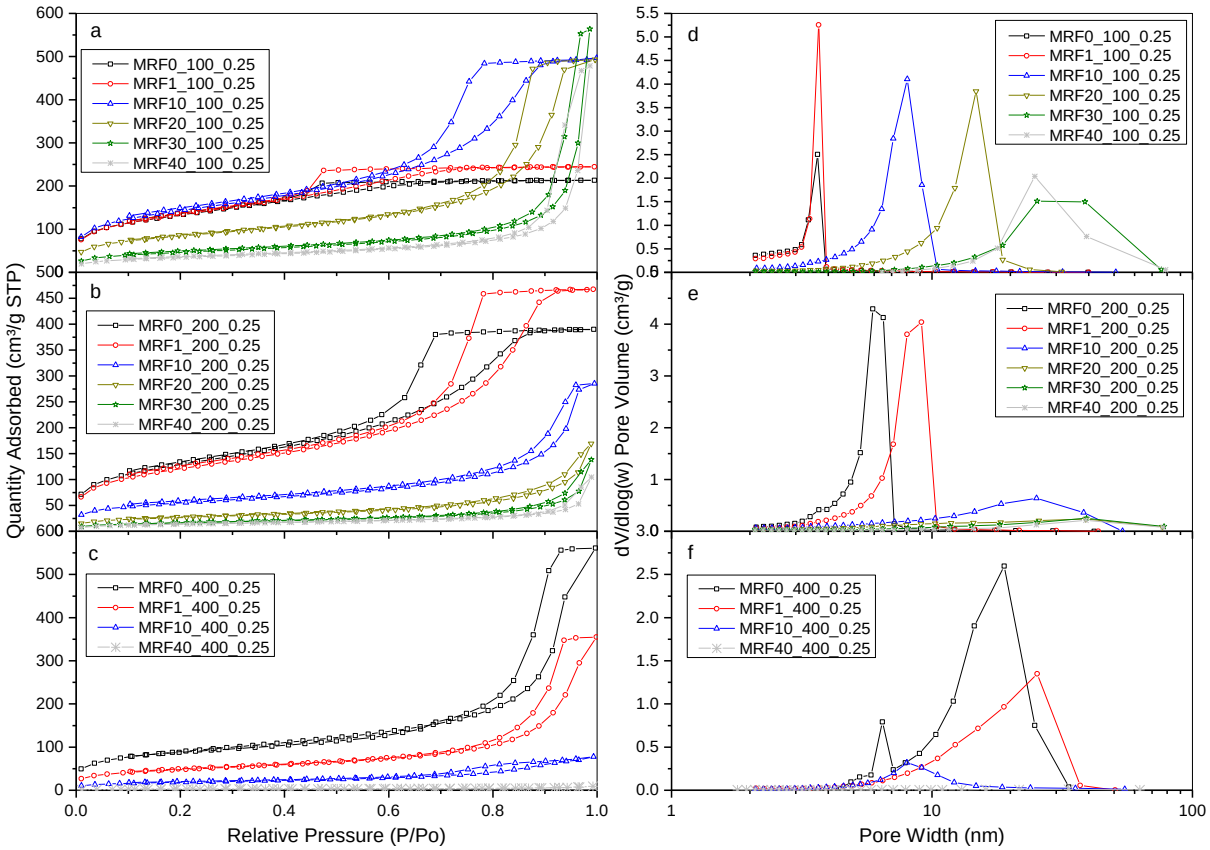

Figure 6: (a) Nitrogen adsorption isotherms and (d) Pore size distributions for Melamine-Resorcinol-Formaldehyde xerogels synthesised using Resorcinol/Catalyst ratio of 100, Resorcinol/Formaldehyde ratio of 0.25 and melamine content 0-40 w/w%; (b) Nitrogen adsorption isotherms and (e) Pore size distributions for Melamine-Resorcinol-Formaldehyde xerogels synthesised using Resorcinol/Catalyst ratio of 200, Resorcinol/Formaldehyde ratio of 0.25, and melamine content of 0-40 w/w%; (c) Nitrogen adsorption isotherms and (f) Pore size distributions for Melamine-Resorcinol-Formaldehyde xerogels synthesised using Resorcinol/Catalyst ratio of 400, Resorcinol/Formaldehyde ratio of 0.25, and melamine content of 0-40 w/w%.

As outlined in the introduction, initial solution pH can markedly affect gel formation; in this study the pH tends to decrease as R/C is increased, as a result of decreased basic catalyst concentration, and also tends to decrease slightly as R/F decreases. In support of the first observation, the lower pKb for sodium carbonate (3.67) means it will have the greatest impact on pH but it is imperative to remember that the concentration of catalyst is small in

comparison to that of R, M or F. In the second case, formalin (F solution) has a pH of 2.8 – 4.0 (as mentioned in Experimental section), therefore, as R/F increases, less formalin is used, and pH is less affected accordingly. As R/C increases, less carbonate is used and, consequently, pH tends to decrease due to the combined effect of less base and higher R concentration (weak acid, pKa 9.15). Consequently, for RF gels, R/C ratio is the main parameter that controls initial solution pH. By comparison, M is an organic base, therefore, as its concentration increases so too does pH; hence, for MRF gels the pH is also affected significantly (especially at high R/C) by M (Figure 7).

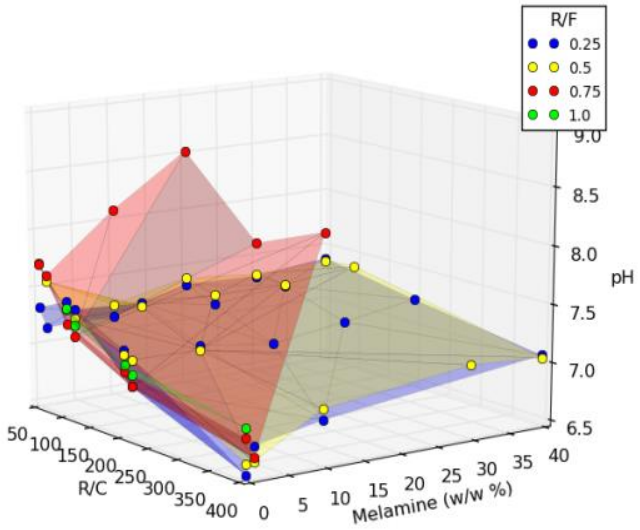

As R/F is increased, the number of F molecules available to provide linkages decreases resulting in weaker gels, as a consequence of reduced crosslinking between clusters, however, it is the effect of initial solution pH (and R/C ratio) that ultimately controls the pore structure of the final xerogel [33]. As pH approaches 8.0 and 8.5 for [M] of 20 and 10 respectively, pH is generally increased as R/F increases creating weaker porous structures and, in most cases, gelation fails. It can also be rationalised that R/F values of 0.75 and 1.0 would produce weaker xerogels, low surfaces area and pore volume as, among other reasons, the high initial solution pH ranges from 7.0 to 8.5 and it is known that initial solution pH has a strong influence on successful gelation. As observed, in this work, for R/F ≥ 0.75, many gels fail to crosslink sufficiently to make further processing possible; such materials are often amorphous non-porous powders and, as a consequence, only those gels created with R/F 0.25 or 0.5 will be considered in the remainder of the paper.

The total surface area of a material can be divided into non-micropore surface area (pores >2 nm width) and micro surface area (pores <2 nm width). For the MRF xerogels synthesised in this work, increasing R/C produces and increasing [M] have a similar effect on surface area, which decreases as either component is increased. It is also notable that if both parameters are increased simultaneously there is a drastic reduction in surface area (Figure 8).

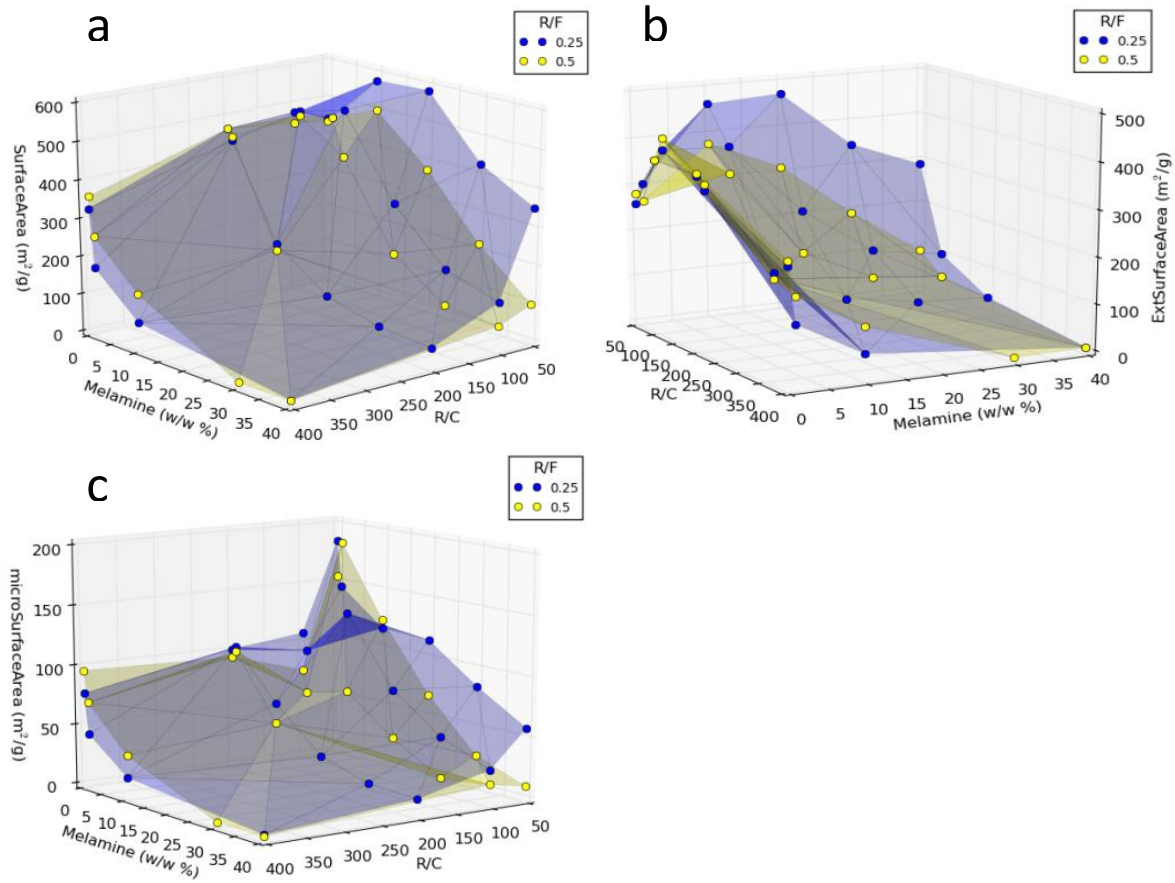

Figure 8: (a) Surface areas, (b) non-micropore surface area and (c) micropore surface area obtained for Melamine-Resorcinol-Formaldehyde xerogels produced with Resorcinol/Formaldehyde ratio of 0.25 or 0.5, Resorcinol/Catalyst ratio of 50-400 and melamine content 0-40 w/w%.

The greatest surface areas (Figure 8) are obtained for MRF 20 and MRF 10; while, MRF 0 and MRF 1 show similar results to each other. After this maximum, surface area drops drastically for melamine contents > 30w/w%. As R/C increases the surface area decreases for all melamine contents, however, this decrease occurs at lower R/C as melamine content increases (see Supporting Information), and this narrows the window available to obtain significant surface areas while incorporating more nitrogen into the material. For MRF 0 and MRF 1, the surface areas determined show little variation in the range of R/C studied (50 to 400), but there is still a notable decrease for R/C >200. As stated above, increasing R/C and melamine content both affect surface area, with marked effects when combined, thereby limiting the working range of values for the three variables studied here. In order to maximise surface area, it is recommended to use R/C of 50-100, R/F <0.5 and melamine content between 0 and 20% (potentially up to 30% for R/C 50).

Microporosity is known to be important when targeting small gas molecules, such as in gas treatment applications. Thus, understanding how varying the synthetic parameters for MRF xerogel synthesis (i.e. R/F, R/C and melamine content) affect the development of

microporosity is critical for material optimisation. It can be seen that increasing R/C, melamine content or R/F tends to counteract the formation of microporosity within MRF materials, while also increasing pore size (Figure 9).

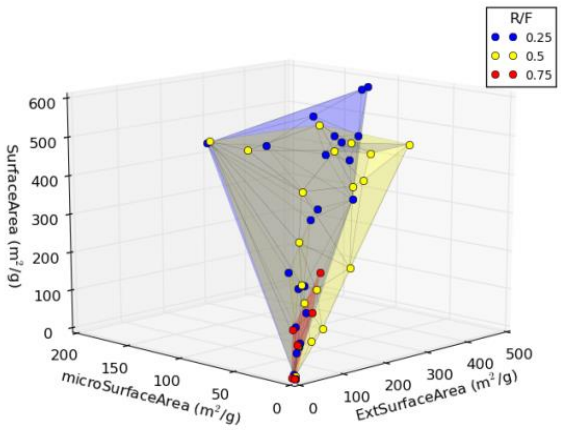

Figure 9: Microporosities obtained for Melamine-Resorcinol-Formaldehyde xerogels synthesised using varying (a) Resorcinol/Catalyst ratio, (b) Resorcinol/Formaldehyde ratio, and (c) melamine content.

As outlined above, R/F values of 0.25 and 0.5 result in better developed gels, offering enhanced control when tuning this type of material by providing improved control of crosslinking during cluster aggregation. R/F directly controls the stoichiometry of the reaction, therefore, the number of substitutions occurring in the ring (R and/or M) and, consequently, the level of crosslinking. Therefore, this affects the formation of voids spaces between the aggregates or clusters, which impact on the pore size and, therefore, the micropore and non-micropore surface areas. R/F values of 0.25 or 0.5 result in gels with high internal area and, conversely, higher R/F values result in weak gels with low surface area. As R/C is increased, fewer R molecules are activated to react with F, as less sodium carbonate is available in solution; which weakens the structure, forming lager pore sizes and quelling microporosity in the material. As shown above, increasing [M] affects pore size in a similar manner as increasing R/C, therefore, microporosity is similarly reduced (see Supporting Information).

Total pore volume is calculated from the maximum N2 uptake observed during BET analysis at the highest pressure (~0.98 bar), and micropore volume is calculated using the t-plot method. Higher total pore volumes were obtained for low [M] (0-20%) and low R/C (50-200), see Figure 10. As the t-plot method is used to determine both micropore volume and micropore surface area, they follow the same trend, as expected. Similarly to the results described above, microporosity tends to decrease as R/C and [M] are increased. Notably, samples synthesised using R/C 50 and 100 exhibit high N2 uptake irrespective of surface area (see Supporting Information), while R/C 200 and 400 demonstrate significant N2 uptake only for a narrow window at low [M]. This means that increasing [M] does not necessarily mean an increase in N2 uptake. Surface area is a greater influence on N2

uptake, which can be tailored by control of R/C and R/F ratio; maximized uptakes are observed at R/C 50-100 and R/F 0.25-0.5 (See Supporting Information).

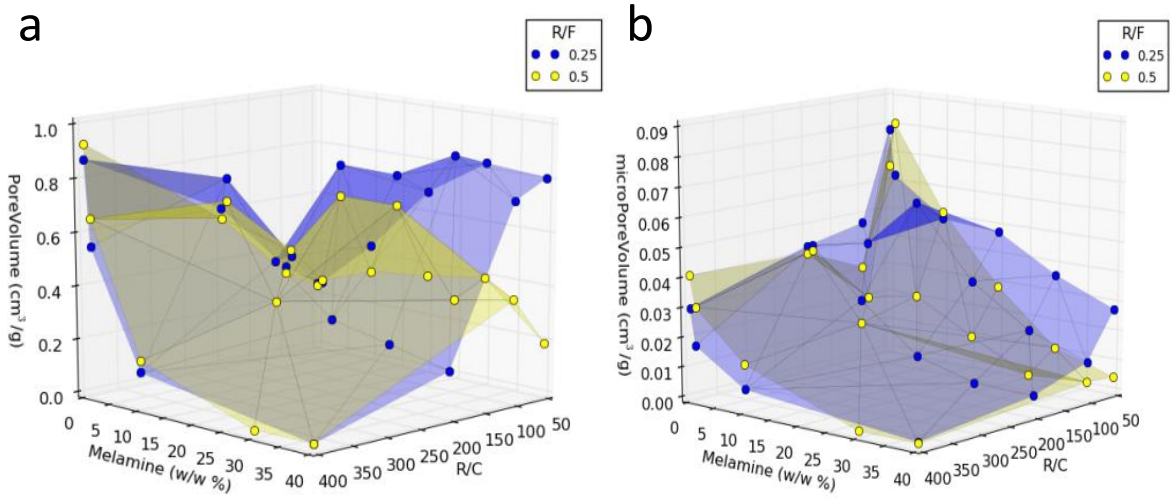

Figure 10: (a) Pore volumes and (b) micro pore volumes obtained for Melamine-Resorcinol-Formaldehyde xerogels synthesised using melamine content of 0-40 w/w%, Resorcinol/Catalyst ratio of 50-400 and Resorcinol/Formaldehyde ratio of 0.25 or 0.5.

Two different behaviours are distinguishable at i) low R/C (50 and 100) and ii) high R/C (400), with regards to both pore volume and nitrogen uptake (Figure 11). At high R/C the largest uptake is seen for low [M] and is decreases progressively as [M] increases, while for low R/C the opposite is observed, where the higher N2 uptake is for higher [M] with a progressive decrease with decreasing [M]. Highest N2 uptakes are observed for pore sizes between 5-15 nm, with a few exceptions, e.g. high [M] and low R/C show high uptakes even at 25 nm. While there is incongruity in pore volume (the two maxima are observed, contrarily at low [M]/high R/C, and high [M]/low R/C), micropore volume tends to uniformly decrease as R/C, R/F and [M] increase; for low R/F, the decrease is not as steep. The maximum micropore volume for each [M] analysed was observed at low R/C (50).

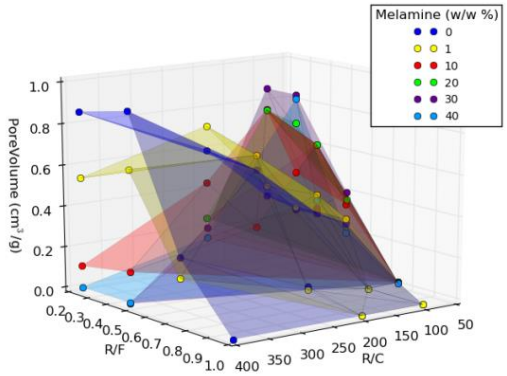

Figure 11: Pore volume of Melamine-Resorcinol-Formaldehyde xerogels synthesised using varying Resorcinol/Formaldehyde ratio and Resorcinol/Catalyst ratio for different melamine content.

It is notable that pore size is only controlled for low R/F (0.25 or 0.5), while higher R/F (0.75 or 1.0) results in randomisation of pore size with a tendency to larger diameters as a result of the associated weak crosslinking and interactions between clusters. Smallest pore sizes are obtained for low R/C (50); the amount of catalyst is greatest, which enhances cluster crosslinking, promoting the formation of small voids and pores. For low R/C (50) and R/F (0.25 or 0.5), pore size increases gradually as [M] is increased; in general, low R/C gels results in smaller pore sizes for low [M], while the opposite is observed for higher R/C (Figure 12).

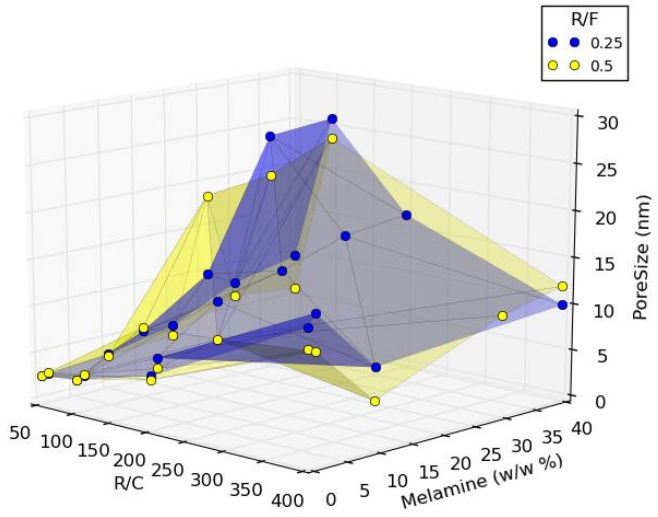

Figure 12: Pore size obtained in Melamine-Resorcinol-Formaldehyde xerogels synthesised using Resorcinol/Formaldehyde ratio of 0.25 or 0.5 as a function of Resorcinol/Catalyst ratio and melamine content.

4. Conclusions

Melamine-Resorcinol-Formaldehyde (MRF) xerogels produced using synthesis parameters of Resorcinol/Catalyst ratio (R/C), Resorcinol/Formaldehyde ratio (R/F) and melamine content ([M]) were examined to show the associated effects on initial solution pH, surface area, pore size and volume. For Resorcinol-Formaldehyde (RF) gels (no melamine) R/C is known to rigidly control pH. By contrast, for MRF gels, [M] also impacts pH, with a stronger effect observed for higher R/C where pH increases as [M] increases; at low R/C pH is, instead, noted to fluctuate at ~7.5, which may be a result of the additional basic character afforded by melamine. R/F controls the reaction stoichiometry, therefore, as the value is increased, the final xerogel structure becomes weaker and, in most cases, gelation fails. Low R/F offers better control of final xerogel properties, such as pore size and also enhances crosslinking. Increasing [M] reduces the carbon content of the final xerogel, and, as expected, nitrogen content increases linearly as [M] is increased. FTIR confirmed that the proportion of hydroxyl functionalities decreased as [M] was increased, as a consequence of substitution of R by M in the reaction; additionally the concentration of imide functionalities is also increased. At constant [M] and R/C, increasing R/F is seen to increase the concentration of methylene bridges; similarly increasing R/C, at constant [M] and R/F,

also results in an increase in bridging moieties and related vibrations. MRF materials exhibit Type IV nitrogen sorption isotherms, and hysteresis loops shifting from Type H2 to H1 as [M] increases, which is related to narrow necked and wide bodied pores; this effect is diminished with increasing R/F. The most notable effect of increasing [M] in these materials is similar to increasing R/C, this being a reduction in surface area, pore volume and N2 uptake, as well as an increase in pore size. If both parameters are increased simultaneously the reduction of these structural parameters is drastic, and in order to obtain higher surface areas, pore volumes and control pore size R/F needs to be <0.5. In order to optimise microporosity in future materials synthesis, low R/C, [M] and R/F are required as increased levels of each variable increase the tendency toward mesopore formation. This means that, for gas treatment applications, careful consideration of the synthetic variables is required to optimise chemical and textural properties in tandem.

5. Acknowledgements

Thanks to the Department of Chemical and Process Engineering and the University of Strathclyde for their support. Authors also want to thank Mr. Francesco Pelizza for script used to generate 3D surface plots.

6. References

1. Mirzaeian, M. and P.J. Hall, The control of porosity at nano scale in resorcinol formaldehyde carbon aerogels. Journal of Materials Science, 2009. 44(10): p. 2705-2713.
2. Pekala, R.W. and D.W. Schaefer, Structure of organic aerogels. 1. Morphology and scaling. Macromolecules, 1993. 26(20): p. 5487-5493.
3. Horikawa, T., J.i. Hayashi, and K. Muroyama, Controllability of pore characteristics of resorcinol–formaldehyde carbon aerogel. Carbon, 2004. 42(8–9): p. 1625-1633.
4. Job, N., et al., Porous carbon xerogels with texture tailored by pH control during sol–gel process. Carbon, 2004. 42(3): p. 619-628.
5. Feng, Y.N., et al., Effects of further adding of catalysts on nanostructures of carbon aerogels. Materials Science and Engineering: B, 2008. 148(1–3): p. 273-276.
6. Mulik, S. and C. Sotiriou-Leventis, Resorcinol-Formaldehyde. Aerogels handbook, 2011: p. 215-34.
7. Gebert, M.S. and R.W. Pekala, Fluorescence and light-scattering studies of sol-gel reactions. Chemistry of Materials, 1994. 6(2): p. 220-226.
8. Yamamoto, T., et al., Control of mesoporosity of carbon gels prepared by sol–gel polycondensation and freeze drying. Journal of Non-Crystalline Solids, 2001. 288(1–3): p. 46-55.
9. Tamon, H.I., H.; Mikami, M.; Okazaki, M., Porous structure of organic and carbon aerogels synthesized by sol-gel polycondensation of resorcinol with formaldehyde. Carbon, 1997. 35(6): p. 791-796.
10. Fung, A.W.P., et al., Relationship between particle size and magnetoresistance in carbon aerogels prepared under different catalyst conditions. Journal of Non-Crystalline Solids, 1995. 186: p. 200-208.

11. Taylor, S.J., et al., Gelation Mechanism of Resorcinol-Formaldehyde Gels Investigated by Dynamic Light Scattering. Langmuir, 2014. 30(34): p. 10231-10240.
12. Fairen-Jimenez, D., F. Carrasco-Marin, and C. Moreno-Castilla, Porosity and surface area of monolithic carbon aerogels prepared using alkaline carbonates and organic acids as polymerization catalysts. Carbon, 2006. 44(11): p. 2301-2307.
13. Bock, V., A. Emmerling, and J. Fricke, Influence of monomer and catalyst concentration on RF and carbon aerogel structure. Journal of Non-Crystalline Solids, 1998. 225: p. 69-73.
14. Zhou, H., et al., Facile preparation and ultra-microporous structure of melamine-resorcinol-formaldehyde polymeric microspheres. Chemical Communications, 2013. 49(36): p. 3763-3765.
15. Pekala, R.W., Organic aerogels from the polycondensation of resorcinol with formaldehyde. Journal of Materials Science, 1989. 24(9): p. 3221-3227.
16. Wu, D., et al., Low-density organic and carbon aerogels from the sol–gel polymerization of phenol with formaldehyde. Journal of Non-Crystalline Solids, 2005. 351(10–11): p. 915-921.
17. Jirglová, H., A.F. Pérez-Cadenas, and F.J. Maldonado-Hódar, Synthesis and Properties of Phloroglucinol−Phenol−Formaldehyde Carbon Aerogels and Xerogels. Langmuir, 2009. 25(4): p. 2461-2466.
18. Mulik, S., C. Sotiriou-Leventis, and N. Leventis, Time-Efficient Acid-Catalyzed Synthesis of Resorcinol− Formaldehyde Aerogels. Chemistry of Materials, 2007. 19(25): p. 6138-6144.
19. Merzbacher, C.I., et al., Carbon aerogels as broadband non-reflective materials. Journal of non-crystalline solids, 2001. 285(1): p. 210-215.
20. Pizzi, A.M., K. L.;, Handbook of adhesive technology: Second edition., ed. I. Marcel Dekker. 2003, New York.
21. Hodgins, T.S., et al., Melamine-Formaldehyde Film-Forming Compositions. Industrial & Engineering Chemistry, 1941. 33(6): p. 769-779.
22. Okano, M. and Y. Ogata, Kinetics of the Condensation of Melamine with Formaldehyde. Journal of the American Chemical Society, 1952. 74(22): p. 5728-5731.
23. Jahromi, S., Storage stability of melamine-formaldehyde resin solutions, 1. The mechanism of instability. Macromolecular Chemistry and Physics, 1999. 200(10): p. 2230-2239.
24. Van Blaaderen, A.V.G., J.; Vrij, A., Monodisperse colloidal silica spheres from tetraalkoxysilanes: Particle formation and growth mechanism. J. Colloid Interface Sci., 1992. 154: p. 481-501.
25. Liu, J., et al., Extension of The Stöber Method to the Preparation of Monodisperse Resorcinol–Formaldehyde Resin Polymer and Carbon Spheres. Angewandte Chemie International Edition, 2011. 50(26): p. 5947-5951.
26. Brunauer, S., P.H. Emmet, and E. Teller, Adsorption of gases in multimolecular layers. Journal of the American Chemical Society, 1938. 60: p. 309-19.
27. Rouquerol, J., P. Llewellyn, and F. Rouquerol, Is the BET equation applicable to microporous adsorbents?, in Studies in Surface Science and Catalysis, F.R.-R.J.R. P.L. Llewellyn and N. Seaton, Editors. 2007, Elsevier. p. 49-56.
28. Barrett, E.P., L.G. Joyner, and P.P. Halenda, The determination of pore volume and area distributions in porous substances. I. Computations from nitrogen Isotherms. Journal of the American Chemical Society, 1951. 73: p. 373-80.
29. Lippens, B.C. and J. De Boer, Studies on pore systems in catalysts: V. The t method. Journal of Catalysis, 1965. 4(3): p. 319-323.

30. Smith, B.C., Fundamentals of Fourier transform infrared spectroscopy. 2011: CRC Press Inc.
31. Williams, D.H. and I. Fleming, Spectroscopic methods in organic chemistry. Fourth edition ed. 1980: McGraw-Hill.
32. Thommes, M., et al., Physisorption of gases, with special reference to the evaluation of surface area and pore size distribution (IUPAC Technical Report). Pure and Applied Chemistry, 2015. 87(9-10): p. 1051-1069.
33. Al-Muhtaseb, S.A. and J.A. Ritter, Preparation and Properties of Resorcinol–Formaldehyde Organic and Carbon Gels. Advanced Materials, 2003. 15(2): p. 101-114.

L2 Paper Under Construction:

Decoupling microporosity and nitrogen content to optimise CO2 adsorption in modified xerogels.

References

11 References

1. *NASA GISS: Science Briefs: Greenhouse Gases: Refining the Role of Carbon Dioxide*. [cited 2016 30/08].
2. Mora, C., *The projected timing of climate departure from recent variability.* Nature., (2013). **502**: p. 183-187.
3. *IPCC fifth assessment report: climate change 2014 synthesis report.*
4. Schreiber, A., Zapp, P. & Kuckshinrichs, W. , *Environmental assessment of German electricity generation from coal-fired power plants with amine-based carbon capture.* Int J Life Cycle Assess, 2009. **14:547**.
5. Odeh, N.A. and T.T. Cockerill, *Life cycle GHG assessment of fossil fuel power plants with carbon capture and storage.* Energy Policy, 2008. **36**(1): p. 367-380.
6. Khan, F.I., K. Hawboldt, and M. Iqbal, *Life cycle analysis of wind–fuel cell integrated system.* Renewable energy, 2005. **30**(2): p. 157-177.
7. EDGAR, E.C. *Emission database for global atmospheric research*. Available from: http://edgar.jrc.ec.europa.eu/overview.php?v=CO2ts1990-2014.
8. Commision, E. *Climate action*.
9. EDGAR. *Emmision database for global atmospheric research*. 2016.
10. Bhown, A.S. and B.C. Freeman, *Analysis and Status of Post-Combustion Carbon Dioxide Capture Technologies.* Environmental Science & Technology, 2011. **45**(20): p. 8624-8632.
11. SM, F., et al., *Guidelines for carbon dioxide capture, transport, and storage.* 2008, Washington: World Resour Inst.
12. Gibbins, J. and H. Chalmers, *Carbon Capture and Storage.* Elsevier, 2008. **36**: p. 4317-4322.
13. Metz, B., et al., *IPCC Special Report on Carbon Dioxide Capture and Storage*. 2005, Cambridge, United Kingdom and New York, NY, USA: Cambridge University Press.
14. Leung, D.Y.C., G. Caramanna, and M.M. Maroto-Valer, *An overview of current status of carbon dioxide capture and storage technologies.* Renewable & Sustainable Energy Reviews, 2014. **39**: p. 426-443.
15. Scholes, C.A., et al., *CO2 capture from pre-combustion processes—Strategies for membrane gas separation.* International Journal of Greenhouse Gas Control, 2010. **4**(5): p. 739-755.
16. Olajire, A.A., *CO2 capture and separation technologies for end-of-pipe applications – A review.* Energy, 2010. **35**(6): p. 2610-2628.
17. Wall, T.F., *Combustion processes for carbon capture.* Proceedings of the Combustion Institute, 2007. **31**(1): p. 31-47.
18. Buhre, B.J.P., et al., *Oxy-fuel combustion technology for coal-fired power generation.* Progress in Energy and Combustion Science, 2005. **31**(4): p. 283-307.
19. Liu, D., T. Wall, and R. Stanger, *CO2 quality control in Oxy-fuel technology for CCS: SO2 removal by the caustic scrubber in Callide Oxy-fuel Project.* International Journal of Greenhouse Gas Control, 2016. **51**: p. 207-217.
20. Ebrahimi, A., et al., *Energetic, exergetic and economic assessment of oxygen production from two columns cryogenic air separation unit.* Energy, 2015. **90, Part 2**: p. 1298-1316.
21. Hossain, M.M. and H.I. de Lasa, *Chemical-looping combustion (CLC) for inherent separations—a review.* Chemical Engineering Science, 2008. **63**(18): p. 4433-4451.
22. Chiu, P.-C. and Y. Ku, *Chemical Looping Process-A Novel Technology for Inherent CO2 Capture.* Aerosol Air Qual. Res, 2012. **12**: p. 1421-1432.

23. Zevenboven, R.K., P., *Control of pollutants in flue gases and fuel gases*. 2002, Espoo/Turku, Finland: The Nordic Energy Research programme Solid Fuel Committee; Helsinki University of Technology.
24. Elwell LC, G.W., *Technology options for capturing CO_2 - special report. Power 2006; 150:60-5.*
25. Adewole, J.K., et al., *Current challenges in membrane separation of CO2 from natural gas: A review.* International Journal of Greenhouse Gas Control, 2013. **17**(0): p. 46-65.
26. Wilcox, J., et al., *Advancing Adsorption and Membrane Separation Processes for the Gigaton Carbon Capture Challenge.* Annual Review of Chemical and Biomolecular Engineering, 2014. **5**(1): p. 479-505.
27. Xu, C.-G. and X.-S. Li, *Research progress of hydrate-based CO2 separation and capture from gas mixtures.* RSC Advances, 2014. **4**(35): p. 18301-18316.
28. Ma, Z.W., et al., *Review of fundamental properties of CO2 hydrates and CO2 capture and separation using hydration method.* Renewable and Sustainable Energy Reviews, 2016. **53**: p. 1273-1302.
29. Li, Z., et al., *Enhanced separation of carbon dioxide from a CO2 + CH4 gas mixture using a hybrid adsorption-hydrate formation process in the presence of coal particles.* Journal of Natural Gas Science and Engineering.
30. Burt, S.B., Andrew; Baxter, Larry, *Cryogenic CO_2 capture to control climate change emissions.* Sustainable Energy Solutions; Brigham Young University.
31. Fu, D., et al., *Absorption capacity and viscosity for CO2 capture process using high concentrated PZ-DEAE aqueous solution.* The Journal of Chemical Thermodynamics, 2016. **101**: p. 123-129.
32. Fu, D., P. Zhang, and L. Wang, *Absorption performance of CO2 in high concentrated [Bmim][Lys]-MDEA aqueous solution.* Energy, 2016. **113**: p. 1-8.
33. zareiekordshouli, F., A. Lashani-zadehgan, and P. Darvishi, *Thermophysical properties and CO2 absorption studies of the amine functionalized [Amim][Tf2N] and the non-functionalized counterpart [bmim][Tf2N] ionic liquids.* International Journal of Greenhouse Gas Control, 2016. **53**: p. 328-337.
34. Samanta, A., et al., *Post-Combustion CO2 Capture Using Solid Sorbents: A Review.* Industrial & Engineering Chemistry Research, 2012. **51**(4): p. 1438-1463.
35. Nwaoha, C., et al., *Carbon dioxide (CO2) capture: Absorption-desorption capabilities of 2-amino-2-methyl-1-propanol (AMP), piperazine (PZ) and monoethanolamine (MEA) tri-solvent blends.* Journal of Natural Gas Science and Engineering, 2016. **33**: p. 742-750.
36. Rochelle, G.T., *Thermal degradation of amines for CO2 capture.* Current Opinion in Chemical Engineering, 2012. **1**(2): p. 183-190.
37. A. Arenillas, K.M.S., T.C. Drage and C.E. Snape, *Fuel*. Vol. 84, 2204. 2005.
38. Takamura, Y., et al., *Application of high-pressure swing adsorption process for improvement of CO2 recovery system from flue gas.* The Canadian Journal of Chemical Engineering, 2001. **79**(5): p. 812-816.
39. Aspelund, A., M.J. Mølnvik, and G. De Koeijer, *Ship Transport of CO2.* Chemical Engineering Research and Design, 2006. **84**(9): p. 847-855.
40. Svensson, R., et al., *Transportation systems for CO2—application to carbon capture and storage.* Energy Conversion and Management, 2004. **45**(15–16): p. 2343-2353.
41. Johnsen, K., et al., *DNV recommended practice: Design and operation of CO2 pipelines.* Energy Procedia, 2011. **4**(0): p. 3032-3039.
42. *Internation Energy Agency Report. CO_2 pipeline infrastructure. Supported by Global CCS Institute*. 2014.

43. Aresta, M. and A. Dibenedetto, *Utilisation of CO2 as a chemical feedstock: opportunities and challenges.* Dalton Transactions, 2007(28): p. 2975-2992.
44. Oldenburg, C.M., *Why we need the 'and' in 'CO2 utilization and storage'.* Greenhouse Gases: Science and Technology, 2012. **2**(1): p. 1-2.
45. Dooley, J.J.D., C.L.; Dahowski, R.T., *An assesment of the commercial availability of carbon dioxide capture and storage technologies as of June 2009.* Report for the US department of Energy under a contract no. DE-ACO5-TGRL01830, PNNL-18520., 2009.
46. *Carbon Recycling International. World's largest CO_2 methanol plant*. 2016 [cited 2016 23 September]; Available from: http://carbonrecycling.is/projects-1/2016/2/14/worlds-largest-co2-methanol-plant.
47. *Novomer. Catalyzing green company.* 2016; Available from: http://www.novomer.com/co2-business-overview-0.
48. *Covestro. From waste gas to raw material.* 2016; Available from: http://www.covestro.com/en/sustainability/carbon-dioxide.
49. Lewis, D., et al., *Assessment of the potential for geological storage of carbon dioxide in Ireland and Northern Ireland.* Energy Procedia, 2009. **1**(1): p. 2655-2662.
50. Solomon, S., M. Carpenter, and T.A. Flach, *Intermediate storage of carbon dioxide in geological formations: A technical perspective.* International Journal of Greenhouse Gas Control, 2008. **2**(4): p. 502-510.
51. Celia, M.A. and J.M. Nordbotten, *Practical Modeling Approaches for Geological Storage of Carbon Dioxide.* Ground Water, 2009. **47**(5): p. 627-638.
52. Bentham, M., et al., *CO2 STORage Evaluation Database (CO2 Stored). The UK's online storage atlas.* Energy Procedia, 2014. **63**: p. 5103-5113.
53. Flores, R.M., *Chapter 9 - Worldwide Coalbed Gas Development*, in *Coal and Coalbed Gas*. 2014, Elsevier: Boston. p. 509-585.
54. Michael, K., et al., *Geological storage of CO2 in saline aquifers—A review of the experience from existing storage operations.* International Journal of Greenhouse Gas Control, 2010. **4**(4): p. 659-667.
55. Yamasaki, A., *An overview of CO2 mitigation options for global warming - emphasizing CO2 sequestration options.* J. Chem. Eng. Jpn., 2003. **36**: p. 361-375.
56. House, K.Z., et al., *Permanent carbon dioxide storage in deep-sea sediments.* Proceedings of the National Academy of Sciences, 2006. **103**(33): p. 12291-12295.
57. Hall-Spencer, J.M., et al., *Volcanic carbon dioxide vents show ecosystem effects of ocean acidification.* Nature, 2008. **454**(7200): p. 96-99.
58. Olajire, A.A., *A review of mineral carbonation technology in sequestration of CO2.* Journal of Petroleum Science and Engineering, 2013. **109**: p. 364-392.
59. Estublier, A., et al., *Long-term fate of CO2 in a saline aquifer: modeling issues.* Energy Procedia, 2014. **63**: p. 3464-3474.
60. Li, Z., et al., *CO2 sequestration in depleted oil and gas reservoirs—caprock characterization and storage capacity.* Energy Conversion and Management, 2006. **47**(11–12): p. 1372-1382.
61. Enting, I.G., D.M. Etheridge, and M.J. Fielding, *A perturbation analysis of the climate benefit from geosequestration of carbon dioxide.* International Journal of Greenhouse Gas Control, 2008. **2**(3): p. 289-296.
62. Chadwick, R.A., B.P. Marchant, and G.A. Williams, *CO2 storage monitoring: leakage detection and measurement in subsurface volumes from 3D seismic data at Sleipner.* Energy Procedia, 2014. **63**: p. 4224-4239.

63. Dethlefsen, F., et al., *Monitoring Approaches for Detecting and Evaluating CO2 and Formation Water Leakages into Near-surface Aquifers.* Energy Procedia, 2013. **37**: p. 4886-4893.
64. Harbert, W., et al., *Progress in monitoring strategies for risk reduction in geologic CO2 storage.* International Journal of Greenhouse Gas Control, 2016. **51**: p. 260-275.
65. Jung, Y., Q. Zhou, and J.T. Birkholzer, *Early detection of brine and CO2 leakage through abandoned wells using pressure and surface-deformation monitoring data: Concept and demonstration.* Advances in Water Resources, 2013. **62, Part C**: p. 555-569.
66. Jenkins, C., T. Kuske, and S. Zegelin, *Simple and effective atmospheric monitoring for CO2 leakage.* International Journal of Greenhouse Gas Control, 2016. **46**: p. 158-174.
67. Susanto, V., et al., *Field test study on leakage monitoring at a geological CO2 storage site using hydrogen as a tracer.* International Journal of Greenhouse Gas Control, 2016. **50**: p. 37-48.
68. Schroder, I.F., et al., *The role of soil flux and soil gas monitoring in the characterisation of a CO2 surface leak: A case study in Qinghai, China.* International Journal of Greenhouse Gas Control, 2016. **54, Part 1**: p. 84-95.
69. Yu, C.-H., C.-H. Huang, and C.-S. Tan, *A review of CO2 capture by absorption and adsorption.* Aerosol and Air Quality Research, 2012. **12**(5): p. 745-769.
70. Tarka, T.J.C., J.P.; Gray, M.L.; Fauth, D., *CO2 capture system using amine enhanced solid sorbents. Presented at the Fifth Annual Conference on Carbon Capture & Sequestration.* (Available on Internet at: https://www.netl.doe.gov/publications/proceedings/06/carbon-seq/Tech%20Session%20152.pdf): Alexandria, VA, USA.
71. Wang, J., et al., *Recent advances in solid sorbents for CO2 capture and new development trends.* Energy & Environmental Science, 2014. **7**(11): p. 3478-3518.
72. Guy, P.K., *Adsorption Technology & Design*

in *Adsorption Technology & Design*. 1998, Butterworth-Heinemann: Oxford. p. ix-x.
73. Sevilla, M., et al., *Highly Porous Renewable Carbons for Enhanced Storage of Energy-Related Gases (H2 and CO2) at High Pressures.* ACS Sustainable Chemistry & Engineering, 2016. **4**(9): p. 4710-4716.
74. Ribeiro, R.P.P.L., C.A. Grande, and A.E. Rodrigues, *Activated carbon honeycomb monolith – Zeolite 13X hybrid system to capture CO2 from flue gases employing Electric Swing Adsorption.* Chemical Engineering Science, 2013. **104**: p. 304-318.
75. Foley, H.C., *Carbogenic molecular sieves: synthesis, properties and applications*. Vol. 4, 407-433. (1995).
76. Burchell, T.D., et al., *A novel process and material for the separation of carbon dioxide and hydrogen sulfide gas mixtures.* Carbon, 1997. **35**(9): p. 1279-1294.
77. Razavi, S.S., S.M. Hashemianzadeh, and H. Karimi, *Modeling the adsorptive selectivity of carbon nanotubes for effective separation of CO(2)/N(2) mixtures.* J Mol Model, 2011. **17**(5): p. 1163-72.
78. Cinke, M., et al., *CO2 adsorption in single-walled carbon nanotubes.* Chemical Physics Letters, 2003. **376**(5–6): p. 761-766.
79. Chester, A.W. and E.G. Derouane, *Zeolite Characterization and Catalysis*. 1 ed.: Springer Netherlands. 360.

80. Jiao, J., et al., *Improvement of adsorbent materials for CO2 capture by amine functionalized mesoporous silica with worm-hole framework structure.* Chemical Engineering Journal, 2016. **306**: p. 9-16.
81. Cecilia, J.A., et al., *Functionalization of hollow silica microspheres by impregnation or grafted of amine groups for the CO2 capture.* International Journal of Greenhouse Gas Control, 2016. **52**: p. 344-356.
82. Zhang, W.-X., et al., *Metal cluster-based functional porous coordination polymers.* Coordination Chemistry Reviews, 2015. **293–294**: p. 263-278.
83. Jahromi, S., *Storage stability of melamine-formaldehyde resin solutions, 1. The mechanism of instability.* Macromolecular Chemistry and Physics, 1999. **200**(10): p. 2230-2239.
84. Caplow, M., *Kinetics of carbamate formation and breakdown.* J. Am. Chem. Soc., 1968. **90**: p. 6795-6803.
85. Danckwerts, P.V., *The reaction of CO_2 with Ethanolamines.* Chem. Eng. Sci., 1976. **34**: p. 443-446.
86. Sartori, G.S., D.W., *Sterically hindered amines for CO_2 removal from gases.* Ind. Eng. Chem. Fundam., 1983. **22**: p. 239-249.
87. Mercedes Maroto-Valer, M., et al., *Sorbents for CO_2 capture from high carbon fly ashes.* Waste Management, 2008. **28**(11): p. 2320-2328.
88. Zhang, Y.M.-V., M. M.;Tang, Z., *Microporous activated carbons produced from unburned carbon fly ash and their application for CO_2 capture.* Div. Fuel Chem., Am. Chem Soc. - Prepr. Symp., 2004. **49**: p. 304-305.
89. Gray, M.L., et al., *CO_2 capture by amine-enriched fly ash carbon sorbents.* Separation and Purification Technology, 2004. **35**(1): p. 31-36.
90. Gray, M.L.S., Y.; Champagne, K. J.; Pennline, H.; Stevens, R. W. Jr.; Toochinda, P.; Chuang, S.S.C., *Solid amine CO_2 capture sorbents.* Div. Fuel Chem., Am. Chem Soc. - Prepr. Symp., 2002. **47**: p. 63-64.
91. Dasgupta, S., et al., *Carbon Di-Oxide Removal with Mesoporous Adsorbents in a Single Column Pressure Swing Adsorber.* Separation Science and Technology, 2009. **44**(16): p. 3973-3983.
92. Jadhav, P.D., et al., *Monoethanol Amine Modified Zeolite 13X for CO2 Adsorption at Different Temperatures.* Energy & Fuels, 2007. **21**(6): p. 3555-3559.
93. Satyapal, S., et al., *Performance and Properties of a Solid Amine Sorbent for Carbon Dioxide Removal in Space Life Support Applications.* Energy & Fuels, 2001. **15**(2): p. 250-255.
94. Birbara, P.J. and T.A. Nalette, *Regenerable supported amine-polyol sorbent*. 1996, Google Patents.
95. Choi, S., J.H. Drese, and C.W. Jones, *Adsorbent Materials for Carbon Dioxide Capture from Large Anthropogenic Point Sources.* ChemSusChem, 2009. **2**(9): p. 796-854.
96. Lee, S., et al., *Screening Test of Solid Amine Sorbents for CO2 Capture.* Industrial & Engineering Chemistry Research, 2008. **47**(19): p. 7419-7423.
97. Xu, X., et al., *Preparation and characterization of novel CO2 "molecular basket" adsorbents based on polymer-modified mesoporous molecular sieve MCM-41.* Microporous and Mesoporous Materials, 2003. **62**(1–2): p. 29-45.
98. Xu, X., et al., *Influence of Moisture on CO2 Separation from Gas Mixture by a Nanoporous Adsorbent Based on Polyethylenimine-Modified Molecular Sieve MCM-41.* Industrial & Engineering Chemistry Research, 2005. **44**(21): p. 8113-8119.

99. Wang, D., et al., *Three-dimensional molecular basket sorbents for CO2 capture: Effects of pore structure of supports and loading level of polyethylenimine.* Catalysis Today, 2014. **233**: p. 100-107.
100. Aroua, M.K., et al., *Adsorption capacities of carbon dioxide, oxygen, nitrogen and methane on carbon molecular basket derived from polyethyleneimine impregnation on microporous palm shell activated carbon.* Separation and Purification Technology, 2008. **62**(3): p. 609-613.
101. Belmabkhout, Y.S., A., *Isothermal versus Non-isothermal Adsorption—Desorption Cycling of Triamine-Grafted Pore-Expanded MCM-41 Mesoporous Silica for CO2 Capture from Flue Gas.* J. Am. Chem. Soc., 2010. **132**: p. 6312-6314.
102. Mirzaeian, M. and P.J. Hall, *The control of porosity at nano scale in resorcinol formaldehyde carbon aerogels.* Journal of Materials Science, 2009. **44**(10): p. 2705-2713.
103. Taylor, S.J., et al., *Gelation Mechanism of Resorcinol-Formaldehyde Gels Investigated by Dynamic Light Scattering.* Langmuir, 2014. **30**(34): p. 10231-10240.
104. Tamon, H.I., H.; Mikami, M.; Okazaki, M., *Porous structure of organic and carbon aerogels synthesized by sol-gel polycondensation of resorcinol with formaldehyde.* Carbon, 1997. **35**(6): p. 791-796.
105. Mulik, S. and C. Sotiriou-Leventis, *Resorcinol-Formaldehyde.* Aerogels handbook, 2011: p. 215-34.
106. Pierre, A.C. and G.M. Pajonk, *Chemistry of Aerogels and Their Applications.* Chemical Reviews, 2002. **102**(11): p. 4243-4266.
107. Hench, L.L. and J.K. West, *The sol-gel process.* Chemical Reviews, 1990. **90**(1): p. 33-72.
108. Arachchige, I.U., J.L. Mohanan, and S.L. Brock, *Sol−Gel Processing of Semiconducting Metal Chalcogenide Xerogels: Influence of Dimensionality on Quantum Confinement Effects in a Nanoparticle Network.* Chemistry of Materials, 2005. **17**(26): p. 6644-6650.
109. Worsley, M.A., J.H. Satcher, and T.F. Baumann, *Synthesis and Characterization of Monolithic Carbon Aerogel Nanocomposites Containing Double-Walled Carbon Nanotubes.* Langmuir, 2008. **24**(17): p. 9763-9766.
110. Pekala, R.W. and D.W. Schaefer, *Structure of organic aerogels. 1. Morphology and scaling.* Macromolecules, 1993. **26**(20): p. 5487-5493.
111. Pekala, R.W., *Organic aerogels from the polycondensation of resorcinol with formaldehyde.* Journal of Materials Science, 1989. **24**(9): p. 3221-3227.
112. Gebert, M.S. and R.W. Pekala, *Fluorescence and light-scattering studies of sol-gel reactions.* Chemistry of Materials, 1994. **6**(2): p. 220-226.
113. Wu, D., et al., *Low-density organic and carbon aerogels from the sol–gel polymerization of phenol with formaldehyde.* Journal of Non-Crystalline Solids, 2005. **351**(10–11): p. 915-921.
114. Jirglová, H., A.F. Pérez-Cadenas, and F.J. Maldonado-Hódar, *Synthesis and Properties of Phloroglucinol−Phenol−Formaldehyde Carbon Aerogels and Xerogels.* Langmuir, 2009. **25**(4): p. 2461-2466.
115. Michel Andre Aegerter, N.L., Matthias M. Koebel, *Aerogels handbook*. 2011: Springer Science & Business Media.
116. Mulik, S., C. Sotiriou-Leventis, and N. Leventis, *Time-Efficient Acid-Catalyzed Synthesis of Resorcinol− Formaldehyde Aerogels.* Chemistry of Materials, 2007. **19**(25): p. 6138-6144.
117. Merzbacher, C.I., et al., *Carbon aerogels as broadband non-reflective materials.* Journal of non-crystalline solids, 2001. **285**(1): p. 210-215.

118. Pizzi, A.M., K. L.;, *Handbook of adhesive technology: Second edition.*, ed. I. Marcel Dekker. 2003, New York.
119. Zhou, H., et al., *Facile preparation and ultra-microporous structure of melamine-resorcinol-formaldehyde polymeric microspheres.* Chemical Communications, 2013. **49**(36): p. 3763-3765.
120. Hodgins, T.S., et al., *Melamine-Formaldehyde Film-Forming Compositions.* Industrial & Engineering Chemistry, 1941. **33**(6): p. 769-779.
121. Okano, M. and Y. Ogata, *Kinetics of the Condensation of Melamine with Formaldehyde.* Journal of the American Chemical Society, 1952. **74**(22): p. 5728-5731.
122. Van Blaaderen, A.V.G., J.; Vrij, A., *Monodisperse colloidal silica spheres from tetraalkoxysilanes: Particle formation and growth mechanism.* J. Colloid Interface Sci., 1992. **154**: p. 481-501.
123. Liu, J., et al., *Extension of The Stöber Method to the Preparation of Monodisperse Resorcinol–Formaldehyde Resin Polymer and Carbon Spheres.* Angewandte Chemie International Edition, 2011. **50**(26): p. 5947-5951.
124. Howard, K.S. and R.A. McAllister, *Surface tension of acetone-water solutions up to their normal boiling points.* AIChE Journal, 1957. **3**(3): p. 325-329.
125. Horikawa, T., J.i. Hayashi, and K. Muroyama, *Controllability of pore characteristics of resorcinol–formaldehyde carbon aerogel.* Carbon, 2004. **42**(8–9): p. 1625-1633.
126. Job, N., et al., *Porous carbon xerogels with texture tailored by pH control during sol–gel process.* Carbon, 2004. **42**(3): p. 619-628.
127. Feng, Y.N., et al., *Effects of further adding of catalysts on nanostructures of carbon aerogels.* Materials Science and Engineering: B, 2008. **148**(1–3): p. 273-276.
128. Yamamoto, T., et al., *Control of mesoporosity of carbon gels prepared by sol–gel polycondensation and freeze drying.* Journal of Non-Crystalline Solids, 2001. **288**(1–3): p. 46-55.
129. Fung, A.W.P., et al., *Relationship between particle size and magnetoresistance in carbon aerogels prepared under different catalyst conditions.* Journal of Non-Crystalline Solids, 1995. **186**: p. 200-208.
130. Fairen-Jimenez, D., F. Carrasco-Marin, and C. Moreno-Castilla, *Porosity and surface area of monolithic carbon aerogels prepared using alkaline carbonates and organic acids as polymerization catalysts.* Carbon, 2006. **44**(11): p. 2301-2307.
131. Bock, V., A. Emmerling, and J. Fricke, *Influence of monomer and catalyst concentration on RF and carbon aerogel structure.* Journal of Non-Crystalline Solids, 1998. **225**: p. 69-73.
132. Mahata, N., et al., *Tuning of texture and surface chemistry of carbon xerogels.* Journal of Colloid and Interface Science, 2008. **324**(1–2): p. 150-155.
133. Magueijo, V., et al., *Polysulfone mixed matrix gas separation hollow fibre membranes filled with polymer and carbon xerogels.* Chemical Engineering Science, 2013. **92**: p. 13-20.
134. Lu, X. and M. Arduini-Schuster, *Thermal conductivity of monolithic organic aerogels.* Science, 1992. **255**(5047): p. 971.
135. Fontana, F., *Memorie Mat.* Soc. ital. Sci., 1777. **1**(679).
136. de Saussure, N.-T., *Gilbert's Ann.* 1814. **47**: p. 113.
137. Mitscherlich, E., *Pogg. Ann.* 1843. **59**(94).
138. Kayser, H., *Wied. Ann.* 1881. **14**(451).
139. Langmuir, I., *The adsorption of gases on plane surfaces of glass, mica and platinum.* Journal of the American Chemical Society, 1918. **40**(9): p. 1361-1403.

140. Le Chatelier, H. and O. Boudouard, *Limits of flammability of gaseous mixtures.* Bull. Soc. Chim.(Paris), 1898. **19**: p. 483-488.
141. Webb, P.A., *introduction to chemical adsorption analytical techniques and their applications to catalysis.* MIC Technical Publications, 2003.
142. Yang, R.T., *Carbon adsorption for pollution control by Nicholas P. Cheremisinoff and Paul N. Cheremisinoff, prentice hall, englewood ciffs, nj, 1993, 216pp., $57.00.* AIChE Journal, 1994. **40**(2): p. 381-381.
143. Gregg, S.J. and K.S.W. Sing, *Adsorption, surface area, and porosity*. 1982, London; New York: Academic Press.
144. London, F., Z. Phys., 1930. **63,245**.
145. Honig, J.M., N. Y. Acad. Sci., 1954. **58, 1247**.
146. Sing, K.S.W., et al., *IUPAC recommendations. Reporting physisorption data for gas/solid systems.* Handbook of Heterogeneous Catalysis (2nd Edition), 2008. **2**: p. 1217-1230.
147. Thommes, M., et al., *Physisorption of gases, with special reference to the evaluation of surface area and pore size distribution (IUPAC Technical Report).* Pure and Applied Chemistry, 2015. **87**(9-10): p. 1051-1069.
148. Henry, W., *Experiments on the quantity of gases absorbed by water, at different temperatures, and under different pressures.* Philosophical Transactions of the Royal Society of London, 1803. **93**: p. 29-276.
149. Lowell, S., et al., *Characterization of porous solids and powders: surface area, pore size and density*. 2004: Springer.
150. Polanyi, M., *The Potential Theory of Adsorption.* Science, 1963. **141**(3585): p. 1010-1013.
151. Butt, H.J., K. Graf, and M. Kappl, Physics and chemistry of interfaces, 2003: p. 193-195.
152. Kapoor, A., J.A. Ritter, and R.T. Yang, *On the Dubinin-Radushkevich equation for adsorption in microporous solids in the Henry's law region.* Langmuir, 1989. **5**(4): p. 1118-1121.
153. Dubinin, M., *A study of the porous structure of active carbons using a variety of methods.* Quarterly Reviews, Chemical Society, 1955. **9**(2): p. 101-114.
154. Bering, B., M. Dubinin, and V. Serpinsky, *Theory of volume filling for vapor adsorption.* Journal of colloid and interface science, 1966. **21**(4): p. 378-393.
155. Talu, O. and A.L. Myers, *Rigorous thermodynamic treatment of gas adsorption.* AIChE journal, 1988. **34**(11): p. 1887-1893.
156. Hacskaylo, J.J. and M.D. LeVan, *Correlation of adsorption equilibrium data using a modified Antoine equation: a new approach for pore-filling models.* Langmuir, 1985. **1**(1): p. 97-100.
157. Marsh, H. and B. Rand, *The characterization of microporous carbons by means of the Dubinin-Radushkevich equation.* Journal of Colloid and Interface Science, 1970. **33**(1): p. 101-116.
158. Langmuir, I., *The adsorption og gases on plane surface of glass, mica and platinum.* . Journal of the American Chemical Society, 1918. **40**(9): p. 1361-1403.
159. Langmuir, I., *The constitution and fundamentals properties of solids and liquids. II. Liquids.* Journal of the American Chemical Society, 1917. **39**(9): p. 1848-1906.
160. Masel, R.I., *Principles of adsorption and reaction on solid surfaces*. Vol. 3. 1996: John Wiley & Sons.
161. Freundlich, H., *Kapillarchemie, eine Darstellung der Chemie der Kolloide und verwandter Gebiete, von Dr. Herbert Freundlich*. 1909: akademische Verlagsgesellschaft.

162. Brunauer, S., P.H. Emmet, and E. Teller, *Adsorption of gases in multimolecular layers.* Journal of the American Chemical Society, 1938. **60**: p. 309-19.
163. Barrett, E.P., L.G. Joyner, and P.P. Halenda, *The determination of pore volume and area distributions in porous substances. I. Computations from nitrogen Isotherms.* Journal of the American Chemical Society, 1951. **73**: p. 373-80.
164. Skinner, L.M. and J.R. Sambles, *The Kelvin equation—a review.* Journal of Aerosol Science, 1972. **3**(3): p. 199-210.
165. S. Lowell, J.E.S., M. A. Thomas, M. Thommes, *Characterization of Porous Solids and Powders: Surface Area, Pore Size and Density.* Particle Technology Series. 2004: Springer Netherlands.
166. Lippens, B.C. and J. De Boer, *Studies on pore systems in catalysts: V. The t method.* Journal of Catalysis, 1965. **4**(3): p. 319-323.
167. Harkins, W.D. and G. Jura, *Surfaces of solids. XIII. A vapor adsorption method for the determination of the area of a solid without the assumption of a molecular area, and the areas occupied by nitrogen and other molecules on the surface of a solid.* Journal of the American Chemical Society, 1944. **66**(8): p. 1366-1373.
168. ASTM-D-6556-01, *Standard test method for carbon black-total and external surface area by nitrogen adsorption.*
169. Rouquerol, J., P. Llewellyn, and F. Rouquerol, *Is the BET equation applicable to microporous adsorbents?*, in *Studies in Surface Science and Catalysis*, F.R.-R.J.R. P.L. Llewellyn and N. Seaton, Editors. 2007, Elsevier. p. 49-56.
170. Fletcher, A.J., Y. Uygur, and K.M. Thomas, *Role of surface functional groups in the adsorption kinetics of water vapor on microporous activated carbons.* The Journal of Physical Chemistry C, 2007. **111**(23): p. 8349-8359.
171. Smith, B.C., *Fundamentals of Fourier transform infrared spectroscopy*. 2011: CRC Press Inc.
172. Williams, D.H. and I. Fleming, *Spectroscopic methods in organic chemistry*. Fourth edition ed. 1980: McGraw-Hill.
173. Egerton, R., *Physical Principles of Electron Microscopy: An Introduction to TEM, SEM, and AEM*. 2016: Springer Science & Business Media.
174. PREGL, F., *Quantitative micro-analysis of organic substances.* Chemistry, 1922-1941, 1999. **2**: p. 28.
175. McMahon, G., *Process Analytical Instrumentation in Industry.* Analytical Instrumentation: A Guide to Laboratory, Portable and Miniaturized Instruments: p. 223-249.
176. Boehm, H.P., *Some aspects of the surface-chemistry of carbon-blacks and other carbons.* Carbon, 1994. **32**(5): p. 759-769.
177. Boehm, H.P., *Surface chemical characterization of carbons from adsorption studies.* Adsorption by carbons, 2008: p. 301-27.
178. Boehm, H.P., *Surface oxides on carbon and their analysis: a critical assessment.* Carbon, 2002. **40**(2): p. 145-149.
179. Goertzen, S.L., et al., *Standardization of the Boehm titration. Part I. CO2 expulsion and endpoint determination.* Carbon, 2010. **48**(4): p. 1252-1261.
180. Oickle, A.M., et al., *Standardization of the Boehm titration: Part II. Method of agitation, effect of filtering and dilute titrant.* Carbon, 2010. **48**(12): p. 3313-3322.
181. Hüfner, S., *Photoelectron spectroscopy: principles and applications*. 2013: Springer Science & Business Media.
182. Hand, D.W., et al., *Prediction of multicomponent adsorption equilibria using ideal adsorbed solution theory.* Environmental science & technology, 1985. **19**(11): p. 1037-1043.

183. Qiao, S., K. Wang, and X. Hu, *Using local IAST with micropore size distribution to predict multicomponent adsorption equilibrium of gases in activated carbon.* Langmuir, 2000. **16**(3): p. 1292-1298.
184. Anderson, L., *The effectof the catalyst on the formation of RF xerogels*, in *Chemical and Process Engineering*

2014, University of Strathclyde: Glasgow, United Kingdom.
185. Chapman, R., P. Averell, and R. Harris, *Solubility of melamine in water.* Industrial & Engineering Chemistry, 1943. **35**(2): p. 137-138.
186. Al-Muhtaseb, S.A. and J.A. Ritter, *Preparation and Properties of Resorcinol–Formaldehyde Organic and Carbon Gels.* Advanced Materials, 2003. **15**(2): p. 101-114.
187. ElKhatat, A.M. and S.A. Al-Muhtaseb, *Advances in tailoring resorcinol-formaldehyde organic and carbon gels.* Advanced materials, 2011. **23**(26): p. 2887-2903.
188. Denn, M.M., *Process fluid mechanics*. 1980: Prentice Hall.
189. Chapman, R.P., P.R. Averell, and R.R. Harris, *Solubility of Melamine in Water.* Industrial & Engineering Chemistry, 1943. **35**(2): p. 137-138.
190. Rasines, G., et al., *N-doped monolithic carbon aerogel electrodes with optimized features for the electrosorption of ions.* Carbon, 2014(0).
191. Głowacz-Czerwonka, D., *Perspektywa zastosowań roztworów melaminy w reaktywnych rozpuszczalnikach w technologii polimerów.* Chemik, 2013. **67**(4): p. 289-300.
192. Głowacz-Czerwonka, D., *Prospects of using melamine solutions in reactive solvents in polymer technology.* Chemik, 2013. **67**: p. 289-300.
193. Ullah, S., et al., *Synthesis and thermal degradation studies of melamine formaldehyde resins.* The Scientific World Journal, 2014. **2014**.
194. Center, Q.d.C.E.R.I., *Pure components properties*.
195. Reid, C. and K. Thomas, *Adsorption of gases on a carbon molecular sieve used for air separation: linear adsorptives as probes for kinetic selectivity.* Langmuir, 1999. **15**(9): p. 3206-3218.
196. Reid, C., I. O'koy, and K. Thomas, *Adsorption of gases on carbon molecular sieves used for air separation. Spherical adsorptives as probes for kinetic selectivity.* Langmuir, 1998. **14**(9): p. 2415-2425.
197. Fletcher, A.J. and K.M. Thomas, *Compensation effect for the kinetics of adsorption/desorption of gases/vapors on microporous carbon materials.* Langmuir, 2000. **16**(15): p. 6253-6266.
198. Webster, C.E., R.S. Drago, and M.C. Zerner, *Molecular dimensions for adsorptives.* Journal of the American Chemical Society, 1998. **120**(22): p. 5509-5516.
199. Sinha, R.K., *Flue gas conditioning for the removal of particulates, hazardous substances, NOx, and SOx*. 1999, Google Patents.
200. Shemwell, B.E., A. Ergut, and Y.A. Levendis, *Economics of an integrated approach to control SO2, NOx, HCl, and particulate emissions from power plants.* Journal of the Air & Waste Management Association, 2002. **52**(5): p. 521-534.
201. Elliott, G. and A. Startin. *Ceramic Filter Elements for Emission Control on Glass Furnaces—Efficient Multi-Pollutant Treatment in a Single Step*. in *Ceramic Engineering and Science Proceedings*. 2010.
202. Amrhein, G.T., S.J. Vecci, and J.M. Rackley, *Furnace ammonia and limestone injection with dry scrubbing for improved simultaneous SOX and NOX removal*. 1993, Google Patents.

203. Sartori, G., et al., *Sterically-hindered amines for acid-gas absorption.* Separation and purification methods, 1987. **16**(2): p. 171-200.
204. Huang, H.Y., et al., *Amine-grafted MCM-48 and silica xerogel as superior sorbents for acidic gas removal from natural gas.* Industrial & Engineering Chemistry Research, 2003. **42**(12): p. 2427-2433.
205. Belmabkhout, Y., G. De Weireld, and A. Sayari, *Amine-bearing mesoporous silica for CO2 and H2S removal from natural gas and biogas.* Langmuir, 2009. **25**(23): p. 13275-13278.
206. Erisman, J.W., et al., *How a century of ammonia synthesis changed the world.* Nature Geoscience, 2008. **1**(10): p. 636.
207. Kandemir, T., et al., *The Haber–Bosch process revisited: on the real structure and stability of "ammonia iron" under working conditions.* Angewandte Chemie International Edition, 2013. **52**(48): p. 12723-12726.
208. Smil, V., *Detonator of the population explosion.* Nature, 1999. **400**(6743): p. 415-415.